Design of new heterogeneous catalysts for renewable energy based on metallic quantum clusters and the surrounding

Mravak, Antonija

University of Split

Faculty of Science

Postgraduate University Study in Biophysics

Doctoral thesis

DESIGN OF NEW HETEROGENEOUS CATALYSTS FOR RENEWABLE ENERGY BASED ON METALLIC QUANTUM CLUSTERS AND THE SURROUNDING

Antonija Mravak

Split, 2023

Sveučilište u Splitu

Prirodoslovno-matematički fakultet

Poslijediplomski sveučilišni studij Biofizika

Doktorski rad

DIZAJN NOVIH HETEROGENIH KATALIZATORA ZA OBNOVLJIVU ENERGIJU TEMELJEN NA METALNIM KVANTNIM KLASTERIMA I OKRUŽENJU

Antonija Mravak

Split, 2023

Sveučilište u Splitu, Prirodoslovno-matematički fakultet

Odjel za fiziku, Poslijediplomski sveučilišni studij Biofizika

DIZAJN NOVIH HETEROGENIH KATALIZATORA ZA OBNOVLJIVU ENERGIJU TEMELJEN NA METALNIM KVANTNIM KLASTERIMA I OKRUŽENJU

Doktorski rad autorice Antonije Mravak kao dio obaveza potrebnih da se dobije doktorat znanosti, izrađen je pod vodstvom mentorice prof. dr. dr. h. c. Vlaste Bonačić-Koutecký i komentora prof. dr. sc. Mile Dželalije.

Dobiveni akademski naziv i stupanj: doktorica prirodnih znanosti iz polja fizika.

Povjerenstvo za ocjenu i obranu doktorskog rada u sastavu:

1. prof. dr. sc. Ante Bilušić ——————————————————
   (Prirodoslovno-matematički fakultet u Splitu, predsjednik)

2. prof. dr. sc. Leandra Vranješ Markić ——————————————————
   (Prirodoslovno-matematički fakultet u Splitu, članica)

3. dr. sc. Stefan Vajda, dr. habil. ——————————————————
   (Institut fizikalne kemije J. Heyrovský u Pragu, član)

potvrđuje da je disertacija obranjena dana ——————————————————

Vršitelj dužnosti voditelja studija

——————————————————

izv. prof. dr. sc. Damir Kovačić

Dekan

——————————————————

prof. dr. sc. Mile Dželalija

BASIC DOCUMENTATION CARD

University of Split, Faculty of Science   Ph.D. thesis

DESIGN OF NEW HETEROGENEOUS CATALYSTS FOR RENEWABLE ENERGY BASED ON METALLIC QUANTUM CLUSTERS AND THE SURROUNDING

Antonija Mravak

Thesis performed at:
Center of Excellence for Science and Technology-Integration of
Mediterranean region (STIM), Faculty of Science, University of Split

Abstract:

The thesis highlights the potential of metallic quantum clusters placed in various surroundings in the design of new classes of heterogeneous catalysts. In this context, new sustainable solutions are addressed through the design of materials for enhancement of fuel cell performance via production and storage of hydrogen as well as the elimination and utilization of carbon monoxide. In addition, catalytic systems for carbon dioxide conversion into useful products are proposed. Density functional theory (DFT) is used to predict the new catalysts by exploring a wide range of systems, providing an insight into the nature of active sites and the role of the surroundings. This is achieved through investigations of structural and electronic properties of the catalysts, as well as energetically favorable pathways leading to the desired products. The strategies for new material design are based on i) integration of a copper-based metallic center within the metal-organic framework and ligand protection of silver hydride cluster, ii) placing ligated ruthenium cluster inside the zeolite, and iii) depositing of monometallic and palladium-doped bimetallic copper clusters on metal oxide support. The results emerging from theoretical calculations are supplemented by experimental results obtained by our collaborators, enabling fundamental understanding and control of the function of new catalysts.

TEMELJNA DOKUMENTACIJSKA KARTICA

Sveučilište u Splitu, Prirodoslovno-matematički fakultet   Doktorski rad

DIZAJN NOVIH HETEROGENIH KATALIZATORA ZA OBNOVLJIVU ENERGIJU TEMELJEN NA METALNIM KVANTNIM KLASTERIMA I OKRUŽENJU

Antonija Mravak

Rad je izrađen na:
Centru izvrsnosti za znanost i tehnologiju-Integracija Mediteranske regije (STIM),
Prirodoslovno-matematički fakultet, Sveučilište u Splitu

Sažetak:

Teza ističe prednosti sustavnog uključivanja metalnih kvantnih klastera unutar različitih okruženja s ciljem dizajniranja novih klasa heterogenih katalizatora. U tom kontekstu, fokus je na novim održivim rješenjima za poboljšanje performansi gorivih članaka kroz materijale za proizvodnju i skladištenje vodika te eliminaciju i korištenje ugljikovog monoksida. Također, predlažu se katalitički sustavi za efikasnu i selektivnu pretvorbu ugljikovog dioksida u korisne produkte. Teorija funkcionala gustoće (DFT) koristi se za predviđanje novih katalizatora kroz istraživanje širokog spektra sustava kako bi se dobio uvid u prirodu aktivnih mjesta i ulogu okruženja. Ovo se postiže kroz istraživanje strukturalnih i elektronskih svojstava katalizatora kao i kroz određivanje energijski povoljnih puteva koji vode do željenih produkata. Strategije dizajna novih materijala temelje se na i) integraciji metalnog bakrenog centra unutar metalo-organske mreže i zaštiti klastera srebrovog hidrida pomoću liganada, ii) prijenosu ligandiranog rutenijevog klastera unutar zeolita te iii) odlaganju monometalnih i bimetalnih bakrenih klastera dopiranih paladijem na površinu metalnog oksida. Teorijski rezultati nadopunjeni su eksperimentalnim rezultatima naših suradnika te omogućuju fundamentalno razumijevanje i kontrolu funkcije novih katalizatora.

(116 stranica, 50 slika, 5 shema, 13 tablica, 147 referenci, 3 priloga, jezik izvornika: engleski)

Rad je pohranjen u:
    Nacionalnoj sveučilišnoj knjižnici u Zagrebu
    Sveučilišnoj knjižnici u Splitu
    Knjižnici Prirodoslovno-matematičkog fakulteta Sveučilišta u Splitu

Ključne riječi: teorija funkcionala gustoće, klasteri srebra, rutenija i bakra, metalo-organska mreža, zeolit, ligandi, površina metalnog oksida

Mentorica: dr. dr. h. c. Vlasta Bonačić-Koutecký, prof.
Komentor: dr. sc. Mile Dželalija, prof.
Ocjenjivači:
    1. dr. sc. Ante Bilušić, prof.
    2. dr. sc. Leandra Vranješ Markić, prof.
    3. dr. sc. Stefan Vajda, dr. habil.
Rad prihvaćen: 12.7.2023.

ACKNOWLEDGMENTS

PUBLICATIONS

The following list of publications constitute the main part of the thesis:

1. Richard A. J. O'Hair, Antonija Mravak, Marjan Krstić, and Vlasta Bonačić-Koutecký. Models facilitating the design of a new metal-organic framework catalyst for the selective decomposition of formic acid into hydrogen and carbon dioxide. *Chem-CatChem*, 11(10), 2019, 2443-2448. DOI: 10.1002/cctc.201900346

2. Howard Z. Ma, Alasdair I. McKay, Antonija Mravak, Michael S. Scholz, Jonathan M. White, Roger J. Mulder, Evan J. Bieske, Vlasta Bonačić-Koutecký, and Richard A. J. O'Hair. Structural characterization and gas-phase studies of the $[Ag_{10}H_8(L)_6]^{2+}$ nanocluster dication. *Nanoscale*, 11(47), 2019, 22880-22889.
DOI: 10.1039/c9nr08321a

3. Antonija Mravak, Marjan Krstić, Sandra M. Lang, Thorsten M. Bernhardt, and Vlasta Bonačić-Koutecký. Intrazeolite CO methanation by small ruthenium carbonyl complexes: Translation from free clusters into the cage. *ChemCatChem*, 12(15), 2020, 3857-3862. DOI: 10.1002/cctc.202000716

4. Avik Halder, Cristina Lenardi, Janis Timoshenko, Antonija Mravak, Bing Yang, Lakshmi K Kolipaka, Claudio Piazzoni, Sönke Seifert, Vlasta Bonačić-Koutecký, Anatoly I. Frenkel, Paolo Milani, and Stefan Vajda. CO_2 methanation on Cu-cluster decorated zirconia supports with different morphology: A combined experimental in situ GIXANES/GISAXS, ex situ XPS and theoretical DFT study. *ACS Catal*, 11(10), 2021, 6210-6224. DOI: 10.1021/acscatal.0c05029

5. Antonija Mravak, Stefan Vajda, and Vlasta Bonačić-Koutecký. Mechanism of catalytic CO_2 hydrogenation to methane and methanol using a bimetallic Cu_3Pd cluster at a zirconia support. *J. Phys Chem. C*, 126(43), 2022, 18306-18312. DOI: 10.1021/acs.jpcc.2c04921

Contents

Contents

Introduction

1.1 Scope and research objectives

New solutions for enhancement of fuel cell performance and mitigation of greenhouse gases are in high demand due to ever-increasing energy and environmental issues. In order to meet these global challenges, advancement of material science is crucial, enabling the transition from an oil and gas-based industry to one based on sustainable energy. The central objective of this study revolves precisely around investigation of challenging sustainability issues through catalyst design for i) hydrogen production and storage, ii) elimination and utilization of carbon monoxide, and iii) carbon dioxide conversion into useful products.

In the areas of energy and environmental research, catalysts play a major role making more than 90% of all industrially produced chemicals [1]. The concept of catalysis originated in the first half of the 19th century [2], but only 21st century offered a significant advancement through investigation of catalysts' efficiency and selectivity. These two aspects have been addressed within this study as they are valuable for understanding of catalytic systems, providing numerous prospects for their application.

Through the reduction of activation energies and enhancement of reaction rates, catalysts enable reactions to be energetically attainable. Unlike homogeneous catalysts, where reactants and products are in the same phase as catalysts, the main distinction of heterogeneous catalysts is the different phase from the reaction mixture [3]. Homogeneous catalysts offer high selectivity and relatively simple engineering but they often suffer from drawbacks such as challenging recycle and leaching out from the reactor [4]. In contrary, thanks to their easy extraction of products, recyclability, thermal stability, and large surface area, heterogeneous catalysts are readily used in industrial processes and offer clear advantages in comparison to the homogeneous ones [5, 6]. Importantly, at the nanoscale the properties of the catalysts can be altered dramatically due to their reduced size and increased surface to volume ratio [7]. In the non-scalable regime where each atom counts, they exhibit quantum size effects [7]. The unique attributes of these subnanometer size species can be exploited to bridge homogeneous and heterogeneous catalysis.

In the present research, the concept of heterogenization of homogeneous catalysts is adapted to implement the knowledge gained from the gas phase within different nanostructured materials. Hence, the research is directed toward the design of new heterogeneous nanocatalysts for broader industrial applications. With that goal, quantum clusters are included within different surroundings such as metal-organic frameworks (MOFs), organic ligands, and metal oxide support (including zeolites).

The wide variety of particle sizes, shapes, and compositions makes modeling of these materials and their properties a challenging task [8]. In addition to the electronic properties of the active site, the nature of the surrounding becomes extremely important, adding to the complexity of such systems. A thorough understanding of their physical and chemical properties is essential to gain an insight into the basic principles of the origin of the nanocatalyst activity and selectivity. For that purpose, a theoretical design based on the density functional theory (DFT), in synergy with experiments, is employed. Overall, the investigation is focused on unraveling the structural and electronic properties of the catalytic center, the role of the surrounding, as well as the reaction mechanism and energetics, for each of the studied catalysts.

The thesis introduction outlines the motivation behind the work and objectives, followed by a brief literature overview and methodology. Next, the main research directions are presented, each systematically summarizing the chosen metallic center, surrounding, and the introduced novelty through the concept of heterogenization. The following chapters are organized as an article collection, with each article addressing the design of a catalytic center inside the surrounding, organized according to the specific application.

1.2 Catalysis for a sustainable future

Growing interest in catalytic materials that produce clean energy products and eliminate the waste is instigated by massive global pollution and energy demand. Although new guidelines for coping with environmental challenges have been put into action, the net-zero CO_2 emission is still beyond the reach [9]. In this respect, the thesis addresses the following grand challenges in the areas of sustainable and renewable energy: i) hydrogen production and storage, ii) elimination and utilization of carbon monoxide, and iii) carbon dioxide conversion into useful products. The first two directions are studied in the context of proton-exchange membrane fuel cells (PEMFCs) improvement. The third one is dedicated to exploring efficient and selective catalyst for CO_2 reutilization and production of methane and methanol. The following subsections provide a concise overview of each challenge, along with summaries of relevant catalysts.

1.2.1 Hydrogen production and storage

Since the fossil fuel supply is in decline, alternative energy sources gradually come into the global focus. With zero carbon emissions and only heat and water as by-products, hydrogen is a promising and attractive clean energy carrier [10]. Although it yields the highest energy content per mass unit [11], its low volumetric energy density presents a critical technical issue for transportation and storage [12]. In particular, physical storage of H_2 in compressed gas or liquid tanks requires high energy input. In recent years, solid materials for the chemical and physical uptake and storage of hydrogen have been extensively explored [13–15]. These materials have high H_2 capacity and are usually based on hydrides, chemical hydrogen, organic liquids, and porous absorbants [16]. However, their use comes with a high energy consumption during H_2 adsorption and release.

Furthermore, 96% of the world's hydrogen production originates from non-renewable fossil fuels [17]. In this context, steam methane reforming is predominantly used with well-established technology that requires high temperatures ($> 700\ ^\circ C$) and results in high CO_2 emission [10]. On the contrary, biomass, solar power, wind, and electrolysis are nondetrimental to the environment and only account for a small fraction of total hydrogen production [10, 18]. Hence, decarbonized and cost-effective H_2 production and storage is the key to its widespread use [18]. Regarding the sustainable production of H_2, electrolysis and dehydrogenation processes are discussed as the most viable options. Recently, the natural gas combined with CO_2 capture has become a new and relatively cheap alternative [19].

In this respect, formic acid is a promising hydrogen carrier with potential application in low-temperature fuel cells. Its high volumetric capacity (53 g of H_2/L), cost-effectiveness, high stability, low flammability, and low toxicity make it an interesting candidate for replacement of traditionally used H_2 storage methods [20, 21]. The decomposition of this chemical has been thoroughly studied since the beginning of the 20th century [22, 23]. It proceeds over two main pathways; dehydrogenation and dehydration [24]. The former route produces hydrogen and carbon dioxide, while the latter produces water and carbon monoxide. Dehydration is dominant in the gas phase experiments. Therefore, a proper choice of catalyst is a prerequisite for selective extrusion of hydrogen. The catalyst search area for the selective decomposition of formic acid is spanned over both homogeneous and heterogeneous catalysts [19, 21, 25–27]. Heterogeneous nanocatalysts range from mono- to trimetallic nanoparticles, and are often based on noble metals such as Au, Ag and Pd [27].

In the search for an efficient heterogeneous catalyst for industrial application in PEMFCs, this study aims to develop a new MOF-based catalyst that offers a solution for H_2 production from formic acid, while also providing the storage.

1.2.2 Elimination and utilization of carbon monoxide

Fuel cells convert chemical into electrical energy with only water and heat as by-products, thus representing a clean source of energy. The polymer electrolyte membrane fuel cell (PEMFC) is one of the most commercially viable fuel cell types, particularly suitable for small appliances and transportation [28]. To initiate the reaction within the PEMFC, hydrogen is oxidized at the platinum-based anode catalyst. As the primary source of hydrogen, the reforming of fossil fuels creates a mixture of various gases, including carbon monoxide [29, 30]. Consequently, its presence within the fuel cell feed gas causes the poisoning of the Pt-anode and results in the decrease of PEMFC's efficiency [29, 31].

The reaction on the anode begins with dissociative chemisorption of H_2 followed by electrochemical oxidation. During the first step, competition between H_2 and CO takes place, with CO binding linearly to one or by bridge binding to two Pt atoms [31]. CO binding is favored at lower temperatures ($\sim 80\,°C$), with the tolerance up to only 10 ppm [32]. On the contrary, the tolerance to CO is significantly better (up to 1000 ppm) at higher temperatures ($\sim 130\,°C$) [32]. To mitigate the negative impact of CO on fuel cell efficiency, different strategies have been used, such as increasing the working temperature and adding oxygen to the feed gas, as well as improving the design of the Pt-based catalyst [29].

Due to a significant impact on the strength of CO binding, the composition of the catalyst, as well as size and geometry of the Pt particles, are used to modulate the catalyst performance [33]. One of the latest advances in the design of the anode catalyst is mixing of Pt with transition metals such as Pd, Ru, Pb, Co, Bi, and Ni [33, 34]. These alloys have modified electronic structure, which results in weakening of CO adsorption. From the binary alloys, Pt/Ru is one of the most notable candidates [35]. In addition, high-entropy alloys where multiple elements of different sizes lead to lattice distortions show unique properties, specially suitable for the design of Pt-based electrocatalysts [36, 37]. Another strategy that is recently investigated is geometry and interface engineering, resulting in Pt-based composites [37]. These compounds consist of metal oxides/hydroxides or carbon-based materials that provide better dispersion of the Pt atoms, ensuring improved electron transfer and enhancement of catalytic performance.

Furthermore, CO poisoning can be suppressed by preferential oxidation (PROX) catalysts which selectively promote conversion of carbon monoxide to carbon dioxide while minimizing hydrogen oxidation into water. These catalysts vary from noble to non-noble metals, with Cu-Ce-based showing superior catalytic activity [38]. Additionally, a new class of catalysts exhibiting a CO electro-oxidation potential based on bimetallic IrRu-N-C have shown a strong antipoisoning ability against CO [39].

Clearly, significant effort has been put into developing different strategies to reduce CO poisoning. The present work aims to tackle that problem through the design of

new highly active and selective catalyst for CO methanation reaction, which can serve for both removal of CO poisoning and the production of valuable methane. Such new heterogeneous catalyst is designed based on leveraging extraordinary catalytic properties of small ligated Ru-clusters within zeolite surrounding.

1.2.3   Carbon dioxide conversion into useful products

Fossil fuel exploitation inevitably leads to significant CO_2 emissions, with 36.6 Gt released just in the energy sector in 2021 [40]. Since CO_2 is a greenhouse gas, its mitigation and development of carbon-neutral energy systems is crucial. One of the best ways to close the CO_2 cycle is through its reutilization [41]. This could provide means for a sustainable future, complying with the goal of 2050 net-zero CO_2 [42].

Conversion of CO_2 through electrochemical, photocatalytic, biochemical and thermo-chemical transformations enables the production of valuable compounds [43]. Electro-chemical transformation requires a considerable amount of electrical energy, making it an economically costly method [44]. On the other hand, photocatalytic conversion is a more environmentally friendly approach, but suffers from low conversion rates and low selectivity [45]. Even though it provides better selectivity, biochemical conversion is inefficient both time- and cost-wise [46]. In this regard, one of the most promising methods for CO_2 valorization is thermal hydrogenation. To overcome the exceptional stability of CO_2, its inertness, and non-oxidizing qualities, it requires a high temperature and an effective catalyst [47]. CO_2 hydrogenation can produce a variety of products, including methane, methanol, carbon monoxide, formic acid, dimethyl ether, higher alcohols, and aromatics [16]. The most noteworthy hydrogenation reactions are the reverse water-gas shift (RWGS) and CO_2 conversion to methane and methanol.

The most widely researched catalysts for CO_2 conversion to methanol are those based on copper [48–53]. Cu is an alternative to the expensive noble metals, such as Pd, Pt, and Au [16]. Its performance can be boosted by doping, alloying and utilizing effects of surrounding. For instance, the Cu/ZnO catalysts, both bulk and supported, have been shown as highly active for methanol yield. This is attributed to the synergistic effect of ZnO which enhances the intrinsic Cu-activity [54–56]. Further promotion of its stability and activity is possible by the addition of alumina [57]. Moreover, small clusters deposited on metal oxide surfaces, such as Cu_4/Al_2O_3, offer high selectivity for methanol at low pressure and temperatures of 225 $^\circ C$ [48, 49]. Among different metal oxide supports, ZrO_2 stands out with its high thermal and mechanical stability. Its advantages are elaborated in more detail in *Subsection 1.4.3*.

Recently, MOF materials have gained significant attention in CO_2 conversion reactions. In particular, Cu nanocrystals, Pt nanoparticles, and bimetallic Cu-Zn centers have been incorporated into different MOF materials to create novel heterogeneous catalysts with

exceptional properties [58–60]. In addition, ionic liquids have gained interest as activating agents and catalysts for CO_2 conversion [61]. Regarding CO_2 methanation, catalysts range from noble metal-based (Ru, Rh, Pd) to non-noble metal (Ni, Co) [16]. Within these groups, Ni is still the most widely used [62], but the development of new promoters and metal oxide supports that are active at temperatures as low as $200°C$ is ongoing.

This study focuses on exploring the catalytic potential of small subnanometer Cu-clusters on metal oxide support for the selective conversion of CO_2 into methane and methanol. By optimizing its size and composition, the goal is to develop new cost-effective heterogeneous catalyst with improved performance.

1.3   Methodology

Modeling heterogeneous catalysis requires a multiscale approach, which essentially describes a reaction at different spatial and time-scales. The first step reveals atomic-level details from electronic structure calculations, providing information on specific intermediate reaction steps [63, 64]. This includes calculating activation barriers and adsorption energies, as well as the invaluable characteristics of the active site. Kinetic modeling as the following step uses information from the DFT calculations and experiments to connect atomic-scale and macroscopic properties (e.g., calculation of reaction rates). The next on the multiscale study is coarse-grained modeling, which enables the use of simplified descriptions of complex systems on a longer timescale. The last step is the macroscopic modeling of heat and mass transport, which describes the energy flow in the reaction tank, as well as the flow of the reactants and the products [63].

Experimental techniques are important for probing reactive centers and identifying the reaction intermediates. Also, their development is crucial to better understand the structure/function relationship, activity, and selectivity of catalysts [8]. The characterization of the catalytic material includes investigating its composition, size, shape, and morphology. Usually, microscopy-based techniques are followed by spectroscopic, X-ray, and scattering techniques that give more in-depth information on the structural and electronic properties of the catalytic surface [65].

Still, the reaction mechanism is often obscure and not entirely accessible through standard experimental procedures. Here, the quantum-mechanical calculations come into play as the foundation of the multiscale approach. They shine light into a black box of reaction mechanism and elucidate the details of the catalytic center and reaction intermediates. The thesis focuses on a DFT study of new heterogeneous materials, accompanied by complementary experimental studies. The main aspects of the DFT method, its challenges, and the main optimization techniques in catalysis are presented in the following subsections.

1.3.1   DFT method

A comprehensive knowledge and understanding of the structural and electronic properties of catalytic systems is essential to predict reactivity [66]. The means to obtain this information lies in quantum mechanics, in other words, in solving Schrödinger equation. However, finding exact solutions to multi-electron problems is unfeasible. The first step in approaching this issue is by employing Born-Oppenheimer approximation that enables decoupling of nuclear and electronic motion [67]. This is possible because nuclei are considered stationary with respect to electrons. The consequence of the Born-Oppenheimer approximation is, therefore, the description of the electron wavefunction in terms of nu-

clear coordinates, reducing the problem exclusively to the electronic part. Notably, only due to the classical aspect of nuclei behavior is inspection of the different molecular configurations and conformations meaningful [67]. Even though the Born-Oppenheimer approximation may break down in certain cases, it remains valid in all problems that have been studied as part of the thesis.

In general, there are two main ways to find an approximate solution to Schrödinger equation; over wavefunction or density function-based methods [66]. These approaches are often regarded as first principles or *ab initio* methods. It should be noted that the problems inspected within the research are limited to the ground state DFT, which implicates the use of a time-independent Schrödinger equation. Electronically excited states, on the other hand, are commonly studied using time-dependent density functional theory (TDDFT).

Density functional theory is based on leveraging electronic density to derive an energy of the system and its properties. Two basic theorems are pivotal for DFT development; Hohenberg-Kohn and Kohn-Sham. The former states that the electron density uniquely determines the ground state energy of the multi-electron system [67]. The related variational theorem states that the electron density minimizing the energy of the functional is the true ground state electron density [67]. It depends only on three spatial coordinates, allowing for simplification of the multi-electron problem. This resolved the issue encountered when dealing with wavefunctions representing a large number of electrons. Nevertheless, the practical application of DFT started only after Kohn-Sham proposed the exact calculation of the electron kinetic energy under the postulation of a non-interacting electron system [67, 68]. Basically, one part of the electron kinetic energy is exactly solvable, and the rest is a small correction term. Hence, the complex many-body problem is simplified to a set of one-electron Kohn-Sham equations. The ground state energy functional of the system is defined as [68]

$$E_{DFT}[\rho] = T_S[\rho] + E_{ne}[\rho] + J[\rho] + E_{xc}[\rho], \tag{1.1}$$

where T_S is kinetic energy functional, given by

$$T_S[\rho] = \sum \langle \phi_i | -\frac{1}{2}\nabla^2 | \phi_i \rangle \tag{1.2}$$

and $\phi_i(\mathbf{r})$ are one-electron Kohn-Sham orbitals. The electron density $\rho(\mathbf{r})$ can be expressed as

$$\rho(\mathbf{r}) = \sum_i |\phi_i(\mathbf{r})|^2. \tag{1.3}$$

E_{ne} is a nuclear-electron interaction functional given by

$$E_{ne}[\rho] = -\sum_A \int \frac{Z_A(\mathbf{R_A})\rho(\mathbf{r})}{|\mathbf{r} - \mathbf{R_A}|} d\mathbf{r} \tag{1.4}$$

with Z_A representing nuclei charges, $\mathbf{r}$ electrons, and $\mathbf{R_A}$ nuclei positions. Moreover, J is a Coulomb self-interaction of the electron density

$$J[\rho] = \frac{1}{2} \int \int \frac{\rho(\mathbf{r})\rho(r')}{|\mathbf{r} - \mathbf{r'}|} d\mathbf{r} d\mathbf{r'}. \tag{1.5}$$

E_{xc} is the exchange-correlation energy, which can be written [69] very generally as

$$E_{xc} = E_x + E_c, \tag{1.6}$$

with E_x being an exchange and E_c correlation energy. This remains an unknown part of the energy and is thus approximated by different functionals.

1.3.2   Challenges in computational catalysis

Although DFT is a powerful tool for predicting the structural and electronic properties of materials, it faces certain challenges. Main limitations are directly associated with exchange-correlation functionals (XC) that cannot be calculated exactly. Hence, improvement of the existing functionals and their proper choice in modeling is pivotal for the appropriate description of adsorption energies and reaction energetics.

The nice illustration of the XC functionals is given by the Jacob's ladder, which starts with the least complex approximations at the bottom, climbing to the chemical accuracy goal (error $<10^{-1}eV$) [66]. The local density approximation (LDA) is at the bottom of this representation and treats the electron density as a uniform electron gas. It is mostly used in solid state physics and is not suitable for bond energies estimation. The exchange correlation energy of LDA is generally given as

$$E_{xc}^{LDA}[\rho] = \int \rho(\mathbf{r})\epsilon_{xc}^{LDA}(\rho(\mathbf{r}))d\mathbf{r}, \tag{1.7}$$

where ϵ_{xc} represents exchange-correlation energy density per particle. Following LDA, the generalized gradient approximation (GGA) introduces improvements through a density gradient $\nabla\rho(\mathbf{r})$

$$E_{xc}^{GGA}[\rho] = \int \rho(\mathbf{r})\epsilon_{xc}^{GGA}(\rho(\mathbf{r}), \nabla\rho(\mathbf{r}))d\mathbf{r}. \tag{1.8}$$

Reaction barriers are generally underestimated by these functionals by several $10^{-1}eV$ [64]. On top of that, the lack of long-range correlation in LDA and GGA limits the

modeling of catalytic complexes with weak interactions, resulting in inaccuracies within the description of van der Waals forces [64, 68, 70]. In general, to consider weak dispersion forces, one option is to add the dispersion term to the DFT calculated electronic energy. Within the thesis, the Grimme GD3 dispersion correction [71] was added to calculations with GGA or hybrid functionals to account for the long-range electron correlation effects for silver ligated hydride, zeolite model, and the metallic clusters at support. These systems contain aromatic rings, ligands, and transition-metal clusters, which are strongly influenced by dispersion forces. The dispersion corrected energy is given by equation [72]

$$E^{DFT-D} = E^{DFT} + E^{D3}, \tag{1.9}$$

where E^{DFT} is DFT calculated electronic energy of the system, and E^{D3} dispersion correction, defined as

$$E^{D3} = -\frac{1}{2} \sum_{A \neq B} \sum_{n=6,8} s_n \frac{C_n^{AB}}{R_{AB}^n} f_{damp,n}^{D3}(R_{AB}). \tag{1.10}$$

C_n is the nth-order dispersion coefficient, R is the distance between two segments, and $f_{damp,n}$ damping function for the nth order long-range terms. Usually, taking the terms up to 8th or 10th order is sufficient to improve energy calculations [73].

Furthermore, the meta-GGA functionals given in the form

$$E_{xc}^{meta-GGA}[\rho] = \int \rho(\mathbf{r}) \epsilon_{xc}^{meta-GGA}(\rho(\mathbf{r}), \nabla\rho(\mathbf{r}), \tau(\mathbf{r})) d\mathbf{r} \tag{1.11}$$

include a non-interacting kinetic energy density term $\tau(\mathbf{r})$, which only slightly improves the accuracy of calculations and limits the self-interaction error [64]. In contrast, due to the introduction of exact exchange E_x^{exact}, hybrid functionals perform better in modeling electronic exchange and correlation effects. The hybrid functional is given by [66]

$$E_{xc}^{hybrid}[\rho] = E_{xc}^{GGA}[\rho] + \alpha(E_x^{exact} - E_x^{GGA}), \tag{1.12}$$

where E_x^{exact} is the exchange energy within GGA and α is the mixing parameter. Therefore, they are positioned high on the Jacob's ladder, becoming some of the most preferable options of XC functionals in chemical calculations. One of such frequently used functionals in this study is B3LYP [74–76].

Improvements in approximations inherently come with a higher computational cost, leading to another DFT limitation associated with modeling large complexes. This can be circumvented by using a larger basis set only for modeling the area around the active site and a smaller basis set for the rest. Alternatively, the quantum mechanical/molecular mechanical (QM/MM) method can be applied in a similar way. Combining GGA functionals with the density fittings [77, 78] can also speed up calculations. This approach has

been applied in the thesis to model large MOF, silver ligated hydride and zeolite models in which the GGA functional PBE [79, 80] has been used.

The highest on the Jacob's ladder and closest to the chemical accuracy ceiling is random phase approximation (RPA). Although RPA precedes DFT, it has been significantly developed since then, becoming an important advanced method in computational chemistry. This approach includes description of van der Waals interactions, uses exact exchange, and accurately describes metallic systems [64]. It is less frequently utilized in catalytic research due to its significant computational cost.

Development of new computational techniques and the increasing availability of high-performance computing resources continues to expand the applicability of DFT in this field. However, catalytic modeling requires inspection of many systems, energy pathways, and intermediate steps, which is often time-consuming. Some alternative methods, such as machine learning, can help exploring these complex reaction networks [81]. Typically, a combination of different approaches is needed to come up with the best solution for a specific catalytic problem.

1.3.3 Modeling of catalytic reactions

To gain an insight into the reaction mechanism, it is necessary to introduce the concept of the potential energy surface (PES), which plays a key role in the field of computational chemistry [82]. More precisely, a simplified two-dimensional PES or an energy profile along one reaction coordinate is calculated. Mathematically, PES is a surface with the potential energy of the structure in relation to its atomic coordinates [83]. Such a description offers numerous possibilities for interpreting molecular geometry, its properties, and reactivity and is a direct consequence of the Born-Oppenheimer approximation [67]. The study of the reaction mechanism involves optimizing each of the reactants, intermediate steps, and products, including transition states (TS), using DFT calculations at $T = 0\ K$. Eventually, optimization steps are followed by verification of the minima and transition states. Values on the energy profile are expressed as energy differences (ΔE)

$$\Delta E = E_{DFT}^{C} - E_{DFT}^{A} - E_{DFT}^{B}, \tag{1.13}$$

where E_{DFT}^{C}, E_{DFT}^{A} and E_{DFT}^{B} represent the DFT calculated energies of product C and reactants A and B, respectively. Additional aspects important for understanding catalytic reactions are the effects of temperature and pressure. Statistical thermodynamics founded on the ideal gas approximation enables inclusion of translational, rotational, and vibrational contributions to the electronic one [66]. Thus, it gives macroscopic information about the system. The energy gained by including the effects of temperature and pressure is a thermocorrected energy. To account for the thermodynamic contributions,

Gibbs free energy has been calculated for the MOF models and the supported nanoclusters. The reaction profile constructed from the relative electronic energies at $T = 0 \ K$ gives otherwise a good indication of the reaction energetics.

Potential energy surface

The most frequently used illustration of PES is an image of a mountain with hills and various valleys and passages [84]. The valleys are equilibrium geometry or minima on the potential energy surface characterized by all positive frequencies (3N-5 for a linear and 3N-6 for a nonlinear molecule; N is the number of atoms) [83]. The top of the hill, on the other hand, represents a transition state or a first-order saddle point on the PES. TS has a maximum in only one direction, which corresponds exactly to the movement from one valley to another [83]. In other words, the transition states are characterized by an imaginary frequency or a negative Hessian eigenvalue. Furthermore, the energy gradient defines the slope of the hill. Clearly, the negative gradient of energy represents the force. The gradient (g) is defined as

$$g_\nu = \left.\frac{\partial E}{\partial \mathbf{r}_\nu}\right|_{\mathbf{r}_\nu = \mathbf{r}_\nu^0}, \tag{1.14}$$

with $\mathbf{r}_\nu$ being nuclei and $\mathbf{r}_\nu^0$ any spatial positions. Another important consideration in the PES characterization is a force constant matrix, or Hessian (H), consisting of the second derivatives of the energy with respect to nuclear coordinates

$$H_{\nu\mu} = \left.\frac{\partial^2 E}{\partial \mathbf{r}_\nu \partial \mathbf{r}_\mu}\right|_{\mathbf{r}_\nu = \mathbf{r}_\nu^0}. \tag{1.15}$$

Force constant matrix provides information on the local curvature of PES [83]. In the physical sense, Hessian describes molecular vibrations and is computationally the most expensive part of PES characterization. Overall, the mathematical representation of the PES around $\mathbf{r}_\nu^0$ is given by the Taylor expansion as [66]

$$E(\mathbf{r}_\nu) = E(\mathbf{r}_\nu^0) + g(\mathbf{r}_\nu - \mathbf{r}_\nu^0) + \frac{1}{2}(\mathbf{r}_\nu - \mathbf{r}_\nu^0)^T H(\mathbf{r}_\nu - \mathbf{r}_\nu^0) + ... \tag{1.16}$$

Minimization techniques

A variety of minimization techniques have been developed so far. Regardless of the method, there are three main steps that are at the core of minimization procedure [83]. At the starting point of optimization, both the energy and derivatives are calculated. Here, the gradients are essential to ensure the proper direction of movement along the PES. This is followed by the structural adjustments that take place as a second step. Finally, the new position is tested to examine if all the conditions are satisfied for the

geometry convergence. The steps are usually followed by a frequency calculation, which is a prerequisite for verification of the stationary point.

One simple minimization algorithm is the steepest descent (SD) method, which approaches the minimum by evaluating the function in the negative gradient direction [85]. However, this method often oscillates around the minimum, limiting its application to locating function minima. The conjugate gradient (CG) method builds on the SD principle but uses a combination of the former search direction and the present negative gradient to achieve better convergence. However, it is limited to detecting only the minima [83]. The most common are Newton-based minimization methods. The Newton-Raphson (NR) method starts with a Taylor expansion of the energy function around the current point with the Newton step (Δx) [82, 83, 85] defined as

$$\Delta x = -H^{-1}g. \tag{1.17}$$

It uses both analytical gradient and analytical Hessian to minimize the energy of the system. Compared to NR, the quasi-Newton (QN) approach is less expensive and uses an approximate Hessian at the beginning of the calculations. Also, the QN method uses the updated approximate Hessian at each subsequent step by using the position change and change in the gradient [85]. The Broyden-Fletcher-Goldfarb-Shanno (BFGS) updating algorithm is commonly applied within Gaussian program calculations [86], including those in the present research. Another alternative minimization method is geometry direct inversion in iterative subspace (GDIIS), centered on linear interpolation and extrapolation methods, superior to NR only for the very flat PES [83]. Depending on the molecule's size, proximity to the minimum, and optimization difficulty, different methods may be used alone or in combination with others.

Transition state search

TS, as a first-order saddle point or a maximum on the PES, represents one of the most challenging parts of the reaction profile calculation. While there are many effective minimization algorithms, TS search generally does not include methods that always work. The two main groups of methods have been used within this research; interpolation and the local information method. The former group of methods is useful when the reactants and products located around the TS area are known. Some of the interpolation methods are linear synchronous (LST), quadratic synchronous transit (QST) and synchronous transit-guided quasi-Newton (STQN) [83]. The LST method involves linearly varying the coordinates without optimization along the path from the reactants to the products. As all variables change synchronously, the highest energy point along the path corresponds to the transition state [83]. In the QST method, the reaction path is approximated by

a parabola while in STQN that is a circle [87, 88]. These two methods are implemented within the Gaussian program [86] as the QST2 and QST3 methods. Usually, finding a TS region is followed by Newton-Raphson optimization [83, 86]. Although both QST2 and QST3 approaches have been applied in the course of this research, they were not very effective for the large investigated models. In comparison to interpolation, local TS search methods do not require prior knowledge of the reactants and products, but instead use an energy function and its first and second derivatives. These methods require a good starting guess for the TS and the explicit force constant matrix which are computationally expensive.

The robust optimization algorithm for both minimization and TS search in Gaussian is Berny, developed by B. Schloegel [89]. For TS search, the calculation of explicit Hessian is required at the beginning, and for complicated cases, also at each optimization step. Sometimes, the scanning of the PES along one reaction coordinate is a helpful approach for locating transition states on a flat surface. The shortcoming is that many time-consuming scans are necessary.

Intrinsic reaction coordinate (IRC)

This method ensures that the TS actually connects two minima of interest [90, 91]. The intrinsic reaction coordinate [83] is defined by

$$\frac{dx(s)}{ds} = -\frac{g}{|g|} = t, \tag{1.18}$$

where s is the length of the path, t is the normalized gradient, and x is the mass weighted coordinate. Along with IRC, the identification of the active reaction coordinate in imaginary frequency offers a reliable way to validate the TS. IRC method can follow the reaction in both the reverse and forward direction but requires the calculation of a force constant matrix at the starting point of optimization. This approach was particularly useful for modeling a complex reaction network of CO_2 methanation, which includes multiple transition states that needed to be verified.

DFT-molecular dynamics (DFT-MD) method

DFT-MD is computational method that describes dynamics of the material at the atomic level by combining the quantum mechanical DFT approach with the classical molecular dynamics. In practice, classical Newton's equations of motion at finite temperature are calculated using numerical algorithm such as Verlet, while DFT calculations provide energies of the system and forces acting upon it. At each time step, electron density is updated based on the current configuration of the atoms. The computational cost of the method depends on the number of steps, as well as the system's size and the choice of

the exchange-correlation functional. DFT-MD has many applications in material science, including the study of catalytic reactions and the exploration of complex material properties. Within this study, it has been used to investigate model of supported bimetallic cluster to examine CO_2 binding at high temperatures.

Overview of the investigation steps

Defining catalyst model: The first step is careful consideration of the catalyst model, which requires appropriate design of metallic center and the surrounding. The modeling usually begins with designing smaller systems and gradually expanding the surrounding environment, ultimately selecting the optimal cluster size representing both the active site and the surrounding.

Calculation set-up: The size and the composition of the model system directly affect the choice of the functional and basis set. Usually, the functionals are chosen between the GGA and hybrid ones depending on the type of the problem and desired accuracy level. To gain insight into the performance of different functionals, previous benchmarks for specific system types are examined. Also, the charge, multiplicity and coordinates have to be specified. At this step, dispersion correction is included in calculations. Additional details regarding computational approaches and methods are given within computational/theoretical sections of the respective papers.

Geometry optimization: The structure is gradually relaxed until the defined convergence criteria is met. Generally, convergence criteria for energy in all calculations is 10^{-8} *Hartree*. The following step is usually extensive search for the lowest energy isomer, typically conducted to identify the most stable configuration of the catalyst.

Study of binding sites and energies: DFT-MD method is helpful for determining the binding site of an adsorbate at certain temperature. Here, the chosen temperature depends on the known experimental values. This step is usually followed by series of optimizations to determine the most stable complex. Also, binding energies are calculated to assess the reactivity and stability of the catalyst.

Calculation of reaction pathway: The modeling of the catalytic reaction involves calculating and mapping out all the minima and transition states. This step requires the use of different optimization algorithms, chosen based on their cost-effectiveness and system complexity. It is crucial to verify each step which typically includes performing frequency calculations and IRC analysis. Finally, the obtained bond lengths and activation energies are compared with previous benchmarks and experimental results to assess the accuracy and reliability of the model. This step is often repeated to explore different reaction branches and pathways.

1.4   Research directions

Advancement of theoretical and experimental methods, coupled with the progress in computing power, enables the exploration of increasingly more complex systems, including heterogeneous catalysts at the nanoscale. A promising approach for the development of these systems is through the inclusion of widely studied metallic clusters from the gas phase within new surroundings. Specifically, these surrounding materials include metal-organic frameworks (MOFs), ligands, zeolites, and metal oxide supports. By leveraging their properties, the aim is to develop new heterogeneous catalysts for a number of energy and environmental applications.

The impact of the surrounding on catalytic properties of metallic clusters ranges from protection, stabilization, improved metal distribution to induced synergy [92–94]. However, some of the effects can be disadvantageous, such as blocking of the active site, as well as its inactivation [95].
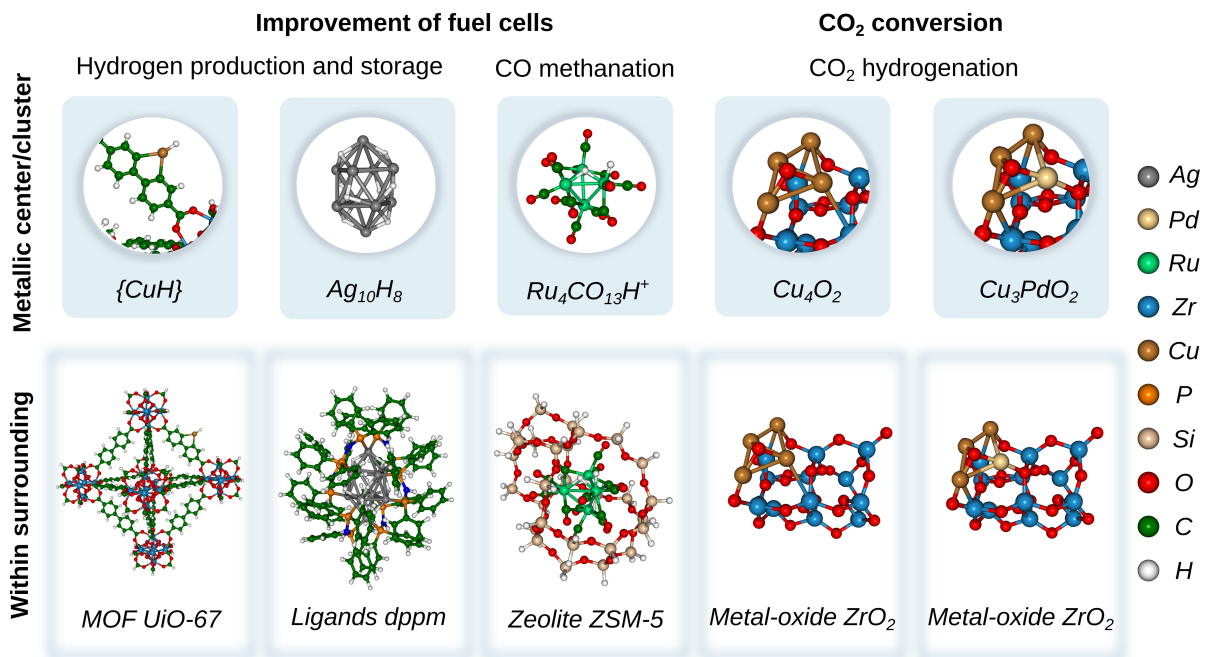
Figure 1.1: An overview of designed nanostructured materials presented in the thesis. For each material, metallic cluster/center and surrounding are highlighted and grouped within a specific research direction. These surroundings include MOF UiO-67, bis(diphenylphosphino)methane (dppm) ligands, zeolite ZSM-5, and ZrO_2 metal oxide support. A color legend is provided on the right.

The transition from homogeneous to heterogeneous catalysis is addressed through following strategies:

i) integration of catalytic metal center within the MOF material (*Chapter 2: Nanostructured materials for hydrogen production and storage, Section 2.1*) and ligand protection

of metal hydride cluster (*Section 2.2*),

ii) placing ligated metal cluster inside the zeolite (*Chapter 3: Nanostructured materials for elimination and utilization of carbon monoxide, Section 3.1*), and

iii) depositing small metal clusters on metal oxide support (*Chapter 4: Nanostructured materials for conversion of carbon dioxide into useful products, Sections 4.1 and 4.2*).

The choice of strategy depends on the specific application requirements and the properties of the surrounding.

This section is structured to present the research directions organized according to both the material design and the proposed application (cf. Figure 1.1). Each new nanostructured material is presented through catalytic metal center/cluster, surrounding, and the concept of their integration. The concept also summarizes the key findings of the relevant research paper included as a part of the thesis.

1.4.1   Designing nanostructured materials for hydrogen production and storage

Metallic center

Hydride compounds with coinage metal atoms (Cu, Ag, Au) have a significant role in organometallic chemistry, exhibiting remarkable properties that stem from the covalent nature of their metal-hydride bonds [96]. Recently, a series of coinage metal complexes were investigated to identify the most active and selective homogeneous catalyst for formic acid decarboxylation [95, 97]. Theoretical and experimental gas phase studies showed that phosphine ligands are responsible for rearranging geometry of the active site, facilitating the formic decarboxylation reaction on silver ligated binuclear hydrides $[LAg_2(H)]^+$ [95]. The cooperative effects of two different coinage metal atoms in ligated binuclear compounds have also been investigated [97]. The $\{Cu_2H\}$ complex emerged as the most promising candidate, since it is highly reactive and cost-effective. The study revealed that one metal atom anchors the formic acid while other enables the hydride transfer. Therefore, a copper-based mononuclear $\{CuH\}$ site, which can be readily integrated within a MOF, was selected as the metallic center for catalyzing formic acid decarboxylation.

I) MOF surrounding

MOFs are promising host environments for the incorporation of single-catalytic sites, offering easy product separation, high recyclability, and thermal stability [98]. Their diverse applications range from gas-phase sorption and catalysis to biomedicine [99]. As nanostructured reactors [15] they offer three possible catalytic sites: organic linkers, metal nodes, and inside of the porous cavity [100, 101]. Furthermore, owing to their high surface area, MOFs are good candidates for CO_2/H_2 separation via pressure swing adsorption

[102]. Their volumetric storage capacity (up to 40 $g \cdot H_2 L^{-1}$ [103]) can be optimized through different engineering approaches [104] and presents an important factor in the potential application for hydrogen storage. Along with MOF serving as a bridge between homogeneous and heterogeneous catalysis, there is also a growing interest in porous organic frameworks (POFs) and covalent organic frameworks (COFs) [105]. Interestingly, MOFs are sometimes regarded as macroligands capable of modifying the electronic properties of the active site [105].

UiO-67 is a frequently employed MOF for catalytic applications, in which biphenyl organic groups serve as linkers and Zr-bipyramid clusters as metal nodes [106]. Previous research demonstrated that the incorporation of open 2,2-bipyridine sites as linkers in UiO-67 can generate robust heterogeneous materials with easily controllable reactivity [107]. Further metalation of such sites opens up numerous possibilities, such as the incorporation of a reactive center. This can modify and ameliorate properties of material, enabling a wide range of catalytic reactions. Considering the factors mentioned above, modified UiO-67 is chosen as a promising MOF host for the design of a new heterogeneous catalyst for the selective decomposition of formic acid.

I) Concept of integrating catalytic metal center into the MOF

In *Section 2.1: MOF-based material* [108], an investigation of new heterogeneous catalyst for the hydrogen production and storage is presented. The main strategy for the material's design is integration of a single reactive site within a modified MOF UiO-67. The study addresses formic acid decarboxylation on different models, ranging from gas phase to complex MOF-based systems with a {CuH} reactive center. Initially, the reaction mechanism of formic acid decomposition is analyzed using DFT on a neutral bipyridine model. An extended bipyridine model is then examined to simulate the organic linker of the MOF. Experimental investigation of the catalyst's viability is performed on a charged ligated bathophen complex. At 65 $°C$, mass spectrometry confirms the catalyst's selectivity for H_2 and CO_2, demonstrating that the reaction proceeds through the formation of a formate intermediate. The effect of the surrounding is considered using a square fragment of the MOF with the single reactive site.

Overall, the selective decomposition of formic acid on the {CuH} reactive site involves a two-step mechanism. The formic acid binds in the first step and progresses through the transition state for H_2 liberation and formate formation. This step is exothermic. In contrast, proton transfer is endothermic and unfeasible, as confirmed by both DFT calculations and experiments. In the following step the formate is rearranged. The final step is the release of CO_2 which completes the catalytic cycle. The mechanism of reaction remains unchanged for all gas phase models, while the MOF environment provides an additional cooperative effect. This makes activation barriers smaller compared to the gas

phase. Moreover, Gibbs free energies are consistent with the trends demonstrated by the calculation of electronic energies.

In summary, the MOF serves as a catalyst for the selective decomposition of formic acid while utilizing the already mentioned advantages of the material. Such direct production of hydrogen shows potential for application in fuel cells. Also, the study suggests that gas phase models represent an effective approach for designing new MOF-based catalytic materials.

II) Ligands surrounding

Ligands can play a crucial role in controlling the reactivity and selectivity of metal catalysts through electronic and steric effects [95]. In some transition metal complexes, the cooperative interaction between the ligand and metallic center can facilitate bond activation [109]. Such synergistic interplay can be utilized for diverse catalytic transformations. Moreover, ligands can protect, stabilize, and have a direct effect on structural and optical properties of clusters and noble metal nanoparticles [110]. In a biological environment, the ligand shell affects their solubility [94]. These various roles of ligands highlight their importance and potential in developing new catalysts. Ligands which are part of the new materials design include carbonyl (-CO) and dppm (bis(diphenylphosphino)methane). The role of carbonyls is presented in the *Section 1.4.2*.

II) Concept of ligand protected silver hydride clusters

Small silver hydride nanoclusters have earlier been studied as catalysts for formic acid decomposition [95]. In addition, they have been considered as hydrogen storage materials, with the possibility to release H_2 upon light irradiation or heat [111, 112]. In this sense, fragmentation under collision-induced dissociation leads to sequential losses of ligands and hydrides releases, eventually forming a ligated silver cluster [113]. The loss of ligands is an endothermic process, which is followed by cluster deformation and exothermic hydrogen loss. Silver ligated hydride clusters belong to homogeneous catalysts, but through reaction with borohydride [113], they undergo transformations to form larger clusters or nanoparticles which present the bridge to heterogeneous catalysts. Therefore, the investigation of silver ligated cluster is included in the thesis serving as an illustration of how ligands create an important surrounding for the silver metallic cluster.

The *Section 2.2: Ligated silver hydride cluster* presents a study [114] on the structural characterization of $[Ag_{10}H_8(L)_6]^{2+}$ (L=dppm), a ligated silver hydride dication with possible application for hydrogen storage. The cluster scaffold is surrounded by dppm ligands that offer protection to the silver metal cluster formed as a bicapped square antiprism. Gas phase experiments with mass spectrometry and X-ray crystallography provide the characterization of the structure and unimolecular reactivity. For the purpose of identify-

ing the eight hydride positions on the metal core, DFT calculations are employed. Results reveal two isomers with four hydrides along the belt and two at each of the pyramid silver caps. Removal of the hydrides from the cluster core leads to a cluster deformation, as also found in the previous study [115]. Calculated vibrational spectrum shows weak intensities of Ag-H vibrations, which overlap with other normal modes. Overall, the ligated sliver hydride complex is theoretically and experimentally characterized. The ligands provide a protective and stabilizing surrounding to the silver metal cluster, while directly influencing the reactivity of the complex.

1.4.2   Designing nanostructured materials for elimination and utilization of carbon monoxide

Metallic cluster

As already established in the *Section 1.2.2*, efficient CO removal is crucial for improving fuel cell efficiency, since the presence of CO in fuel cell feed gas has a significant impact on its quality. Therefore, the development of an efficient catalyst for CO elimination is essential. One promising reaction for CO removal is its hydrogenation to methane and water. In the presence of CO_2, the reverse water gas shift (rWGS) reaction leads to H_2 loss and increased formation of CO. Therefore, the catalyst for CO methanation should be highly selective for CO and inert to CO_2.

In this context, small supported Ru-particles have been demonstrated as active and selective catalysts for CO methanation [116–122]. Earlier works by Eckle *et al.* [116, 118] motivated investigation [123] of small ruthenium nanocatalysts to understand the basis of their activity and selectivity. The study focused on the size-selected ruthenium clusters, Ru_n^+ ($n = 2-6$), which showed high activity towards CO and inactivity towards CO_2. The cooperative effect between CO and H_2 adsorption followed by promoted H_2 dissociation was identified as one of the critical factors in catalytic performance. Also, the presence of undercoordinated Ru atom sites was reported to favor H_2 activation, thus enhancing its catalytic activity.

Moreover, gas phase experiments revealed that these small Ru-clusters bind to CO in a specific manner, forming unique Ru-carbonyl complexes with extraordinary stability [124]. This behavior arises from their electronic structure, where each apex Ru atom has a closed-shell valence electron number. These findings provided valuable insights into the design of new catalysts for CO methanation, particularly the importance of coordination of catalytic sites, cooperative H_2 coadsorption, and the relationship between cluster size and Ru-complex formation [123]. $Ru_4(CO)_{13}H_2^+$ which satisfies all the necessary conditions, is proposed as a promising candidate for intrazeolite anchoring.

Zeolite surrounding

Zeolites are crystalline materials characterized by microporous size, chemical, and thermal robustness [125]. They consist of TO_4 tetrahedra, with T generally being aluminum or silicon. These tetrahedral units are linked in various ways to form small cages, single and double rings, which create a network of interconnected channels and cavities [125, 126]. Although zeolites have traditionally been used for adsorption and separation of chemicals, they have gained a significant interest in the field of catalysis due to their unique structural properties.

One of the key advantages of zeolites is their ability to encapsulate different species, including metal clusters and nanoparticles [126–128]. Zeolite cavities create a unique environment that allows the protection of guest molecules from external conditions. Also, they offer improved stability, increased selectivity, and the prevention of unwanted side reactions [126, 127]. One such example is the copper binuclear center inserted within the zeolite on a "ship in a bottle" principle [129]. This showed a new approach to design a zeolite-based catalyst for formic acid decomposition. Here, zeolite was used as a cage, providing an inert environment for the inserted metallic center. Pore sizes and shapes of zeolites can be tailored to suit specific applications, making them a versatile catalytic materials. Furthermore, reengineering the framework by insertion of basic sites directly influences their reactivity [128, 130].

Shen *et al.* [131, 132] previously reported on the synthesis of ruthenium carbonylated compounds within the faujasite zeolite, showing promising results in CO/H_2 reactions. This led the authors to propose the introduction of carbonylated ruthenium clusters within other types of zeolites [133]. ZSM-5 is widely used in industry, offering high stability and a large pore size [134]. As a result, it is selected as a host zeolite surrounding for confinement of Ru-ligated complex to form a new heterogeneous catalyst for CO removal.

Concept of ligated ruthenium cluster inside the zeolite cage

Section 3.1: Zeolite-based material presents the study [135] of a new heterogeneous catalyst for CO removal in the context of fuel cell application. This research direction is based on placing the ligated $Ru_4(CO)_{13}H_2^+$ cluster within the ZSM-5, thus allowing heterogenization of a previously well-explored gas phase catalyst. To examine the interaction between the Ru-cluster and the zeolite, a bare Ru_4^+ is first placed inside the ZSM-5. The results show that there is a strong bonding between Ru atoms and O atoms of the framework, resulting in cluster distortion and charge transfer from the framework to the cluster. However, the cluster structure is not affected by placing the Ru-carbonyl complex inside the cage. This is also in contrast to faujasite zeolite, which strongly interacts with carbonyl groups due to the presence of Na^+ sites within its framework [136]. These findings demonstrate an important role of ligands in protecting the metallic cluster from

interaction with the zeolite. Moreover, the only interaction between the Ru-complex and ZSM-5 is attributed to the weak dispersion forces.

Additionally, to examine the potential influence of Al^-, a bare Ru_4^+ cluster was placed within a modified framework in which a single Si atom was replaced by Al^-. In this case, the charge transfer is slightly reduced with a relatively unchanged cluster structure. This suggests that the presence of Al^- does not have a pronounced effect on the catalytic center.

Calculations of the energy profile for CO methanation on the intrazeolite anchored Ru-complex show that the reaction mechanism and energetics remain the same as in the gas phase model. The first reaction step starts with barrierless H_2 adsorption and dissociation. This is followed by hydride transfer to carbon and formation of formyl, which is a rate-determining step. The intermediate steps are the formation of water and methyne, and finally the release of methane, resulting in an overall exothermic reaction.

Altogether, zeolite acts as a nanocontainer, which does not interfere with the reaction, while ligands provide the protection of the metal core. The study demonstrates that the $Ru_4(CO)_{13}H_2^+$ cluster inside the ZSM-5 zeolite cage is a feasible approach to design a solid heterogeneous catalyst for the removal of CO and the production of methane.

1.4.3   Designing nanostructured materials for conversion of carbon dioxide into useful products

Metallic cluster

Supported subnanometer metallic clusters hold great promise as a new class of active and selective catalysts for a wide range of chemical reactions. The size, composition, and structure of these clusters can be precisely controlled, allowing the fine-tuning of activity and selectivity [137]. One of their key advantages is a high number of undercoordinated surface atoms, which are often active sites important for adsorption and reactivity [137, 138]. Furthermore, the small cluster size facilitates the theoretical prediction of catalytic properties and the elucidation of reactive centers. The dynamic behavior of clusters is an additional aspect to consider, since their restructuring can impact catalytic activity [139].

Catalysts based on copper are extensively investigated for CO_2 hydrogenation reactions due to their availability and low cost [48–53]. In a study by Zhang et al. [50], adsorption energies for CO and O on small Cu-clusters were used as descriptors of catalytic reactivity in CO_2 hydrogenation reaction. The unique catalytic behavior of these catalysts was attributed to their discrete energy levels and molecule-like electronic properties as well as the d-band position which influences adsorption strength and activity [50]. Another study explored the catalytic properties of small size-selected Cu-clusters ($n = 3, 4, 20$) supported on alumina for the reaction of CO_2 conversion to methanol [49].

The results showed that Cu_4 exhibits the best performance for methanol formation under low-temperature and low-pressure conditions [48, 49]. In addition, a single-atom change, such as a size reduction from Cu_4 to Cu_3, significantly reduces catalyst activity.

Based on these findings, Cu_4 is selected as a supported metallic cluster due to its potential to catalyze CO_2 conversion reactions. To optimize catalyst performance, doping by single-atom replacement is also explored.

Metal oxide support surrounding

In heterogeneous catalysis, metal oxides are often used as supports. In addition, they can serve as catalytically active materials, offering an additional active catalytic region at the interface between the catalyst and the support. By providing stability and prevention of sintering, they increase the catalyst durability [137]. Also, the structural defects of the support as well as the electron transfer to the cluster modify catalyst performance [140].

Metal oxides can support different metal species, ranging from single atoms, clusters, to nanoparticles. These supports have influence on the mobility of metal species, providing an environment with specific electronic effects, as well as electrostatic interactions [137].

Zirconium oxide is a promising catalytic support because of its stability in oxidizing and reducing conditions. Additionally, it offers weak acid and basic sites that are beneficial for catalysis [141]. These materials exist in several phases, including monoclinic, tetragonal, cubic, and amorphous, each offering a different set of properties that are suited for specific catalytic purposes [142]. Beyond its role as a metal oxide support, ZrO_2 exhibits an intrinsic reactivity [141] and a synergistic effect through its interaction with the metallic clusters [93]. Given these factors and the fact that ZrO_2 has been successfully utilized in CO_2 hydrogenation reactions earlier [93], it is selected as the promising metal oxide environment for the deposition of small Cu_4 clusters.

I) Concept of depositing small copper cluster on a metal oxide support

Section 4.1: Supported metallic nanocluster introduces the experimental and theoretical investigation of new heterogeneous catalysts for CO_2 conversion to methane and methanol [143]. These catalysts consist of small Cu-clusters (Cu_4 and Cu_{12}) deposited on a ZrO_2 atomic layer deposited (ALD) and nanostructured (NS) support. State-of-the-art experimental techniques are used to prepare these catalysts with atomic-level precision. Results demonstrate that both cluster sizes are more active on NS zirconia, with Cu_4 activating CO_2 at 275 °C and Cu_{12} at 175 °C. The oxidation state is also found to affect cluster activity. Furthermore, Cu_{12} on NS zirconia shows the highest rate of methane formation, although with reduced recyclability.

Underlying mechanism of CO_2 methanation is elucidated by DFT calculations. The proposed theoretical model is based on a rhombic Cu_4O_2 cluster deposited on a Zr_nO_{2n}

($n = 12$) zirconia fragment, with the Cu-cluster bound to the surface over O and Zr atoms. The Cu-cluster has oxidation state 1, as also demonstrated by the Mulliken charges. All the reactions species are directly connected to two Cu atoms, showing the key role of the Cu$_2$ subunit. The zirconia support provides stabilization through strong anchoring of Cu$_4$O$_2$, resulting in a large binding energy. The calculated energy profile demonstrates the complexity of the new energy pathway. Methanation is a four-step reaction, with CO$_2$ and H$_2$ binding within the initial exothermic step providing enough energy for CO$_2$ activation. The CO$_2$ methanation can progress along a formate or carboxylate route, with the latter requiring larger activation barriers. The reaction proceeds along the formate formation, followed by water release, methoxy, and methane formation in the third step, and the second water formation in the fourth step. In the third step, the alternative pathway that branches from the methoxy intermediate is also shown to lead to the formation of methanol.

Overall, this study provides valuable insights into the mechanism of CO$_2$ methanation, as well as information on the reactive site and the role of the surrounding. Experimental findings demonstrate the effect of various zirconia morphologies, as well as of cluster size, on catalyst activity. This paves the way for future efforts to tailor the catalyst properties for specific applications.

II) Concept of replacing a single Cu atom by Pd

An idea of catalyst tunability is explored through the concept of replacing a single Cu atom in a Cu$_4$O$_2$ cluster by a single Pd atom. Pd is chosen as a dopant because of its ability to facilitate H$_2$ dissociation. The study is presented in *Section 4.2: Supported bimetallic nanocluster* [144] and focuses on the investigation of new bimetallic catalysts for CO$_2$ conversion. The key subunit of Cu$_3$PdO$_2$/Zr$_{12}$O$_{24}$ model catalyst is CuPd, with all reaction species bound to either Cu or Pd. In contrast, the remaining Cu$_2$ unit does not actively participate in the reaction steps. Natural charges along with the bond length indicate a smaller charge transfer between the cluster and the support compared to that of the monometallic catalyst. Furthermore, the activation of CO$_2$ is followed by CO$_2$ bending and electron gain, which is also smaller for the bimetallic model catalyst. Consequently, the energy profile is higher-lying, resulting in lower stability.

Investigation of the energy profile reveals several routes for CO$_2$ conversion that allows to directly compare the reaction steps at Cu and Pd atoms. The preferential pathway was found to be the formate one, with the same intermediate steps as in the monometallic case. The transition states that include H$_2$ dissociation at the Pd atom are significantly lower in energy compared to the steps occurring at Cu, which are energetically close to equivalent steps in a monometallic model catalyst. This important conclusion indicates that atomic-level doping can be used not only for CO$_2$ conversion but also for other rele-

vant reactions. In contrast to the higher temperatures necessary for methane formation, methanol formation is possible at lower reaction temperatures.

This research opens an avenue for the design of new heterogeneous catalysts based on small supported clusters that can be tuned by single-atom doping.

Nanostructured materials for hydrogen production and storage

2.1 MOF-based material

Reproduced from:

Richard A. J. O'Hair, <u>Antonija Mravak</u>, Marjan Krstić, and Vlasta Bonačić-Koutecký. Models facilitating the design of a new metal-organic framework catalyst for the selective decomposition of formic acid into hydrogen and carbon dioxide. *ChemCatChem*, 11(10), 2019, 2443-2448. Reproduced with permission from the John Wiley & Sons.
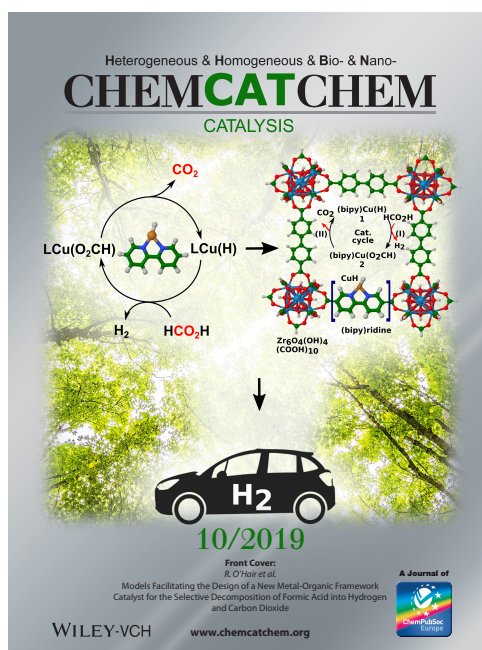
Figure 2.1: Cover page of *ChemCatChem* [108] featuring design of new MOF-based material for hydrogen production and storage. Reproduced with permission from the John Wiley & Sons.
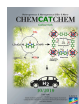
Models Facilitating the Design of a New Metal-Organic Framework Catalyst for the Selective Decomposition of Formic Acid into Hydrogen and Carbon Dioxide

Richard A. J. O'Hair,*[a] Antonija Mravak,[b] Marjan Krstić,[b] and Vlasta Bonačić-Koutecký*[b, c]

Dedicated to Professor Veronica Bierbaum on the occasion of her retirement.

Here we describe a new conceptual approach for the design of a heterogeneous metal-organic framework (MOF) catalyst based on UiO-67 for the selective decarboxylation of formic acid, a reaction with important applications in hydrogen storage and *in situ* generation of H_2. Models for the {CuH} reactive catalytic site at the organic linker are assessed. In the first model system, gas-phase mass spectrometry experiments and DFT calculations on a fixed charge bathophen ligated copper hydride complex, $[(phen^*)Cu(H)]^{2-}$, were used to demonstrate that it acts as a catalyst for the selective decomposition of formic acid into H_2 and CO_2 via a two-step catalytic cycle. In the first step liberation of H_2 to form the carboxylate complex, $[(phen^*)Cu(O_2CH)]^{2-}$ occurs, which in the second step selectively decomposes via CO_2 extrusion to regenerate the hydride complex. DFT calculations on four other model systems showed that changing the catalyst to neutral $[(LCu(H)]$ complexes or embedding it within a MOF results in mechanisms which are essentially identical. Thus catalytic active sites located on the organic linker of a MOF appear to be close to a gas-phase environment, thereby benefitting from the favorable characteristics of gas-phase reactions and validating the use of gas-phase models to design new MOF based catalysts.

Introduction

Thirty years ago Robson proposed the rational design and construction of a novel class of porous materials composed of metal centers as nodes that connect to organic ligands as rods (linkers).[1,2] In two landmark papers he provided remarkable visions for a new field of chemistry for these coordination polymers,[3] which were subsequently rebranded as metal-organic frameworks (MOFs).[4] He noted that "*despite Nature's abhorrence of a vacuum it may be possible to devise rods with sufficient rigidity to support the existence of solids with relatively huge empty cavities*"[2] and prophesied that "*{r}elatively unimpeded migration of species throughout the lattice {MOF} may allow chemical functionalization of the rods {linkers} subsequent to the construction of the framework. The introduction of one or more catalytic centers per rod may thereby be straightforward. The very open structure should again ensure both easy access of substrates to catalytic sites and ready release of catalytic products*".[2] The prediction of post-synthetic modification (PSM) of a MOF[5] to build a supported catalyst had to wait over a decade until Lin's pioneering work on a MOF based heterogeneous asymmetric catalyst for the addition of diethyzinc to aromatic aldehydes to afford chiral secondary alcohols.[6]

Although much progress has since been made in constructing a wide range of MOF catalysts,[7] the vacuum like environment within MOFs suggested to us a tantalizing new concept for the design of novel MOF based catalysts, where gas-phase studies are used to examine the likely reactivity of a catalytic metal site within a MOF (Scheme 1). The use of gas-phase models seemed plausible given that our previous reaction-mechanisms approach, where gas-phase studies using multistage mass spectrometry experiments (MS^n) in an ion trap are blended with DFT calculations,[8] was successfully applied to the design of new catalysts from the ground up[9–12] and the invention of new reactions for use in organic synthesis.[13] In the former studies, through a sequence of iterations in which different ligands and metal sites were evaluated, we developed a series of ligated binuclear coinage metal hydride cationic catalysts for the selective decarboxylation of formic acid (Scheme 1a, b),[14] a reaction of considerable interest for the use of formic acid in hydrogen storage applications.[15] In all cases a two-step catalytic cycle operates (Scheme 1a) in which the metal hydride complex, **1**, reacts in **Step I** with formic acid to liberate hydrogen and form a coordinated metal formate, **2**, which in **Step II** liberates CO_2 under conditions of collision-induced dissociation (CID). For these first generation catalysts the best ligand for the silver hydride was 1,1-bis(diphenylphos-

[a] Prof. R. A. J. O'Hair
School of Chemistry
and BIO21 Molecular Science
and Biotechnology Institute
The University of Melbourne
30 Flemington Rd, Parkville, VIC 3010 (Australia)
E-mail: rohair@unimelb.edu.au

[b] A. Mravak, Dr. M. Krstić, Prof. V. Bonačić-Koutecký
Center of Excellence for Science and Technology
– Integration of Mediterranean Region (STIM) at Interdisciplinary
Center for Advanced Sciences and Technology (ICAST)
University of Split
Poljička cesta 35, 21000 Split (Croatia)

[c] Prof. V. Bonačić-Koutecký
Chemistry Department
Humboldt University of Berlin
Brook-Taylor-Strasse 2, 12489 Berlin (Germany)
E-mail: vbk@cms.hu-berlin.de

💻 Supporting information for this article is available on the WWW under
https://doi.org/10.1002/cctc.201900346
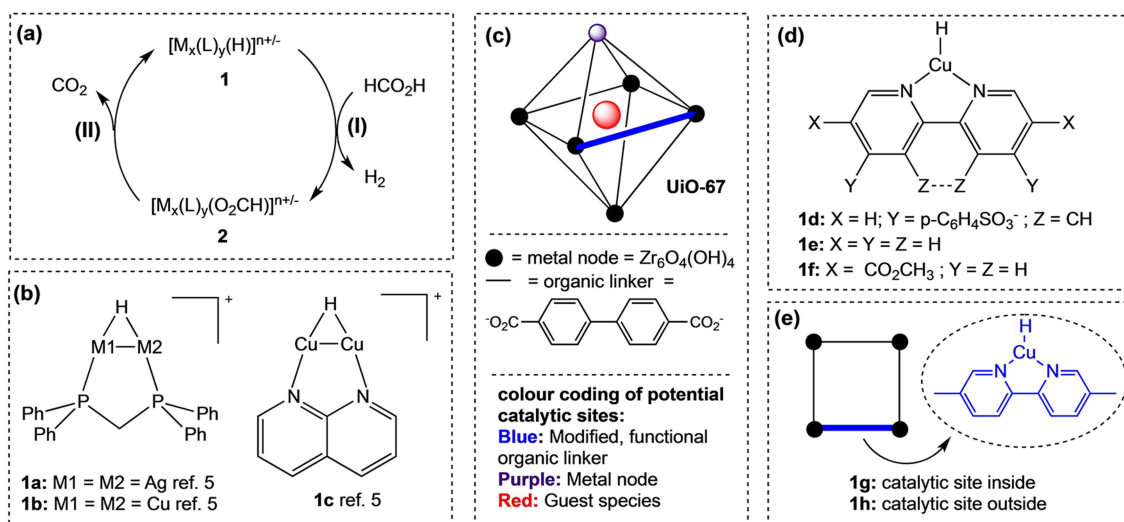
Scheme 1. Design principles for coinage metal hydrides for the selective decarboxylation of formic acid: (a) two-step catalytic cycle. Step (I) is an ion-molecule reaction with formic acid; Step (II) involves liberation of CO_2 under CID conditions. (b) 1st (**1a**), 2nd (**1b**) and 3rd (**1c**) generation gas-phase binuclear coinage metal hydride catalysts previously reported. (c) examples of potential catalytic sites within the MOF **UiO-67**; (d) Gas-phase models for mononuclear copper hydride catalysts located at the organic linker; (e) models for the heterogenization of a gas-phase homogenous catalyst located at the organic linker in a MOF.

phino)methane (dppm) to give complex **1a** (Scheme 1b), and solution phase studies confirmed the liberation of H_2 and CO_2 at a relatively low temperature of 65 C.[9] Although the exact nature of the stoichiometry of the solution phase catalysts is unknown, subsequent gas phase studies highlighted that tetranuclear silver hydride cluster complexes were unreactive towards formic acid.[10] This spurred us onto examining the role of the metal center, where all possible homo and hetero coinage metal complexes were explored to establish that the best gas-phase catalyst for both steps in the catalytic cycle was the biscopper complex **1b**.[11] Given the difficulty of establishing the nature of the solution phase catalyst, we were interested in translating the gas-phase homogeneous catalysts into a heterogenous system. Unfortunately, the second generation catalyst **1b** was shown by DFT calculations not to fit into the framework of a ZSM-5 zeolite, which resulted in the development of a new, less bulky catalyst **1c** based upon the N-based 1,8-naphthyridine ligand.[12] This catalytic site was found to fit neatly into the framework a ZSM-5 zeolite. Due to the experimental challenges of developing these zeolite-based "ship in a bottle" catalysts,[16] we were tempted by the "heterogenization of a homogenous catalyst" strategy to use gas-phase studies to design a MOF based catalyst where the metal site is part of the framework. There are three types of potential catalytic sites within a MOF as illustrated for the UiO-67 MOF (Scheme 1c): (i) the organic linker, which can be functionalized to introduce a catalytic site as per Robson's original proposal; (ii) the metal node; (iii) insertion of a guest catalyst (essentially a "ship in a bottle" catalyst). While all three types of MOF catalysts have been demonstrated,[7] we were attracted to developing organic linkers functionalized by a copper hydride catalytic site. Here we use DFT calculations to show that the mechanisms and energetics associated with the two-step catalytic cycle of simple gas-phase catalysts **1d**–**1f** (Scheme 1d) are very similar to those of the models **1g** and **1h** of UiO-67 MOF (Scheme 1e).
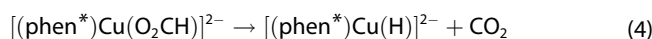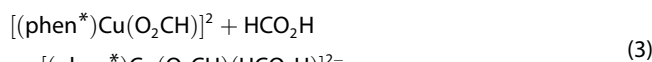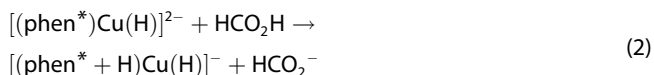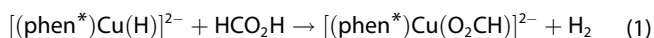
Results and Discussion

Since there are no known 1,8-naphthyridine based ligands for the construction of MOFs that would support a binuclear $\{Cu_2H\}^+$ catalytic site related to **1c**, we decided to adopt the 5,5′-dicarboxy-2,2′-bipyridine ligand as an organic linker since: (i) it has been shown to be able to be incorporated into the robust UiO-67 MOF;[17] (ii) PSM of such MOFs with metal sites have been used to prepare catalysts.[18] We first wanted to use experiment and theory in concert to establish that a mononuclear hydride {CuH} complex could act as a catalyst for the selective decarboxylation of formic acid. Since the {CuH} sites in MOFs have no net charge while the mass spectrometry experiments require the use of ions for mass-selection, reaction and detection, we turned to the well-established use of fixed charge ligands.[19] We chose 4,7-diphenyl-1,10-phenanthroline-disulfonic acid disodium salt as the fixed charge ligand (phen*) since it should allow ready formation of the copper formate complex **2d** via electrospray ionization (ESI) and the sulfonate sites: (i) are well away from the {CuH} reactive site and should not significantly perturb reactivity; (ii) have a low gas-phase basicity and should not deprotonate formic acid.[20] Gratifyingly **1d** was readily formed via CID of **2d** and reacts cleanly with formic acid to give the formate complex ([Eq. (1)] and Figure 1a) at the collision rate, consistent with DFT calculations which predict that the reaction is exothermic by 1.07 eV and has a barrier lying below the separated reactants (as discussed further below). No proton transfer is observed [Eq. (2)], consistent with the low basicity of the chosen sulfonate fixed charges[20] and with DFT calculations which predict that the reaction is
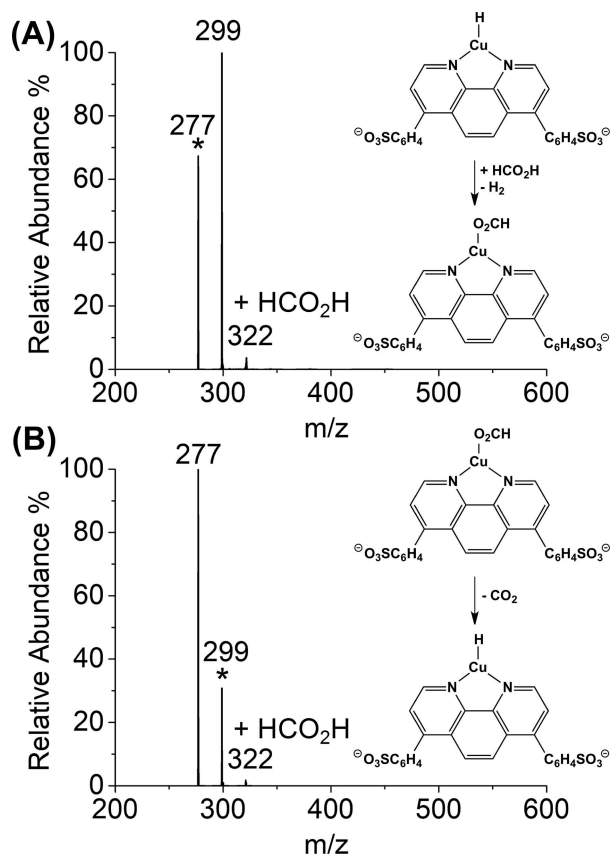
Figure 1. LTQ mass spectra obtained for the MS^n CID (or IMR) experiments of: (a) IMR of [(phen*)^{63}Cu(H)]$^{2-}$ (m/z 277), **1 d**, with formic acid; (b) CID of [(phen*)^{63}Cu(O$_2$CH)]$^{2-}$ (m/z 299), **2 d**. An activation time of 30 ms was used for the CID experiments and 500 ms for the IMR experiments. A * represents the mass-selected precursor ion.

endothermic by 0.48 eV. A minor secondary product is formed by reaction of formic acid with the copper formate complex **2 d** [Eq. (3)] as confirmed by mass selection of m/z 299 and this adduct fragments via formic acid loss upon CID (data not shown). CID of [(phen*)Cu(O$_2$CH)]$^{2-}$ cleanly regenerates [(phen*)Cu(H)]$^{2-}$ via decarboxylation [Eq. (4)].

$$[(phen^*)Cu(H)]^{2-} + HCO_2H \rightarrow [(phen^*)Cu(O_2CH)]^{2-} + H_2 \quad (1)$$

$$[(phen^*)Cu(H)]^{2-} + HCO_2H \rightarrow [(phen^* + H)Cu(H)]^- + HCO_2^- \quad (2)$$

$$[(phen^*)Cu(O_2CH)]^2 + HCO_2H \rightarrow [(phen^*)Cu(O_2CH)(HCO_2H)]^{2-} \quad (3)$$

$$[(phen^*)Cu(O_2CH)]^{2-} \rightarrow [(phen^*)Cu(H)]^{2-} + CO_2 \quad (4)$$

To examine the mechanistic aspects responsible for the selective decomposition of formic acid into H$_2$ and CO$_2$ via reaction steps **I** and **II** within the catalytic cycle (Scheme 1a), DFT energy profiles have been determined for five systems: (i) [(phen*)Cu(H)]$^{2-}$, **1 d** (Scheme 1d), which has been experimentally investigated in the gas phase (Figure 1), (ii) [(bipy)Cu(H)], **1 e** (Scheme 1d); (iii) [(bipy*)Cu(H)], **1 f** (Scheme 1d), which contains the organic linker present in MOF UiO-67, and capped as a diester; and models for MOF UiO-67[21] in which the octahedron is simplified as a square consisting of three biphenyl organic linkers, one (bipy*)Cu(H) organic linker containing the catalytic site and four Zr$_6$O$_4$(OH)$_4$(COOH)$_{10}$ nodes in the corners, with the CuH catalytic pointing (iv) into the center of the square, [UiO-67(bipy)Cu(H)in], **1 g** (Scheme 1e); (v) outside of the square, [UiO-67(bipy)Cu(H)out], **1 h** (Scheme 1e). The DFT calculated energy profiles are shown in Figures 2, S2, 3, 4 and S4 respectively and Table 1 compares the energies of all key species for all model systems. The most noteworthy aspect of comparing the energy profiles and associated structures is that the mechanistic features are similar for all model systems, with small perturbations to the energetics. In all cases the formic acid binds to the CuH catalytic center to generate complex **3**. For step I, breaking of the formic acid O–H bond and formation of H$_2$ occurs over an energy barrier associated with **TS3-2**, which is below the energy at the separated reactants in the case of all the gas phase systems (**1 d**, **1 e** and **1 f**) while for the MOF models **1 g** and **1 h**, the formation of **2** with concomitant release of H$_2$ occurs without a barrier (cf. Figures 2–4). In all cases loss of H$_2$ to form the copper formate subunit, CuO$_2$CH is energetically favorable. For the first step of the reaction, the N,N-bidentate {CuH} subunit represents the key reactive site consistent with the calculated HOMOs (Figure S3).

For the loss of CO$_2$ associated with **step II** and to close the catalytic cycle, two energy barriers have to be overcome. **TS2-2′** is associated with the required conformational change of the formate ligand to form the reactive conformer **2′** for decarboxylation, which surmounts **TS2′-4** to yield the hydride complex **4**,

Table 1. Summary of key energies associated with Steps I and II for all systems studied.

Model	3	TS3-2	2	TS2-2′	2′	TS2′-4	4
[(phen*)Cu(H)]$^{2-}$, **1 d**[a]	−0.64	−0.41 (0.23)	−1.07	−0.88 (0.19)	−0.92	−0.05 (0.87)	−0.17
[(bipy)Cu(H)], **1 e**[b]	−0.61	−0.41 (0.2)	−1.01	−0.61 (0.4)	−0.67	0.18 (0.85)	−0.15
[(bipy*)Cu(H)], **1 f**[c]	−0.52	−0.42 (0.1)	−0.93	−0.56 (0.37)	−0.63	+0.27 (0.9)	−0.12
[UiO-67(bipy)Cu(H)in], **1 g**[d]	−0.96	–[f]	−1.04	−0.61 (0.43)	−0.65	−0.11 (0.54)	−0.15
[UiO-67(bipy)Cu(H)out], **1 h**[e]	−0.97	–[f]	−1.01	−0.58 (0.43)	−0.80	−0.04 (0.76)	−0.12

[a] Potential energy diagram with structures is given in Figure 2. [b] Potential energy diagram with structures is given in Figure S2. [c] Potential energy diagram with structures is given in Figure 3. [d] Potential energy diagram with structures is given in Figure 4. [e] Potential energy diagram with structures is given in Figure S4. [f] Barrierless process as transition state not found.
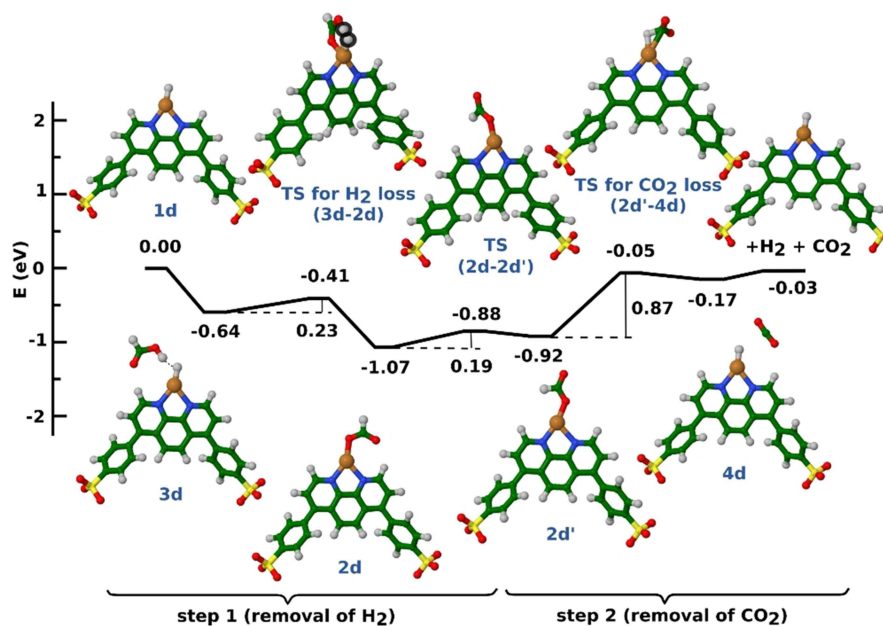
Figure 2. DFT-calculated energy profile for the two reaction steps in the catalytic cycle for [(phen*)Cu(H)]$^{2-}$, **1d** in the gas-phase. All structures were fully optimized using DFT method with the hybrid B3LYP functional and def2-TZVP atomic basis set which has been used for all atoms. Color coding of atoms: green – carbon, red – oxygen, white – hydrogen, blue – nitrogen, yellow – sulfur, brown – copper.
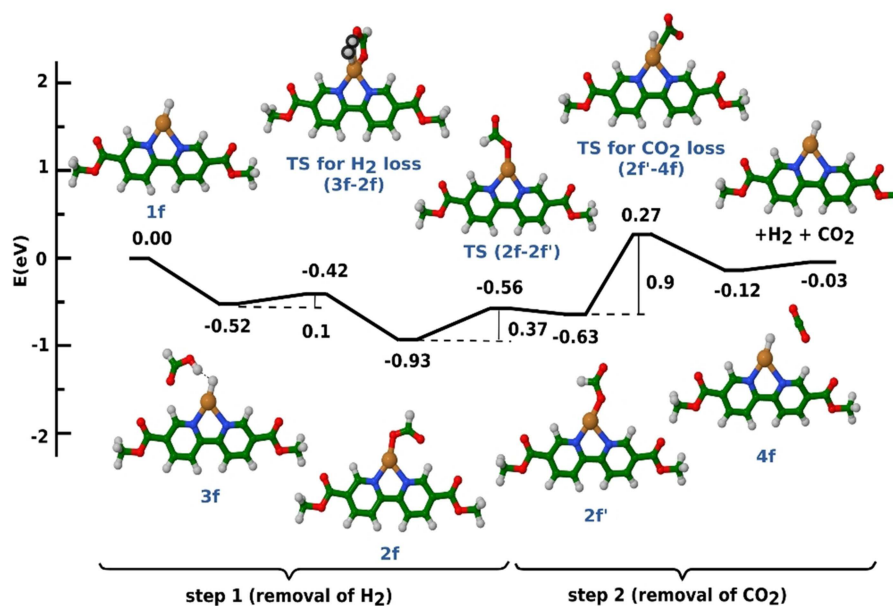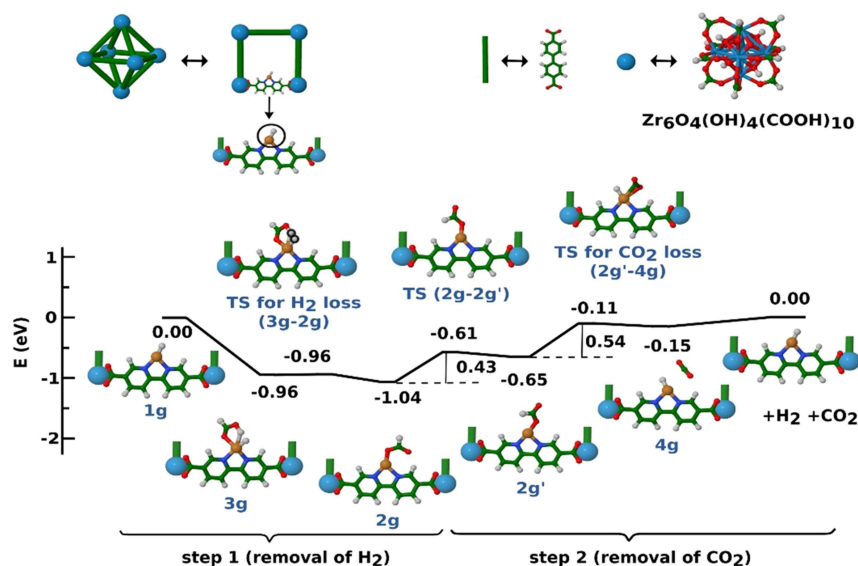

Figure 3. DFT-calculated energy profile for the two reaction steps in the catalytic cycle for [(bipy*)Cu(H)], **1f** in the gas-phase. All structures were fully optimized using DFT method with the hybrid B3LYP functional and def2-TZVP atomic basis set which has been used for all atoms. Color coding of atoms: green – carbon, red – oxygen, white – hydrogen, blue – nitrogen, brown – copper.

in which CO$_2$ is loosely interacting (with Cu–O distance of around 3.7 Å) and from which CO$_2$ is readily lost to generate **1**.

An examination of Table 1 reveals that some species related to the catalytic cycle are influenced by the electronic effects associated with the various ligands used in the different models. The phen*, bipy and bipy* ligands of the gas-phase models **1d**, **1e** and **1f** have little influence on the energetics for **3**, **TS3-2**

and **2** associated with Step I, whereas species **TS2-2′**, **2′** and **TS2′-4** associated with step **II** are slightly higher for the gas-phase **1e** and **1f**. Comparing the gas-phase model **1f** to the MOF models **1g** and **1h** reveals that the MOF environment provides a cooperative effect in which the energetics of virtually all species becomes more favorable. This is likely due to electric field effects, which have generated much recent interest in

Figure 4. DFT-calculated energy profile for the two reaction steps in the catalytic cycle for the model MOF system **1g**. Based on X-ray [21] quadratic structure of octahedron base, the structural local minima and transition states have been determined using DFT method with the PBE functional with resolution of identity method (W06) with def2-SVP atomic basis set and relativistic ECP for Zr atoms. Square of the octahedron consists of 3 biphenyl chains labeled by green sticks, 1 (bipy*)Cu(H) chain and 4 $Zr_6O_4(OH)_4(COOH)_{10}$ nodes in the corners labeled by blue spheres.

enhancing organic reactions[22] but which appear to have been limited to discussions of the separation of gases in the context of MOFs.[23] It is worth noting that the Gibbs free energies associated with key species for Steps I and II for **1d**, **1f** and **1g** which are given in Table S1 show the same trends as the corresponding energies presented in Table 1.

Conclusion

Here we have extended the "heterogenization of a homogenous catalyst" strategy to use gas-phase studies to design a MOF based catalyst. In particular, we have used mass spectrometry experiments to model an organic linker with a {CuH} catalytic site and show that both steps of the catalytic cycle are selective for H_2 and CO_2 formation. DFT calculations have revealed that the mechanism associated with both steps of the catalytic cycle are essentially identical for three gas-phase models and are very similar to those of the two UiO-67 MOF models. Thus catalytic active sites located on the organic linker of MOFs appear to be close to a gas-phase environment, and thereby benefit from the favorable characteristics of gas-phase reactions. These include selectivity and enhanced rate of reaction due to lack of solvent effects.[24] Indeed if a MOF catalyst operates to process gaseous reactants and products, selectivity should be observed.[25] Our new conceptual approach opens routes towards the use of new MOF materials based on UiO-67 as novel catalysts for selective decomposition of formic acid into H_2 and CO_2. Studies are underway to prepare and evaluate the performance of such MOF catalysts.[26]

Experimental Section

Mass spectrometry experiments: Gas-phase experiments on [(phen*)Cu(H)]$^{2-}$, formed as discussed in the Supporting Information, were carried out using a Finnigan linear quadrupole (LTQ) mass spectrometer modified to allow the study of IMR.[27,28] The unimolecular fragmentation/dissociation of mass-selected [(phen*)Cu(O$_2$CH)]$^{2-}$ occurred via CID using a normalized collision energy of 20 and an activation time of 30 ms. The CID isolation width was 1 m/z. IMRs were carried by delivering a measured concentration of formic acid into the helium bath gas.

Theoretical Methods

Determination of energy profiles for reactions included searches for minima and transition states using the Gaussian suite of programs.[29] For the gas-phase models of [(phen*)Cu(H)]$^{2-}$, **1d**, [(bipy)Cu(H)], **1e** and [(bipy*)Cu(H)], **1f** hybrid B3LYP[30] functional with def2-TZVP[31] atomic basis set were taken. The differences in the electronic energies are used rather than the ΔG for the following reasons due to the experimental conditions: (1) the ion-molecule reaction (step I) occurs under low-pressure conditions leading to unfavorable entropy effects arising from loss of degrees of freedom in the entrance channel where two gas-phase molecules react to form a single encounter complex;[32] (2) for the low energy CID reaction (step II) the effective temperature at which decarboxylation occurs is unknown since the precursor ions undergo multiple collisions with the helium bath gas resulting in slow "heating" until fragmentation occurs.[33] For the model MOF systems [UiO-67(bipy)Cu(H)in], **1g** and [UiO-67(bipy)Cu(H)out], **1h**, PBE[34] functional with resolution of identity method (W06)[35] in combination with def2-SVP[36] was used. Zirconium atoms have been treated with Stuttgart relativistic effective core potential[37] with corresponding atomic orbital basis set.

Acknowledgements

Conflict of Interest

The authors declare no conflict of interest.

[1] B. F. Hoskins, R. Robson, *J. Am. Chem. Soc.* **1989**, *111*, 5962–5964.
[2] B. F. Hoskins, R. Robson, *J. Am. Chem. Soc.* **1990**, *112*, 1546–1554.
[3] R. Robson, *Dalton Trans.* **2008**, 5113–5131.
[4] O. M. Yaghi, H. Li, *J. Am. Chem. Soc.* **1995**, *117*, 10401.
[5] S. M. Cohen, *J. Am. Chem. Soc.* **2017**, *139*, 2855–2863.
[6] C.-D. Wu, A. Hu, L. Zhang, W. Lin, *J. Am. Chem. Soc.* **2005**, *127*, 8940–8941.
[7] a) Y.-B. Huang, J. Liang, X.-S. Wang, R. Cao, *Chem. Soc. Rev.* **2017**, *46*, 126–157; b) J.-S. Qin, S. Yuan, C. Lollar, J. Pang, A. Alsalme, H.-C. Zhou, *Chem. Commun.* **2018**, *54*, 4231–4249.
[8] a) R. A. J. O'Hair, *Chem. Commun.* **2006**, 1469–1481; b) R. A. J. O'Hair, N. J. Rijs, *Acc. Chem. Res.* **2015**, *48*, 329–340.
[9] A. Zavras, G. N. Khairallah, M. Krstić, M. Girod, S. Daly, R. Antoine, P. Maitre, R. J. Mulder, S.-A. Alexander, V. Bonačić-Koutecký, P. Dugourd, R. A. J. O'Hair, *Nat. Commun.* **2016**, *7*, 11746.
[10] A. Zavras, J. M. White, R. A. J. O'Hair, *Dalton Trans.* **2016**, *45*, 19408–19415.
[11] A. Zavras, M. Krstić, P. Dugourd, V. Bonačić-Koutecký, R. A. J. O'Hair, *ChemCatChem* **2017**, *9*, 1298–1302.
[12] M. Krstić, Q. Jin, G. N. Khairallah, R. A. J. O'Hair, V. Bonačić-Koutecký, *ChemCatChem* **2018**, *10*, 1173–1177.
[13] a) A. Noor, J. Li, G. N. Khairallah, Z. Li, H. Ghari, A. J. Canty, A. Ariafard, P. S. Donnelly, R. A. J. O'Hair, *Chem. Commun.* **2017**, *53*, 3854–3857; b) Y. Yang, A. Noor, A. J. Canty, A. Ariafard, P. S. Donnelly, R. A. J. O'Hair, *Organometallics.* **2019**, *38*, 424–435.
[14] In the absence of a catalyst, decomposition of formic acid proceeds via two competing primary pathways: decarboxylation to yield H_2 and CO_2 and dehydration to produce H_2O and CO. Although decarboxylation is slightly exothermic (by around 0.15 eV using experimental heats of formation from H. Y. Afeefy, J. F. Liebman, S. E. Stein "Neutral Thermochemical Data", in NIST Chemistry WebBook, NIST Standard Reference Database Number 69, Eds. P. J. Linstrom and W. G. Mallard, National Institute of Standards and Technology, Gaithersburg MD, 20899, https://doi.org/10.18434/T4D303, (retrieved March 27, 2019)), it suffers from a high activation barrier (Figure S1) and is thus the minor reaction channel. For lead experimental and theoretical references, see: a) K. Saito, T. Shiose, O. Takahashi, Y. Hidaka, F. Aiba, K. Tabayashi, *J. Phys. Chem. A* **2005**, *109*, 5352–5357; b) J.-G. Chang, H.-T. Chen, S. Xu, M. C. Lin, *J. Phys. Chem. A* **2007**, *111*, 6789–6797.
[15] M. Grasemann, G. Laurenczy, *Energy Environ. Sci.* **2012**, *5*, 8171–8181.
[16] For reviews covering aspects on the preparation and reactions of "ship-in-a-bottle" catalysts see: a) G. A. Ozin, C. Gil, *Chem. Rev.* **1989**, *89*, 1749–1764; b) M. Ichikawa, *Platinum Met. Rev.* **2000**, *44*, 3–14; c) C. Li, *Catalysis Rev.* **2004**, *46*, 419–492.
[17] a) L. Li, S. Tang, C. Wang, X. Lv, M. Jiang, H. Wua, X. Zhao, *Chem. Commun.* **2014**, *50*, 2304–2307; b) H. Fei, S. M. Cohen, *Chem. Commun.* **2014**, *50*, 4810–4812.
[18] T. Toyao, K. Miyahara, M. Fujiwaki, T.-H. Kim, S. Dohshi, Y. Horiuchi, M. Matsuoka, *J. Phys. Chem. C* **2015**, *119*, 8131–8137.
[19] For reviews on the use of charged ligands in catalysis, see: a) D. M. Chisholm, J. S. McIndoe, *Dalton Trans.* **2008**, 3933–3945; b) J. Limberger, B. C. Leal, A. L. Monteiro, J. Dupont, *Chem. Sci.* **2015**, *6*, 77–94.
[20] Sulfonates are known to be amongst the weakest bases in the gas phase: J. D. Smith, R. A. J. O'Hair, T. D. Williams, *Phos. Sulf. Silicon Rel. Elements*, **1996**, *119*, 49–59. For example, the gas-phase basicity (anion proton affinity) of $PhSO_3^-$ is 13.4 eV while that of HCO_2^- is 15 eV (data from J. E. Bartmess, "Negative Ion Energetics Data" by in NIST Chemistry WebBook, NIST Standard Reference Database Number 69, Eds. P. J. Linstrom and W. G. Mallard, National Institute of Standards and Technology, Gaithersburg MD, 20899, https://doi.org/10.18434/T4D303, retrieved February 26, 2019).
[21] Crystal structure (CSD-1441659): a) C. R. Groom, I. J. Bruno, M. P. Lightfoot, S. C. Ward, *Acta Crystallogr.* **2016**, *B72*, 171–179; b) C. L. Hobday, R. J. Marshall, C. F. Murphie, J. Sotelo, T. Richards, D. R. Allan, T. Düren, F.-X. Coudert, R. S. Forgan, C. A. Morrison, S. A. Moggach, T. D. Bennett, *Angew. Chem. Int. Ed.* **2016**, *55*, 2401.
[22] For lead references of electric field effects in organic chemistry, see: a) A. C. Aragonès, N. L. Haworth, N. Darwish, S. Ciampi, N. J. Bloomfield, G. G. Wallace, I. Diez-Perez, M. L. Coote, *Nature* **2016**, *531*, 88–91; b) S. Shaik, R. Ramanan, D. Danovich, D. Mandal, *Chem. Soc. Rev.* **2018**, *47*, 5125–5145; c) L. Yue, N. Wang, S. Zhou, X. Sun, M. Schlangen, H. Schwarz, *Angew. Chem. Int. Ed.* **2018**, *57*, 14635–14639.
[23] For a discussion of electric field effects in MOFs, see: C. H. Hendon, A. J. Rieth, M. D. Korzyński, M. Dincă, *ACS Cent. Sci.* **2017**, *3*, 554–563.
[24] C. H. DePuy, *J. Org. Chem.* **2002**, *67*, 2393–2401.
[25] A. B. Redondo, F. L. Morel, M. Ranocchiari, J. A. van Bokhoven, *ACS Catal.* **2015**, *5*, 7099–7103
[26] A reviewer has correctly pointed out that production of minor amounts (even at ppm levels) of CO from the decomposition of formic acid to CO and H_2O rather than CO_2 and H_2 will affect the performance of fuel cells. Although we find no evidence in the mass spectrum for CO formation in competition with decarboxylation of **2 d** in step II of the catalytic cycle, the evaluation of the performance of MOF will require the analysis of all gaseous products to establish whether CO production is an issue.
[27] W. A. Donald, C. J. McKenzie, R. A. J. O'Hair, *Angew. Chem. Int. Ed.* **2011**, *50*, 8379–8383
[28] a) S. Gronert, *J. Am. Soc. Mass Spectrom.* **1998**, *9*, 845–848; b) W. A. Donald, G. N. Khairallah, R. A. J. O'Hair, *J. Am. Soc. Mass Spectrom.* **2013**, *24*, 811–815.
[29] Gaussian 09 (Revision D.01): M. J. Frisch et al., Gaussian, Inc., *Wallingford CT*, **2013**.
[30] a) A. D. Becke, *Phys. Rev.* **1988**, *38*, 3098–3100; b) A. D. Becke, *J. Chem. Phys.* **1993**, *98*, 5648–5652; c) C. Lee, W. Yang, R. G. Parr, *Phys. Rev. B* **1988**, *37*, 785–789.
[31] A. Schäfer, C. Huber, R. Ahlrichs, *J. Chem. Phys.* **1994**, *100*, 5829–5835.
[32] S. A. McLuckey, D. E. Goeringer, *J. Mass Spectrom.* **1997**, *32*, 461–474.
[33] P. D. Dau, P. B. Armentrout, M. C. Michelini, J. K. Gibson, *Phys. Chem. Chem. Phys.* **2016**, *18*, 7334–7340.
[34] a) J. P. Perdew, K. Burke, M. Ernzerhof, *Phys. Rev. Lett.* **1996**, *77*, 3865–3868; b) J. P. Perdew, K. Burke, M. Ernzerhof, *Phys. Rev. Lett.* **1997**, *78*, 1396.
[35] a) F. Weigend, R. Ahlrichs, *Phys. Chem. Chem. Phys.* **2005**, *7*, 3297–3305; b) F. Weigend, *Phys. Chem. Chem. Phys.* **2006**, *8*, 1057–1065.
[36] a) A. Schäfer, H. Horn, R. Ahlrichs, *J. Chem. Phys.* **1992**, *97*, 2571–2577; b) K. Eichkorn, F. Weigend, O. Treutler, R. Ahlrichs, *Theor. Chem. Acc.* **1997**, *97*, 119–124.
[37] D. Andrae, U. Haeussermann, M. Dolg, H. Stoll, H. Preuss, *Theor. Chim. Acta* **1990**, *77*, 123–141.

2.2   Ligated silver hydride cluster

Reproduced from:

Howard Z. Ma, Alasdair I. McKay, Antonija Mravak, Michael S. Scholz, Jonathan M. White, Roger J. Mulder, Evan J. Bieske, Vlasta Bonačić-Koutecký, and Richard A. J. O'Hair. Structural characterization and gas-phase studies of the $[Ag_{10}H_8(L)_6]^{2+}$ nanocluster dication. *Nanoscale*, 11(47), 2019, 22880-22889. Reproduced with permission from the Royal Society of Chemistry.

PAPER

Structural characterization and gas-phase studies of the [Ag₁₀H₈(L)₆]²⁺ nanocluster dication†

Howard Z. Ma,[a] Alasdair I. McKay, [iD][a] Antonija Mravak, [iD][b] Michael S. Scholz, [iD][a] Jonathan M. White, [iD][a] Roger J. Mulder, [iD][c] Evan J. Bieske, [iD][a] Vlasta Bonačić-Koutecký[b,d] and Richard A. J. O'Hair [iD]*[a]

The reactions between silver salts and borohydrides produce a rich set of products that range from discrete mononuclear compounds through to silver nanoparticles and colloids. Previous studies using electrospray ionization mass spectrometry (ESI-MS) to track the cationic products in solutions containing sodium borohydride, silver(I) tetrafluoroborate and the bisphosphine ligands, L, bis(diphenylphosphino)methane (dppm) and bis(diphenylphosphino)amine (dppa) have identified the dications [Ag₁₀H₈(L)₆]²⁺. Here we isolate and structurally characterize [Ag₁₀H₈(dppa)₆](BF₄)₂, and [Ag₁₀H₈(dppa)₆](NO₃)₂ *via* X-ray crystallography. Both dications have nearly identical structural features consisting of a Ag₁₀ scaffold with the atoms lying on vertices of a bicapped square antiprism. DFT calculations were carried out to suggest potential sites for the hydrides. Ion-mobility mass spectrometry experiments revealed that [Ag₁₀H₈(dppa)₆]²⁺ and [Ag₁₀H₈(dppm)₆]²⁺ have similar collision cross sections, while multistage mass spectrometry experiments were used to compare their unimolecular gas-phase chemistry. Although the same initial sequential ligand loss followed by cluster fission and H₂ evolution is observed, the more acidic N−H of the dppa provides a more labile H for H₂ loss and H/D scrambling processes as revealed by isotope labelled experiments.

Introduction

Coinage metal nanoclusters (CMNCs) continue to attract attention due to their diverse structures, interesting optoelectronic properties and potential roles in catalysis.[1,2] This class of materials for which the size ranges from a few atoms to a few hundred atoms, equivalent to a cross section of <2 nm,[3] are important intermediates in the formation of nanoparticles.[4] Unlike larger nanoparticles, CMNCs can often be well characterized by molecular techniques such as electrospray ionization mass spectrometry (ESI-MS) and single crystal X-ray diffraction.[5] Whilst chalcogenolate ligands have been traditionally employed to afford robust CMNCs,[6] CMNCs employing phosphine ligands are typically more hydride-rich facilitating their

application in a range of areas including: catalysis; transformation of organic substrates,[7] as potential precursors to naked metal clusters,[8,9] as models for energy storage.[10]

The reactions of coinage metal salts with borohydrides in the presence of capping ligands gives rise to a diverse array of ligated CMNCs.[6,7,11] We have been using an approach that blends ESI-MS to direct the bulk synthesis of hydride-rich CMNCs, high resolution mass spectrometry (HRMS) together with comparisons of the ESI-MS of NaBH₄ and NaBD₄ reaction mixtures to "count" the number of hydrides thereby allowing confident assignment of the molecular formula, X-ray crystallography, neutron diffraction and NMR spectroscopy for structural characterization, and multistage mass spectrometry (MSⁿ) experiments in conjunction with Density Functional Theory (DFT) calculations to examine the fundamental unimolecular chemistry of CMNCs.[12–22] Scheme 1 shows the range of CMNCs that can be formed by reacting coinage metal salts with borohydride in the presence of the small bite angle bisphosphine ligands bis(diphenylphosphino)methane (dppm) and bis(diphenylphosphino)amine (dppa) under different reaction conditions. A common structural motif has been a trinuclear metal center capped by one hydride binding in a (μ₃-H) fashion to give the dication 1²⁺ (ref. 13) or binding an additional chloride anion[12] or borohydride anions[14–17] to give the cations 2⁺ and 3⁺ (Scheme 1). The [Ag₁₀H₈(L)₆]²⁺ cluster dication, is a major ion in the ESI-MS of solutions con-
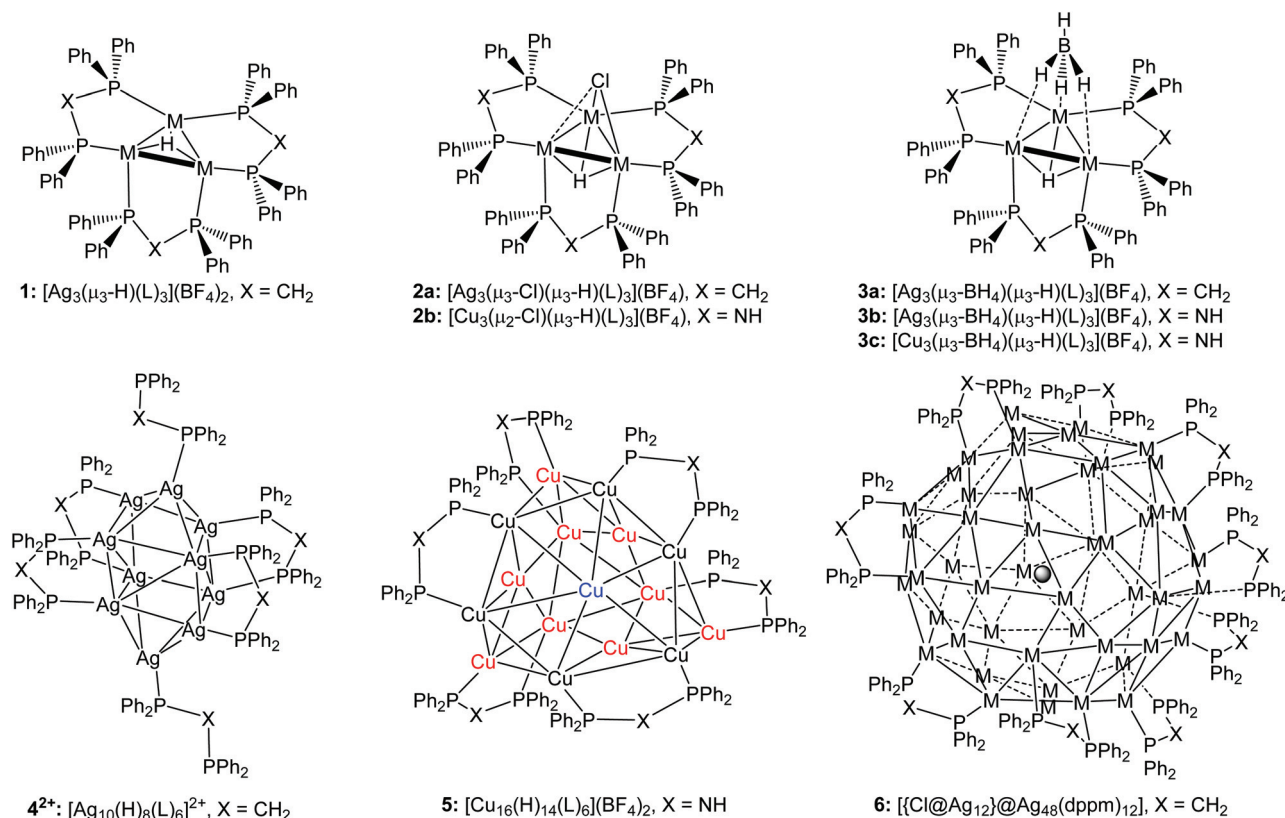
ᵃSchool of Chemistry and Bio21 Molecular Science and Biotechnology Institute, University of Melbourne, 30 Flemington Rd, Parkville, Victoria 3010, Australia. E-mail: rohair@unimelb.edu.au; Fax: (+)61 3 9347 8124
ᵇCenter of Excellence for Science and Technology-Integration of Mediterranean Region (STIM) at Interdisciplinary Center for Advanced Sciences and Technology (ICAST), University of Split, Poljička cesta 35, Split 21000, Croatia
ᶜCSIRO Manufacturing, Research Way, Clayton, Victoria 3168, Australia
ᵈChemistry Department, Humboldt University of Berlin, Brook-Taylor-Strasse 2, Berlin 12489, Germany
†Electronic supplementary information (ESI) available. CCDC 1919380–1919385. For ESI and crystallographic data in CIF or other electronic format see DOI: 10.1039/c9nr08321a

1: $[Ag_3(\mu_3\text{-}H)(L)_3](BF_4)_2$, X = CH$_2$

2a: $[Ag_3(\mu_3\text{-}Cl)(\mu_3\text{-}H)(L)_3](BF_4)$, X = CH$_2$
2b: $[Cu_3(\mu_2\text{-}Cl)(\mu_3\text{-}H)(L)_3](BF_4)$, X = NH

3a: $[Ag_3(\mu_3\text{-}BH_4)(\mu_3\text{-}H)(L)_3](BF_4)$, X = CH$_2$
3b: $[Ag_3(\mu_3\text{-}BH_4)(\mu_3\text{-}H)(L)_3](BF_4)$, X = NH
3c: $[Cu_3(\mu_3\text{-}BH_4)(\mu_3\text{-}H)(L)_3](BF_4)$, X = NH

4^{2+}: $[Ag_{10}(H)_8(L)_6]^{2+}$, X = CH$_2$

5: $[Cu_{16}(H)_{14}(L)_6](BF_4)_2$, X = NH

6: $[\{Cl@Ag_{12}\}@Ag_{48}(dppm)_{12}]$, X = CH$_2$

Scheme 1 Diversity in cluster structure and stoichiometry upon reaction of silver or copper salts with borohydrides in the presence of small bite angle bisphosphine ligands. Three bis(diphenylphosphino)methane (dppm) ligands which bind as bidentate ligands around the front face of the cluster in **6** are omitted for clarity reasons to highlight the metallic core. The grey ball in **6** represents the interstitial chloride within the icosahedral silver core.

taining AgBF$_4$, dppm and NaBH$_4$. Whilst ESI-MS facilitates optimization of conditions to maximise production of the Ag$_{10}$ cluster dication, all attempts to structurally characterize it in the condensed phase were unsuccessful. Our previous best efforts at characterizing its structure employed gas-phase VUV photoionization in conjunction with DFT to predict structure **4**$^{2+}$ with a distorted bicapped square antiprism (Johnson solid J$_{17}$) as the silver core (Scheme 1).[18] The six bisphosphine ligands were placed so that each silver atom is ligated by a single phosphine. The silver atoms which form the vertices of the antiprism are ligated by four bridging ligands, whilst the capping silver atoms are ligated in a monodentate binding mode. In the optimized structure two different coordination modes were adopted by the hydrides, four as μ$_2$-hydride and four as μ$_3$-hydride ligands. Switching to [Cu(MeCN)$_4$](BF$_4$), the related dppa ligand and tetrabutylammonium borohydride resulted in the [Cu$_{16}$H$_{14}$(L)$_6$]$^{2+}$ dication, **5**$^{2+}$, which this time could be isolated with X-ray crystallography identifying a new CMNC core structure consisting of a Cu$_9$ frustum cupola on top of a Cu$_7$ distorted hexagonal-shape base.[19] The growth process to form large clusters remains poorly understood, but may involve assembly from smaller clusters. For example, after publishing our work on [Ag$_3$(μ$_3$-H)(μ$_3$-BH$_4$)(dppm)$_3$](BF$_4$), **3a**,[14] we noticed that an NMR tube used to characterize this sample

contained a crystal with a different color (orange) and morphology. Although the disorder in the crystal precluded establishing the presence of potential counteranion(s) and solvent molecules, X-ray crystallography clearly revealed the formation of a new nanocluster, [{Cl@Ag$_{12}$}@Ag$_{48}$(dppm)$_{12}$], **6**.[21]

During recent efforts at preparing and studying the reactions of [Ag$_3$(μ$_3$-H)(μ$_3$-BH$_4$)(dppa)$_3$](BF$_4$), **3b**,[17] we noticed an additional low intensity signal at m/z 1699 in the ESI-MS, which is formulated as: [Ag$_{10}$H$_8$(dppa)$_6$]$^{2+}$, **7**$^{2+}$. Here we use X-ray crystallography to determine the structures of two cluster salts [Ag$_{10}$H$_8$(dppa)$_6$](BF$_4$)$_2$, **7(BF$_4$)$_2$**, and [Ag$_{10}$H$_8$(dppa)$_6$](NO$_3$)$_2$, **7(NO$_3$)$_2$**, which each contain essentially identical [Ag$_{10}$H$_8$(dppa)$_6$]$^{2+}$ clusters. We then use DFT calculations to suggest potential sites for the hydrides and describe attempts at further characterizing this cluster using NMR, IR and UV-Vis spectroscopy. Finally, we use gas-phase experiments to characterize the structure and unimolecular reactivity of **7**$^{2+}$.

Experimental

General considerations

All reactions and synthetic manipulations in affording crystalline material of [Ag$_{10}$H$_8$(L)$_6$](X)$_2$, X = BF$_4$, NO$_3$, were carried out

using standard Schlenk techniques under an atmosphere of pure nitrogen. Dichloromethane, acetonitrile and diethyl ether, were dried using a solvent purification system and stored over 3 Å molecular sieves prior to use. All other chemicals were used without further purification: $AgBF_4$, dppa (Strem); $NaBH_4$ (Ajax); $NaBD_4$ (98 atom % D, Sigma Aldrich), dppm (Merck), acetonitrile-d_3 (99.8% atom D, Cambridge Isotope Laboratories), dichloromethane-d_2 (99.8% atom D, Cambridge Isotope Laboratories).

Syntheses of $[Ag_{10}H_8(L)_6]^{2+}$ and $[Ag_{10}D_8(L)_6]^{2+}$ for MS analyses

$AgBF_4$ (20 mg, 0.10 mmol) and L = dppa, dppm (40 mg, 0.10 mmol; 40 mg, 0.10 mmol) were dissolved in CH_3CN (25 mL). $NaBH_4$ or $NaBD_4$ (38 mg, 1.0 mmol; 41 mg, 1.0 mmol) was then added and allowed to mix for 15 min. A 50 μM aliquot was then taken for mass spectrometry experiments which are described further below.

Synthesis of crystalline $[Ag_{10}H_8(dppa)_6](X)_2$, where X = BF_4, NO_3

$AgBF_4$ or $AgNO_3$ (0.39 g, 2.0 mmol, 0.34 g, 2.0 mmol) and dppa (0.77 g, 2.0 mmol) were dissolved in acetonitrile (60 mL). The colorless reaction mixture was cooled to 0 °C and stirred. To a separate Schlenk flask was added $NaBH_4$ (0.76 g, 20.0 mmol), to which the colorless reaction mixture was transferred by cannula and stirred for a further 3 h in the absence of light. The resultant yellow solution was filtered, the solvent was then removed under vacuum. The obtained powder was then extracted into dichloromethane, filtered and the solvent was again removed under vacuum. The resultant light-yellow solid was then washed with diethyl ether (3 × 5 mL), then dried under vacuum to afford a light-yellow powder (0.61 g). This material was then recrystallized at −4 °C by solvent diffusion. Crystals of $[Ag_{10}H_8(dppa)_6](BF_4)_2$ were grown by diffusion of pentane into a dichloromethane solution, whilst crystals of $[Ag_{10}H_8(dppa)_6](NO_3)_2$ were grown by diffusion of diethyl ether into an acetonitrile solution.

Mass spectrometry

Mass spectra were recorded on either: an Orbitrap Fusion Lumos mass spectrometer (Thermo Scientific, San Jose, California); a modified QExactive Orbitrap mass spectrometer (Thermo Fisher Scientific, Bremen, Germany); or a modified Finnigan LTQ linear ion trap mass spectrometer (Bremen, Germany). For experiments recorded on the Orbitrap Fusion Lumos, samples were introduced *via* nanoESI (nESI) using an Advion Triversa Nanomate (Advion, Ithaca, NY, USA). Further details on mass spectrometry experiments are included in the ESI.†

Ion mobility-mass spectrometry

The custom-built ion mobility-mass spectrometer has been previously described.[23] Briefly, silver cluster cations generated by electrospray ionization from a 10^{-4} M acetonitrile solution were introduced through a desolvation capillary into an ion funnel. An electrostatic gate at the end of the ion funnel was opened at 20 Hz to introduce packets of ions into a 0.9 m drift

tube filled with N_2 gas at ∼6 Torr and with an electric field of ∼44 V cm^{-1} sustained by a series of ring electrodes. At the end of the drift tube, the ions were collected by a second ion funnel before being guided through a differentially-pumped region by an octupole ion guide. Finally, the ions were mass selected by a quadrupole mass filter and detected at a channel electron multiplier connected to a multichannel scaler. An arrival time distribution (ATD) was built up as a histogram representing ion count *versus* drift time. Collision cross sections with N_2 buffer gas were calibrated with respect to the cross sections for a series of tetraalkylammonium salts, the details of which have been described previously.[23]

X-ray crystallography

Single crystal X-ray diffraction data for all samples were collected as follows: a typical crystal was mounted on a MiTeGen Micromounts using perfluoropolyether oil and cooled rapidly to 100.0(1) K in a stream of nitrogen gas using an Oxford Cryostream cooling device. Diffraction data were collected (ω-scans) on a Rigaku XtaLAB Synergy or Synergy-S diffractometer equipped with a Hypix detector using Cu-K$_\alpha$ radiation (λ = 1.54184 Å). Raw frame data were reduced using CrysAlisPro. The structures were solved using SHELXT,[24] and the refinement was carried out with SHELXL (version 2018/3)[25] employing full-matrix least-squares on F^2 using either the OLEX2 or WinGX software packages.[26,27] All non-hydrogen atoms were refined anisotropically. The hydrogen atoms were placed in geometrically calculated positions and refined using a riding model. Selected crystallographic data and comments about individual crystal structures can be found in the ESI.†

Computational methods

The Gaussian suite of programs[28] was used with the Perdew–Burke–Ernzerhof (PBE) functional[29,30] with resolution of identity method (W06)[31,32] and 19-electron relativistic effective core potential (19e-RECP) basis set[33] for silver atoms in combination with the split-valence-plus polarization (SVP) atomic basis set for all other atoms[34,35] to fully optimize structures of isomers of the silver nanocluster dication $[Ag_{10}X_8(L)_6]^{2+}$ (X = H or D) and $[Ag_{10}(L)_6]^{2+}$. Dispersion correction GD3[36] has been employed due to the presence of phenyl rings.

Collision cross sections for the relevant silver cluster cations were modelled using the trajectory method in a version of MOBCAL parametrized for N_2 buffer gas.[37–39] Errors are generated using 3σ from the MOBCAL output. The silver atoms, for which no parametrization presently exists, were modelled using the Lennard-Jones parameters for silicon. Input charge distributions were calculated with the BP86 density functional, along with the same basis set as above, using the CHELPG scheme as implemented in the ORCA program.

NMR spectroscopy

NMR spectra were performed on a Bruker Avance 400 NMR spectrometer (400.13 MHz ^1H frequency) equipped with a 5 mm triple resonance broadband probe (BB/^2H–^1H/^{19}F) at −10 °C. Chemical shifts for ^1H spectra were referenced

to the residual protonated solvent signal peaks (CD$_2$Cl$_2$: ^{1}H δ 5.32 ppm or CD$_3$CN: ^{1}H δ 1.94 ppm). Chemical shifts for all heteronuclear experiments are referenced using the Unified Scale relative to 0.3% tetramethylsilane in deuteriochloroform.[40,41]

Results and discussion

ESI-MS and X-ray crystallography reveal polydisperse mixtures of clusters

We have previously used electrospray ionization mass spectrometry (ESI-MS) to direct the synthesis and characterization of **3b** from the reaction of AgBF$_4$, dppa and NaBH$_4$ in acetonitrile.[17] A 1 : 1 : 3 ratio of the starting materials was found to give an excellent signal for the cation [Ag$_3$(H)(BH$_4$)(dppa)$_3$]$^+$ (m/z 1491 (exp)/m/z 1491 (calc.)). Following this report, we noticed an additional low intensity signal at m/z 1699, which, based on isotope patterns (Fig. 1), high resolution accurate mass measurements and a selective deuterium labelling experiment in which NaBH$_4$ is replaced by NaBD$_4$ (Fig. 1D), is formulated as: [Ag$_{10}$H$_8$(dppa)$_6$]$^{2+}$ (m/z 1693.9012 (exp)/m/z 1693.9010 (calc.)). This dicationic cluster, **7^{2+}**, is directly related to the [Ag$_{10}$H$_8$(dppm)$_6$]$^{2+}$ cluster, **4^{2+}**, we have previously reported.[12,18,20] The identity of the bisphosphine ligand is likely to play a significant role in both the cluster assembly as well as the overall cluster stability. For example, we have previously shown that when the smaller bisphosphine ligand, bis(dimethylphosphino)methane (dmpm), was used, a signal for [Ag$_{10}$H$_8$(dmpm)$_6$]$^{2+}$ was not observed in the ESI-MS.[20]

It has been reported that an increase in the borohydride ion concentration facilitates the formation of larger nanoclusters and nanoparticles.[4] To this end, we have increased the ratio of NaBH$_4$ relative to the Ag$^+$ salt and the bisphosphine ligand, discovering that the intensity of the [Ag$_{10}$H$_8$(dppa)$_6$]$^{2+}$ peak was significantly increased (Fig. 1A). Despite this however, a plethora of clusters are still evident in solution, including: [Ag$_3$H(dppa)$_3$]$^{2+}$ (m/z 740), [Ag(dppa)$_2$]$^+$ (m/z 879), [Ag$_3$H(dppa)$_4$]$^{2+}$ (m/z 933), [Ag$_2$H(dppa)$_2$]$^+$ (m/z 987), [Ag$_3$H(BH$_4$)(dppa)$_3$]$^+$ (m/z 1496), and [Ag$_3$H(Cl)(dppa)$_3$]$^+$ (m/z 1516).

Unfortunately, all attempts to isolate pure **7(BF$_4$)$_2$** on a synthetic scale such as to enable characterization by other spectroscopic techniques such as multinuclear NMR (Fig. S1–S6†), IR (Fig. S7 and S8†) and UV-vis (Fig. S9 and S10†) were not successful. Thus the spectra collected are likely to be contaminated by other species and so are not informative. Indeed, an ESI-MS spectrum of the sample post recrystallization revealed the presence of several other smaller clusters amongst **7^{2+}** (Fig. 1B). Several of these were characterized by X-ray crystallography, as discussed further below (Scheme 2). The NMR spectra of the recrystallized reaction mixtures are consistent
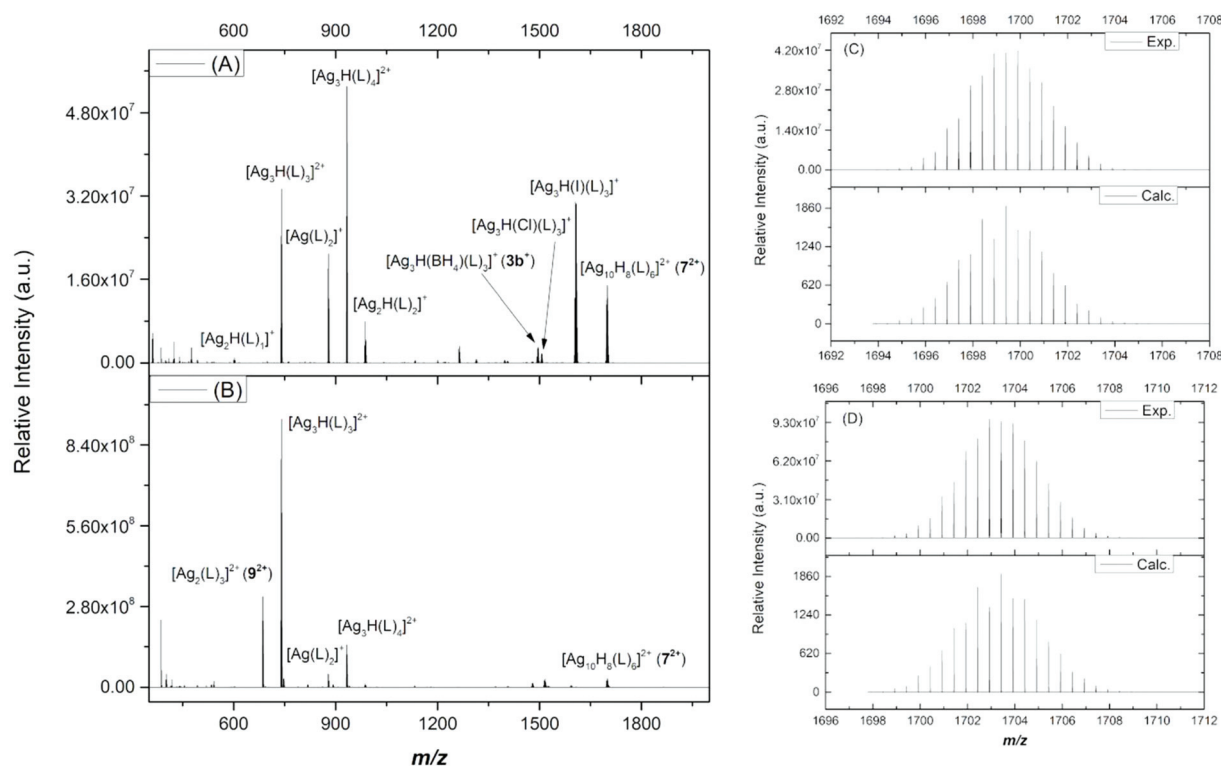
Fig. 1 Full ESI-MS in the positive mode of (A) reaction mixture of (1 : 1 : 10) AgBF$_4$: dppa : NaBH$_4$ 15 min after preparation showing the formation of multiple cluster species; (B) post work up of a reaction mixture from a large scale reaction. The formation of [Ag$_3$H(L)$_3$]$^{2+}$ (m/z 740) is likely formed in source from **3b$^+$**; (C) full high resolution isotope envelope of [Ag$_{10}$H$_8$(dppa)$_6$]$^{2+}$ (**7^{2+}**) (expt. *vs.* calc.), and; (D) full isotope envelope of [Ag$_{10}$D$_8$(dppa)$_6$]$^{2+}$ (**7$_D$$^{2+}$**) (expt. *vs.* calc.) (m/z 1697.9252 (expt.)/m/z 1697.9261 (calc.)).

$$AgX + Ph_2PNHPPh_2 + NaBH_4 \xrightarrow{CH_3CN}$$

7²⁺: $[Ag_{10}(H)_8(L)_6]^{2+}$ **8**: $[Ag_2(\mu_2\text{-}(L\text{-}H))_2]$ **9²⁺**: $[Ag_2(\mu_2\text{-}(L)_3]^{2+}$ **10⁺**: $[Ag_3(\mu_3\text{-}Cl)_2(L)_3]^{+}$
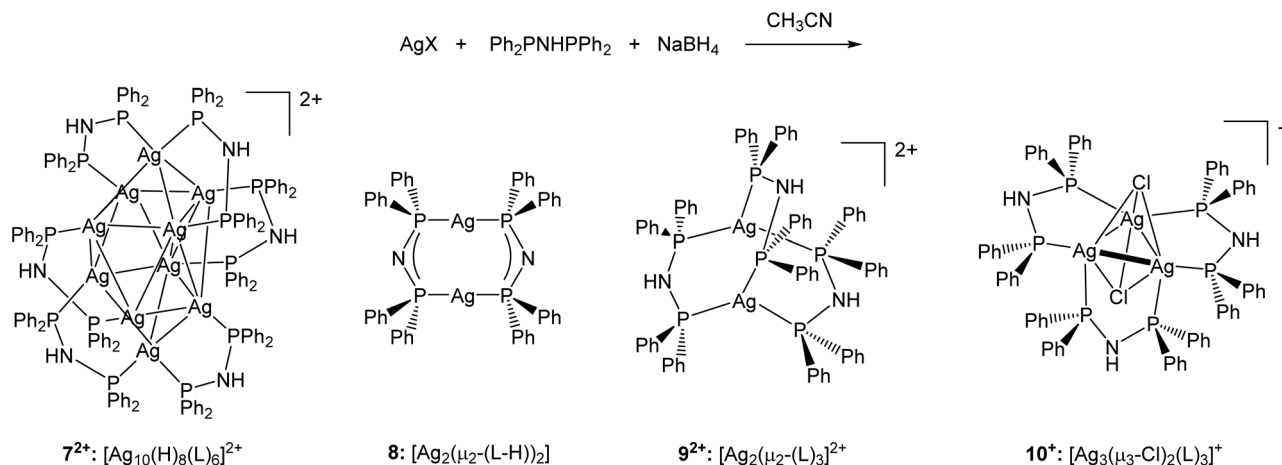
Scheme 2 Crystallographically characterized silver clusters obtained from bulk crystalline material formed from reaction mixtures of AgX (X = BF₄ or NO₃), dppa (L) and sodium borohydride in acetonitrile, with subsequent recrystallization from a series of different solvents (see text).

with intractable mixtures of cationic and neutral silver complexes, such that the ^1H, ^2H and $^{31}P\{^1H\}$ resonances of **7(BF₄)₂** or **7$_D$(BF₄)₂** could not be assigned with any certainty. A resonance at δ 4.60 ppm was consistently observed in the ^1H NMR spectra (CD₃CN) even at low temperatures (−10 °C), which we assign to dissolved H₂.[42] Similarly, a signal for HD was observed in the ^1H NMR spectrum of crude **7$_D$(BF₄)₂**. These data suggest slow decomposition of silver hydride nanoclusters during spectrum acquisition, further confounding their structural assignment *via* NMR spectroscopy. The poor thermal stabilities of silver polyhydrido clusters is well established.[43]

Batches of crystalline material were examined and single crystals were characterized by X-ray crystallography. Amongst these crystals, a darker amber colored crystal of different habit was identified. An X-ray diffraction study revealed this to be **7(BF₄)₂**, and the UV-Vis spectrum of the bulk material shows an absorption at around 350 nm (Fig. S9†), consistent with the observed color of **7(BF₄)₂**. The structure solves in the orthorhombic space group *Pbcn* with a half cluster and two molecules of dichloromethane in the asymmetric unit (Fig. S11†). Whilst the final structure is of poor quality, atom connectivity is unambiguous. The poor aerobic and light stability of these crystals prevented them from being readily separated by hand for further characterization by NMR.[44]

In attempts to produce better quality crystals of this nanocluster, we replaced the silver precursor, AgBF₄ salt with AgNO₃, which upon recrystallization from a mixture of acetonitrile and diethyl ether afforded a few amber crystals, from which a good quality structure of **7(NO₃)₂** was obtained by X-ray crystallography. This is one of the largest homometallic silver polyhydrido clusters to be structurally characterized,[43] with the previously reported silver nanocluster $[Ag_{40}(dmbt)_{24}(PPh_3)_8]$ (where dmbt = 2,4-dimethylbenzenethiolate)[45,46] only very recently being reassigned as the silver hydride nanocluster dication $[Ag_{40}H_{12}(dmbt)_{24}(PPh_3)_8]^{2+}$.[47] The structure of **7(NO₃)₂** solves in the orthorhombic space group $P2_12_12_1$ with a full molecule in the asymmetric unit. The structure features a Ag₁₀ scaffold with the atoms lying on vertices of a bicapped square antiprism (Fig. 2). The Ag–Ag distances span 2.7704(9)–3.2605(10) Å, which lies within the range of contacts 2.82–3.38 Å reported for other silver clusters.[48] A similar geometry was reported for $[Rb(2,2,2\text{-crypt})]_2[Ge_{10}](en)_{1.5}$, where the germanium atoms lie on the vertices of a bicapped square antiprism.[49] The six bisphosphine ligands are arranged such that each capping silver atom is bound by two phosphorous atoms from different dppa ligands. These bisphosphines further ligate silver atoms on the square antiprism, to afford a planar Ag₃(dppa)₂ unit. The remaining silver atoms on the square antiprism are bridged by dppa ligands, with each displaying a short N–H···O–NO₂ contact (Fig. 2). A similar interaction to the $[BF_4]^-$ anion was not observed in the **7(BF₄)₂** structure. It is noteworthy that while the core configuration of silver atoms is similar to that predicted for **4²⁺** from our previous gas-phase study,[20] the arrangement and binding of the dppa ligands is quite different. For instance, each capping silver atom was predicted to be ligated by a monodentate
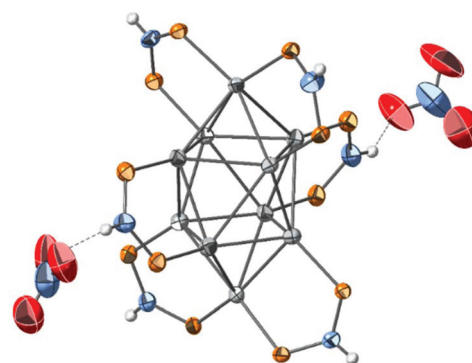
Fig. 2 Solid-state structure of **7²⁺** from the **7(NO₃)₂** salt (50% displacement ellipsoids). All low occupancy disorder components, phenyl groups and solvent molecules omitted for clarity. Color legend: Ag (silver); P (orange); N (blue); H (white) and O (red).

dppa, with the non-bound phosphine occupying space above. Unfortunately, the positions of the hydrides in 7^{2+} could not be located. We therefore turned to other means of characterization including Density Functional Theory (DFT) calculations, the results of which are discussed below.

We now return to the structural characterization of other species present in the bulk crystalline material formed from both the AgBF$_4$ and AgNO$_3$ salts. Amongst the colorless blocks of $3b$,[17] colorless rectangular prisms were found to be the neutral dimer [Ag$_2$(μ-P(Ph)$_2$NPPh$_2$)$_2$], 8. Whilst this complex was previously reported by Usón and coworkers,[50] it has not been previously structurally characterized. The solid-state structure consists of a planar eight-membered Ag$_2$P$_4$N$_2$ ring with crystallographic inversion symmetry (Fig. S13†). The Ag···Ag distance of 2.9070(3) Å is comparable to those in the related cationic complexes [Ag$_2$(μ-dppm)$_2$](ClO$_4$)$_2$ (2.9532(7) Å)[51] and [Ag$_2$(μ-P(Ph)$_2$N(Me)PPh$_2$)$_2$(THF)$_2$](BF$_4$)$_2$ (2.911 Å).[52] Whilst the P–N bond lengths in 8 (1.621(2) and 1.620(3) Å) are shorter than those in [Ag$_2$(μ-dppa)$_3$](BF$_4$)$_2$ (1.676(9)–1.725(9) Å),[53] consistent with deprotonation of the ligand set in the former. Colorless crystals of [Ag$_2$(μ-dppa)$_3$](BF$_4$)$_2$, 9(BF$_4$)$_2$, and [Ag$_2$(μ-dppa)$_3$](NO$_3$)$_2$, 9(NO$_3$)$_2$, were also identified and characterized by X-ray crystallography. The former had been previously characterized by Hill.[53] However, unlike the former the latter contains a short contact to the anion (Fig. S14†), similar to that in 7(NO$_3$)$_2$, which bridges an adjacent cluster. Yellow crystals were also obtained when a dichloromethane/pentane mixture was employed for the recrystallization. X-ray crystallographic characterization revealed these to be [Ag$_3$(μ$_3$-Cl)$_2$(dppa)$_3$](BF$_4$), 10(BF$_4$) and [Ag$_3$(μ$_3$-Cl)$_2$(dppa)$_3$](NO$_3$), 10(NO$_3$). As signals for 10^+ are absent from the ESI-MS of the worked up reaction mixtures (Fig. 1B), these species are

thought to arise from chloride abstraction from the dichloromethane solvent on the crystallization timescale, as has been previously reported.[54,55] These structures feature an Ag$_3$(μ$_3$-Cl)$_2$ core arranged in a trigonal bipyramid (Fig. S15 and S16†), which closely resembles those in similar complexes such as [Ag$_3$(μ$_3$-Cl)$_2$(dppm)$_3$](BF$_4$).[12] Once again the structure of the nitrate complex, 10(NO$_3$), features a short contact to the anion, which is not present in the tetrafluoroborate complex, 10(BF$_4$).

DFT calculations to suggest locations for the positions of the hydrides in 7^{2+}

In order to elucidate the position of the hydrides in 7^{2+}, we have turned to DFT calculations. We created two models based on the possible occupancy sites of the hydrides around the Ag$_{10}$ core obtained from X-ray crystallography. Our two starting models are illustrated in Fig. 3, the DFT calculations were conducted using the cartesian coordinates from the crystal structure and allowing them to relax in the gas-phase in the absence of counter anions. In isomer $7a^{2+}$; the hydrides are initially arranged along each face of the two opposing capped ends of the Ag$_{10}$ core, whereas in isomer $7b^{2+}$; the hydrides are initially spread across the middle belt of the Ag$_{10}$ core (Fig. 3B).

In both cases, upon optimization at the RI-PBE/RECP-def2-SVP level of theory, the hydrides appear to spread themselves out over the entire Ag$_{10}$ core, as illustrated in Fig. 3B and C. Isomer $7a^{2+}$ is slightly energetically favored by 0.01 eV compared to isomer $7b^{2+}$. In both isomeric structures, two H atoms cap opposing faces of the pyramid in a μ$_3$-H fashion on each of upper and lower capping pyramids. Whilst along the belt, two of the four H atoms are located at opposing Ag$_3$ faces
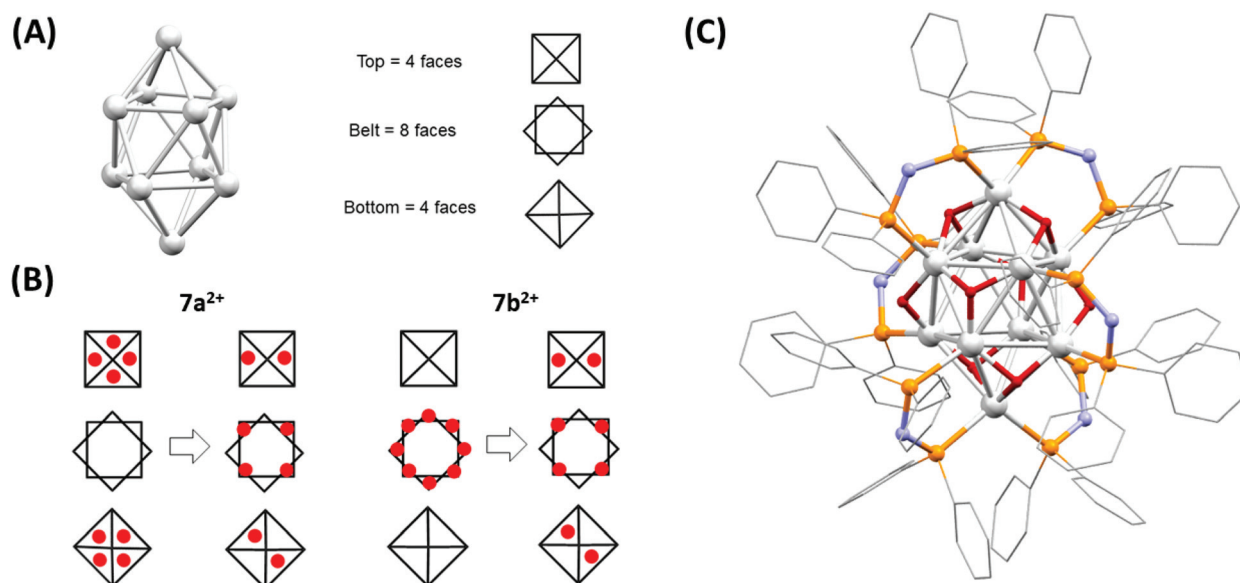
Fig. 3 (A) Simple representation of the top, middle belt and bottom of cluster 7^{2+} showing all possible triangular faces. (B) Initial placement of hydrides, represented by red circles, on the triangular faces for two isomers, before and after optimization. (C) Fully optimized structure of isomer $7a^{2+}$ of [Ag$_{10}$H$_8$(dppa)$_6$]$^{2+}$, non-hydride hydrogens omitted for clarity. Color legend: Ag (silver); P (orange); N (blue); H (red) and C (gray).

of the belt in a μ_3 position, the two other H atoms form a μ_2-bridge along the edges of the antiprism. Overall, after geometric optimization both isomeric structures do not differ in the core subunit as well as in the position of the hydrides, while the only difference between them occurs in the position of the ligands. To explore the impact of the hydride ligands on the core structure of $[Ag_{10}H_8(dppa)_6]^{2+}$, $\mathbf{7^{2+}}$ we have adopted the approach of Takano *et al.*,[56] whom carried out DFT studies on model systems of bimetallic clusters $[PdAu_8(PMe_3)_8]^{2+}$ and interstitially H doped $[HPdAu_8(PMe_3)_8]^+$ and compared the calculated structures. The authors found that upon incorporation of a hydride, a deformation of the cluster core was observed. Upon optimization of the structures of $[Ag_{10}(dppa)_6]^{2+}$ derived from isomer $\mathbf{7a^{2+}}$ and $\mathbf{7b^{2+}}$ in which all eight hydrides were removed, the original bicapped square antiprism Ag_{10} scaffold collapses to a bicapped (μ_3) irregular parallelepiped (Fig. S17†). This suggests that both hydride and bisphosphine ligands play an important role in stabilization of the Ag_{10} core geometry.

We have also calculated the vibrational spectra of $\mathbf{7a^{2+}}$ and $\mathbf{7a_D^{2+}}$ illustrating the likely vibrations of the Ag–H bonds (Fig. S18†). Many of the Ag–H modes lie below 1000 cm^{-1}, have weak intensities and overlap with other modes. This coupled with the experimental complications of not having a pure sample means that the experimentally determined IR spectra (Fig. S7 and S8†) provide no definite proof on the location of the hydrides.
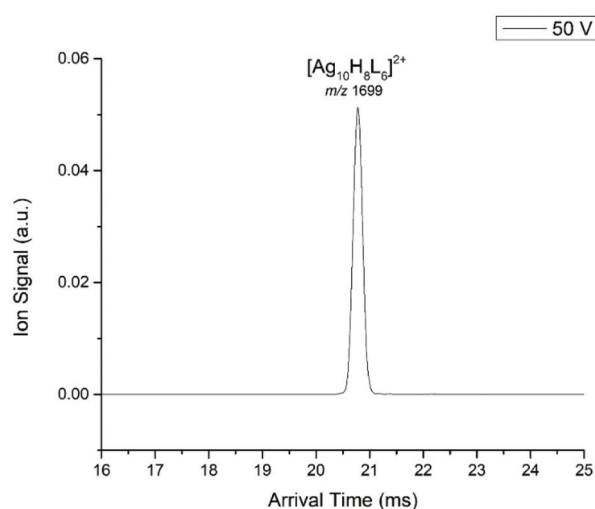
Fig. 4 Ion mobility arrival time distribution (ATD) of $[Ag_{10}H_8(dppa)_6]^{2+}$ showing one peak likely corresponding to a single isomeric structure.

Ion mobility-mass spectrometry of $[Ag_{10}H_8(dppa)_6]^{2+}$ and $[Ag_{10}H_8(dppm)_6]^{2+}$

Given that the $[Ag_{10}H_8(dppm)_6]^{2+}$ dication cluster has eluded structural characterization *via* X-ray crystallography, we were interested in comparing the gas-phase structures of both Ag_{10} clusters. Ion mobility spectrometry has in the past been used to study the structures of the all silver-alkynyl clusters $[Ag_{14}(C{\equiv}CtBu)_{12}Cl]^+$ and hetero-silver–copper-alkynyl clusters $[Ag_8Cu_6(C{\equiv}CtBu)_{12}Cl]^+$,[57] since the collision cross-section is sensitive to the 'shape' or 'size' of the ion, and to determine the presence of any potential isomeric structures.[58] We thus used this method to examine whether the gas-phase structures of the Ag_{10} clusters, based upon their collision cross-sections (CCS), were consistent with the structure of $[Ag_{10}H_8(dppa)_6]^{2+}$ observed *via* X-ray crystallography and to postulate the structure of $[Ag_{10}H_8(dppm)_6]^{2+}$.

Arrival time distributions of $[Ag_{10}H_8(dppa)_6]^{2+}$ suggest that the ligated silver hydride clusters maintains one structure in the gas-phase (Fig. 4). The CCS values of $[Ag_{10}H_8(dppa)_6]^{2+}$ and $[Ag_{10}H_8(dppm)_6]^{2+}$ were experimentally determined to be 528 ± 5 Å^2 and 534 ± 5 Å^2, respectively (Fig. S19†). These values are close to those calculated for the gas-phase optimized geometry from the crystal structure of $\mathbf{7^{2+}}$ (560 ± 20 Å^2), but are significantly different to the values calculated from the isomeric structures $\mathbf{4a^{2+}}$, $\mathbf{4b^{2+}}$ and $\mathbf{4c^{2+}}$ based on our previous models for $[Ag_{10}H_8(dppm)_6]^{2+}$ (Scheme 1) which were around 630 ± 20 Å^2. This suggests that $[Ag_{10}H_8(dppa)_6]^{2+}$ and $[Ag_{10}H_8(dppm)_6]^{2+}$ likely have similar gas-phase structures. Our results would suggest that the structure of $[Ag_{10}H_8(dppm)_6]^{2+}$ is more like that of the crystal structure of $\mathbf{7^{2+}}$ rather than our initial model $\mathbf{4^{2+}}$. Analysis of computed CCS values for several isomers $[Ag_{10}H_8(dppa)_6]^{2+}$ and $[Ag_{10}H_8(dppm)_6]^{2+}$ supports our hypothesis (Table 1).

Gas-phase fragmentation chemistry of $[Ag_{10}H_8(dppa)_6]^{2+}$ and $[Ag_{10}H_8(dppm)_6]^{2+}$

Since the ion mobility results are consistent with similar structures for $[Ag_{10}H_8(dppm)_6]^{2+}$ and $[Ag_{10}H_8(dppa)_6]^{2+}$, we wanted to find out whether their fragmentation chemistry is the same. Multistage mass spectrometry experiments have been previously conducted on $[Ag_{10}H_8(dppm)_6]^{2+}$ whereby a mass selection window of 15 *m/z* units was used to isolate the precursor ion, thereby subjecting the entire isotopic pattern of the selected parent cluster to CID.[20] The various observed fragmentation channels are summarized in Scheme 3. To compare the chemistry of $[Ag_{10}H_8(dppm)_6]^{2+}$ and $[Ag_{10}H_8(dppa)_6]^{2+}$

Table 1 Comparison of experimentally determined and computationally predicted gas-phase CCS values of several isomers of the $[Ag_{10}H_8(L)_6]^{2+}$ (L = dppa or dppm) clusters

Species	CCS (Å^2) expt.	$\mathbf{7a^{2+}}$	$\mathbf{7b^{2+}}$	$\mathbf{4a^{2+}}$	$\mathbf{4b^{2+}}$	$\mathbf{4c^{2+}}$
$[Ag_{10}H_8(dppa)_6]^{2+}$	528 ± 5	562 ± 20	565 ± 20	569 ± 20^a	580 ± 20^a	588 ± 20^a
$[Ag_{10}H_8(dppm)_6]^{2+}$	534 ± 5	570 ± 20	571 ± 20	635 ± 20	623 ± 20	643 ± 20

^{a} These CCS values are obtained from geometry optimizations which did not terminate, presumably due to a flat potential energy surface along ligand rotation and torsion coordinates.
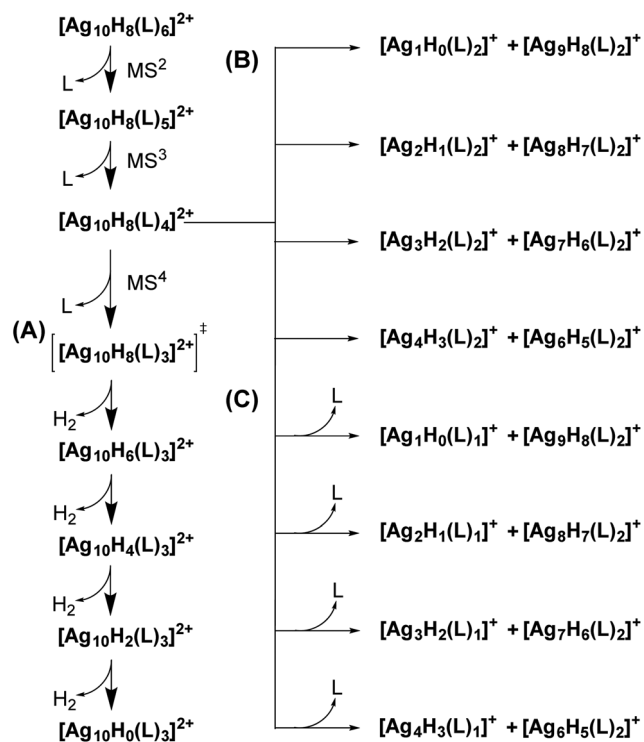
Scheme 3 Results of multistage mass spectrometry experiments of the dicationic species $[Ag_{10}H_8(dppa)_6]^{2+}$ and/or $[Ag_{10}H_8(dppm)_6]^{2+}$ highlighting the unique chemistry that is initiated upon ligand loss from the parent ion. (A) Sequential H_2 loss; (B) formation of complementary monocations; (C) further ligand loss. L = bis(diphenylphosphino)amine = dppa or bis(diphenylphosphino)methane = dppm.

under identical ion-activation conditions, we have carried out single-isotope MS^n experiments by isolating the monoisotopic ion of both parent clusters and subjecting them to low energy CID (see Fig. S20†). We have also employed other ion activation methods including Higher Energy Collision-Induced Dissociation (HCD) and laser induced dissociation (LID) in order to investigate the full breadth of their unimolecular fragmentation chemistry. The results of which suggest similar fragmentation channels to that discussed below (see Fig. S21–S24†).

Under CID conditions, both clusters $[Ag_{10}H_8(dppa)_6]^{2+}$ (m/z 1693.9009) and $[Ag_{10}H_8(dppm)_6]^{2+}$ (m/z 1690.9135) initially undergo sequential ligand loss to give $[Ag_{10}H_8(L)_4]^{2+}$ (L = dppa: m/z 1308.7853/L = dppm: m/z 1306.7949). Isolation of the de-ligated product ion followed by another stage of CID led to the formation of three subsets of ions; (A) a silver dication $[Ag_{10}(L)_3]^{2+}$ via loss of another ligand and subsequent spontaneous H_2 evolution; (B) complementary singly charged ion pairs via fission of the cluster core, and; (C) secondary fragment ions arising from either ligand loss followed by core fission and/or by loss of a ligand from one of the ions formed in (B). Indeed, these are the same pathways we have previously observed with cluster $[Ag_{10}H_8(dppm)_6]^{2+}$.[20]

The MS^3 spectra of clusters $[Ag_{10}H_8(dppm)_6]^{2+}$ and $[Ag_{10}H_8(dppa)_6]^{2+}$ are compared in Fig. S20.† Whilst the MS^3 spectra appear similar, one distinction is apparent when switching from L = dppm = $((Ph_2P)_2CH_2)$ to L = dppa =

$((Ph_2P)_2NH)$. Owing to the lability of the N–H of the dppa ligand, an extra H is available for further H_2 loss. For example, in the formation of the species $[Ag_9H_8(L)_2]^+$, a single peak is observed where L is dppm corresponding to the desired ion (m/z 1738.4447 (expt.)/m/z 1738.4473 (calc.)). When L = dppa however, the corresponding $[Ag_9H_8(L)_2]^+$ ion is not the major species formed. Instead, an ion 2 m/z units lighter is in greater abundance, suggesting a loss of H_2 from $[Ag_9H_8(L)_2]^+$. In order to determine whether this spontaneous loss of H_2 was from the hydrides, we carried out a deuterium labelled study and looked at the formation of $[Ag_9D_8(L)_2]^+$. Fig. S25c† shows a mass difference of 3 m/z units from $[Ag_9D_8(L)_2]^+$ corresponding to HD loss and thus indicating the involvement of the N–H dppa ligand in the process. The less acidic methylene proton on the dppm ligand is unavailable for this pathway and as such no further H_2 loss is observed from $[Ag_{10}H_8(dppm)_6]^{2+}$. These results are consistent with the earlier ^1H NMR spectroscopic data, where the formation of HD was also observed.

One channel of interest was that of the formation of an all-silver cluster with the formula $[Ag_{10}(L)_3]^{2+}$ via the liberation of four molecules of H_2 (Scheme 3A). Previously, we hypothesized that the loss of four units of molecular H_2 occurred sequentially and spontaneously from the metastable $[Ag_{10}H_8(L)_3]^{2+}$ cluster.

However, we were unable to show the formation of the individual ions en-route to $[Ag_{10}(L)_3]^{2+}$. Here, via Higher Energy Collision-induced Dissociation-tandem mass spectrometry (HCD-MS/MS) experiments, we present evidence of the loss of H_2 from $[Ag_{10}H_8(L)_3]^{2+}$ and D_2 from $[Ag_{10}D_8(L)_3]^{2+}$ (see Fig. 5
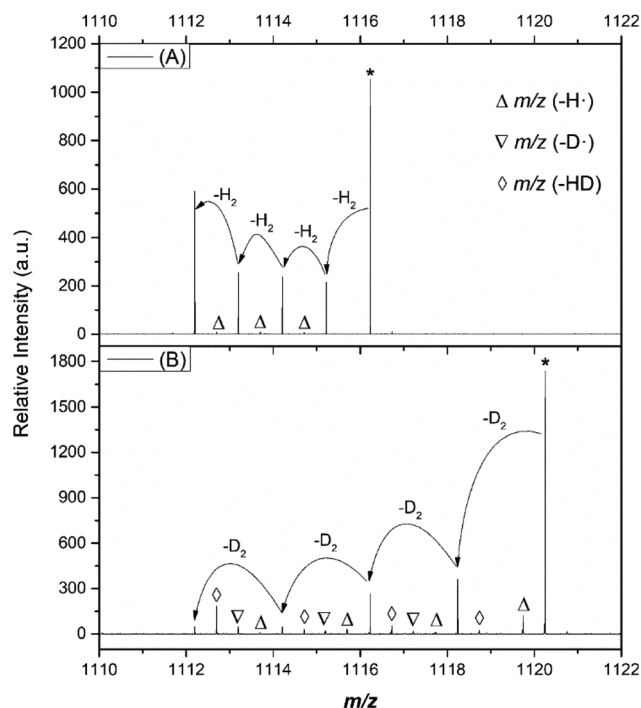
Fig. 5 HCD-MS/MS fragmentation of (A) $[Ag_{10}H_8(dppa)_6]^{2+}$ illustrating the sequential liberation of H_2 to form $[Ag_{10}(dppa)_3]^{2+}$ and; (B) $[Ag_{10}D_8(dppa)_6]^{2+}$ illustrating multiple fragmentation channels derived from liberation of D_2, HD, H and D loss. For each individual ion formed, see Table S13 in the ESI.†

and Fig. S26†). The accompanied losses of H and D have been observed for deuterio-analogues of the copper clusters $[Cu_{16}H_{14}(dppa)_6]^{2+}$ (5^{2+}) and $[Cu_{18}H_{16}(dppe)_6]^{2+}$ (dppe = bis(diphenylphosphino)ethane = $Ph_2PCH_2CH_2PPh_2$).[19]

Conclusions

This work highlights the fascinating array of nanoclusters that can be formed upon mixing silver salts and borohydrides in the presence of capping ligands. Under reaction conditions aimed at optimizing $[Ag_{10}H_8(dppa)_6]^{2+}$, we find that the bulk crystalline material consists of a polydisperse mixture of charged and neutral silver species (Scheme 2). While $[Ag_{10}H_8(dppa)_6](BF_4)_2$, $7(BF_4)_2$, and $[Ag_{10}H_8(dppa)_6](NO_3)_2$, $7(NO_3)_2$, are amongst the largest homometallic silver polyhydrido cluster to be structurally characterized by X-ray crystallography, the fact that they are formed as a polydisperse mixture together with the complexity of their spin systems and inherent poor stability is an obstacle for their characterization by other analytical methods such as NMR. The recent reassignment of the formula of the previously reported silver nanocluster $[Ag_{40}(dmbt)_{24}(PPh_3)_8]$ (where dmbt = 2,4-dimethylbenzenethiolate)[45,46] as the silver hydride nanocluster dication $[Ag_{40}H_{12}(dmbt)_{24}(PPh_3)_8]^{2+}$,[47] highlights that the molecular formulas of atomically precise nanoclusters (APNCs) formed *via* reactions of metal salts with reductants such as $NaBH_4$ should be assigned using both HRMS together with comparisons of the ESI-MS of $NaBH_4$ and $NaBD_4$ prepared APNCs. Any shifts of the isotope envelopes to higher m/z values would confirm the presence and allow the "counting" of the number of hydrides. Here we have demonstrated the value of using ion-mobility mass spectrometry to relate the gas-phase collision cross section to the X-ray structure and predict structures of related clusters in the gas phase. Complementary to experimental techniques, a computational approach with DFT methods allow for the likely positions of hydrides to elucidated. Altogether, the bicapped square antiprism structure of the core with associated H atoms seems to be common to ligated $[Ag_{10}H_8(L)_6]^{2+}$ clusters with L = dppm, dppa.

Conflicts of interest

There are no conflicts to declare.

Acknowledgements

Notes and references

1 In the recent special issue "Toward Atomic Precision in Nanoscience" of *Acc. Chem. Res.*, many of the aricles focussed on coinage metal nanoclusters. See: R. Jin, Y. Pei and T. Tsukuda, *Acc. Chem. Res.*, 2019, **52**, 1.

2 N. Goswami, J. Li and J. Xie, in *Frontiers of Nanoscience*, ed. T. Tsukuda and H. Häkkinen, Elsevier, 2015, vol. 9, ch. 11, pp. 297–345.

3 R. Jin, *Nanoscale*, 2010, **2**, 343.

4 R. S. Dhayal, W. E. van Zyl and C. W. Liu, *Acc. Chem. Res.*, 2016, **49**, 86.

5 A. W. Cook and T. W. Hayton, *Acc. Chem. Res.*, 2018, **51**, 2456.

6 R. Jin, C. Zeng, M. Zhou and Y. Chen, *Chem. Rev.*, 2016, **116**, 10346.

7 A. J. Jordan, G. Lalic and J. P. Sadighi, *Chem. Rev.*, 2016, **116**, 8318.

8 R. S. Dhayal, H.-P. Chen, J.-H. Liao, W. E. van Zyl and C. W. Liu, *ChemistrySelect*, 2018, **3**, 3603.

9 M. Jash, A. C. Reber, A. Ghosh, D. Sarkar, M. Bodiuzzaman, P. Basuri, A. Baksi, S. N. Khanna and T. Pradeep, *Nanoscale*, 2018, **10**, 15714.

10 R. S. Dhayal, W. E. van Zyl and C. W. Liu, *Dalton Trans.*, 2019, **48**, 3531.

11 M. S. Bootharaju, R. Dey, L. E. Gevers, M. N. Hedhili, J.-M. Basset and O. M. Bakr, *J. Am. Chem. Soc.*, 2016, **138**, 13770.

12 A. Zavras, G. N. Khairallah, T. U. Connell, J. M. White, A. J. Edwards, P. S. Donnelly and R. A. J. O'Hair, *Angew. Chem., Int. Ed.*, 2013, **52**, 8391.

13 A. Zavras, G. N. Khairallah, T. U. Connell, J. M. White, A. J. Edwards, R. J. Mulder, P. S. Donnelly and R. A. J. O'Hair, *Inorg. Chem.*, 2014, **53**, 7429.

14 A. Zavras, A. Ariafard, G. N. Khairallah, J. M. White, R. J. Mulder, A. J. Canty and R. A. J. O'Hair, *Nanoscale*, 2015, **7**, 18129.

15 J. Li, J. M. White, R. J. Mulder, G. E. Reid, P. S. Donnelly and R. A. J. O'Hair, *Inorg. Chem.*, 2016, **55**, 9858.

16 H. Z. Ma, J. Li, A. J. Canty and R. A. J. O'Hair, *Dalton Trans.*, 2017, **46**, 14995.

17 H. Z. Ma, J. M. White, R. J. Mulder, G. E. Reid, A. J. Canty and R. A. J. O'Hair, *Dalton Trans.*, 2018, **47**, 14713.

18 S. Daly, M. Krstić, A. Giuliani, R. Antoine, L. Nahon, A. Zavras, G. N. Khairallah, V. Bonačić-Koutecký, P. Dugourd and R. A. J. O'Hair, *Phys. Chem. Chem. Phys.*, 2015, **17**, 25772.

19 J. Li, H. Z. Ma, G. E. Reid, A. J. Edwards, Y. Hong, J. M. White, R. J. Mulder and R. A. J. O'Hair, *Chem. – Eur. J.*, 2018, **24**, 2070.

20 M. Krstić, A. Zavras, G. N. Khairallah, P. Dugourd, V. Bonačić-Koutecký and R. A. J. O'Hair, *Int. J. Mass Spectrom.*, 2017, **413**, 97.

21 A. Zavras, A. Mravak, M. Bužančić, J. M. White, V. Bonačić-Koutecký and R. A. J. O'Hair, *Chin. J. Chem. Phys.*, 2019, **32**, 182.

22 A. J. Clark, A. Zavras, G. N. Khairallah and R. A. J. O'Hair, *Int. J. Mass Spectrom.*, 2015, **378**, 86.

23 B. D. Adamson, N. J. A. Coughlan, P. B. Markworth, R. E. Continetti and E. J. Bieske, *Rev. Sci. Instrum.*, 2014, **85**, 123109.

24 G. Sheldrick, *Acta Crystallogr., Sect. A: Found. Adv.*, 2015, **71**, 3.

25 G. Sheldrick, *Acta Crystallogr., Sect. C: Struct. Chem.*, 2015, **71**, 3.

26 O. V. Dolomanov, L. J. Bourhis, R. J. Gildea, J. A. K. Howard and H. Puschmann, *J. Appl. Crystallogr.*, 2009, **42**, 339.

27 L. Farrugia, *J. Appl. Crystallogr.*, 2012, **45**, 849.

28 M. J. Frisch, G. W. Trucks, H. B. Schlegel, G. E. Scuseria, M. A. Robb, J. R. Cheeseman, G. Scalmani, V. Barone, G. A. Petersson, H. Nakatsuji, X. Li, M. Caricato, A. Marenich, J. Bloino, B. G. Janesko, R. Gomperts, B. Mennucci, H. P. Hratchian, J. V. Ortiz, A. F. Izmaylov, J. L. Sonnenberg, D. Williams-Young, F. Ding, F. Lipparini, F. Egidi, J. Goings, B. Peng, A. Petrone, T. Henderson, D. Ranasinghe, V. G. Zakrzewski, J. Gao, N. Rega, G. Zheng, W. Liang, M. Hada, M. Ehara, K. Toyota, R. Fukuda, J. Hasegawa, M. Ishida, T. Nakajima, Y. Honda, O. Kitao, H. Nakai, T. Vreven, K. Throssell, J. A. Montgomery Jr., J. E. Peralta, F. Ogliaro, M. Bearpark, J. J. Heyd, E. Brothers, K. N. Kudin, V. N. Staroverov, T. Keith, R. Kobayashi, J. Normand, K. Raghavachari, A. Rendell, J. C. Burant, S. S. Iyengar, J. Tomasi, M. Cossi, J. M. Millam, M. Klene, C. Adamo, R. Cammi, J. W. Ochterski, R. L. Martin, K. Morokuma, O. Farkas, J. B. Foresman and D. J. Fox, *Gaussian 09, Revision D.01*, Gaussian, Inc., Wallingford, CT, 2013.

29 J. P. Perdew, K. Burke and M. Ernzerhof, *Phys. Rev. Lett.*, 1996, **77**, 3865.

30 J. P. Perdew, K. Burke and M. Ernzerhof, *Phys. Rev. Lett.*, 1997, **78**, 1396.

31 F. Weigend and R. Ahlrichs, *Phys. Chem. Chem. Phys.*, 2005, **7**, 3297.

32 F. Weigend, *Phys. Chem. Chem. Phys.*, 2006, **8**, 1057.

33 D. Andrae, U. Haeussermann, M. Dolg, H. Stoll and H. Preuss, *Theor. Chim. Acta*, 1990, **77**, 123.

34 A. Schäfer, H. Horn and R. Ahlrichs, *J. Chem. Phys.*, 1992, **97**, 2571.

35 K. Eichkorn, F. Weigend, O. Treutler and R. Ahlrichs, *Theor. Chim. Acta*, 1997, **97**, 119.

36 S. Grimme, J. Antony, S. Ehrlich and H. Krieg, *J. Chem. Phys.*, 2010, **132**, 154104.

37 A. A. Shvartsburg and M. F. Jarrold, *Chem. Phys. Lett.*, 1996, **261**, 86.

38 M. F. Mesleh, J. M. Hunter, A. A. Shvartsburg, G. C. Schatz and M. F. Jarrold, *J. Phys. Chem.*, 1996, **100**, 16082.

39 I. Campuzano, M. F. Bush, C. V. Robinson, C. Beaumont, K. Richardson, H. Kim and H. I. Kim, *Anal. Chem.*, 2012, **84**, 1026.

40 R. K. Harris, E. D. Becker, S. M. Cabral de Menezes, R. Goodfellow and P. Granger, *Pure Appl. Chem.*, 2001, **73**, 1795.

41 R. K. Harris, E. D. Becker, S. M. Cabral de Menezes, P. Granger, R. E. Hoffman and K. W. Zilm, *Pure Appl. Chem.*, 2008, **80**, 59.

42 G. R. Fulmer, A. J. M. Miller, N. H. Sherden, H. E. Gottlieb, A. Nudelman, B. M. Stoltz, J. E. Bercaw and K. I. Goldberg, *Organometallics*, 2010, **29**, 2176.

43 A. W. Cook, T.-A. D. Nguyen, W. R. Buratto, G. Wu and T. W. Hayton, *Inorg. Chem.*, 2016, **55**, 12435.

44 Crystals changed color from amber to black with concurrent loss of crystallinity.

45 J. Chai, S. Yang, Y. Lv, T. Chen, S. Wang, H. Yu and M. Zhu, *J. Am. Chem. Soc.*, 2018, **140**, 15582.

46 M. Bodiuzzaman, A. Ghosh, K. S. Sugi, A. Nag, E. Khatun, B. Varghese, G. Paramasivam, S. Antharjanam, G. Natarajan and T. Pradeep, *Angew. Chem., Int. Ed.*, 2019, **58**, 189.

47 X. Yuan, C. Sun, X. Li, S. Malola, B. K. Teo, H. Häkkinen, L.-S. Zheng and N. Zheng, *J. Am. Chem. Soc.*, 2019, **141**, 11905.

48 J.-W. Liu, H.-F. Su, Z. Wang, Y.-A. Li, Q.-Q. Zhao, X.-P. Wang, C.-H. Tung, D. Sun and L.-S. Zheng, *Chem. Commun.*, 2018, **54**, 4461.

49 M. M. Bentlohner, C. Fischer and T. F. Fässler, *Chem. Commun.*, 2016, **52**, 9841.

50 R. Usón, A. Laguna, M. Laguna and M. C. Gimeno, *J. Chem. Soc., Dalton Trans.*, 1989, 1883.

51 B. Ahrens and P. G. Jones, *Acta Crystallogr., Sect. C: Cryst. Struct. Commun.*, 1998, **54**, 16.

52 C. S. Browning, D. H. Farrar and D. C. Frankel, *Z. Kristallogr. – New Cryst. Struct.*, 1997, **212**, 201.

53 E. J. Sekabunga, M. L. Smith, T. R. Webb and W. E. Hill, *Inorg. Chem.*, 2002, **41**, 1205.

54 V. Rosa, C. Fliedel, A. Ghisolfi, R. Pattacini, T. Avilés and P. Braunstein, *Dalton Trans.*, 2013, **42**, 12109.

55 A. Ghisolfi, C. Fliedel, P. de Frémont and P. Braunstein, *Dalton Trans.*, 2017, **46**, 5571.

56 S. Takano, H. Hirai, S. Muramatsu and T. Tsukuda, *J. Am. Chem. Soc.*, 2018, **140**, 12314.

57 S. Daly, C. M. Choi, A. Zavras, M. Krstić, F. Chirot, T. U. Connell, S. J. Williams, P. S. Donnelly, R. Antoine, A. Giuliani, V. Bonačić-Koutecký, P. Dugourd and R. A. J. O'Hair, *J. Phys. Chem. C*, 2017, **121**, 10719.

58 P. Weis, *Int. J. Mass Spectrom.*, 2005, **245**, 1.

Nanostructured materials for elimination and utilization of carbon monoxide

3.1 Zeolite-based material
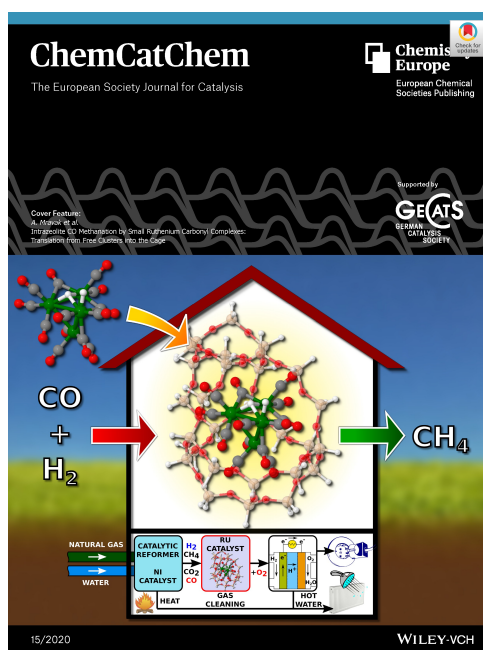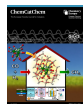
Reproduced from:

Figure 3.1: Cover page of *ChemCatChem* [135] featuring zeolite-based material for CO elimination. Reproduced with permission from the John Wiley & Sons.

Intrazeolite CO Methanation by Small Ruthenium Carbonyl Complexes: Translation from Free Clusters into the Cage

Antonija Mravak,[a] Marjan Krstić,[a, b] Sandra M. Lang,*[c] Thorsten M. Bernhardt,[c] and Vlasta Bonačić-Koutecký*[a, d, e]

Catalytic CO methanation represents an important reaction to improve the feed gas quality for hydrogen fuel cells. Previously, the large potential of small bare and ligated ruthenium clusters as highly selective and active catalysts has been shown by employing gas phase clusters as model systems. Now, density functional theory (DFT) calculations are employed to demonstrate the possibility to translate the gas phase CO methanation reaction mediated by a ligated $Ru_4(CO)_{13}H_2^+$ complex into the framework of a ZSM-5 zeolite. Such a translation, manifested by a reaction pathway which is mechanistically and energetically similar to the gas phase analogue, is possible since the zeolite framework does not influence the reactive center. Furthermore, we reveal the important role of the CO ligand environment in protecting the Ru_4^+ metal core from formation of bonds with the zeolite and in the creation of the reactive center by promoting the cooperatively enhanced adsorption and dissociation of H_2.

Introduction

In order to decrease the carbon footprint from fossil fuels in the context of atmospheric greenhouse gases and climate change, it is obvious that the development of "green" renewable energy is crucial. Therefore, the direct conversion of chemical into electrical energy represents one of the key technologies since it is efficient, clean and environmentally compatible. The conversion is realized in a fuel cell, in which feed gas, typically a mixture of hydrogen and oxygen, reacts electrochemically producing electricity.[1] One of the central problems for the performance of the proton exchange membrane fuel cells (PEMFC) – a fuel cell which has attracted much attention for applications in transportation and small appliances – is the purity of the hydrogen feed gas.[2] Often produced via steam reformation of fossil fuels, hydrogen feed gas contains a small fraction of CO (~ 0.4 mol%)[3] which, however is sufficient to poison the Pt anode of PEMFCs.[2] Thus, the development of new techniques to improve the feed gas quality by minimizing the CO fraction is highly desirable in the context of the future application of PEMFC fuel cells. One promising procedure is the catalytic conversion of CO with hydrogen to methane and water (CO methanation).[2,4] Since, however, the hydrogen feed gas typically not only contains CO but also a rather large fraction of CO_2 (about 11 mol%)[3] this technique is only affordable when the simultaneous conversion of CO_2 via methanation (leading to loss of H_2) or the reverse water-gas shift reaction (leading to production of additional CO) can be suppressed.

For this purpose ruthenium based catalysts[5] and in particular very small Ru particles (< 1 nm) exhibit superior properties.[6] To elucidate the origin of the outstanding activity and selectivity for CO methanation of such small clusters, we have previously employed gas phase ruthenium, Ru_x^+ ($x = 2$–6), and Wade-type ruthenium carbonyl clusters, $Ru_4(CO)_{14}^+$ and $Ru_6(CO)_{18}^+$, as model systems.[7] Using ion trap mass spectrometry together with density functional (DFT) calculations, we have identified three fundamental properties of these clusters: (i) the high reactivity towards CO in combination with an intrinsic inertness towards CO_2 resulting in a high CO methanation selectivity; (ii) the facilitation of hydrogen co-adsorption and dissociation by ruthenium carbonyl clusters without any indication for CO poisoning; (iii) the presence of low coordi-

[a] A. Mravak, Dr. M. Krstić, Prof. V. Bonačić-Koutecký
Center of Excellence for Science and Technology - Integration of Mediterranean region (STIM)
Faculty of Science
University of Split
Ruđera Boškovića 33
21000 Split (Croatia)
E-mail: vbk@chemie.hu-berlin.de
[b] Dr. M. Krstić
Department of Physics
Faculty of Science
University of Split
Ruđera Boškovića 33
21000 Split (Croatia)
[c] Dr. S. M. Lang, Prof. T. M. Bernhardt
Institute of Surface Chemistry and Catalysis
University of Ulm
Albert-Einstein-Allee 47
89069 Ulm (Germany)
E-mail: sandra.lang@uni-ulm.de
[d] Prof. V. Bonačić-Koutecký
Interdisciplinary Center for Advanced Science and Technology (ICAST) at University of Split
Meštrovićevo šetalište 45
21000 Split (Croatia)
[e] Prof. V. Bonačić-Koutecký
Chemistry Department
Humboldt University of Berlin
Brook-Taylor-Straße 2
12489 Berlin (Germany)

ChemCatChem

Full Papers
doi.org/10.1002/cctc.202000716

**Chemistry
Europe**

European Chemical
Societies Publishing

nated Ru-atoms, which present suitable sites for dissociative H_2 adsorption and thus the formation of a reactive center and subsequent CO methanation.[7b] Based on these results, we proposed to employ intrazeolite anchored Ru carbonyl and hydrido carbonyl complexes as new catalytic systems for fuel cell feed gas purification.

First attempts to synthesize such Ru based materials (Ru/ NaY) have already been reported in 1980 indicating the formation of Ru carbonyl clusters comprising at least three Ru atoms.[8] However, only fifteen years later Shen et al. reported a "ship-in-a-bottle" synthesis of ruthenium carbonyl and hydrido carbonyl complexes such as $Ru_3(CO)_{12}$, $Ru_4(CO)_{12}H_4$, $Ru_6(CO)_{18}^{2-}$, and $Ru_6(CO)_{18}H^-$ inside the faujasite cages of $Na_{56}Y$ and $Na_{56}X$ zeolites.[9] Detailed structural analysis of the synthesized material revealed the anchoring of the Ru carbonyls via a strong interaction between the Na^+ cations of the zeolite and the CO molecules.[10] Most interestingly, subsequent reaction studies with CO/H_2 showed the formation of a complex mixture of both hydrocarbons and oxygenates with the highest rate for methane formation.[9a] Based on these studies the authors have suggested the synthesis of Ru carbonyls in other zeolites such as ZSM-5.[11] However, so far most efforts towards the preparation of Ru/ZSM-5 materials have focused on the formation of nanometer sized Ru particles, which, due to their size do usually not fit inside the pores and most likely reside at the edge of the zeolite (see e.g. References [12]). Although such catalysts appear to be active for a variety of different reactions they have not been considered for CO methanation so far. In contrast, the superior performance of a Ru/zeolite catalyst (containing a not further specified zeolite) over metal oxide supported analogs for CO methanation has been demonstrated by kinetic and spectroscopic measurements. This increased activity and selectivity has been attributed to the presence of very small (< 1 nm)[13] metallic and oxidic Ru particles residing inside the zeolite pores.[6a]

In this contribution we now generalize our initial gas phase study showing the origin of the high activity and selectivity of small Ru and Ru carbonyl clusters by transforming the gas phase methanation reaction into the framework of a ZSM-5 zeolite. In particular, we employ DFT calculations to show that the translation of the CO methanation reaction mediated by gas phase $Ru_4(CO)_{13}H_2^+$ clusters is possible since the reactive center of the catalyst is not influenced by the zeolite. This behavior is attributed to the protecting nature of the CO ligand environment which inhibits strong interaction of the metal cluster core with the zeolite and at the same time creates the reactive center by promoting the cooperatively enhanced dissociative H_2 adsorption.

Results and Discussion

Intrazeolite anchoring of Ru_4^+ and $Ru_4(CO)_{13}H_2^+$

To model the ZSM-5 zeolite a cutout of the crystal structure representing the typical repeating structure of the extended framework was used (cf. Figure S1.) This zeolite fraction consists

of two differently sized pores with a total of 28 silicon and 77 oxygen atoms. The 6Si-rings (comprising six Si atoms linked by bridging oxygen atoms), spanning the small pores, have a cross section of 5.2×5.8 Å, whereas the 10Si-rings (comprising ten Si atoms linked by bridging oxygen atoms), spanning the large pores, have a cross section of 8.2×8.8 Å. In order to replace the broken SiO bonds in the calculations, the terminal oxygen atoms were substituted by 42 hydrogen atoms.

Placing a bare distorted tetrahedron-like Ru_4^+ cluster into the large pore of the ZSM-5 model leads to a rather strong interaction between the cluster and the zeolite (binding energy $E_b = 3.35$ eV) resulting in the formation of three Ru—O bonds with lengths of 2.43 Å, 2.55 Å and 2.54 Å, respectively, accompanied by a considerable distortion of the cluster with changes of Ru—Ru bonds lengths of up to 0.45 Å (cf. Figure 1a and Table S1) and partial electron transfer from the zeolite to the Ru_4^+ cluster (cf. Mulliken charges in Figure S2). A similar influence of the zeolite leading to changes of the geometric and/or electronic structure of the particle has e.g. also been found for bare Pt_6 clusters as well as Ru nanoparticles, both anchored in a ZSM-5 zeolite.[14]

However, a recent gas phase study showed that the exposure of Ru_4^+ to a mixture of CO and H_2 in an ion trap leads to the facile formation of hydrido carbonyl complexes $Ru_4(CO)_{14-m}H_{2m+1}^+$ (m = 0–3).[7] As a model for these complexes, we have previously established the complex $Ru_4(CO)_{13}H_2^+$ as a starting configuration for the subsequent theoretical exploration of the CO methanation reaction. In the lowest energy
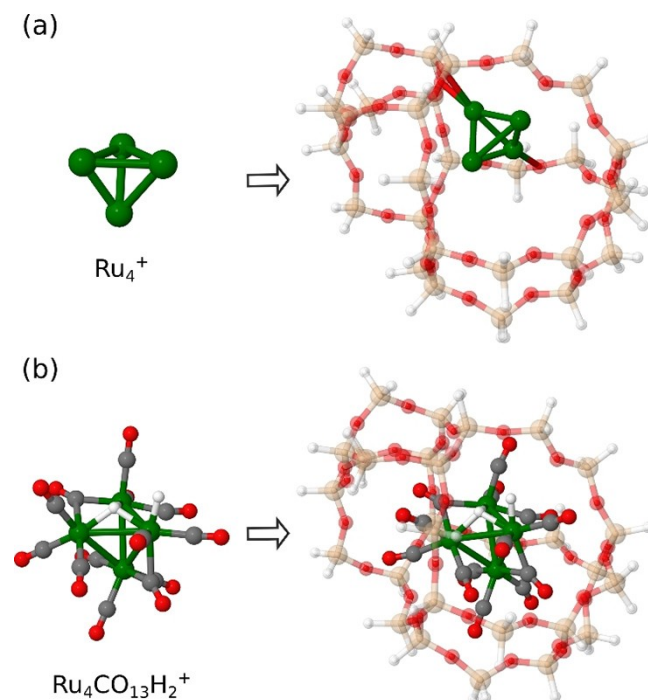

Figure 1. Optimized lowest energy structures with doublet ground state for (a) the bare cluster Ru_4^+, (b) the hydrido carbonyl complex $Ru_4(CO)_{13}H_2^+$ as well as Ru_4^+ and $Ru_4(CO)_{13}H_2^+$ placed in the large pore of the ZSM-5 zeolite model. Ru, C, O, H, and Si atoms are depicted by green, grey, red, white and pink spheres, respectively.

configuration, the Ru_4^+ cluster core is nearly tetrahedral and is covered with eleven terminally and two μ^2-bridge bound CO molecules. Furthermore, it has been shown that formation of a carbonyl complex facilitates the co-adsorption of hydrogen, leading to the disappearance of the activation barrier for the dissociation of the first H_2 molecule, and stabilizing the dissociated hydrogen (one H atom in a μ^3-bridge and one H atom in a terminal position). Placing this complex into the large pore of the ZSM-5 model hardly changes the cluster core structure (changes of Ru–Ru distances are 0.02–0.11 Å, cf. Figure 1b and Table S1) as well as the Ru-ligand environment (cf. Table S2) clearly demonstrating the protecting role of the CO ligand environment. This protection of the metal cluster core by CO ligands can be traced back to only a very weak interaction between the hydrido carbonyl complex and the zeolite arising from dispersion forces (binding energy $E_b = 0.11$ eV). This finding appears to be in contrast to the intra-zeolite anchoring of ruthenium carbonyl and hydrido carbonyl clusters in faujasite cages ($Na_{56}X$ and $Na_{56}Y$) for which a strong interaction between the Na^+ cation and the CO ligands was suggested.[10]

Most importantly, however, the property of the carbonyl cluster to facilitate the barrier free H_2 dissociation and thus, to create a reactive center is maintained inside the ZSM-5 zeolite pore. Although a Mulliken charge analysis[16] shows that placing $Ru_4(CO)_{13}H_2^+$ into the zeolite results in some electron transfer to the metal cluster core (cf. insets in Figure 2), the charge on the reactive center (terminally bound H atom) is hardly affected by the zeolite. The rather small influence of the zeolite on $Ru_4(CO)_{13}H_2^+$ is also reflected in the vibrational spectra of free and zeolite anchored $Ru_4(CO)_{13}H_2^+$ displayed in Figure 2. In particular, the band centers of linearly and bridge bound CO only shift from 2087 cm^{-1} and 1933 cm^{-1} for the free complexes to 2073 cm^{-1} and 1945 cm^{-1} (with one additional mode at 1886 cm^{-1}) for the intrazeolite anchored complexes. For comparison, a frequency difference of about 100 cm^{-1} has been reported for the C≡O stretch mode of CO terminally bound on free cationic and anionic ruthenium clusters, respectively.[17]

To summarize, anchoring of a bare Ru_4^+ cluster inside a ZSM-5 pore leads to covalent binding between the cluster and the zeolite and a strong influence of the zeolite on the metal cluster's geometric and electronic structure. In contrast, an appropriate ligand environment (in this case formed by CO molecules) does not only protect the Ru_4^+ cluster core from chemical bonding with the zeolite framework but at the same time facilitates H_2 dissociation and thus, prepares the cluster for further reaction. Most importantly, the formed reactive center (dissociated hydrogen) is not influenced by the zeolite framework. The similarity between the gas phase and intrazeolite anchored hydrido carbonyl complexes suggest that a 'ship-in-a-bottle' synthesis of $Ru_x(CO)_yH_z$/ZSM-5 catalyst should lead to the same ruthenium hydrido carbonyls as observed in the gas phase experiment.
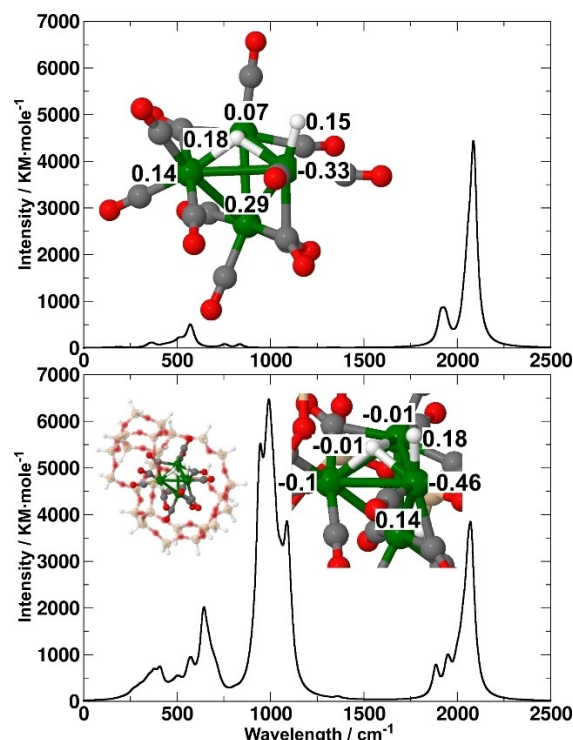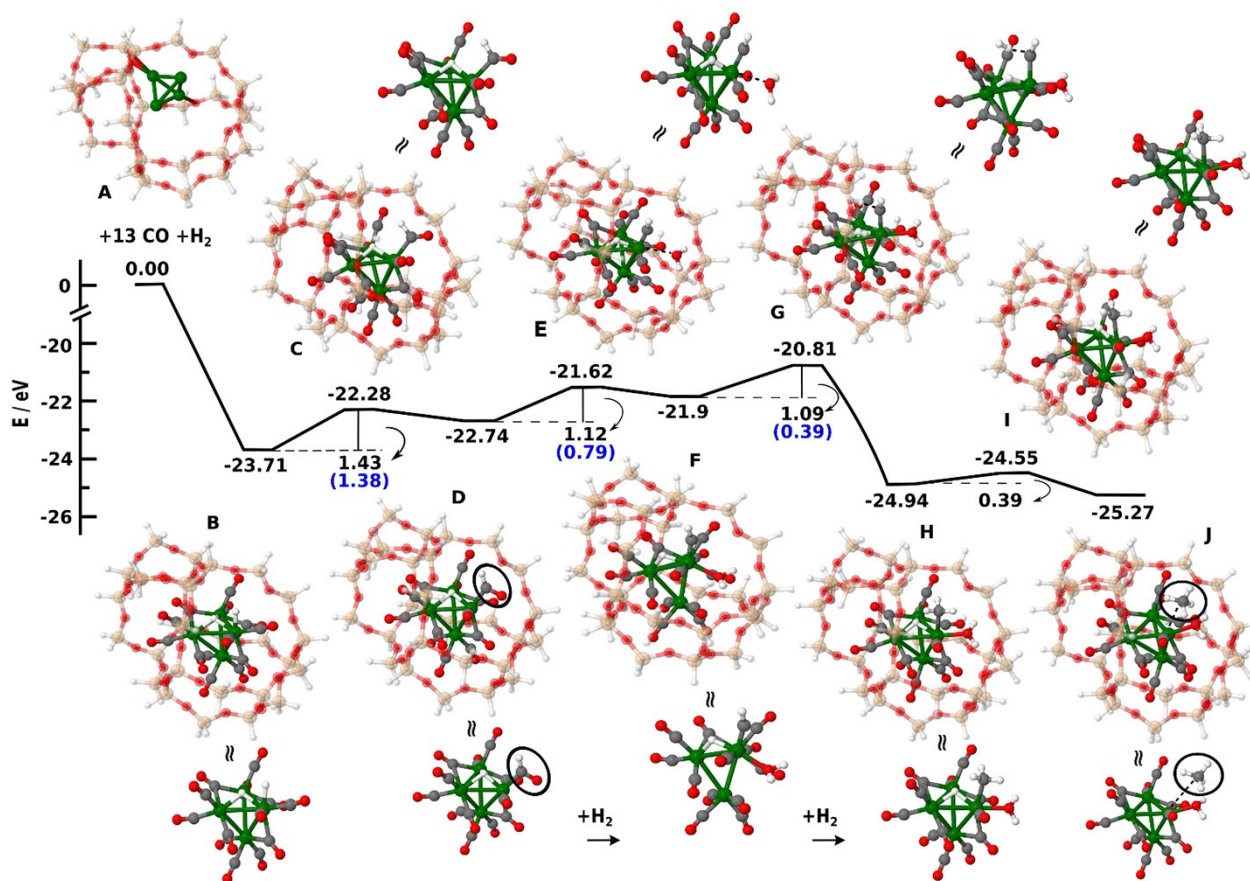

Figure 2. Calculated vibrational spectra of (top) free $Ru_4(CO)_{13}H_2^+$ and (bottom) intrazeolite anchored $Ru_4(CO)_{13}H_2^+$. The bands around 2000 cm^{-1} are characteristic for the C≡O stretch motion, the bands around 1000 cm^{-1} correspond to motions of the zeolite framework, and the bands below 600 cm^{-1} contain contributions from the CO ligands, the SiO zeolite framework as well as the Ru cluster core (< 300 cm^{-1}).[15] The insets show the structure of the models as well as the Mulliken charges[16] localized on the Ru and H atoms.

Intrazeolite translation of gas phase CO methanation

In the following we will now explore the potential CO methanation reaction mediated by the intrazeolite anchored ruthenium hydrido carbonyl $Ru_4(CO)_{12}H_2^+$. In principle, CO methanation might proceed via hydrogenation of either the CO carbon or oxygen atom. However, since our previous gas phase study has shown that hydration of the oxygen atom is energetically not feasible,[7b] we will only consider the reaction proceeding via hydrogenation of the carbon atom here. Figure 3 displays the calculated energy profile and the corresponding structures for this CO methanation reaction channel. Starting with the optimized structure of the intrazeolite anchored $Ru_4(CO)_{13}H_2^+$ complex containing a reactive center (dissociatively adsorbed H_2) the reaction proceeds over a first activation barrier of 1.43 eV (B→C→D). This barrier is associated with the transfer of the terminally bound hydrogen atom to a neighboring carbon atom and leads to the formation of a formyl intermediate. Although this reaction step appears to be endothermic by $\Delta E_{BD} = 0.97$ eV, the formation of a formyl-type intermediate has experimentally been shown to be feasible e.g. in the oxygenate formation from CO and H_2 on bimetallic ruthenium-cobalt ($RuCo_3$) carbonyl complexes embedded in $Na_{56}Y$[18] as well as in the CO methanation on small ruthenium

ChemCatChem

Full Papers
doi.org/10.1002/cctc.202000716

Chemistry
Europe
European Chemical
Societies Publishing

Figure 3. Calculated energy profile for CO methanation by reaction of intrazeolite anchored $Ru_4(CO)_{13}H_2^+$ with two sequentially adsorbed H_2 molecules. Also shown are the structures of the local minima and transition states for the $Ru_4(CO)_{13}H_2^+$/ZSM-5 model as well as the corresponding gas phase reaction (shown in Figure S5). The numbers denote the relative energies in eV. Activation barrier heights are given for $Ru_4(CO)_{13}H_2^+$/ZSM-5 in black and for free $Ru_4(CO)_{13}H_2^+$ in blue. Ru, C, O, H, and Si atoms are depicted by green, grey, red, white and pink spheres, respectively.

nanoparticles supported inside the pores of a zeolite.[6a] Subsequent addition of a second H_2 molecule leading to the formation of a water molecule and a methyne (CH) group requires an energy of 1.12 eV (D→E→F, $\Delta E_{DF} = 0.84$ eV). A further H_2 molecule directly interacts with the methyne group under formation of a methyl (CH_3) group by overcoming an activation barrier of 1.09 eV (F→G→H). In contrast to the first two endothermic reaction steps, this reaction step is highly exothermic by −3.04 eV. The final transfer of the μ^3-bound hydrogen atom to form and eliminate methane only requires an energy of 0.39 eV (H→I→J) and results in structure J.

Most importantly, this reaction pathway is mechanistically and energetically very similar to the previously reported pathway starting from gas phase $Ru_4(CO)_{13}H_2^+$ (cf. Figure S3 and Table S3). In particular, the key intermediate, a formyl-type structure, and the associated barrier of 1.43 eV are almost identical to the gas phase case with an activation barrier of 1.38 eV. Although, intrazeolite anchoring appears to result in somewhat larger barriers for methyne and methyl formation, the overall reaction starting form $Ru_4(CO)_{13}H_2^+$ is with −1.56 eV even slightly more exothermic inside the zeolite (compare to −1.25 eV for gas phase).

The calculated reaction profile demonstrates that the previously found gas phase CO methanation reaction mediated by a tetra-ruthenium hydrido carbonyl cluster can be translated from the gas phase into a zeolite without changing the reaction mechanism and the energetics of the key (i.e. rate determining) reaction steps. Such a transfer appears to be possible since the zeolite framework does not influence the reactive center of the ruthenium catalyst due to the protective nature of the CO ligand environment. This finding is in line with the recently reported translation of formic acid decomposition mediated by a ligated $Cu_2(H)^+$ center in the same ZSM-5 pore.[19] Intrazeolite anchoring of $[(napy)Cu_2(H)]^+$ was shown to lead to clear changes in the Mulliken charges, however the structure of the reactive $Cu_2(H)^+$ center was maintained resulting in a mechanistic and energetically very similar reaction pathway for formic acid decomposition.

Conclusions

DFT calculations reveal that the mechanism and energetics of the gas phase CO methanation reaction mediated by a tetra-

ChemCatChem

Full Papers
doi.org/10.1002/cctc.202000716

**Chemistry
Europe**
European Chemical
Societies Publishing

ruthenium hydrido carbonyl cluster, $Ru_4(CO)_{13}H_2^+$, is maintained when translated into the framework of a ZSM-5 zeolite pore model. This translation is possible since the CO ligand environment protects the Ru_4^+ cluster core by inhibiting the formation of strong chemical bonds with the zeolite. Besides maintaining the cluster's geometric structure, the CO ligands also facilitate H_2 co-adsorption and dissociation and thus the formation of a reactive center. Since this reactive center is not directly influenced by the zeolite the reaction can proceed along a similar pathway as in the gas phase. Based on this finding, it can be concluded that the translation of the gas phase reactions into the framework of a zeolite cage should always be possible as long as the reactive center is not substantially influenced by the zeolite. This pre-requisite is fulfilled by our current model of the ZSM-5 zeolite pore. Further studies addressing additional effects which might occur in commercially available ZSM-5 zeolites e.g. due to the presence of a small amount of aluminum or water are currently in progress. In a first attempt to study the influence of a negatively charged Al^- center we have substituted the Si atom nearest to the bare Ru_4^+ with an Al atom and optimized this structure. (cf. Figure S4 and Table S4). Compared to the Si-only zeolite model, the binding energy of Ru_4^+ increases from 3.35 eV to 5.71 eV leading to shorter Ru–O bonds. However, the overall structure of the Ru_4^+ is maintained (Al^- ion does not replace a Ru atom in the cluster) and the partial electron transfer from the zeolite to the cluster is even reduced which suggest that the facile formation of hydrido carbonyl complexes will not be hindered and the reactive center will not be affected by the presence of Al^-.

Thus, the present study shows that the great advantage of fundamental research on ligated gas phase clusters - which is manifested in the unique possibility to have complete control over cluster size, composition, and the nature of the ligand environment - can be utilized to identify particularly reactive cluster catalysts whose chemical properties can be directly translated into a zeolite. This conceptual insight might guide the tailor-made "ship-in-a-bottle" synthesis of novel catalysts and thus open up completely new avenues for the future design of such materials.

Computational Section

The structures and reactive properties of the ruthenium carbonyl and hydrido carbonyl complexes as well as the ZSM-5 zeolite model were studied by employing density functional theory (DFT) calculations with the software package Gaussian 16.[20] The computations were performed using the PBE (Perdew-Burke-Ernzerhof)[21] functional with the density fitting method W06[22] to speed up calculations. For the Ru atoms the Stuttgart relativistic core potential (ECPs)[23] were employed together with the triple-ζ-valence-plus-polarization basis set[24] which was also used for the C, O, H, and Si atoms. In addition, for the intrazeolite complexes Grimme's dispersion with the original D3 damping function GD3[25] were applied to account for a long-range electron correlation effect of CO ligands to zeolite.

Extensive search for the lowest energy structures with different positions of H_2 to obtain $Ru_4CO_{13}H_2^+$ inside the zeolite model has been performed by fully relaxing all atoms. The lowest energy minimum was subsequently used to calculate local minima and transition states along the reaction path from which the energy profile was constructed. For geometry optimization of these local minima and transition states the H atoms replacing the broken Si–O bonds were held fixed while all other atoms were allowed to relax.

Conflict of Interest

The authors declare no conflict of interest.

[1] a) R. Srinivasan, R. Mosdale, P. Stevens, C. Yang, *Ann. Rev. Energy Environ.* **1999**, *24*, 281-328; b) L. Carrette, K. A. Friedrich, U. Stimming, *ChemPhysChem* **2000**, *1*, 162–193.

[2] E. D. Park, D. Lee, H. C. Lee, *Catal. Today* **2009**, *139*, 280–290.

[3] D. L. Trimm, Z. I. Önsan, *Catal. Rev.* **2001**, *43*, 31-84.

[4] A. Mishra, R. Prasad, *Bull. Chem. React. Eng. Catal.* **2011**, *6*, 1–14.

[5] H. Wang, Y. Pei, M. Qiao, B. Zong, *Catalysis, Vol. 29*, The Royal Society of Chemistry **2017**, pp. 1–28.

[6] a) S. Eckle, Y. Denkwitz, R. J. Behm, *J. Catal.* **2010**, *269*, 255–268; b) S. Tada, R. Kikuchi, K. Urasaki, S. Satokawa, *Appl. Catal. A* **2011**, *404*, 149–154.

[7] a) S. M. Lang, S. U. Förtig, T. M. Bernhardt, M. Krstić, V. Bonačić-Koutecký, *J. Phys. Chem. A* **2014**, *118*, 8356–8359; b) S. M. Lang, T. M. Bernhardt, M. Krstić, V. Bonačić-Koutecký, *Angew. Chem. Int. Ed.* **2014**, *53*, 5467–5471; *Angew. Chem.* **2014**, *126*, 5571–5575.

[8] J. G. Goodwin, C. Naccache, *J. Catal.* **1980**, *64*, 482–486.

[9] a) G.-C. Shen, A.-M. Liu, T. Shido, M. Ichikawa, *Top. Catal.* **1995**, *2*, 141–154; b) M. Ichikawa, W. Pan, Y. Imada, M. Yamaguchi, K. Isobe, T. Shido, *J. Mol. Catal. A* **1996**, *107*, 23–38.

[10] G.-C. Shen, A. M. Liu, M. Ichikawa, *Inorg. Chem.* **1998**, *37*, 5497–5506.

[11] G.-C. Shen, A. M. Liu, M. Ichikawa, *J. Chem. Soc. Faraday Trans.* **1998**, *94*, 1353–1362.

[12] a) S. Scirè, R. Fiorenza, A. Gulino, A. Cristaldi, P. M. Riccobene, *Appl. Catal. A* **2016**, *520*, 82–91; b) B. Zhang, Q. Wu, C. Zhang, X. Su, R. Shi, W. Lin, Y. Li, F. Zhao, *ChemCatChem* **2017**, *9*, 3646–3654; c) W. Luo, P. C. A. Bruijnincx, B. M. Weckhuysen, *J. Catal.* **2014**, *320*, 33–41.

[13] S. Eckle, M. Augustin, H.-G. Anfang, R. J. Behm, *Catal. Today* **2012**, *181*, 40-51.

[14] a) M. N. Mikhailov, L. M. Kustov, V. B. Kazansky, *Catal. Lett.* **2008**, *120*, 8–13; b) S. Scirè, C. Crisafulli, R. Maggiore, S. Minicò, S. Galvagno, *Catal. Lett.* **1998**, *51*, 41–45.

[15] C. Kerpal, D. J. Harding, D. M. Rayner, J. T. Lyon, A. Fielicke, *J. Phys. Chem. C* **2015**, *119*, 10869–10875.

[16] R. S. Mulliken, *J. Chem. Phys.* **1955**, *23*, 1833–1840.

[17] J. T. Lyon, P. Gruene, A. Fielicke, G. Meijer, D. M. Rayner, *J. Chem. Phys.* **2009**, *131*, 184706.

[18] J. G. C. Shen, M. Ichikawa, *J. Phys. Chem. B* **1998**, *102*, 5602–5613.

[19] M. Krstić, Q. Jin, G. N. Khairallah, R. A. J. O'Hair, V. Bonačić-Koutecký, *ChemCatChem* **2018**, *10*, 1173–1177.

[20] M. J. Frisch, G. W. Trucks, H. B. Schlegel, G. E. Scuseria, M. A. Robb, et al., *Gaussian 16*, Revision C.01, Gaussian, Inc., Wallingford CT **2016**.

[21] a) J. P. Perdew, K. Burke, M. Ernzerhof, *Phys. Rev. Lett.* **1996**, *77*, 3865–3868; b) J. P. Perdew, K. Burke, M. Ernzerhof, *Phys. Rev. Lett.* **1997**, *78*, 1396–1396.

[22] a) F. Weigend, R. Ahlrichs, *Phys. Chem. Chem. Phys.* **2005**, *7*, 3297–3305; b) F. Weigend, *Phys. Chem. Chem. Phys.* **2006**, *8*, 1057–1065.

[23] D. Andrae, U. Haeussermann, M. Dolg, H. Stoll, H. Preuss, *Theor. Chim. Acta* **1990**, *77*, 123–141.

[24] A. Schäfer, H. Huber, R. Ahlrichs, *J. Chem. Phys.* **1994**, *100*, 5829–5835.

[25] S. Grimme, J. Antony, S. Ehrlich, H. Krieg, *J. Chem. Phys.* **2010**, *132*, 154104.

Nanostructured materials for conversion of carbon dioxide into useful products
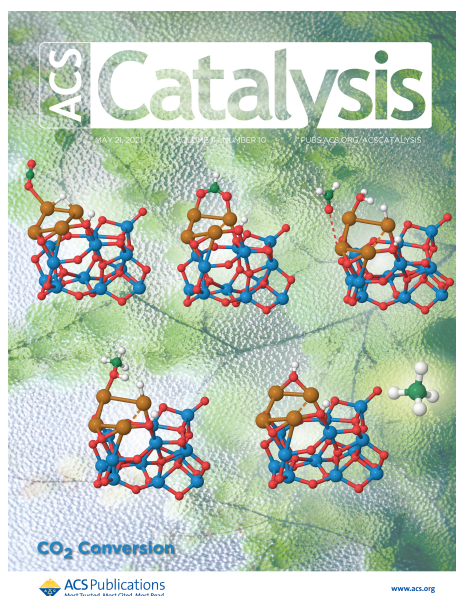
4.1 Supported metallic nanocluster

Figure 4.1: Supplementary cover page of *ACS Catal.* [143] featuring monometallic Cu-cluster at zirconia support for CO_2 conversion into methane. Copyright 2021, American Chemical Society.

CO$_2$ Methanation on Cu-Cluster Decorated Zirconia Supports with Different Morphology: A Combined Experimental In Situ GIXANES/ GISAXS, Ex Situ XPS and Theoretical DFT Study

Avik Halder,◆ Cristina Lenardi,◆ Janis Timoshenko,◆ Antonija Mravak,◆ Bing Yang,
Lakshmi K Kolipaka, Claudio Piazzoni, Sönke Seifert, Vlasta Bonačić-Koutecký, Anatoly I. Frenkel,
Paolo Milani,* and Stefan Vajda*

ACCESS | Metrics & More | Article Recommendations | SI Supporting Information

ABSTRACT: Subnanometer copper tetramer−zirconia catalysts turn out to be highly efficient for CO$_2$ hydrogenation and its conversion to methane. The cluster size and substrate morphology are controlled to optimize the catalytic performance. The two types of zirconia supports investigated are prepared by atomic layer deposition (∼3 nm thick film) and supersonic cluster beam deposition (nanostructured film, ∼100 nm thick). The substrate plays a crucial role in determining the activity of the catalyst as well as its cyclability over repeated thermal ramps. A temperature-programmed reaction combined with in situ X-ray character-ization reveals the correlation between the evolution in the oxidation state and catalytic activity. Ex situ photoelectron spectroscopy indicates Cu clusters with stronger interactions with the nanostructured film, which can be the cause for the higher activity of this catalyst. Density functional theory calculations based on the Cu$_4$O$_2$ cluster supported on a ZrOx subunit reveal low activation barriers and provide mechanism for CO$_2$ hydrogenation and its conversion to methane. Altogether, the results show a new way to tune the catalytic activity of CO$_2$ hydrogenation catalysts through controlling the morphology of the support at the nanoscale.

KEYWORDS: CO$_2$ conversion, copper cluster, support effect, reaction mechanism, XANES, GISAXS, XPS, DFT
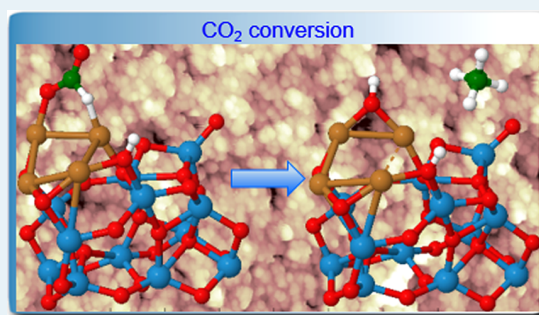
INTRODUCTION

Catalytic conversion of CO$_2$ to useful fuels such as methane, methanol, and longer chain hydrocarbons can help to simultaneously mitigate the emission of greenhouse gas CO$_2$ and enrich the resource of chemical feedstock compounds to reduce the dependency on fossil fuels.[1,2] The interest in developing cheap catalyst with optimized performance is obvious and Cu based catalysts have already been heavily explored.[2,3] However, in most cases one has to use high pressure and temperature as the reaction conditions to achieve high conversion efficiency for CO$_2$ at the industrial level.[4−6] There has recently been reports of highly efficient conversion of CO$_2$ to methanol using Cu cluster based catalysts (Cu$_n$ deposited on hydroxylated alumina supports) at temperatures as low as 125 °C and 1.1 atm pressure. However, the methane signal appeared only at temperatures of around 375 °C[7,8] also observed during the course of reaction dynamically forming and disintegrating nanoassemblies made of subnanometer Cu clusters.[9] Iron oxide doped with Cu nanoparticles on the other hand was found to have a high selectivity for CO$_2$ hydrogenation with methane as the major usable product.[10]

Zirconia supports have been of interest due to their high mechanical and thermal stability, and the copper/zirconia catalyst was found to be a stable catalyst for conversion of syngas to methanol.[11,12] Some of the commonly used Cu/zirconia catalysts for CO$_2$ conversion include copper and copper oxides mixed with microcrystalline zirconia present in amorphous, tetragonal, or monoclinic phases;[13−16] carbon nanofiber based Cu/zirconia catalyst;[17] and copper nanocrystals encapsulated in Zr based metal−organic frameworks.[18] Herein we prepared a catalyst with monodisperse Cu clusters supported on zirconia substrates prepared by two different deposition methods. The first method, atomic layer deposition[19] (ALD ZrOx) creates a smooth zirconia surface which is about 3 nm thick. The second method, supersonic cluster deposition (SCBD), fabricates

cluster-assembled nanostructured zirconia films of 100 nm in thickness (NS ZrOx).[20,21]

SCBD produces nanostructured films with nanoscale topography and roughness that can be quantitatively controlled over a wide interval of parameters:[20] the morphology of cluster-assembled materials is characterized by arrangements of nanoscale building blocks in larger units up to a certain critical length scale determined by the time of the deposition process.[21] Cluster-assembled zirconia films are characterized by high specific area and porosity at the nano- and subnanometer scales.[20,21] Cluster-assembled zirconia substrates are rich in undercoordinated defects,[20] very stable against thermal treatments and have high surface area.[22] These aspects make cluster-assembled zirconia a very interesting catalytic substrate where the effect of metallic cluster decoration can be investigated.[23]

The copper clusters were created with atomic precision. Such systems have the capability to perform catalytic reactions with high activity and selectivity; hence, one can determine the most active catalytic moiety.[24,25] In the present study Cu_n/zirconia catalysts were investigated in search for an efficient catalyst for CO_2 methanation. Methane forms a major source of stored energy and is usually produced using complex processes at high temperature and under high presssure[26,27] or extracted from natural sources.[28−32] Thus, an affordable catalyst which can produce methane by conversion of CO_2 is highly desirable.

Pure Cu clusters of controlled atomicity were generated in a high vacuum system, free of any ligands and deposited on zirconia substrates with different morphologies. Using X-ray photoelectron spectroscopy (XPS) the binding energies of the clusters on zirconia surfaces have been measured. The temperature-programmed reaction with mass spectroscopic detection was used to monitor the evolution of the products in real time, where the changes in the composition and oxidation state of copper during the reaction were monitored using in situ grazing incidence X-ray absorption near-edge spectroscopy (GIXANES). Simultaneous in situ grazing incidence small-angle X-ray scattering (GISAXS) was employed to check for any assembly formation or coalescence of clusters. The analysis of oxidation states and structures of metal clusters in reaction conditions was performed by spectral decomposition of GIXANES data.

In order to understand the role of the copper cluster and support, DFT calculations have been carried out on a model reactive center formed by oxidized copper tetramer and Zr_xO_{2x} subunit, providing energy profile and identifying key steps of the mechanism, thus proposing energetically favorable reaction pathway during the activation and hydrogenation steps of CO_2 on route to its conversion to methane.

■ EXPERIMENTAL SECTION

Design of ALD and Nanostructured Zirconia Supports. The ALD ZrOx support was prepared using tetrakis-(dimethylamido)zirconium(IV) (ZrTDMA) precursor purchased from Aldrich. The film was deposited at a reactor temperature of 200 °C with the manifold at 150 °C. ZrTDMA (75 °C) and deionized water were used for the growth of ZrO_2, with a pulsing sequence of 0.4−10−0.015−10 s.[19]

Nanostructured zirconia (NS ZrOx) thin films were produced using a supersonic cluster beam deposition (SCBD) apparatus equipped with a Pulsed Microplasma Cluster Source (PMCS)[33] as described in detail in refs 20 and 21. In brief, the deposition apparatus consists of two differentially pumped vacuum stages. A PMCS is mounted outside the first chamber (expansion chamber) on the axis of the apparatus. The PMCS is operated in a pulsed regime: high-pressure Ar pulses with a duration of a few hundreds of microseconds are injected at the repetition rate of 4 Hz. The gas injection is followed by an electrical discharge between the cathode (zirconium rod) and an anode buried in the source body. A subsequent condensation of sputtered atoms results in cluster nucleation. The inert gas-clusters mixture is then extracted from the PMCS into high vacuum ($p \approx 10^{-6}$ mbar) to form a seeded supersonic cluster beam. Cluster deposition takes place in the deposition chamber where the supersonic beam impinges on silicon substrates mounted on a x-y-z motorized sample holder.

In the PMCS metallic Zr clusters are produced. Nevertheless, a substantial oxidation of the clusters takes place very rapidly because of the interaction of the Zr clusters with oxygen and water molecules, upon exposure of the sample to air, resulting in cluster-assembled nanostructured ZrOx films (NS ZrOx) with $x \approx 2$.
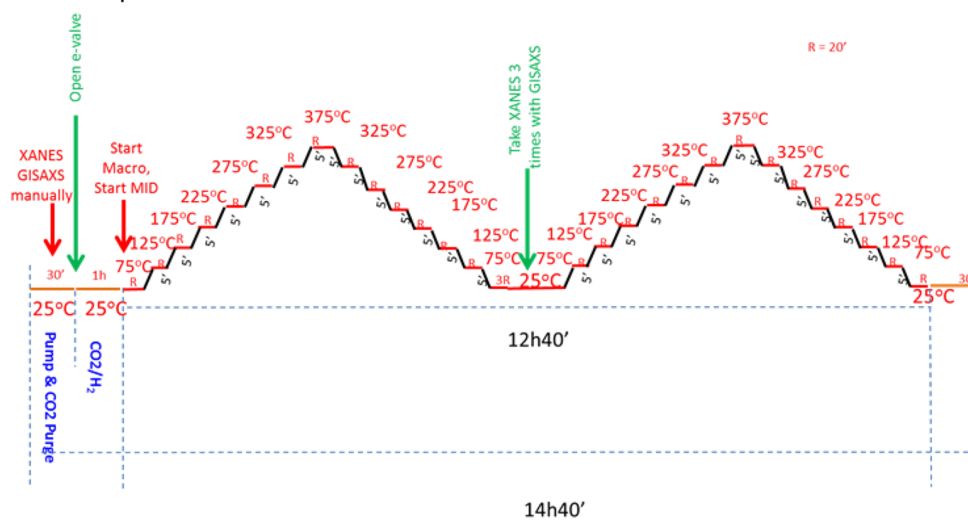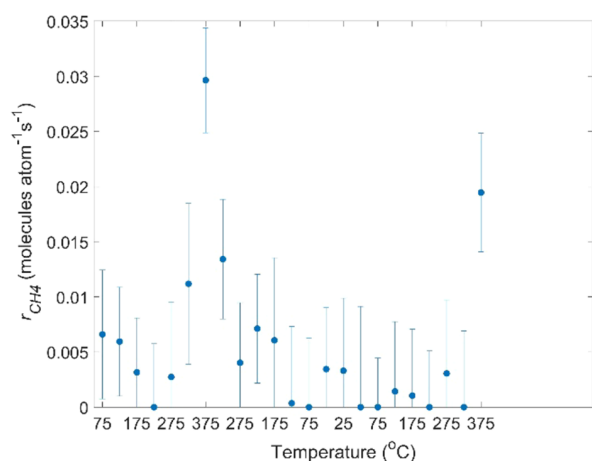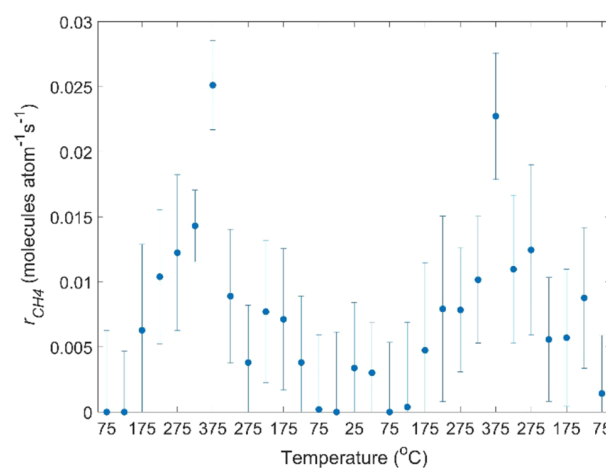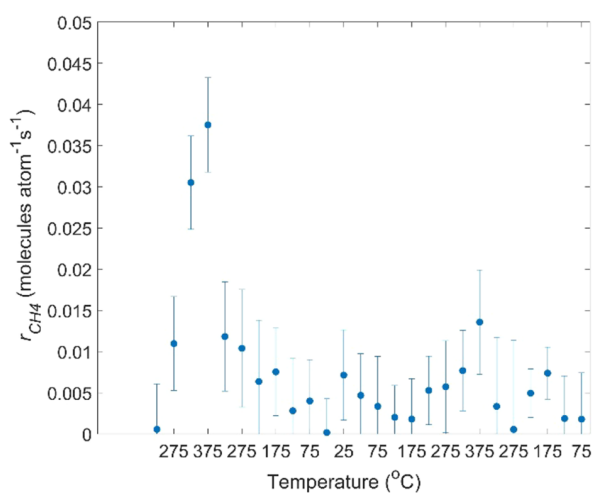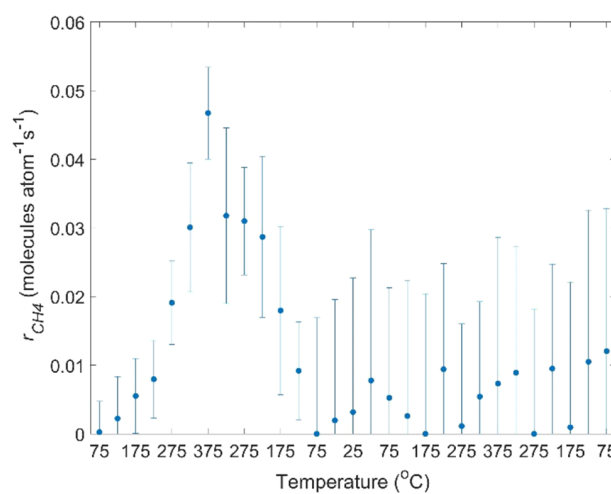
We characterized by atomic force microscopy (AFM) the evolution of the samples morphological properties as a function of the surface coverage, which is defined as the ratio between the projected area occupied by clusters on the surface and the scanned area.[20] Nanostructured films with a thickness of 125 nm and roughness of 17 nm (see Figure S1) were grown under the ballistic deposition regime where clusters stick on the substrate upon landing without significant mobility and fragmentation due to their low kinetic energy.[21] The NS ZrOx film was characterized by the BET method obtaining a specific surface area of approximately 300 m^2/g and nanosized pores with sizes in the range of 10−50 nm.[22]

Copper Cluster Deposition. Cu clusters were produced in a liquid nitrogen cooled magnetron sputtering source, the details for which can be found in Supporting Information and in ref 34. Briefly, the clusters were produced in a magnetron sputtering source (Figure S2) and the clusters of desired single size were mass-selected from the molecular beam and soft-landed on the ALD and NS ZrOx supports at controlled loading of copper metal. The copper loading per cluster spot in these samples was about 5 ng, corresponding to 4.45×10^{13} Cu atoms.
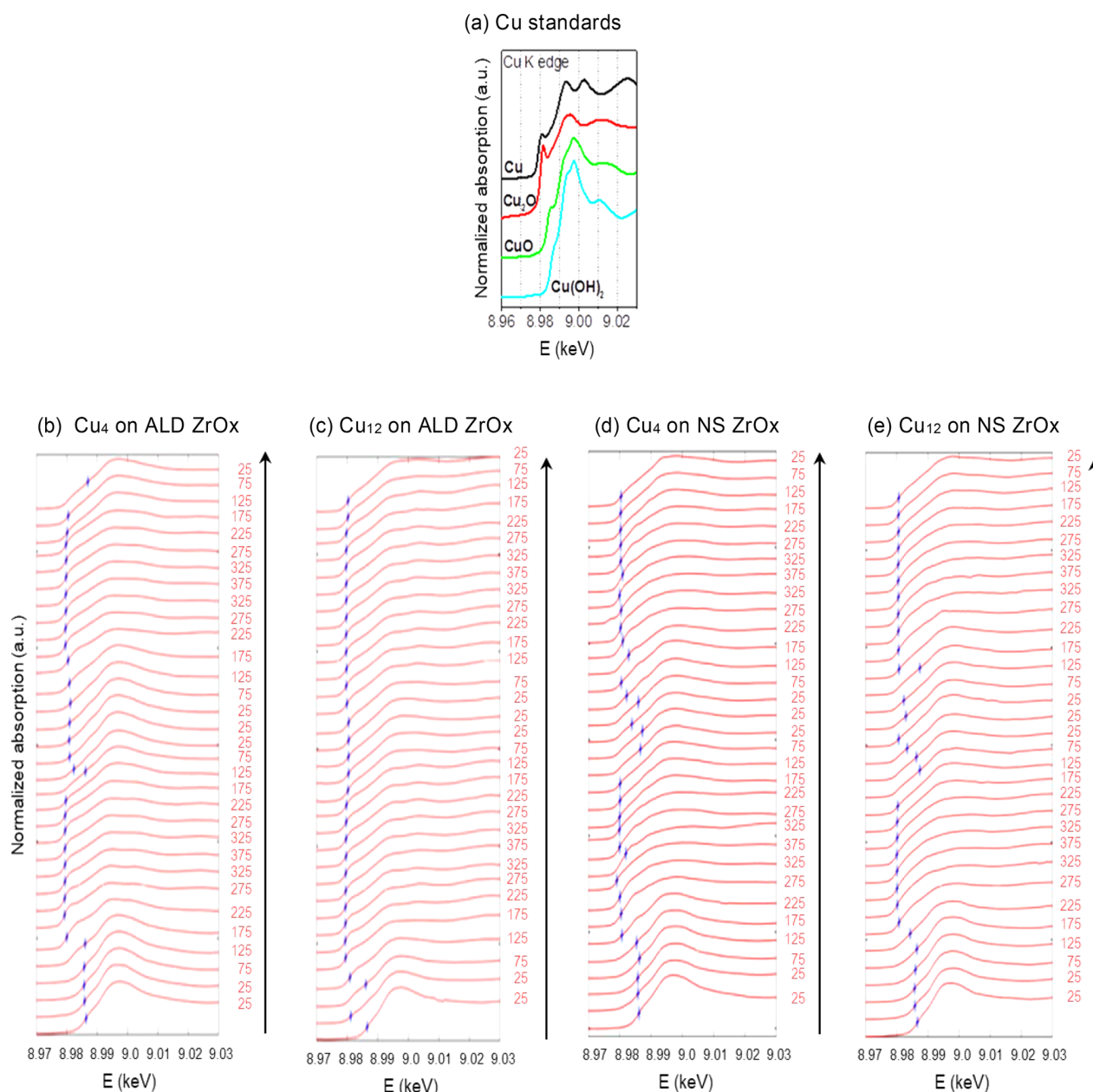
In Situ GIXANES, GISAXS, and TPRx. The testing of performance and characterization of the working catalyst was performed in a home-built reactor at beamline 12-ID-C of the Advanced Photon Source at the Argonne National Laboratory.[35] This experimental setup allows in situ X-ray monitoring of changes in the size of the clusters by small-angle X-ray scattering at grazing incidence (GISAXS) and to follow the changes in the oxidation state of the metal by grazing incidence X-ray absorption near edge spectroscopy with fluorescence mode detection (GIXANES), as well as to simultaneously monitor reaction product formation during a temperature-programmed reaction (TPRx). A brief description of the multiprobe approach is given in the Supporting Information and in detail elsewhere.[35,36] The reaction was performed using a uniform double heat and cool ramp (see the Results and Discussion section), at a pressure of 1.1 atm under continuous flow of 18 sccm of pure CO_2 and H_2 in 1:3 ratio.

The spectra of the Cu metal foil, Cu_2O, CuO, and $Cu(OH)_2$ bulk standards were collected at the 12-BM beamline of the Advanced Photon Source in transmission mode. These spectra were used as reference spectra for linear combination fit (LCF) analysis of the XANES spectra. Note here that the local structure in ultrasmall clusters deviates from that in the bulk materials such as the standards used in this study. Therefore, in this work

Figure 1. Catalytic activity of Cu_4 and Cu_{12} clusters on ALD ZrOx and NS ZrOx. (a) Temperature ramp; (b) Cu_4 on ALD zirconia with a reproducible activity for methane formation from CO_2 on consecutive ramps; (c) Cu_{12} on ALD zirconia with a reproducible activity for methane formation from CO_2 on consecutive ramps; (d) Cu_4 on NS ZrOx with a activity for methane formation from CO_2 significantly decreased during the second ramp; and (e) Cu_{12} on NS ZrOx with a activity for methane formation from CO_2 quenched during second ramp.

Figure 2. XANES spectra collected at the Cu K-edge during the double ramp shown in Figure 1a. (a) Cu bulk standards; (b) Cu_4 on ALD ZrOx; (c) Cu_{12} on ALD ZrOx; (d) Cu_4 on NS ZrOx; and (e) Cu_{12} on NS ZrOx. The blue bar in the plots indicates the position of the edge of the spectra, calculated by the location of the first peak of the derivative in the XANES spectra. It is shifted toward lower or higher energies, indicating the change in the oxidation state to the lower or higher values, respectively.

we complement the LCF approach by a multivariate curve resolution - alternating least squares (MCR-ALS) method,[37] which has proven to be instrumental for speciation of mixtures, when the exact reference spectra for pure components are not known.

Using an X-ray beam of 9.1 keV energy, 2-dimensional GISAXS images were collected to monitor possible agglomeration of Cu clusters during the reaction can be obtained[35,38−40] and the scattering patterns were analyzed with the Modeling II tool in the Irena tool suite.[41]

GIXANES Spectra Analysis. GIXANES data were analyzed to obtain the changes in the oxidation state of the clusters using two different techniques:

LCF Technique. The Cu clusters XANES spectra were fitted as a linear combination of bulk Cu standard XANES spectra, Cu (Cu^0), Cu_2O (Cu^+), CuO (Cu^{2+}), and $Cu(OH)_2$ (Cu^{2+}). The spectra were processed by using a linear least-squares optimization algorithm, which provides the contributions from individual motifs to the ensemble-average spectrum of the clusters.[42,43] (see Figure S3) By performing LCF analysis for spectra collected at all temperatures, one can obtain the evolution of unique subsets of clusters during the reaction can be obtained. This method assumes prior knowledge of the standards and requires independent validation that the standards adequately represent the states of the clusters in reaction condition.
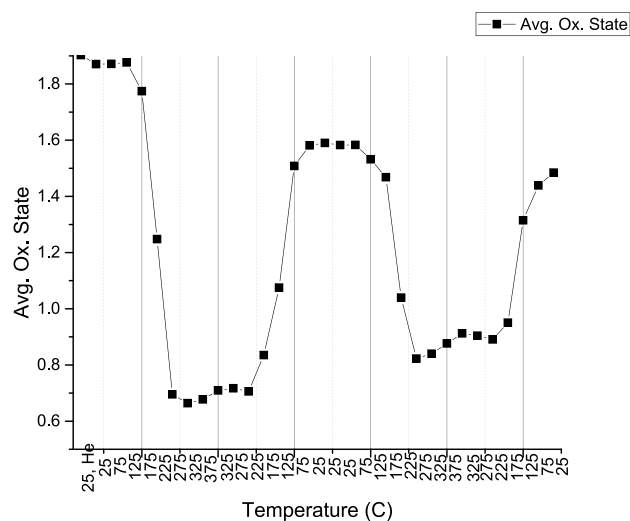
Figure 3. Evolution of oxidation state of copper in the clusters during the reaction, form LCF fitting of XANES spectra and corresponding compositions shown in Figure S3. (a) Cu$_4$ on ALD ZrOx; (b) Cu$_{12}$ on ALD ZrOx; (c) Cu$_4$ on NS ZrOx; and (d) Cu$_{12}$ on NS ZrOx.

MCR-ALS Technique. The accuracy of the LCF approach discussed above can be limited by the fact that the local structure of nanostructured materials and hence their X-ray absorption spectra can be quite different from those in corresponding bulk materials. In the MCR-ALS approach, in turn, the spectra corresponding to pure compounds (which are not known a priori for nanosized materials) are determined automatically from the series of experimental data for mixtures. The MCR-ALS method and its application to XANES data analysis are discussed in refs 37 and 44−48. In particular, ref 46 is a good example of application of the MCR-ALS method for identification of different species in copper-based nanocatalysts from temperature-dependent Cu K-edge XANES data and demonstrates clearly the limitations of the LCF technique. For example, it was shown that LCF may severely overestimate contribution of Cu$^+$ species in the speciation of nanosized copper catalysts.[46] Briefly, MCR-ALS method is applicable if a set of experimental XANES spectra μ_i is available, where each

spectrum can be expressed as a linear combination of a few spectra s_j that correspond to pure compounds, weighted with w_{ij}: $\mu_i(E) = \sum_j w_{ij} s_j(E)$. Using matrix notation, this set of equations can be rewritten as $M = WS$, where the matrices M, W, and S are formed from experimental spectra $\mu_i(E)$, weights w_{ij} and spectra for pure compounds $s_j(E)$, correspondingly. To obtain unique results for W and S, the following constraints are imposed: 1) all elements of matrices W and S should be non-negative and 2) $\sum_j w_{ij} = 1$. Elements of W and S are then refined in an iterative process. One starts with a rough initial estimation of matrix W (in our case, the initial guesses of concentration profiles can be obtained from the conventional LCF analysis). To obtain the initial approximations of spectra for pure compounds, linear least-squares problem is then solved with respect to S to minimize the norm $\|M - WS\|$. Next, elements of matrix W are similarly updated, by solving least-squares problem with respect to W and taking into account the above-mentioned constraints. The process is repeated until there is no more significant

reduction of the norm $\|M - WS\|$. If the initial guess of matrix W is not too far from the true values, MCR-ALS method is able to recover the spectra for pure compounds, as well as the weights of the pure compounds spectra in each of the experimentally acquired spectrum (see Figure S4). To illustrate and validate the MCR-ALS method for the analysis of Cu K-edge XANES data, in the Supporting Information, Figure S6, we apply it to analyze a set of model data, constructed as artificial linear combinations of experimental XANES for bulk reference compounds: metallic copper, Cu_2O, CuO, and $Cu(OH)_2$. As shown in Figure S7, the MCR-ALS method in this case is able to reconstruct quite reliably all four reference spectra and also their contributions to each of the mixtures.

Importantly, as part of the MCR-ALS analysis procedure, we have also verified that two components should be sufficient to describe experimental data for each of the samples by using principal component analysis (PCA).[49−51]

XPS Analysis. The XPS measurements were performed with a Leybold LHS 10/12 UHV apparatus equipped with a hemispherical electron analyzer and a conventional X-ray source (Mg $K\alpha$ = 1253.6 eV). The high resolution spectra were acquired in the constant step energy mode with E_{pass} = 30 eV. The overall energy resolution was 0.8 eV. The pressure in the experimental chamber during experiments was below 6×10^{-9} mbar. The binding energy scale of the spectrometer was calibrated via the Au 4f7/2 core level line (located at 83.97 eV) of a clean polycrystalline Au sample. Due to the moderate charging in all of the analyzed samples and considering that the substrates are all zirconium oxide, the spectra were aligned by using as reference the adventitious carbon peak conventionally positioned at 284.8 eV. The spectra were fitted with a Shirley background or with linear background that was subsequently removed for zirconium and oxygen spectra. The oxygen and zirconium spectra were fitted with a linear combination of Gaussian and Lorentzian line-shapes with larger weight of the Gaussian component. The least-squares curve-fitting were performed with the code WinSpec, developed at the LISE laboratory, Namur, Belgium.

■ RESULTS AND DISCUSSION

Cu clusters on both ALD coated and nanostructured zirconia were found to be highly active and selective toward methane production. The reaction was performed using a uniform double heat and cool ramp (Figure 1a), at a pressure of 1.1 atm under continuous flow of 18 sccm of pure CO_2 and H_2 in 1:3 ratio. An initial look at the reactivity data (reaction rates) can be summarized as follows. During the first ramp, the activity of Cu_4/NS ZrOx was found to be approximately 30% higher than that of Cu_4/ALD ZrOx, and the activity of Cu_{12}/NS ZrOx was approximately twice that of the activity of Cu_{12}/ALD ZrOx. However, the activity of Cu_{12}/NS ZrOx drops over a repeated cycle, as discussed below.

The comparison of activity and X-ray results revealed a strong correlation between the activity and oxidation state of the clusters:

Cu Clusters on ALD ZrOx. The spectra of the Cu metal foil, Cu_2O, CuO, and $Cu(OH)_2$ used as bulk standards are shown in Figure 2a. The spectrum of copper in Cu_4 clusters supported on ALD ZrOx indicate a $Cu(OH)_2$-like structure at room temperature, as deducted from XANES spectrum collected under flowing He before the beginning of the heating ramp (Figure 2b). The evolution of the oxidation state of copper in the

Cu_4 and Cu_{12} cluster during the applied temperature ramp obtained from LCF analysis is shown in Figure 3a,b, respectively

XPS characterization was carried out ex situ before and after the complete thermal treatment. Figure 4 shows the high
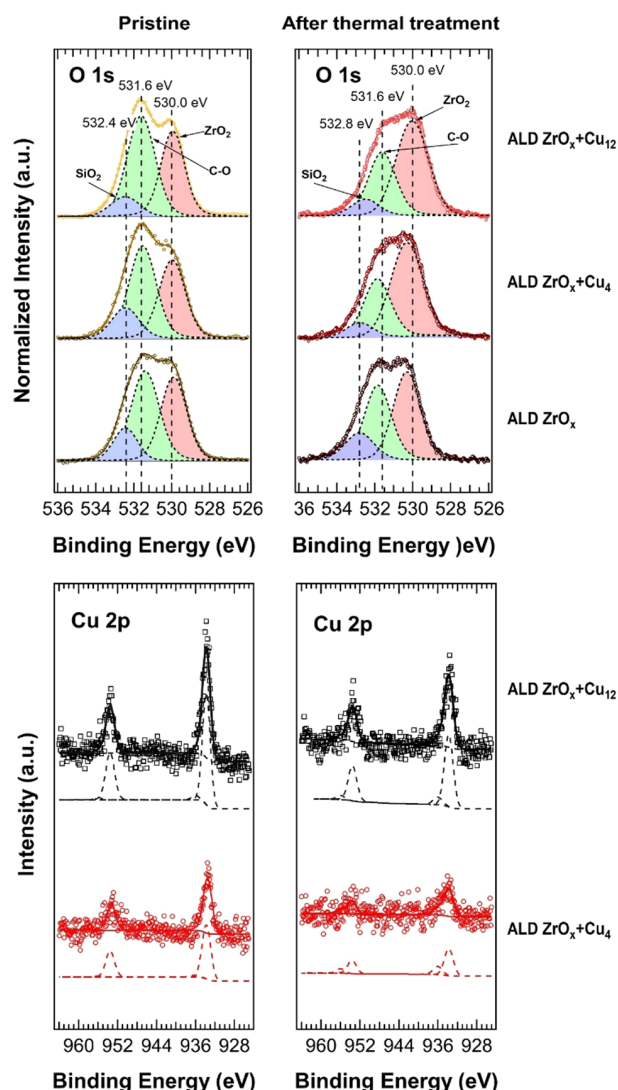
Figure 4. XPS spectra of pristine and after the complete thermal process of ALD ZrO_x samples. Upper panels: fitted normalized O 1s spectra; bottom panels: fitted Cu 2p spectra.

resolution XPS spectra and the peak fitting of O 1s edges of the ALD ZrOx, namely the pristine sample and the sample after the thermal treatment without and with the Cu_4 and Cu_{12} clusters.

Figure S4 shows the corresponding Zr 3d spectra. The fwhm of the Zr 3d peaks is about 1.5 eV. The Zr 3d 5/2 peak is found at 182.0 eV with spin−orbit splitting of 2.3 eV. This BE could be referred to oxygen-deficient zirconia (ZrO_{2-x}), as also assessed by the evaluation of the stoichiometry obtained by the ratio between the area of Zr 3d peak and the area of the fitted oxygen peak corresponding to the lattice oxygen (Zr^{4+}) centered at 530.0 eV (red filled peaks in Figure 4, upper panels). The complete thermal process promotes the oxidation of zirconium. In O 1s spectra the feature centered at 531.6 eV (green filled peaks in Figure 4) is related to the contribution of oxygen bonded to carbon in organic species and oxygen bonded to zirconium but with no lattice occupancy that is either an
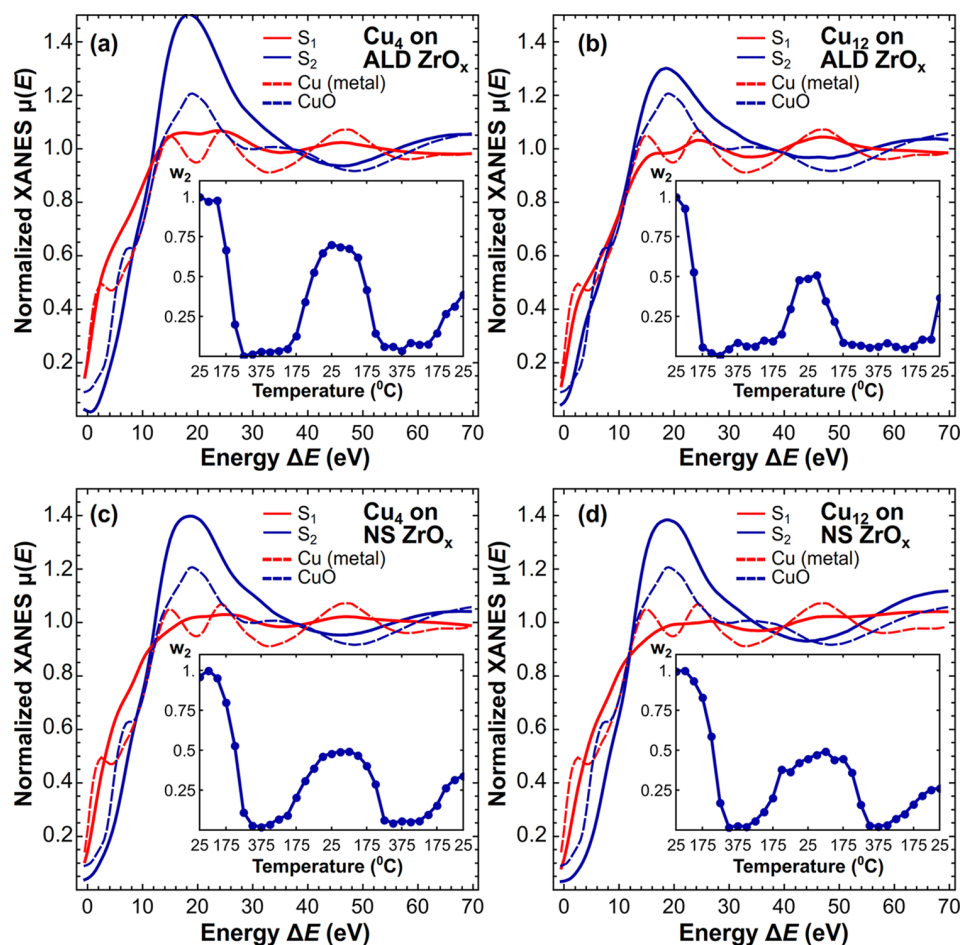
Figure 5. Evolution of Cu cluster composition during the reaction as obtained from MCR-ALS analysis for Cu_4 on ALD ZrOx (a), Cu_{12} on ALD ZrOx (b), Cu_4 on NS ZrOx (c), and Cu_{12} on NS ZrOx (d). XANES spectra S_1 and S_2 for two species identified by the MCR-ALS method are shown as solid lines and compared with experimental spectra for bulk reference materials (metallic Cu and CuO, dashed lines). Temperature-dependencies of the weight of contribution of S_2 (which resembles the spectrum for oxide) to the total spectra are shown in the insets.

indication of oxygen vacancies and a certain degree of surface hydroxylation of the support.[52,53] The possible contribution of copper oxides should also be in the BE region between 529.5 and 530.5 eV but, due to the low content of the element, its amount is expected to be negligible with respect to the exceeding O−Zr contribution and no reliable deconvolution of the two metal oxides can then be performed. In O 1s spectra silicon dioxide is also detected (blue filled peak at 532.4 eV). Its contribution comes from the support on which the thin ALD zirconia film was deposited in accordance with the intense silicon peak observed in the wide spectrum (not shown). In Zr 3d and O 1s spectra no evident features ascribable to the presence of copper clusters arise. Figure 4 (bottom panel) shows the Cu 2p peaks of the ALD ZrO_x samples before and after the complete thermal process. All of the samples show the main Cu $2p_{3/2}$ at 933.7 eV with a spin orbit splitting of 20.0 eV. The peak position and the narrow shape of the $2p_{3/2}$ peaks of the pristine samples are strong indications that Cu is mainly in metallic form (Cu(0)) or in oxidation state Cu(I) since these two contributions are not easily distinguishable, according to the reference spectra of copper oxides reported by Pauly et al.[54] The component Cu(II), identified via a small fitting peak at higher BE,[54] is negligible for the pristine sample.

The catalyst changes its composition drastically when heated in the presence of CO_2 and H_2. Indeed, above 175 °C the Cu_2O

and CuO phase appear (see Figure S3a). At 275 °C the composition further changed to a mixture of Cu_2O and metallic Cu with contributions of 70% and 30%, respectively. Note, however, that, as demonstrated in ref 46, the significant contribution of Cu_2O at high temperatures may be an artifact of the LCF procedure in this case. The composition remained constant as the clusters were heated up to 375 °C. The oxidation state dropped from +2 at room temperature to 0.7 at 225 °C and was stable at higher temperatures. The changes of the composition and oxidation state of copper were reversible as seen from the cool-down ramp. The oxidation state started to increase when the samples were cooled below 225 °C and rose to 1.6 at room temperature. The changes in the oxidation state were identical in the next cycle. MCR-ALS results for Cu_4 clusters on ALD zirconia are shown in Figure 5a and are in qualitative agreement with LCF results discussed below. Two components (S_1 and S_2) were identified, such that experimental spectra, acquired at different temperatures, can be expressed as linear combinations of S_1 and S_2. The representative fits of experimental XANES spectra with linear combinations of S_1 and S_2 are shown in the Supporting Information, Figure S7. Nearly perfect MCR-ALS fit indicates that two components are sufficient to describe the whole experimental data set. Existence of additional species cannot be ruled out completely, but they need to be either extremely short-lived (i.e., contributing to a

single experimental spectrum only), or their concentration should be completely correlated with the concentration of some other species. By comparing the spectral components, yielded by MCR-ALS technique, with the spectra of reference compounds (Supporting Information, Figure S5), one can conclude that component S_1 corresponds to metallic copper, while component S_2 can be associated with a spectrum of oxidized copper species. At the same time, one can see clearly the differences between S_1 and S_2 and XANES data for bulk reference compounds. In particular, one can note that the spectrum for metallic species (S_1) has much broader, smoother features than XANES for bulk metallic copper, as expected for metallic clusters of very small size.[46,55] The observed differences between S_1 and S_2 and XANES data for bulk references is a warning sign that conventional LCF may be inaccurate in this case,[46] and there is a need for a complementary MCR-ALS approach. The temperature dependence of the weight of the S_2 component, which can be associated with the fraction of oxidized Cu species, is shown in the inset in Figure 5a. The as-prepared Cu_4 sample on ALD zirconia sample is nearly completely oxidized, and preserves its state up to ca. 150 °C. Upon further temperature increase, the sample is rapidly reduced, and is almost completely metallic at 225 °C. The fact that MCR-ALS suggests that the sample is reduced almost completely is the main difference between MCR-ALS and LCF results. As mentioned above, this difference can be explained by the known artifact of the LCF procedure for nanosized catalysts.[46] Upon subsequent cooling, the sample is partially reoxidized. Similarly to the conclusions made on the basis of the LCF analysis, MCR-ALS suggests that reoxidation occurs sharply when the temperature falls below 225−175 °C.

The activity of the catalyst followed from the measured TPRx signal showed highest activity for methane (m/z = 15) production, whereas no detectable signal was seen for methanol (m/z = 31). Methane production started at 275 °C and peaked at 375 °C with r_{CH4} of 0.03 molecules atom^{-1} s^{-1} as shown in Figure 1b for Cu_4 on ALD ZrOx. It was also found that the activity measured during the slow heat and cooling ramps is symmetric which shows that there is no deactivation of the catalyst by the heating to a high temperature. The catalyst is cycled for two consecutive ramps with a 90 min rest at room temperature in between the two ramps. The sample with Cu_4 clusters in the second ramp lost about 30% of its activity, for which we have no unambiguous explanation. We speculate that this drop could be caused due to changes in the ALD ZrOx support and clusters getting partially embedded into the support.

The XANES spectra measured under He for the Cu_{12} clusters showed that copper in the clusters was present as $Cu(OH)_2$ similar to Cu_4 clusters as seen in Figures 2c and S3b, respectively. However, the changes observed in the Cu_{12} clusters exhibited a more gradual pattern as the oxidation state of copper started dropping as soon as the reactant gases were introduced within the reactor. As seen from Figures 2c and 3b the oxidation state of the clusters dropped to 0.8 above 175 °C and did not change while the clusters are heated up to 375 °C and also during cooling until 175 °C. On further cooling to room temperature the oxidation state increased to 1.2. The change in the oxidation state occurred in the same manner in the following cycle. The final oxidation state for copper in the dodecamer clusters at 375 °C was the same; however, the clusters were composed of about 50% metallic Cu and the rest of the

composition was in an oxidized state. The changes in the composition were reproducible over the two consecutive ramps.

In XPS (see Figure 4), after the thermal process the detected Cu 2p signal shows a larger spread. The fit highlights a more intense peak arising at higher BE, attributable to an increased amount of the Cu(II) phase, more evident for the samples with Cu_4 clusters. The reduction in peak intensities with respect to pristine sample can be mainly attributed to the diffusion of the copper clusters in/on the zirconia support.

MCR-ALS results for Cu_{12} clusters on ALD ZrOx (Figure 5b) are, again, in qualitative agreement with LCF results and also suggest a more gradual initial reduction compared to the Cu_4 sample. At the same time, the completely reduced state was reached faster, at lower temperature (175 °C for Cu_{12} clusters in comparison to 225 °C for Cu_4) clusters. This may explain the differences in catalytic properties for these systems, vide infra. Upon consequent cooling, the Cu_{12} sample was also reoxidized to a lesser degree than the Cu_4 sample, in agreement with LCF. We note that, following a similar procedure in analyzing experimental XANES data for both Cu_4 and Cu_{12} clusters (spectra for each of the samples were analyzed separately), we have found that MCR-ALS decomposition of experimental spectra into mixtures of two components is able to reproduce reasonably experimental spectra for all samples, and inclusion of the third component in the analysis does not improve results significantly.

Cu_{12} clusters were active at temperatures as low 175 °C, which is about 100 °C lower than the onset temperature seen for Cu_4 clusters. This temperature is lower than any of the previously reported catalysts in literature and at atmospheric pressure.[56−60] r_{CH4} reaches 0.025 molecules atom^{-1} s^{-1} at 375 °C during the first ramp and maintains about 90% of its activity during the second cycle which makes Cu_{12} as one of the most active low pressure catalyst for CO_2 conversion to methane. From GIXANES we could already ascertain that the clusters maintain their composition and oxidation state over the cycles. GISAXS results from Figure S8a,b show no evidence that the clusters aggregate under the reaction conditions.

Cu Clusters on Nanostructured Zirconia. Cu_4 clusters on the NS ZrOx support showed a gradual change in the oxidation state of copper, reaching 0.9 at 375 °C from 1.8 at 25 °C. At room temperature the clusters start off as $Cu(OH)_2$, a component (see Figure S3c) which gradually decreases with increasing temperature and finally vanishes at 175 °C as shown in Figure 2d and for average copper oxidation state in these cluster in Figure 3c. Above this temperature, copper stays in a mixed phase of Cu (20%), Cu_2O (60%), and CuO (20%) as shown in Figure S3c. During cooling the oxidation state starts to increase, reaching 1.5 at room temperature. During the second cycle a similar trend is observed but copper stays more oxidized at 375 °C with an oxidation state of 1 and a higher fraction of CuO component (30%). MCR-ALS for the Cu_4 sample on NS ZrOx suggests a more gradual sample reduction upon heating and a more gradual reoxidation upon cooling in comparison to samples on ALD supports. After reoxidation, the fraction of the metallic phase is found to be lower for the copper tetramer on NS ZrOx.

The methane signal appears at 275 °C and rises to 0.04 at 375 °C and, thus, the same onset temperature for Cu_4 clusters on both ALD and NS ZrOx. However, the activity of Cu_4 on NS ZrOx is 30% higher compared to ALD ZrOx. The most drastic changes are observed during the cooling phase as the activities at 325 °C during the heating and cooling are 0.03 and 0.01

respectively. In the second cycle the maximum activity at 375 °C dropped to 0.01 which is a 75% drop in activity compared to the first ramp. The big change in activity implies a possible restructuring taking place on the NS ZrOx surface during the heating which leads to quenching the Cu_4 activity. Since, in comparison with studies of similar clusters under different conditions,[9] no unambiguous indication of noticeable agglomeration of Cu_4 clusters was observed in GISAXS patterns (Figure S8c), a possible explanation for the drop in activity could be that the clusters are less exposed to the reactants, for example by migrating into pores or getting submerged into the surface of NS ZrOx, as evidenced by the drop of Cu-signal intensity in XPS on the NS ZrOx support.

Figure 6 shows the Zr 3d and O 1s spectra of NS ZrOx pristine samples and after thermal treatment without and with clusters.

The fwhm of the Zr 3d peaks is larger than in the previously discussed samples (approximately 2.1 eV). This peak spread is due to the intrinsic nature of the nanostructures, that are
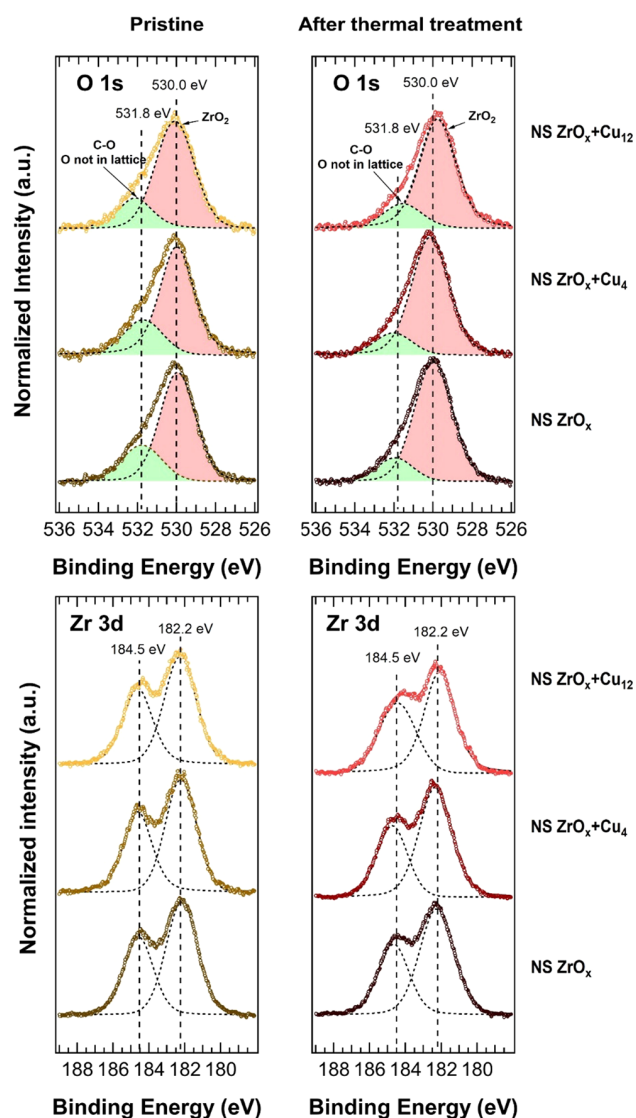
characterized by nonbulk like bond length relaxation, as well as to the coexistence of cubic crystalline phase and amorphous component in these samples. Thermal treatments promotes the evolution of the nanocrystals toward the monoclinic phase.[20] The Zr 3d 5/2 peak for all the samples is located at 182.2 eV with spin−orbit splitting of 2.3 eV. This peak spreading is related to the copresence of the different crystalline phases, and the value of the BE indicates an almost full oxidation of the samples (Zr^{4+}) as confirmed also by the stoichiometry evaluation. Also at a glance, the deconvoluted oxygen components show an increase of the area under the oxygen in the ZrO_2 lattice and a concomitant decrease of the area of the oxygen not in the regular lattice (531.8 eV). Furthermore, taking into account the porosity and the largest exposed surface of the NS ZrO_x samples with respect to ALD zirconia, the contribution of adventitious species bonded to carbon is expected to be more relevant. In these films there are no silicon fingerprints detectable for the accessible depth with XPS as assessed in the wide scan (not shown); thus no peak at 532.8 eV comes out from the fitting of the oxygen peak. No features interfering with those observed for copper clusters were identified which could have complicated an unambiguous assignment of peaks for the latter samples.

The oxidation state of Cu_{12} clusters on NS ZrOx at room temperature is found to be 1.9 (with a composition of $Cu(OH)_2$, Figure S3d) which drops to 1.1 at 325 °C and does not change any further as the sample is heated up until 375 °C and when subsequently cooled to 225 °C as seen (Figures 2e and 3d). Below 225 °C the oxidation state rises and increases to 1.4 at room temperature. The composition of the clusters is a mixture of Cu, Cu_2O, and CuO in equal proportion (Figure S3d). In the second cycle the oxidation state also shows a drop reaching 1.1 at 375 °C with a similar composition as that in the first cycle, thus indicating reversible changes in the nature of the catalyst. No indication of sintering of Cu_{12} clusters was observed by GISAXS (Figure S8d) in comparison with earlier studies.[9]

Cu_{12} becomes active at a temperature of about 175 °C and attains a rate of methane formation r_{CH4} of 0.05 molecules atom^{-1} s^{-1} at 375 °C. The r_{CH4} is similar at all temperatures recorded during the heating and cooling ramp showing that the changes on the surface of NS ZrOx does not affect the activity of Cu_{12} clusters. The activity significantly drops during the second cycle to about 20% of that observed in the first cycle. Interestingly, according to MCR-ALS, the evolution of the oxidation state for Cu_{12} on NS ZrOx is very similar to that in Cu_4 on NS ZrO_x. Thus, unlike it was observed for samples on ALD support, the cluster size does not affect significantly the reducibility of the samples on NS ZrOx.

For nanostructured zirconia the signal at Cu 2p edge was very low also for a possible shadowing and burying effects on Cu clusters due to the rough morphology of the NS ZrOx substrates. Again, after the described data processing, the Cu appears, as in the case of ALD samples, before and after thermal treatment, mainly in CuO phase for both types of Cu clusters.

Results, obtained by MCR-ALS analysis of Cu K-edge XANES data, for the nanostructured zirconia-supported catalysts are shown in Figure 5c,d. For each of the samples two components (S_1 and S_2) were identified, such that experimental spectra, acquired at different temperatures, can be expressed as linear combinations of S_1 and S_2. Representative fits of experimental XANES spectra with linear combinations of S_1 and S_2 are shown in the Supporting Information, in Figure S7.

Component S_1 resembles the XANES spectrum for metallic copper, while component S_2 can be associated with a spectrum

Figure 6. XPS spectra at O 1s (upper panels) and Zr 3d (bottom panels) edges and peaks fitting of NS ZrOx samples. The spectra of the pristine sample (left column) and after complete thermal process (right column) without and with the Cu clusters are shown.

of oxidized copper species. At the same time, one can see clearly the differences between S_1 and S_2 and XANES data for bulk reference compounds.

The temperature-dependencies of the weight of S_2 component, which can be associated with the fraction of oxidized Cu species, are shown in the insets in Figure 5. Overall, the results obtained via MCR-ALS approach qualitatively agree with the results of conventional LCF analysis. All as-prepared samples are nearly completely oxidized. Upon temperature increase, all samples are reduced. The reduction is more rapid for samples on ALD ZrOx, which are nearly completely metallic at 175−225 °C. Higher reduction temperatures are required for samples on NS ZrOx (325−375 °C). Upon subsequent cooling, all samples are partially reoxidized. For samples on ALD ZrOx reoxidation occurs sharply, when the temperature falls below 175−125 °C. More gradual changes are observed for samples on NS ZrOx. Interestingly, the evolution of the oxidation state for Cu_4 on NS ZrOx and Cu_{12} on NS ZrOx is very similar, suggesting that the cluster size does not affect significantly the reducibility of these samples.

Activation Energy. The activation energy of the Cu clusters on zirconia substrates is evaluated from the Arrhenius plots shown in Figure S9 and are tabulated in Table 1. The r_{CH4} data

Table 1. Activation Energy for Cu Clusters on Zirconia Supports

catalyst	E_a	
	(kJ/mol)	(eV)
Cu_4/ALD ZrOx	70.92	0.74
Cu_{12}/ALD ZrOx	15.29	0.16
Cu_4/NS ZrOx	40.03	0.41
Cu_{12}/NS ZrOx	25.89	0.27

used for calculation are those obtained during the first cycle. Cu_4 on ALD ZrOx has an activation energy of E_a of 70.92 kJ/mol which is comparable to those reported for bulk catalysts for CO_2 methanation;[2] for example on the Ni(100) surface an E_a of 88.7 kJ/mol has been reported.[61] Cu_4 on Nano ZrOx has higher activity than Cu_4/ALD ZrOx and has an E_a of 40.03 kJ/mol. A lower E_a of ∼40 kJ/mol has recently been reported for Cu nanoparticle doped iron nanocomposites for CO_2 methanation.[10] The Cu_{12} cluster on ALD ZrOx and NS ZrOx has an E_a of 15.29 and 25.89 kJ/mol, respectively, and were also found to be

more active compared to the Cu_4 clusters on the same supports. This low E_a is consistent with the highest activity that we discussed for the Cu_{12} clusters in the previous section.

In passing we note that similar size Cu clusters dispersed on various supports produced different products, ranging from methanol[7,8,62] to hydrocarbons,[9,62] thus underlining the pronounced support effects on both activity and selectivity of subnanometer size clusters.

Mechanism and Energy Profile of CO_2 Methanation Reaction. In order to elucidate the reaction mechanism responsible for CO_2 methanation on the Cu_4O_2 cluster at the zirconium oxide support, the DFT calculations have been carried out involving four hydrogenation steps of the reaction. Concerning the model of ZrO support, ZrO_2 subunits have been considered because they are involved in crystalline growth and the subunit $Zr_{12}O_{24}$ has been selected based on findings from previous reactivity studies on Zr oxide.[63] The chosen subunit of $Zr_{12}O_{24}$ with Cu_4O_2 has been optimized, and after an extensive search of isomers (cf. Figure S10), the lowest energy structure has been selected as a model. The above-described $Zr_{12}O_{24}$ subunit (Figure 7a) supporting Cu_4O_2 cluster with oxidation number 1 (based on the experimentally determined Cu oxidation state of about 1) with bound HCO_2 (Figure 7b) forms the reactive center $Cu_4O_2Zr_4O_5H\text{-}HCO_2$ (Figure 7c). Notice that contribution of the support through the Zr_4O_5 subunit offers functionalization of the copper tetramer with its dual role, since two Cu atoms participate actively in hydrogenation and the other two bind to Zr atoms of the model for support. Mulliken charge analysis provides information that Cu_4 is positively charged.

These results have been obtained based on density functional theory using the B3LYP functional[64−66] and TZVP AO[67,68] basis set as well as relativistic effective core potential RECP for Zr atoms.[69] The minima and transition states along the reaction pathway have been determined employing the Gaussian 16 program package.[70] In addition, an extensive structural search has been carried out determining the position of CO_2 and H_2 at $Cu_4O_2Zr_{12}O_{24}$ (cf. Figure S11).

The calculated energy profile for CO_2 methanation which involves four hydrogenation steps is presented in Figure 8. The starting point (A) of the reaction is a Cu_4O_2 unit on $Zr_{12}O_{24}$ with CO_2 bound to one of the copper atoms. The first hydrogenation step (B) has been obtained by adding an H_2 molecule, in which one H atom is bound to oxygen and the other one is bridging two Cu atoms gaining 2.04 eV of energy. The barrier for the
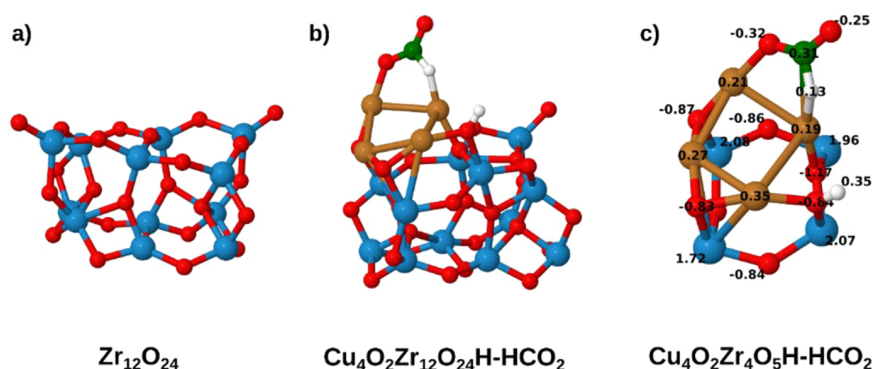
Figure 7. DFT determined structures for (a) $Zr_{12}O_{24}$ subunit, (b) $Cu_4O_2Zr_{12}O_{24}H\text{-}HCO_2$ presenting binding of CO_2 and H_2 on $Zr_{12}O_{24}$, and (c) reactive subunit $Cu_4O_2Zr_4O_5H\text{-}HCO_2$ evidencing participation of copper cluster and part of support. Mulliken population analysis has been also included. The calculated binding energy of Cu_4O_2 at $Zr_{12}O_{24}$ is 8.14 eV.
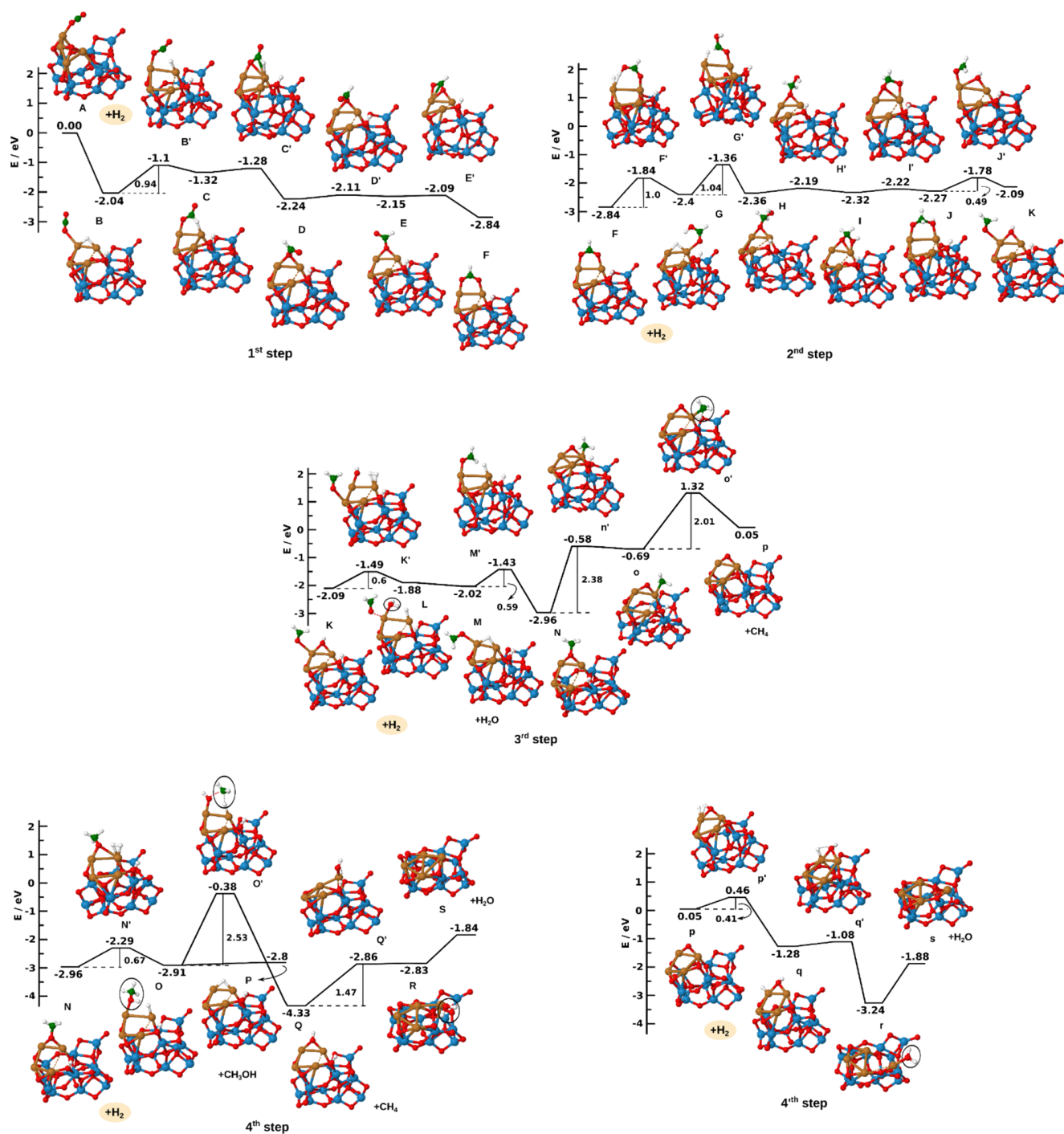
Figure 8. Calculated reaction pathways of CO_2 methanation on an oxidized copper tetramer (Cu_4O_2) supported by $Zr_{12}O_{24}$ following four steps of hydrogenation (1st step A−F, 2nd step F−K, 3rd step K−p, and 4th step N−S or 4th p−s). Letters label minima, and letters with primes denote transition states.

activation of CO_2 (B′) and formation of HCOO is 0.94 eV. Conformational changes of the HCOO unit located between two Cu atoms lead to a stable configuration of HCOO (F). The subsequent addition of the second H_2 molecule leads to formation of HCOOH (G) over a barrier of 1 eV (F′). In addition, a barrier of 1.04 eV (G′) has to be overcome in order to form H_2COOH (H). The steps H-J lead to conformational changes of the H_2COOH unit over small energy barriers, and the activation energy of 0.49 eV (J′) is needed for separation of H_2COOH to OCH_2 and OH (K). According to Cu_4O_2 at the

$Zr_{12}O_{24}$ subunit, methanation of CO_2 proceeds energetically favorable over formation of Cu_2−HCOO (1st step) and OCH_2 (2nd step). Thus, the reaction mechanism within the first two hydrogenation steps directly involves interaction between two copper atoms with CO_2 and H_2 opening the opportunity to form methane and water within the next two hydrogenation steps described below. In order to consider the possibility of other pathways of hydrogenation, we examined the binding of hydrogen on oxygen instead of carbon. However, the transition state over formation of COOH is considerably higher (2.9 eV, cf.

Figure S12) than the one needed for formation of HCOO (0.94 eV). Therefore, we continued to investigate the methanation reaction following the formation of HCOO shown in Figure 8.

An addition of the third H_2 molecule leads to formation of H_2O (L) and the barrier of 0.59 eV (M′) has to be overcome to create OCH_3 (N). Furthermore, the reaction can follow two pathways, one within the third step and the 4′th step (labeled by small letters) and the second one within the fourth step. Along the first branch of the pathway, in order to separate CH_4 two barriers have to be overcome, the first one of 2.38 eV (n′) which involves breaking of CO bond by forming Cu_2O and $CuCH_3$ and the second barrier that requires 2.01 eV(o′) forming CH_4 bound to a copper atom. However, this requires 1.32 eV with respect to the starting point of reaction. Along the second branch of the pathway within the fourth step, the H_2 molecule added to the OCH_3 unit forms CH_3OH (O) over a barrier of 0.67 eV (N′) and the CH_4 formation originating from $Cu-CH_3OH$ needs to overcome an activation barrier of 2.53 eV (O′). Comparing both branches of the pathway, the second branch is energetically favorable (N−S) and accessible at $T = 0$ K. The first one is accessible by higher temperatures (N-s) due to a barrier of 2.01 eV, since the corresponding transition state is above starting point of the reaction pathway.

In the fourth step and 4′th step, after separation of CH_4, the formation of water can also be followed by two branches of the pathway. The one along steps p-s requires the energy of 0.46 eV above the starting point of the reaction and therefore is energetically unfavorable at 0 K. The other one involving steps Q′−S is energetically favorable at 0 K. The above-described findings allow us to elucidate the CO_2 methanation reaction and indicate that the mechanism of the CO_2 methanation reaction directly involves two copper atoms from Cu_4O_2 stabilized by a Zr_4O_5 subunit which is accessible to H_2 molecules.

In summary, theoretical modeling based on participation of the Cu_4O_2 subunit and $Zr_{12}O_{24}$ as a model for support provides the mechanism of reaction, as well as energetically favorable pathways for CO_2 methanation. It is worth mentioning that the participation of the support is essential. Our results fully support experimental findings which showed that Cu_4O_2 at the zirconium oxide surface is responsible for CO_2 methanation. However, in order to design the most efficient reactive center and model support, the consideration of metallic Cu_4 and a bimetallic tetramer interacting with $Zr_{12}O_{24}$ might also be of interest in the future.

CONCLUSIONS

Cu clusters on zirconia supports form a sintering-resistant catalyst with high activity for CO_2 conversion and high selectivity toward methane formation. The Cu_4/NS ZrOx is about 30% more active compared to Cu_4/ALD ZrOx, whereas Cu_{12}/NS ZrOx is 100% more active compared to Cu_{12}/ALD ZrOx. During CO_2 hydrogenation, copper was found to be partially oxidized. The Cu_4 clusters activate CO_2 at 275 °C, whereas Cu_{12} does the same already at 175 °C. The activation energy E_a of methane formation on the clusters has been found to be strongly dependent on its size and the support interaction. The subnanometer sized Cu clusters on zirconia supports investigated herein were found to have lower E_a and higher efficiency for methane formation compared to clusters deposited on alumina supports.[7,8] The zirconia supports with Cu clusters have been found to be one of the more efficient catalyst for CO_2 methanation. The measured r_{CH4} for Cu_{12}/NS ZrOx makes this catalyst among the best reported so far; however, it was found

that its activity drops during the repeated cycle, most likely due to the possible migration of the clusters into the pores and voids with more limited access to reactants. Preprocessing of the substrate may thus be extremely important so that the catalyst does not lose its catalytic activity and at the same time has higher stability.

The ex situ XPS measurements have assessed the different nature of the zirconia substrates and the fact that copper before and after the process is predominantly in the Cu(I) oxidation state with also a small contribution of Cu(II) in both cases After the cyclic treatment the possible enhanced burying of the Cu clusters on the NS ZrOx substrate is mirrored by a very low Cu 2p signal which could be related to the observed higher activity for the Cu/NS ZrOx catalysts with respect to the Cu/ALD ZrOx systems, underlining the pronounced effect of the morphology of the support on nanocatalysts' performance, demonstrating the potential of its use in the development of new classes of nanostructured catalysts. With the example of Cu_4, accompanying theoretical investigations provide supporting evidence on its dual role and into the intrinsically high activity of zirconia-supported copper clusters and fundamental insights into the conversion of CO_2 to methane.

Putting this into a broader perspective, this study contributes to the understanding of support effects in catalysis, where selectivity may be switched by altering the support or its morphology.

ASSOCIATED CONTENT

Supporting Information

The Supporting Information is available free of charge at https://pubs.acs.org/doi/10.1021/acscatal.0c05029.

> Description of cluster synthesis; description of the in situ experiment; AFM image of the support material; mass spectrum of clusters produced; composition of Cu as a function of reaction temperature; XPS spectra of ALD ZrOx; fits of XANES spectra; validation of the MCR-ALS method and its use to fit XANES data; GISAXS cuts; Arrhenius plots; calculated isomers of the catalytic site and its complexes with the reactants; calculated alternative reaction pathway; and supporting references (PDF)

AUTHOR INFORMATION

Corresponding Authors

Paolo Milani − *C.I. Ma.I.Na., Dipartimento di Fisica, Università degli Studi di Milano, I-20133 Milano, Italy;* Email: Paolo.Milani@mi.infn.it

Stefan Vajda − *Materials Science Division, Argonne National Laboratory, Lemont, Illinois 60439, United States; Department of Nanocatalysis, J. Heyrovský Institute of Physical Chemistry, Czech Academy of Sciences, CZ-18223 Prague 8, Czech Republic;* orcid.org/0000-0002-1879-2099; Email: stefan.vajda@jh-inst.cas.cz

Authors

Avik Halder − *Materials Science Division, Argonne National Laboratory, Lemont, Illinois 60439, United States*

Cristina Lenardi − *C.I. Ma.I.Na., Dipartimento di Fisica, Università degli Studi di Milano, I-20133 Milano, Italy;* orcid.org/0000-0002-5522-6803

Janis Timoshenko − *Department of Materials Science and Chemical Engineering, Stony Brook University, Stony Brook, New York 11794, United States*

Antonija Mravak − *Center of Excellence for Science and Technology - Integration of Mediterranean region (STIM), Faculty of Science, University of Split, CR-21000 Split, Croatia;* ⓘ orcid.org/0000-0002-1252-7390

Bing Yang − *Materials Science Division, Argonne National Laboratory, Lemont, Illinois 60439, United States;* ⓘ orcid.org/0000-0003-3515-0642

Lakshmi K Kolipaka − *Materials Science Division, Argonne National Laboratory, Lemont, Illinois 60439, United States;* ⓘ orcid.org/0000-0002-1812-4277

Claudio Piazzoni − *C.I. Ma.I.Na., Dipartimento di Fisica, Università degli Studi di Milano, I-20133 Milano, Italy*

Sönke Seifert − *X-ray Science Division, Argonne National Laboratory, Lemont, Illinois 60439, United States*

Vlasta Bonačić-Koutecký − *Center of Excellence for Science and Technology - Integration of Mediterranean region (STIM), Faculty of Science, University of Split, CR-21000 Split, Croatia; Interdisciplinary Center for Advanced Science and Technology (ICAST), University of Split, CR-21000 Split, Croatia; Chemistry Department, Humboldt University of Berlin, D-12489 Berlin, Germany*

Anatoly I. Frenkel − *Department of Materials Science and Chemical Engineering, Stony Brook University, Stony Brook, New York 11794, United States; Division of Chemistry, Brookhaven National Laboratory, Upton, New York 11973, United States;* ⓘ orcid.org/0000-0002-5451-1207

Complete contact information is available at:
https://pubs.acs.org/10.1021/acscatal.0c05029

Author Contributions

◆A.H., C.L., J.T., and A.M. are equally contributing (first) authors.

Notes

The authors declare no competing financial interest.

REFERENCES

(1) Aresta, M.; Dibenedetto, A.; Angelini, A. Catalysis for the Valorization of Exhaust Carbon: from CO2 to Chemicals, Materials, and Fuels Technological Use of CO2. *Chem. Rev.* **2014**, *114* (3), 1709−1742.

(2) Wei, W.; Jinlong, G. Methanation of carbon dioxide: an overview. *Front. Chem. Sci. Eng.* **2011**, *5* (1), 2−10.

(3) Ahouari, H.; Soualah, A.; Le Valant, A.; Pinard, L.; Magnoux, P.; Pouilloux, Y. Methanol synthesis from CO2 hydrogenation over copper based catalysts. *React. Kinet., Mech. Catal.* **2013**, *110* (1), 131−145.

(4) Behrens, M.; Studt, F.; Kasatkin, I.; Kühl, S.; Hävecker, M.; Abild-Pedersen, F.; Zander, S.; Girgsdies, F.; Kurr, P.; Kniep, B.-L.; Tovar, M.; Fischer, R. W.; Nørskov, J. K.; Schlögl, R. The Active Site of Methanol Synthesis over Cu/ZnO/Al₂O₃ Industrial Catalysts. *Science* **2012**, *336* (6083), 893−897.

(5) Graciani, J.; Mudiyanselage, K.; Xu, F.; Baber, A. E.; Evans, J.; Senanayake, S. D.; Stacchiola, D. J.; Liu, P.; Hrbek, J.; Sanz, J. F.; Rodriguez, J. A. Highly active copper-ceria and copper-ceria-titania catalysts for methanol synthesis from CO₂. *Science* **2014**, *345* (6196), 546−550.

(6) Waugh, K. C. Methanol Synthesis. *Catal. Today* **1992**, *15* (1), 51−75.

(7) Liu, C.; Yang, B.; Tyo, E.; Seifert, S.; DeBartolo, J.; von Issendorff, B.; Zapol, P.; Vajda, S.; Curtiss, L. A. Carbon Dioxide Conversion to Methanol over Size-Selected Cu4 Clusters at Low Pressures. *J. Am. Chem. Soc.* **2015**, *137* (27), 8676−8679.

(8) Yang, B.; Liu, C.; Halder, A.; Tyo, E. C.; Martinson, A. B. F.; Seifert, S.; Zapol, P.; Curtiss, L. A.; Vajda, S. Copper Cluster Size Effect in Methanol Synthesis from CO2. *J. Phys. Chem. C* **2017**, *121* (19), 10406−10412.

(9) Halder, A.; Kioseoglou, J.; Yang, B.; Kolipaka, K. L.; Seifert, S.; Ilavsky, J.; Pellin, M.; Sowwan, M.; Grammatikopoulos, P.; Vajda, S. Nanoassemblies of ultrasmall clusters with remarkable activity in carbon dioxide conversion into C1 fuels. *Nanoscale* **2019**, *11* (11), 4683−4687.

(10) Halder, A.; Kilianová, M.; Yang, B.; Tyo, E. C.; Seifert, S.; Prucek, R.; Panáček, A.; Suchomel, P.; Tomanec, O.; Gosztola, D. J.; Milde, D.; Wang, H.-H.; Kvítek, L.; Zbořil, R.; Vajda, S. Highly efficient Cu-decorated iron oxide nanocatalyst for low pressure CO2 conversion. *Appl. Catal., B* **2018**, *225*, 128−138.

(11) Gasser, D.; Baiker, A. Hydrogenation of carbon dioxide over copper—zirconia catalysts prepared by in-situ activation of amorphous copper—zirconium alloy. *Appl. Catal.* **1989**, *48* (2), 279−294.

(12) Koeppel, R. A.; Baiker, A.; Schild, C.; Wokaun, A., Effect of Preparation Variables on Catalytic Behaviour of Copper/Zirconia Catalysts for the Synthesis of Methanol from Carbon Dioxide. In *Stud. Surf. Sci. Catal.*; Poncelet, G., Jacobs, P. A., Grange, P., Delmon, B., Eds.; Elsevier: 1991; Vol. 63, pp 59−68.

(13) Wang, Y. H.; Gao, W. G.; Wang, H.; Zheng, Y. E.; Na, W.; Li, K. Z. Structure-activity relationships of Cu-ZrO2 catalysts for CO2 hydrogenation to methanol: interaction effects and reaction mecha-nism. *RSC Adv.* **2017**, *7* (14), 8709−8717.

(14) Samson, K.; Śliwa, M.; Socha, R. P.; Góra-Marek, K.; Mucha, D.; Rutkowska-Zbik, D.; Paul, J. F.; Ruggiero-Mikołajczyk, M.; Grabowski, R.; Słoczyński, J. Influence of ZrO2 Structure and Copper Electronic State on Activity of Cu/ZrO2 Catalysts in Methanol Synthesis from CO2. *ACS Catal.* **2014**, *4* (10), 3730−3741.

(15) Tada, S.; Watanabe, F.; Kiyota, K.; Shimoda, N.; Hayashi, R.; Takahashi, M.; Nariyuki, A.; Igarashi, A.; Satokawa, S. Ag addition to CuO-ZrO2 catalysts promotes methanol synthesis via CO2 hydrogenation. *J. Catal.* **2017**, *351*, 107−118.

(16) Tada, S.; Katagiri, A.; Kiyota, K.; Honma, T.; Kamei, H.; Nariyuki, A.; Uchida, S.; Satokawa, S. Cu Species Incorporated into Amorphous ZrO2 with High Activity and Selectivity in CO2-to-Methanol Hydrogenation. *J. Phys. Chem. C* **2018**, *122* (10), 5430−5442.

(17) Din, I. U.; Shaharun, M. S.; Naeem, A.; Tasleem, S.; Rafie Johan, M. Carbon nanofibers based copper/zirconia catalysts for carbon dioxide hydrogenation to methanol: Effect of copper concentration. *Chem. Eng. J.* **2018**, *334*, 619−629.

(18) Rungtaweevoranit, B.; Baek, J.; Araujo, J. R.; Archanjo, B. S.; Choi, K. M.; Yaghi, O. M.; Somorjai, G. A. Copper Nanocrystals Encapsulated in Zr-based Metal−Organic Frameworks for Highly Selective CO2 Hydrogenation to Methanol. *Nano Lett.* **2016**, *16* (12), 7645−7649.

(19) Riha, S. C.; Jin, S.; Baryshev, S. V.; Thimsen, E.; Wiederrecht, G. P.; Martinson, A. B. F. Stabilizing Cu2S for Photovoltaics One Atomic Layer at a Time. *ACS Appl. Mater. Interfaces* **2013**, *5* (20), 10302−10309.

(20) Borghi, F.; Sogne, E.; Lenardi, C.; Podestà, A.; Merlini, M.; Ducati, C.; Milani, P. Cluster-assembled cubic zirconia films with tunable and stable nanoscale morphology against thermal annealing. *J. Appl. Phys.* **2016**, *120* (5), 055302.

(21) Borghi, F.; Podestà, A.; Piazzoni, C.; Milani, P. Growth Mechanism of Cluster-Assembled Surfaces: From Submonolayer to Thin-Film Regime. *Phys. Rev. Appl.* **2018**, *9* (4), 044016.

(22) Galli, A.; Maffioli, E.; Sogne, E.; Moretti, S.; Di Cairano, E. S.; Negri, A.; Nonnis, S.; Norata, G. D.; Bonacina, F.; Borghi, F.; Podesta, A.; Bertuzzi, F.; Milani, P.; Lenardi, C.; Tedeschi, G.; Perego, C. Cluster-assembled zirconia substrates promote long-term differentiation and functioning of human islets of Langerhans. *Sci. Rep.* **2018**, *8* (1), 9979.

(23) Chen, H.-Y. T.; Tosoni, S.; Pacchioni, G. Hydrogen Adsorption, Dissociation, and Spillover on Ru10 Clusters Supported on Anatase TiO2 and Tetragonal ZrO2 (101) Surfaces. *ACS Catal.* **2015**, *5* (9), 5486−5495.

(24) Timoshenko, J.; Halder, A.; Yang, B.; Seifert, S.; Pellin, M. J.; Vajda, S.; Frenkel, A. I. Subnanometer Substructures in Nano-assemblies Formed from Clusters under a Reactive Atmosphere Revealed Using Machine Learning. *J. Phys. Chem. C* **2018**, *122* (37), 21686−21693.

(25) Tyo, E. C.; Vajda, S. Catalysis by clusters with precise numbers of atoms. *Nat. Nanotechnol.* **2015**, *10*, 577.

(26) Veselovskaya, J. V.; Parunin, P. D.; Okunev, A. G. Catalytic process for methane production from atmospheric carbon dioxide utilizing Renew Energy. *Catal. Today* **2017**, *298*, 117−123.

(27) Al-Swai, B. M.; Osman, N. B.; Abdullah, B. Catalytic performance of Ni/MgO catalyst in methane dry reforming. *AIP Conf. Proc.* **2017**, *1891* (1), 020028.

(28) Themelis, N. J.; Ulloa, P. A. Methane generation in landfills. *Renewable Energy* **2007**, *32* (7), 1243−1257.

(29) Klassen, V.; Blifernez-Klassen, O.; Wibberg, D.; Winkler, A.; Kalinowski, J.; Posten, C.; Kruse, O. Highly efficient methane generation from untreated microalgae biomass. *Biotechnol. Biofuels* **2017**, *10* (1), 186.

(30) Fuertez, J.; Nguyen, V.; McLennan, J. D.; Adams, D. J.; Han, K.-B.; Sparks, T. D. Optimization of biogenic methane production from coal. *Int. J. Coal Geol.* **2017**, *183*, 14−24.

(31) Ahlberg-Eliasson, K.; Nadeau, E.; Levén, L.; Schnürer, A. Production efficiency of Swedish farm-scale biogas plants. *Biomass Bioenergy* **2017**, *97*, 27−37.

(32) Borole, A. P.; Klasson, K. T.; Ridenour, W.; Holland, J.; Karim, K.; Al-Dahhan, M. H. Methane Production in a 100-L Upflow Bioreactor by Anaerobic Digestion of Farm Waste. In *Twenty-Seventh Symposium on Biotechnology for Fuels and Chemicals*; McMillan, J. D.,

Adney, W. S., Mielenz, J. R., Klasson, K. T., Eds.; Humana Press: Totowa, NJ, 2006; pp 887−896.

(33) Wegner, K.; Piseri, P.; Tafreshi, H. V.; Milani, P. Cluster beam deposition: a tool for nanoscale science and technology. *J. Phys. D: Appl. Phys.* **2006**, *39* (22), R439−R459.

(34) Yin, C.; Tyo, E.; Kuchta, K.; von Issendorff, B.; Vajda, S. Atomically precise (catalytic) particles synthesized by a novel cluster deposition instrument. *J. Chem. Phys.* **2014**, *140* (17), 174201.

(35) Lee, S.; Lee, B.; Seifert, S.; Vajda, S.; Winans, R. E. Simultaneous measurement of X-ray small angle scattering, absorption and reactivity: A continuous flow catalysis reactor. *Nucl. Instrum. Methods Phys. Res., Sect. A* **2011**, *649* (1), 200−203.

(36) Lei, Y.; Mehmood, F.; Lee, S.; Greeley, J.; Lee, B.; Seifert, S.; Winans, R. E.; Elam, J. W.; Meyer, R. J.; Redfern, P. C.; Teschner, D.; Schlögl, R.; Pellin, M. J.; Curtiss, L. A.; Vajda, S. Increased Silver Activity for Direct Propylene Epoxidation via Subnanometer Size Effects. *Science* **2010**, *328* (5975), 224−228.

(37) Martini, A.; Borfecchia, E. Spectral Decomposition of X-ray Absorption Spectroscopy Datasets: Methods and Applications. *Crystals* **2020**, *10* (8), 664.

(38) Lee, B.; Seifert, S.; Riley, S. J.; Tikhonov, G.; Tomczyk, N. A.; Vajda, S.; Winans, R. E. Anomalous grazing incidence small-angle x-ray scattering studies of platinum nanoparticles formed by cluster deposition. *J. Chem. Phys.* **2005**, *123* (7), 074701.

(39) Keshari, A. K.; Pandey, A. C. Size and Distribution: A Comparison of XRD, SAXS and SANS Study of II–VI Semiconductor Nanocrystals. *J. Nanosci. Nanotechnol.* **2008**, *8* (3), 1221−1227.

(40) Wyrzgol, S. A.; Schafer, S.; Lee, S.; Lee, B.; Vece, M. D.; Li, X.; Seifert, S.; Winans, R. E.; Stutzmann, M.; Lercher, J. A.; Vajda, S. Combined TPRx, in situ GISAXS and GIXAS studies of model semiconductor-supported platinum catalysts in the hydrogenation of ethene. *Phys. Chem. Chem. Phys.* **2010**, *12* (21), 5585−5595.

(41) Ilavsky, J.; Jemian, P. R. Irena: tool suite for modeling and analysis of small-angle scattering. *J. Appl. Crystallogr.* **2009**, *42* (2), 347−353.

(42) Passalacqua, R.; Parathoner, S.; Centi, G.; Halder, A.; Tyo, E. C.; Yang, B.; Seifert, S.; Vajda, S. Electrochemical behaviour of naked sub-nanometre sized copper clusters and effect of CO2. *Catal. Sci. Technol.* **2016**, *6* (18), 6977−6985.

(43) Alayon, E. M. C.; Nachtegaal, M.; Bodi, A.; van Bokhoven, J. A. Reaction Conditions of Methane-to-Methanol Conversion Affect the Structure of Active Copper Sites. *ACS Catal.* **2014**, *4* (1), 16−22.

(44) Felten, J.; Hall, H.; Jaumot, J.; Tauler, R.; de Juan, A.; Gorzsás, A. Vibrational spectroscopic image analysis of biological material using multivariate curve resolution−alternating least squares (MCR-ALS). *Nat. Protoc.* **2015**, *10* (2), 217−240.

(45) Ruckebusch, C.; Blanchet, L. Multivariate curve resolution: a review of advanced and tailored applications and challenges. *Anal. Chim. Acta* **2013**, *765*, 28−36.

(46) Cassinelli, W. H.; Martins, L.; Passos, A. R.; Pulcinelli, S. H.; Santilli, C. V.; Rochet, A.; Briois, V. Multivariate curve resolution analysis applied to time-resolved synchrotron X-ray Absorption Spectroscopy monitoring of the activation of copper alumina catalyst. *Catal. Today* **2014**, *229*, 114−122.

(47) Voronov, A.; Urakawa, A.; Beek, W. v.; Tsakoumis, N. E.; Emerich, H.; Rønning, M. Multivariate curve resolution applied to in situ X-ray absorption spectroscopy data: An efficient tool for data processing and analysis. *Anal. Chim. Acta* **2014**, *840*, 20−27.

(48) Nayak, C.; Bhattacharyya, D.; Jha, S. N.; Sahoo, N. K. In Situ XAS Study on Growth of PVP-Stabilized Cu Nanoparticles. *ChemistrySelect* **2018**, *3* (25), 7370−7377.

(49) Frenkel, A. I.; Kleifeld, O.; Wasserman, S. R.; Sagi, I. Phase speciation by extended x-ray absorption fine structure spectroscopy. *J. Chem. Phys.* **2002**, *116* (21), 9449−9456.

(50) Wang, X.; Hanson, J. C.; Frenkel, A. I.; Kim, J.-Y.; Rodriguez, J. A. Time-resolved Studies for the Mechanism of Reduction of Copper Oxides with Carbon Monoxide: Complex Behavior of Lattice Oxygen

and the Formation of Suboxides. *J. Phys. Chem. B* **2004**, *108* (36), 13667−13673.

(51) Wang, Q.; Hanson, J. C.; Frenkel, A. I. Solving the structure of reaction intermediates by time-resolved synchrotron x-ray absorption spectroscopy. *J. Chem. Phys.* **2008**, *129* (23), 234502.

(52) Nong, S.; Dong, W.; Xiao, Y.; Riaz, M. S.; Dong, C.; Zhao, Y.; Liu, Z.; Wang, R.; Huang, F. Highly Hydroxylated Porous Nanozirconia for Complete Trace Cr(VI) Removal. *ACS Appl. Nano Mater.* **2020**, *3* (4), 3315−3322.

(53) Scotti, N.; Bossola, F.; Zaccheria, F.; Ravasio, N. Copper−Zirconia Catalysts: Powerful Multifunctional Catalytic Tools to Approach Sustainable Processes. *Catalysts* **2020**, *10* (2), 168.

(54) Pauly, N.; Tougaard, S.; Yubero, F. Determination of the Cu 2p primary excitation spectra for Cu, Cu2O and CuO. *Surf. Sci.* **2014**, *620*, 17−22.

(55) Timoshenko, J.; Lu, D.; Lin, Y.; Frenkel, A. I. Supervised Machine-Learning-Based Determination of Three-Dimensional Structure of Metallic Nanoparticles. *J. Phys. Chem. Lett.* **2017**, *8* (20), 5091−5098.

(56) Weatherbee, G. D.; Bartholomew, C. H. Hydrogenation of CO2 on group VIII metals: I Specific activity of NiSiO2. *J. Catal.* **1981**, *68* (1), 67−76.

(57) Chang, F.-W.; Hsiao, T.-J.; Shih, J.-D. Hydrogenation of CO2 over a Rice Husk Ash Supported Nickel Catalyst Prepared by Deposition−Precipitation. *Ind. Eng. Chem. Res.* **1998**, *37* (10), 3838−3845.

(58) Chang, F.-W.; Tsay, M.-T.; Liang, S.-P. Hydrogenation of CO2 over nickel catalysts supported on rice husk ash prepared by ion exchange. *Appl. Catal., A* **2001**, *209* (1), 217−227.

(59) Bebelis, S.; Karasali, H.; Vayenas, C. G. Electrochemical promotion of CO2 hydrogenation on Rh/YSZ electrodes. *J. Appl. Electrochem.* **2008**, *38* (8), 1127−1133.

(60) Papaioannou, E. I.; Souentie, S.; Hammad, A.; Vayenas, C. G. Electrochemical promotion of the CO2 hydrogenation reaction using thin Rh, Pt and Cu films in a monolithic reactor at atmospheric pressure. *Catal. Today* **2009**, *146* (3), 336−344.

(61) Peebles, D. E.; Goodman, D. W.; White, J. M. Methanation of carbon dioxide on nickel(100) and the effects of surface modifiers. *J. Phys. Chem.* **1983**, *87* (22), 4378−4387.

(62) Yang, B.; Yu, X.; Halder, A.; Zhang, X.; Zhou, X.; Mannie, G. J. A.; Tyo, E.; Pellin, M. J.; Seifert, S.; Su, D.; Vajda, S. Dynamic Interplay between Copper Tetramers and Iron Oxide Boosting CO2 Conversion to Methanol and Hydrocarbons under Mild Conditions. *ACS Sustainable Chem. Eng.* **2019**, *7* (17), 14435−14442.

(63) Nößler, M.; Mitrić, R.; Bonačić-Koutecký, V. Binary Neutral Metal Oxide Clusters with Oxygen Radical Centers for Catalytic Oxidation Reactions: From Cluster Models Toward Surfaces. *J. Phys. Chem. C* **2012**, *116* (21), 11570−11574.

(64) Becke, A. D. Density-functional exchange-energy approximation with correct asymptotic behavior. *Phys. Rev. A: At., Mol., Opt. Phys.* **1988**, *38* (6), 3098−3100.

(65) Becke, A. D. Density-functional thermochemistry III The role of exact exchange. *J. Chem. Phys.* **1993**, *98* (7), 5648−5652.

(66) Lee, C.; Yang, W.; Parr, R. G. Development of the Colle-Salvetti correlation-energy formula into a functional of the electron density. *Phys. Rev. B: Condens. Matter Mater. Phys.* **1988**, *37* (2), 785−789.

(67) Schäfer, A.; Huber, C.; Ahlrichs, R. Fully optimized contracted Gaussian basis sets of triple zeta valence quality for atoms Li to Kr. *J. Chem. Phys.* **1994**, *100* (8), 5829−5835.

(68) Eichkorn, K.; Weigend, F.; Treutler, O.; Ahlrichs, R. Auxiliary basis sets for main row atoms and transition metals and their use to approximate Coulomb potentials. *Theor. Chem. Acc.* **1997**, *97* (1), 119−124.

(69) Andrae, D.; Häußermann, U.; Dolg, M.; Stoll, H.; Preuß, H. Energy-adjustedab initio pseudopotentials for the second and third row transition elements. *Theor. Chim. Acta* **1990**, *77* (2), 123−141.

(70) Frisch, M. J.; et al. *Gaussian 16*, revision C.01; Gaussian Inc.: Wallingford, CT, 2016.

4.2   Supported bimetallic nanocluster

Antonija Mravak, Stefan Vajda, and Vlasta Bonačić-Koutecký. Mechanism of catalytic CO_2 hydrogenation to methane and methanol using a bimetallic Cu_3Pd cluster at a zirconia support. *J. Phys Chem. C*, 126(43), 2022, 18306-18312.
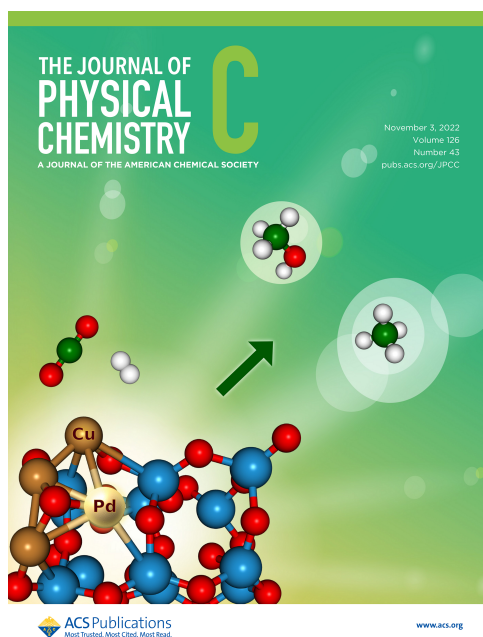

Figure 4.2: Supplementary cover page of *J. Phys. Chem. C* [144] featuring bimetallic Pd-doped Cu-cluster at zirconia support for CO_2 conversion into methane and methanol.

Article

Mechanism of Catalytic CO_2 Hydrogenation to Methane and Methanol Using a Bimetallic Cu_3Pd Cluster at a Zirconia Support

Antonija Mravak, Stefan Vajda,* and Vlasta Bonačić-Koutecký*

Read Online

ACCESS | Metrics & More | Article Recommendations | Supporting Information

ABSTRACT: For very small nanocluster-based catalysts, the exploration of the influence of the particle size, composition, and support offers precisely variable parameters in a wide material search space to control catalysts' performance. We present the mechanism of the CO_2 methanation reaction on the oxidized bimetallic Cu_3Pd tetramer (Cu_3PdO_2) supported on a zirconia model support represented by $Zr_{12}O_{24}$ based on the energy profile obtained from density functional theory calculations on the reaction of CO_2 and H_2. In order to determine the role of the Pd atom, the performance of Cu_3PdO_2 with monometallic Cu_4O_2 at the same support has been compared. Parallel to methane formation, the alternative path of methanol formation at this catalyst has also been investigated. The results show that the exchange of a single atom in Cu_4 with a single Pd atom improves catalyst/s performance via lowering the barriers associated with hydrogen dissociation steps that occur on the Pd atom. The above-mentioned results suggest that the doping strategy at the level of single atoms can offer a precise control knob for designing new catalysts with desired performance.

Bimetallic catalyst for CO_2 conversion
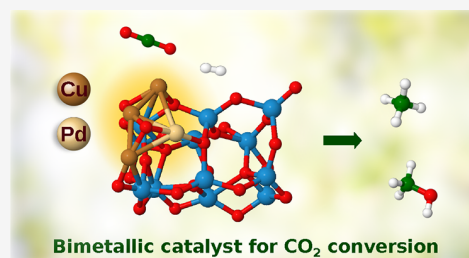
INTRODUCTION

The capture of CO_2 and its catalytic conversion to hydrocarbons, alcohols, and various hydrocarbon derivatives have been of large interest, as an attractive solution for addressing environmental issues by the production of value-added chemicals and fuels. Multiple studies have been reported on the promising performance of copper-based bulk and nanoscale catalysts.[1−13] Recently, catalysts based on small size-selected subnanometer copper clusters and their nanoscale assemblies have been explored extensively both experimentally and theoretically in the conversion of CO_2 into various products, such as methane and methanol.[14−18] Also, the studies should be mentioned which yield other important products such as a diesel fuel surrogate dimethyl ether,[19,20] including catalysts with the copper content. The latter boosts catalyst performance and selectivity toward dimethyl ether.

In order to expand the material search space, cluster-based catalysts allow us to examine the effect of catalytic moiety's size on performance and influence of the composition of the cluster and of the support. In their size and composition, well-defined clusters anchored to the model of a support oxide can be treated by density functional theory (DFT) to gain basic understanding of the function of the catalytic site and the mechanism of the reaction which can ultimately initiate new focused experiments guided by predictions to take various paths. In a joint theoretical and experimental study, we have recently found that subnanometer copper tetramers supported by zirconia are highly efficient for CO_2 hydrogenation and its conversion to methane at high temperature, where catalytic performance was dependent on the cluster size and substrate

morphology. DFT simulations on the Cu_4O_2 cluster supported by the $Zr_{12}O_{24}$ subunit ($Cu_4O_2/Zr_{12}O_{24}$) provided a mechanism for CO_2 hydrogenation along the way to conversion to methane, confirming the experimental findings but identifying also methanol formation. These results stimulated us to investigate the possible effect of exchanging a single Cu atom in the cluster with a Pd atom in the tetramer, on the example of Cu_3PdO_2 at $Zr_{12}O_{24}$, on altering performance. In addition to the generally expected effect of an ad-/dopant atom on the electronic structure of the cluster, Pd was chosen also due its well-known role in activation and dissociation of H_2. In other words, the aim of the present study is to optimize the catalytic performance of these copper-based tetramers in CO_2 hydrogenation, by leveraging the proven potential of palladium in the efficient activation of molecular hydrogen, thus providing a control knob on the atomic scale to fine-tune catalyst performance in an atom-by-atom doping fashion. It is to be noted that partially oxidized tetramers were taken into account, based on the reported oxidation states of copper and palladium in mono- and bimetallic clusters studied in situ on the same or similar cluster-based catalysts in
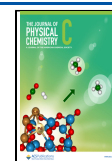
compatible hydrogenation and dehydrogenation reactions.[14−16,18,21−27]

Here, we will first present the mechanism and energy profile of the CO_2 methanation reaction on the bimetallic tetramer (Cu_3PdO_2) at the model zirconia support represented by $Zr_{12}O_{24}$. We will also compare the predicted performance of this mixed tetramer with that of the monometallic Cu_4O_2 cluster at the same support. In addition, we will carry out a parallel investigation of methanol formation on these catalysts, the other major hydrogenation route. This set of exploratory calculations is to support the main hypothesis of this study, namely, to find hints about how a modification of the composition of the catalyst by an exchange of a single metal atom in it shows sufficient advantages in comparison to a monometallic cluster. In this context, detailed comparative investigations of the dominant reaction pathways are being executed as prerequisites for predicting the functioning of the chosen model catalysts that will ultimately lead to computational design of catalysts performing on demand.

COMPUTATIONAL METHODS

All the reactive species on the supported bimetallic cluster were optimized employing DFT theory using the Gaussian 16 software package.[28] Calculations of the doublet ground-state structures were performed with the Becke-3-parameter-Lee-Yang-Parr (B3LYP) hybrid functional[29−31] and triple-zeta-valence-plus-polarization (TZVP) basis set[32] for all atoms. In addition, Stuttgart relativistic core potential (ECP)[33] has been used for palladium and zirconium atoms. Structural and electronic properties of both monometallic and bimetallic transition metal clusters can be influenced by dispersion forces.[34] Hence, the Grimme-D3 dispersion correction[35] (GD3) was included to account for the effect of van der Waals (vdW) interactions on the structure and stability of reactive species. To compare energy profiles at bimetallic Cu_3PdO_2 and metallic cluster Cu_4O_2 at the ZrO_2 model support, previous results on the methanation reaction at the supported metallic oxide[18] were recalculated with the addition of the GD3 dispersion. The DFT-computed corrections of relative energies of minima and transition states have been obtained based on Gibbs free energies at 298.15 K and 1 atm as shown in Tables S1 and S2. Activation energies have not been considerably influenced, but relative Gibbs free energies have increased by 0.5−1.5 eV.

RESULTS AND DISCUSSION

In this contribution, we first address structural properties of $Cu_3PdO_2/Zr_{12}O_{24}$ in comparison with those of $Cu_4O_2/Zr_{12}O_{24}$ and then attend the reaction pathways for methane and methanol formation, with the goal to determine the role of a single Pd atom and the mechanism involving four necessary hydrogenation steps. In addition, the comparison of results between the monometallic and the bimetallic clusters at the support is of importance because optimization of the composition of the metallic tetramer can be used to improve the performance of the catalyst.

Modeling of the Structural Properties. A model for the bimetallic Cu_3PdO_2 cluster at the support has been investigated by alternatively replacing one by one each of the Cu atoms of the copper tetramer by a Pd atom in a monometallic Cu_4O_2 cluster at the metal oxide support represented by $Zr_{12}O_{24}$ (Figure S1a). Notice that small clusters

do not have rigid structures; they can undergo restructuring along the reaction path. Structural fluxionality depends on cluster size, composition, and reaction conditions, as discussed, for example, in the case of copper and palladium clusters of similar size.[24] In our study, the cluster structures are relaxed for every step along the reaction pathway; thus, restructuring/fluxionality is implicitly addressed.

The model for the support $Zr_{12}O_{24}$ has been selected based on previous reactivity studies on the Zr oxide.[36] The lowest energy structure for $Cu_3PdO_2/Zr_{12}O_{24}$ includes the Cu_3Pd tetramer built from CuPd and Cu_2 units which are bound to Zr and O atoms of the support (Figure 1a). This allows the simultaneous formation of the reactive center and connection with the support.
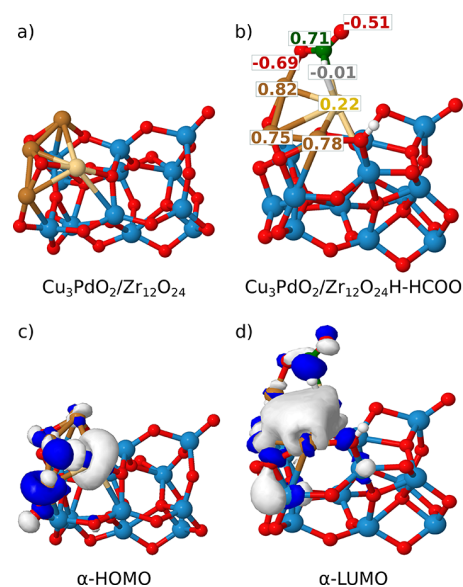
Figure 1. DFT-determined structures for (a) $Cu_3PdO_2/Zr_{12}O_{24}$ and (b) representing binding of structure (a) with CO_2 and H_2 forming $Cu_3PdO_2/Zr_{12}O_{24}H−HCOO$. Values of natural charges are shown in the context of charge transfer within $Cu_3Pd−HCOO$. (c) α-HOMO orbital demonstrating electron delocalization within the oxidized Cu_3Pd cluster. (d) α-LUMO of the structure (b) illustrating electron delocalization within the reactive center $Cu_3PdO_2/Zr_4O_5−HCOO$. Cu, Pd, O, C, H, and Zr atoms are depicted by brown, yellow, red, green, white, and blue spheres, respectively.

The preferential site for CO_2 binding has been identified at the Cu atom (see isomers in Figure S1b), which was also confirmed by DFT molecular dynamics (DFT-MD) simulations at T = 573.15 K (cf. Figure S2). This temperature was chosen since it is slightly higher than 548.15 K, which is the temperature of CO_2 activation at zirconia-supported Cu_4.[18] Based on natural charge analysis, Pd and Cu atoms have positive values, indicating that the Cu_3Pd cluster is oxidized (Figure 1b). The natural charges of 0.22 for Pd and ∼0.8 for Cu atoms reveal polarization of the bimetallic cluster arising from the difference in electronegativity of the Cu and Pd atom (1.9 for Cu vs 2.2 for the Pd atom). The first step of the methanation reaction includes CO_2 activation accompanied by structural adjustment and charge transfer to the CO_2 molecule forming highly reactive CO_2^-.[37] To support these findings, we have examined the charge transfer to adsorbed CO_2 of the structure $Cu_3PdO_2/Zr_{12}O_{24}H−HCOO$ (cf. Figure 1b) and compared it with that of the complementary monometallic
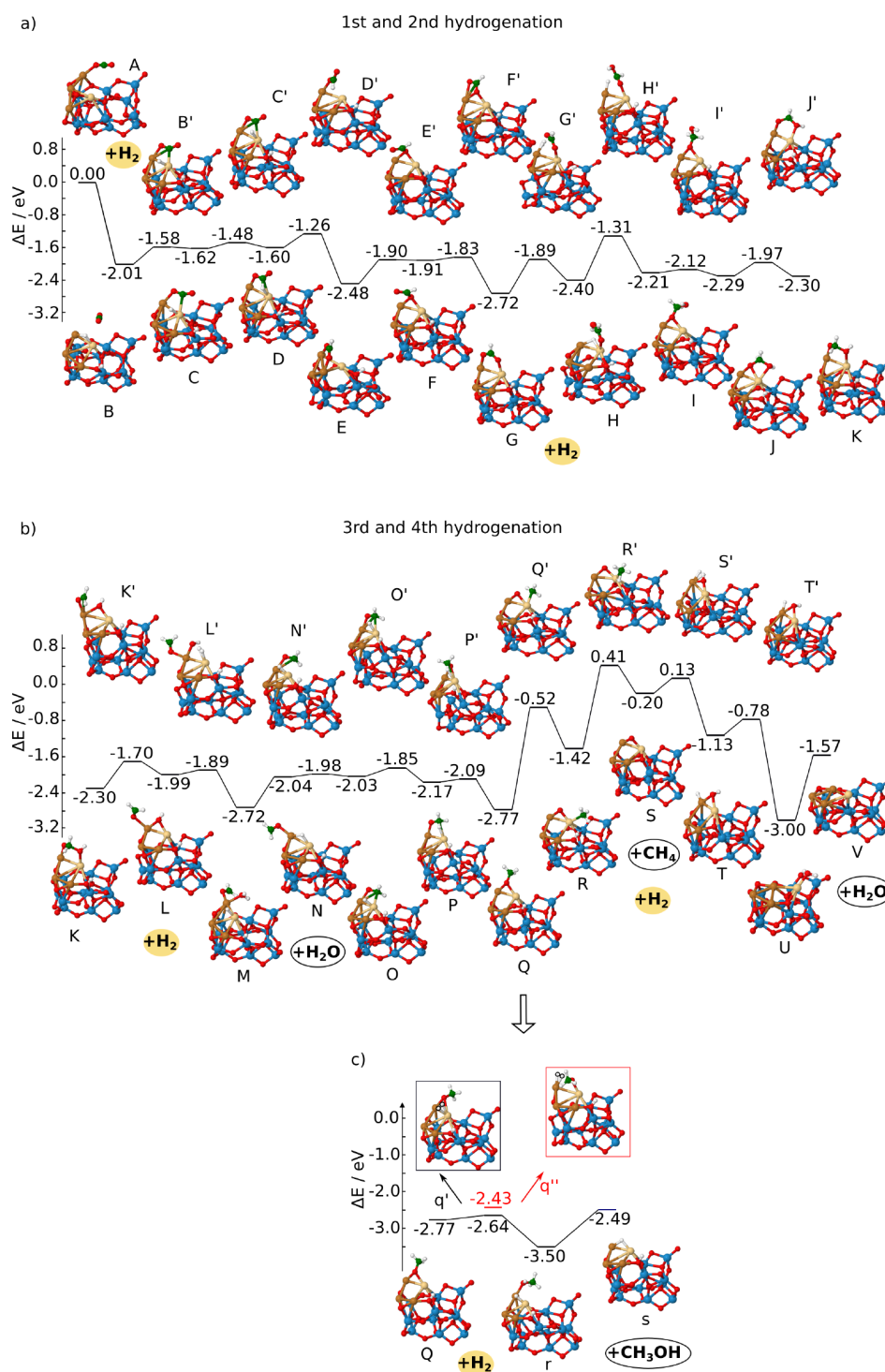
Figure 2. DFT-calculated energy profiles for the CO_2 hydrogenation reaction on the Cu_3PdO_2 cluster supported by $Zr_{12}O_{24}$ including four hydrogenation steps for methane formation in 2(a,b) [first step (A−G), second step (G−L), third (L−S), and fourth (S−V)]. The methanol energy profile is shown in (c). The letters label minima, and letters with primes label transition states.

cluster/support. The electron gain is smaller on the bimetallic (−0.49) versus monometallic oxide cluster at the support (−0.68) confirming gas-phase results from the literature.[38] In addition, the analysis of bond lengths for Pd−C (2.5 Å) versus Cu−C (2.3 Å) supports the fact that higher charge transfer to bound CO_2 occurs within the monometallic than in the bimetallic case (cf. Figure S3).

The highest occupied α molecular orbital (α-HOMO) of $Cu_3PdO_2/Zr_{12}O_{24}$ shows electron delocalization at the oxidized Cu_3Pd cluster (Figure 1c). In order to illustrate charge distribution after H−HCOO binding (Figure 1d), we also demonstrate the lowest unoccupied α molecular orbital (α-LUMO) for the structure from Figure 1b. The electron delocalization is present within −HCOO attached to the cluster and the subunit of the support.

A comparison of structural properties between the bimetallic and monometallic cluster at the support illustrates bond length changes within bonding of Pd with O and Zr, and difference in distortion between Cu_3Pd and Cu_4 is also present (cf. Figure S3). The latter may play a central role in exploiting structural changes in the catalytic moiety by the morphology of the underlying support, for example, in structure-sensitive reactions.[4,39−44]

Altogether, described structural properties illustrate the starting point of the reaction pathway including Cu_3PdO_2 at the model of the surface interacting with CO_2 and H_2.

Mechanism of Methane Formation. Conversion of CO_2 to methane by the bimetallic Cu_3PdO_2 cluster at the support involves four hydrogenation steps for which the DFT-calculated energy profile is shown in Figure 2 and in Scheme 1. Analysis of the energy profile provides the mechanism for the methanation reaction.

Scheme 1. Reaction Pathway of CO_2 Hydrogenation at $Cu_3PdO_2/Zr_{12}O_{24}$ Following Figure 2 According to Steps (A−Q), Where Q Is Branching to V and to s[a]
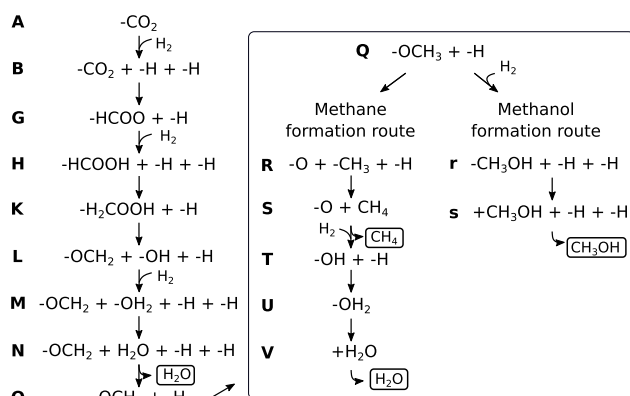
[a]"-" is the symbol for adsorbed species.

At the starting point of the reaction, CO_2 is bound to the Cu atom according to the results of the search for the lowest energy structure. Parallel to the previous investigation of the methanation reaction on monometallic Cu_4O_2 at the support,[18] the formate pathway has been chosen. Therefore, the first hydrogenation step on bimetallic Cu_3PdO_2 at the support shows the formation of −HCOO bound to Cu and Pd atoms. Notice that in order to reach minimum D, which has been addressed in the context of structural properties previously (Figure 1b), relatively small barriers have to be overcome (0.43 and 0.14 eV) between B and D minima. The other steps (E−G) are responsible for additional stabilization of −HCOO. Altogether, the first step is exothermic by −0.71 eV (B → G).

Within the second hydrogenation step, −HCOOH and −H_2COOH species are formed involving two barriers of 0.83 eV (G') and 1.09 eV (H'). After stabilization (Figure 2K), −H_2COOH decomposes into formaldehyde (−OCH_2) bound to the Cu atom and hydroxyl (−OH) bound to both Cu and Pd atoms (Figure 2L), overcoming a barrier of 0.6 eV. The mechanism within the second hydrogenation step requires bond breaking resulting in an endothermic pathway (G → L) by 0.73 eV. We investigate also whether the other branches can lower the barriers within the part of the second step. In fact, as shown in Figure S4, hydrogenation at the Pd atom lowers the

barriers to 0.34 (e') and 0.99 eV (f'). These results show that the hydrogenation at the Pd atom can be energetically favorable, suggesting a new role of the Pd atom.

The first H_2O molecule is produced within the third step of hydrogenation overcoming a small activation energy of 0.1 eV. After desorption of H_2O, the methoxy (−OCH_3) is created over three steps with barriers of 0.06, 0.18, and 0.08 eV (Figure 2N′−P′). The two barriers corresponding to 2.25 (Figure 2Q′) and 1.83 eV (Figure 2R′) are responsible for breaking the O−CH_3 bond and formation of the methane, respectively. Therefore, the third hydrogenation step is endothermic by 1.79 eV (L → S).

The last hydrogenation step includes the formation of the second H_2O molecule over barriers of 0.33 eV (S') and 0.35 eV (T'), which is exothermic by −1.37 eV (S → V).

In addition, we investigated within the fourth step of the methanation reaction the two more branches. They involve (I) removal of the second water molecule before methane formation (Figure S5) and (II) the fourth hydrogenation taking place at the Pd atom with the aim to determine its role (Figure S6).

The branch (I) was examined to verify if there is an energetically more favorable route for the fourth hydrogenation step. The barrier of 0.37 eV ($\overline{r}'$) has to be overcome for the creation of −OH via hydrogenation at the Cu site. Although a similar barrier value has been found for S′ (Figure 2), the two higher stabilization steps within the branch (I) are present ($\overline{s}$, −2.57 eV and $\overline{u}$, −2.87 eV). The barrier between $\overline{s}$ and $\overline{u}$ is larger ($\overline{s}'$, 1.07 eV), but it is energetically compensated for due to the binding of −CH_3 to both Cu and Pd ($\overline{u}$). Despite the large barrier necessary for the formation of CH_4 ($\overline{u}'$), there is sufficient energy available for this endothermic pathway in comparison to that in R′ (cf. Figure 2). Moreover, the branch (I) is energetically accessible and lies below the starting point of the reaction.

The branch (II) serves to examine the energy profile for the pathway using the advantage of binding H_2 at the Pd atom. In fact, starting from the structure S of Figure 2, removal of H_2O is energetically favorable proving an important role of the Pd atom, which involves dissociation of H_2 and stabilization of intermediate steps (cf. u and v of Figure S6).

In summary, only CuPd actively participates in hydrogenation steps. Hydrogen dissociation seems to be well promoted by the Pd atom since it reduces corresponding barriers. Altogether, the mechanism of the CO_2 methanation reaction within four hydrogenation steps involves the formation of −HCOO, −HCOOH, and −H_2COOH intermediate steps. In order to produce CH_4 and H_2O, the breaking of the −H_2COOH into −OCH_2 and OH and of O−CH_3 into O and −CH_3 take place. The latter one is the rate-determining step for the methanation reaction along investigated pathways.

In addition to the formate, we have also considered a reverse water−gas shift reaction (rWGS) pathway, as shown in Figure S7. The route proceeds over the transition state for −COOH formation with a barrier of 1.15 eV and lies below the starting point of the reaction. However, the calculation of the transition state for −OCH formation along this route requires 1.97 eV and is energetically demanding. Overall, the rWGS pathway includes higher energies compared to the formate route.

Mechanism of Methanol Formation. Hydrogenation of methoxy species, which is bound over oxygen to Cu and Pd atoms, yields Cu−CH_3OH (Figure 2c). The transition state can proceed over adsorbed H_2 to either Cu or to the Pd side of
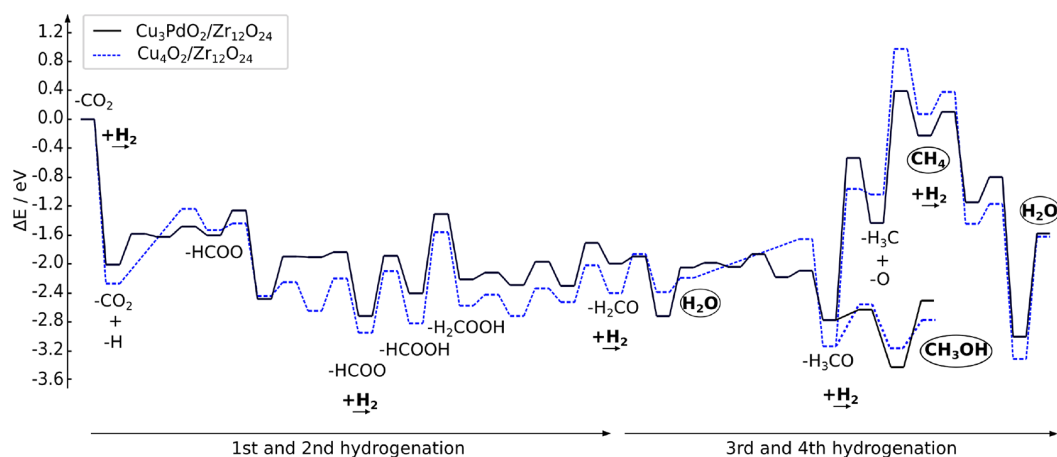
Figure 3. Comparison of DFT energy profiles for four hydrogenation steps of bimetallic Cu_3PdO_2 with the monometallic cluster Cu_4O_2 at the support $(Zr_{12}O_{24})$ involving the two pathways leading to methane and methanol formation.

the methoxy, with barriers of 0.34 and 0.13 eV, respectively. The desorption of methanol from the Cu atom is endothermic by 1.01 eV. The rate-determining step of the methanol pathway is the transition state for the formation of $-H_2COOH$. Altogether, the formation of methanol is energetically favorable on the zirconia-supported bimetallic Cu_3Pd cluster. Our simulations thus suggest an opportunity to convert CO_2 to both methane and methanol depending on the reaction temperature.

Monometallic versus Pd-Doped Bimetallic Oxidized Tetramer Clusters at the Support. Energy profiles of the monometallic and Pd-doped oxidized copper tetramer at the support are compared in Figure 3. Within the first and second hydrogenation steps, both reactions are energetically similar. The first step is exothermic by −0.68 eV for monometallic versus −0.71 eV for bimetallic. The second step is endothermic by 0.55 versus 0.73 eV. Production of the water molecule in the third hydrogenation step requires a higher barrier at Cu_4O_2 (0.54 vs 0.1 eV for bimetallic). This is due to the fact that dissociation of H_2 occurs at the Pd atom. In contrast to the single barrier for the formation of methoxy $(-OCH_3)$ at Cu_4O_2 (0.54 eV), three smaller barriers have to be overcome at the bimetallic cluster (0.06, 0.18, and 0.08 eV). Similar barriers at monometallic and bimetallic clusters are present for breaking the $O-CH_3$ bond (2.19 vs 2.25 eV) and formation of the methane (2.02 vs 1.83 eV). This step is more endothermic for Cu_4O_2 (2.5 eV vs 1.79 eV at bimetallic). The barrier for $-CH_3OH$ formation at Cu_4O_2 is 0.56 eV in comparison to smaller barriers at bimetallic species (0.13 eV at Pd or 0.34 eV at Cu). The activation energies required for the formation of second H_2O within the fourth hydrogenation step are similar (0.3 and 0.28 eV vs 0.33 and 0.35 eV). The rate-determining step for both cases is the transition state for breaking of the $O-CH_3$ bond and formation of $Cu-CH_3$ or $Pd-CH_3$. For comparison of energies, see Tables S1−S4.

Overall, the energetic pathways of CO_2 hydrogenation (Figure 3) for both mono- and bimetallic clusters at the zirconia support show that the route for methanol formation is energetically lower compared to the one for the methane formation. This is in line with the earlier theoretical and experimental findings on monometallic Cu_4 at the alumina support,[14] where the methanol was the primary product of the CO_2 hydrogenation at the lower reaction temperatures. On the other hand, methane formation required significantly higher

reaction temperatures. Furthermore, experimental investigation of CO_2 hydrogenation at the Cu cluster at the zirconia support[18] revealed that methane is the main product of the reaction, and the methanol signal was not observed at high temperatures. In this context, we conclude that methane versus methanol production is temperature-dependent, regardless of the single atom substitution of the cluster at the support.

In summary, the analysis of the HOMO, LUMO (cf. Figure S8), and charge transfer based on natural charges (Table S5) together with comparison of energy profiles shows the following trends:

  (i) In the case of the bimetallic cluster, the CuPd unit presents an interface with the support and has a key role in the hydrogenation steps.

  (ii) Hydrogenation steps on the Cu_4O_2 cluster at the support are energetically similar to those occurring at the Cu atom of Cu_3PdO_2. In contrast, the difference between the Pd-doped bimetallic and monometallic cluster is evident when dissociation of H_2 occurs due to the presence of the Pd atom.

  (iii) In both cases, the support plays the key role since the metal atoms of tetramers interact directly with Zr and O atoms of the support.

  (iv) Production of methane and methanol on both mono- and bimetallic clusters at the zirconia support is temperature-dependent.

  (v) In general, the stability of the monometallic cluster at the support is larger than that of the bimetallic one since the charge transfer (cf. Figure S9) from the cluster to the support is larger at the monometallic cluster.

In conclusion, the formate reaction pathway and the obtained mechanism for both monometallic and Pd-doped tetramers at the zirconia support allowed us to identify the synergistic role of the Pd atom in hydrogenation steps. Therefore, the incorporation of palladium in new catalysts might be advantageous, which is also beyond the reaction of interest of the present study, including other reactions where addition or removal of hydrogen takes place. The question which should be addressed in the future is whether an increased number of Pd atoms in a tetramer would improve catalytic performance.

Altogether, very small metallic clusters with extraordinary structural and electronic properties stabilized and affected by

the support and doped by other metal atoms show their potential in improving catalyst activity.

CONCLUSIONS

The aim of this study was to computationally explore new ways of tuning catalyst performance down at the atomic level by high-level control of the composition of the catalytic moiety, on the case study of the monometallic copper tetramer and its modification with one of the copper atoms exchanged for a palladium atom yielding the Cu_3Pd bimetallic cluster. Overall, the results show (i) the central role of the CuPd unit in reaction steps; (ii) the influence of the Pd atom on the hydrogenation steps in which it directly participates, demonstrated by lowering the energy barriers along the reaction coordinate; (iii) the key role of the support due to interaction of the tetramers with Zr and O atoms by charge transfer and its redistribution within the different metal atoms in the clusters; (iv) the finding that production of methanol and methane can be influenced by the choice of temperature, and this is independent from the Pd atom substitution; and (v) higher stability of the monometallic than that of the bimetallic cluster evidenced by the larger charge transfer from the cluster to the support. Finally, we conclude that atomic-level doping energetically lowers hydrogenation steps, offering a potential to tailor performance of the catalyst.

ASSOCIATED CONTENT

Ⓢ Supporting Information

The Supporting Information is available free of charge at https://pubs.acs.org/doi/10.1021/acs.jpcc.2c04921.

Tables with values of relative electronic and Gibbs free energies for hydrogenation steps at the bimetallic/ support; tables with values of relative electronic energies for hydrogenation steps at the monometallic cluster/ support; DFT-calculated isomers of the catalytic complex; results of the DFT-MD calculations of CO_2 binding to the bimetallic/support; comparison of chosen bond lengths; alternative branch for the second hydrogenation step; branches of the energy profile for the methane formation within the fourth hydrogenation step; rWGS pathway at the bimetallic cluster/support; orbitals of selected reaction species; table with charge transfer at the Cu or Pd atom associated with hydrogenation steps for both the bimetallic and monometallic cluster/support; and analysis of natural charges for the bimetallic and monometallic cluster/ support (PDF)

AUTHOR INFORMATION

Corresponding Authors

Stefan Vajda − *Department of Nanocatalysis, Czech Academy of Sciences, J. Heyrovský Institute of Physical Chemistry, Prague 8 18223, Czech Republic;* ⓞ orcid.org/0000-0002-1879-2099; Email: stefan.vajda@jh-inst.cas.cz

Vlasta Bonačić-Koutecký − *Center of Excellence for Science and Technology—Integration of Mediterranean Region (STIM), Faculty of Science, University of Split, Split 21000, Croatia; Interdisciplinary Center for Advanced Science and Technology (ICAST) at University of Split, Split 21000, Croatia; Chemistry Department, Humboldt University of Berlin, Berlin 12489, Germany;* ⓞ orcid.org/0000-0001-6142-5932; Email: vbk@cms.hu-berlin.de

Author

Antonija Mravak − *Center of Excellence for Science and Technology—Integration of Mediterranean Region (STIM), Faculty of Science, University of Split, Split 21000, Croatia;* ⓞ orcid.org/0000-0002-1252-7390

Complete contact information is available at:
https://pubs.acs.org/10.1021/acs.jpcc.2c04921

Notes

The authors declare no competing financial interest.

ACKNOWLEDGMENTS

REFERENCES

(1) Olah, G. A. Beyond Oil and Gas: The Methanol Economy. *Angew. Chem., Int. Ed.* **2005**, *44*, 2636−2639.

(2) Centi, G.; Perathoner, S. Opportunities and Prospects in the Chemical Recycling of Carbon Dioxide to Fuels. *Catal. Today* **2009**, *148*, 191−205.

(3) Peters, M.; Köhler, B.; Kuckshinrichs, W.; Leitner, W.; Markewitz, P.; Müller, T. E. Chemical Technologies for Exploiting and Recycling Carbon Dioxide into the Value Chain. *ChemSusChem* **2011**, *4*, 1216−1240.

(4) Behrens, M.; Studt, F.; Kasatkin, I.; Kühl, S.; Hävecker, M.; Abild-Pedersen, F.; Zander, S.; Girgsdies, F.; Kurr, P.; Kniep, P.; et al. The Active Site of Methanol Synthesis over $Cu/ZnO/Al_2O_3$ Industrial Catalysts. *Science* **2012**, *336*, 893−897.

(5) Mac Dowell, N.; Fennell, P. S.; Shah, N.; Maitland, G. C. The Role of CO_2 Capture and Utilization in Mitigating Climate Change. *Nat. Clim. Change* **2017**, *7*, 243−249.

(6) Choi, Y. H.; Jang, Y. J.; Park, H.; Kim, W. Y.; Lee, Y. H.; Choi, S. H.; Lee, J. S. Carbon Dioxide Fischer-Tropsch Synthesis: A New Path to Carbon-Neutral Fuels. *Appl. Catal., B* **2017**, *202*, 605−610.

(7) Roy, S.; Cherevotan, A.; Peter, S. C. Thermochemical CO_2 Hydrogenation to Single Carbon Products: Scientific and Technological Challenges. *ACS Energy Lett.* **2018**, *3*, 1938−1966.

(8) Palomino, R. M.; Ramírez, P. J.; Liu, Z.; Hamlyn, R.; Waluyo, I.; Mahapatra, M.; Orozco, I.; Hunt, A.; Simonovis, J. P.; Senanayake, S. D.; et al. Hydrogenation of CO_2 on ZnO/Cu (100) and ZnO/Cu (111) Catalysts: Role of Copper Structure and Metal−Oxide Interface in Methanol Synthesis. *J. Phys. Chem. B* **2018**, *122*, 794−800.

(9) Halder, A.; Kilianová, M.; Yang, B.; Tyo, E. C.; Seifert, S.; Prucek, R.; Panáček, A.; Suchomel, P.; Tomanec, O.; Gosztola, D. J.; et al. Highly Efficient Cu-Decorated Iron Oxide Nanocatalyst for Low Pressure CO_2 Conversion. *Appl. Catal., B* **2018**, *225*, 128−138.

(10) De, S.; Dokania, A.; Ramirez, A.; Gascon, J. Advances in the Design of Heterogeneous Catalysts and Thermocatalytic Processes for CO_2 Utilization. *ACS Catal.* **2020**, *10*, 14147−14185.

(11) Ra, E. C.; Kim, K. Y.; Kim, E. H.; Lee, H.; An, K.; Lee, J. S. Recycling Carbon Dioxide through Catalytic Hydrogenation: Recent

Key Developments and Perspectives. *ACS Catal.* **2020**, *10*, 11318–11345.

(12) Zhong, J.-Q.; Shaikhutdinov, S.; Roldan Cuenya, B. Structural Evolution of Ga–Cu Model Catalysts for CO_2 Hydrogenation Reactions. *J. Phys. Chem. C* **2021**, *125*, 1361–1367.

(13) Simkovicová, K.; Qadir, M. I.; Žilková, N.; Olszówka, J. E.; Sialini, P.; Kvítek, L.; Vajda, Š. Hydrogenation of CO_2 on Nanostructured Cu/FeO_x Catalysts: The Effect of Morphology and Cu Load on Selectivity. *Catalysts* **2022**, *12*, 516.

(14) Liu, C.; Yang, B.; Tyo, E.; Seifert, S.; DeBartolo, J.; von Issendorff, B.; Zapol, P.; Vajda, S.; Curtiss, L. A. Carbon Dioxide Conversion to Methanol over Size-Selected Cu_4 Clusters at Low Pressures. *J. Am. Chem. Soc.* **2015**, *137*, 8676–8679.

(15) Yang, B.; Liu, C.; Halder, A.; Tyo, E. C.; Martinson, A. B.; Seifert, S.; Zapol, P.; Curtiss, L. A.; Vajda, S. Copper Cluster Size Effect in Methanol Synthesis from CO_2. *J. Phys. Chem. C* **2017**, *121*, 10406–10412.

(16) Halder, A.; Kioseoglou, J.; Yang, B.; Kolipaka, K. L.; Seifert, S.; Ilavsky, J.; Pellin, M.; Sowwan, M.; Grammatikopoulos, P.; Vajda, S. Nanoassemblies of Ultrasmall Clusters with Remarkable Activity in Carbon Dioxide Conversion into C1 Fuels. *Nanoscale* **2019**, *11*, 4683–4687.

(17) Yang, B.; Yu, X.; Halder, A.; Zhang, X.; Zhou, X.; Mannie, G. J.; Tyo, E.; Pellin, M. J.; Seifert, S.; Su, D.; et al. Dynamic Interplay between Copper Tetramers and Iron Oxide Boosting CO_2 Conversion to Methanol and Hydrocarbons under Mild Conditions. *ACS Sustain. Chem. Eng.* **2019**, *7*, 14435–14442.

(18) Halder, A.; Lenardi, C.; Timoshenko, J.; Mravak, A.; Yang, B.; Kolipaka, L. K.; Piazzoni, C.; Seifert, S.; Bonačić-Koutecký, V.; Frenkel, A. I.; et al. CO_2 Methanation on Cu-Cluster Decorated Zirconia Supports with Different Morphology: A Combined Experimental In Situ GIXANES/GISAXS, Ex Situ XPS and Theoretical DFT Study. *ACS Catal.* **2021**, *11*, 6210–6224.

(19) Pechenkin, A.; Potemkin, D.; Badmaev, S.; Smirnova, E.; Cherednichenko, K.; Vinokurov, V.; Glotov, A. CO_2 Hydrogenation to Dimethyl Ether over In_2O_3 Catalysts Supported on Aluminosilicate Halloysite Nanotubes. *Green Process. Synth.* **2021**, *10*, 594–605.

(20) Pechenkin, A.; Potemkin, D.; Rubtsova, M.; Snytnikov, P.; Plyusnin, P.; Glotov, A. CuO-In_2O_3 Catalysts Supported on Halloysite Nanotubes for CO_2 Hydrogenation to Dimethyl Ether. *Catalysts* **2021**, *11*, 1151.

(21) Mammen, N.; Spanu, L.; Tyo, E. C.; Yang, B.; Halder, A.; Seifert, S.; Pellin, M. J.; Vajda, S.; Narasimhan, S. Reversing Size-Dependent Trends in the Oxidation of Copper Clusters through Support Effects. *Eur. J. Inorg. Chem.* **2018**, *2018*, 16–22.

(22) Timoshenko, J.; Halder, A.; Yang, B.; Seifert, S.; Pellin, M. J.; Vajda, S.; Frenkel, A. I. Subnanometer Substructures in Nanoassemblies Formed from Clusters under a Reactive Atmosphere Revealed using Machine Learning. *J. Phys. Chem. C* **2018**, *122*, 21686–21693.

(23) Liu, Y.; Marcella, N.; Timoshenko, J.; Halder, A.; Yang, B.; Kolipaka, L.; Pellin, M. J.; Seifert, S.; Vajda, S.; Liu, P.; et al. Mapping XANES Spectra on Structural Descriptors of Copper Oxide Clusters using Supervised Machine Learning. *J. Chem. Phys.* **2019**, *151*, 164201.

(24) Zandkarimi, B.; Sun, G.; Halder, A.; Seifert, S.; Vajda, S.; Sautet, P.; Alexandrova, A. N. Interpreting the Operando XANES of Surface-Supported Subnanometer Clusters: When Fluxionality, Oxidation State, and Size Effect Fight. *J. Phys. Chem. C* **2020**, *124*, 10057–10066.

(25) Halder, A.; Lee, S.; Yang, B.; Pellin, M. J.; Vajda, S.; Li, Z.; Yang, Y.; Farha, O. K.; Hupp, J. T. Structural Reversibility of Cu Doped NU-1000 MOFs under Hydrogenation Conditions. *J. Chem. Phys.* **2020**, *152*, 084703.

(26) Halder, A.; Ha, M.-A.; Zhai, H.; Yang, B.; Pellin, M. J.; Seifert, S.; Alexandrova, A. N.; Vajda, S. Oxidative Dehydrogenation of Cyclohexane by Cu vs Pd Clusters: Selectivity Control by Specific Cluster Dynamics. *ChemCatChem* **2020**, *12*, 1307–1315.

(27) Liu, Y.; Halder, A.; Seifert, S.; Marcella, N.; Vajda, S.; Frenkel, A. I. Probing Active Sites in Cu_xPd_y Cluster Catalysts by Machine-Learning-Assisted X-Ray Absorption Spectroscopy. *ACS Appl. Mater. Interfaces* **2021**, *13*, 53363–53374.

(28) Frisch, M. J.; Trucks, G. W.; Schlegel, H. B.; Scuseria, G. E.; Robb, M. A.; Cheeseman, J. R.; Scalmani, G.; Barone, V.; Petersson, G. A.; Nakatsuji, H.; et al. *Gaussian 16*; Revision A.03; Gaussian Inc.: Wallingford CT, 2016.

(29) Becke, A. D. Density-Functional Exchange-Energy Approximation with Correct Asymptotic Behavior. *Phys. Rev. A* **1988**, *38*, 3098–3100.

(30) Lee, C.; Yang, W.; Parr, R. G. Development of the Colle-Salvetti Correlation-Energy Formula into a Functional of the Electron Density. *Phys. Rev. B* **1988**, *37*, 785–789.

(31) Becke, A. D. Density-Functional Thermochemistry. III. The Role of Exact Exchange. *J. Chem. Phys.* **1993**, *98*, 5648–5652.

(32) Weigend, F.; Ahlrichs, R. Balanced Basis Sets of Split Valence, Triple Zeta Valence and Quadruple Zeta Valence Quality for H to Rn: Design and Assessment of Accuracy. *Phys. Chem. Chem. Phys.* **2005**, *7*, 3297–3305.

(33) Andrae, D.; Häußermann, U.; Dolg, M.; Stoll, H.; Preuß, H. Energy-Adjusted Ab Initio Pseudopotentials for the Second and Third Row Transition Elements. *Theor. Chim. Acta* **1990**, *77*, 123–141.

(34) Luna-Valenzuela, A.; Cabellos, J. L.; Alonso, J. A.; Posada-Amarillas, A. Effects of Van der Waals Interactions on the Structure and Stability of $Cu_{8-x}Pd_x$ (x= 0, 4, 8) Cluster Isomers. *Mater. Today Commun.* **2021**, *26*, 102024.

(35) Grimme, S.; Antony, J.; Ehrlich, S.; Krieg, H. A Consistent and Accurate Ab Initio Parametrization of Density Functional Dispersion Correction (DFT-D) for the 94 Elements H-Pu. *J. Chem. Phys.* **2010**, *132*, 154104.

(36) Nößler, M.; Mitrić, R.; Bonačić-Koutecký, V. Binary Neutral Metal Oxide Clusters with Oxygen Radical Centers for Catalytic Oxidation Reactions: From Cluster Models toward Surfaces. *J. Phys. Chem. C* **2012**, *116*, 11570–11574.

(37) Álvarez, A.; Borges, M.; Corral-Pérez, J. J.; Olcina, J. G.; Hu, L.; Cornu, D.; Huang, R.; Stoian, D.; Urakawa, A. CO_2 Activation over Catalytic Surfaces. *ChemPhysChem* **2017**, *18*, 3135–3141.

(38) Álvarez-García, A.; Flórez, E.; Moreno, A.; Jimenez-Orozco, C. CO_2 Activation on Small Cu-Ni and Cu-Pd Bimetallic Clusters. *Mol. Catal.* **2020**, *484*, 110733.

(39) Goodman, D. W. Ethane Hydrogenolysis over Single Crystals of Nickel: Direct Detection of Structure Sensitivity. *Surf. Sci. Lett.* **1982**, *123*, L679–L685.

(40) Kirlin, P.; Knoezinger, H.; Gates, B. C. Mononuclear, Trinuclear, and Metallic Rhenium Catalysts Supported on Magnesia: Effects of Structure on Catalyst Performance. *J. Phys. Chem.* **1990**, *94*, 8451–8456.

(41) McCrea, K. R.; Somorjai, G. A. SFG-Surface Vibrational Spectroscopy Studies of Structure Sensitivity and Insensitivity in Catalytic Reactions: Cyclohexene Dehydrogenation and Ethylene Hydrogenation on Pt (111) and Pt (100) Crystal Surfaces. *J. Mol. Catal. A: Chem.* **2000**, *163*, 43–53.

(42) Andersson, M.; Abild-Pedersen, F.; Remediakis, I.; Bligaard, T.; Jones, G.; Engbæk, J.; Lytken, O.; Horch, S.; Nielsen, J.; Sehested, J.; et al. Structure Sensitivity of the Methanation Reaction: H_2-Induced CO Dissociation on Nickel Surfaces. *J. Catal.* **2008**, *255*, 6–19.

(43) Van Santen, R. A. Complementary Structure Sensitive and Insensitive Catalytic Relationships. *Acc. Chem. Res.* **2009**, *42*, 57–66.

(44) Goergen, S.; Yin, C.; Yang, M.; Lee, B.; Lee, S.; Wang, C.; Wu, P.; Boucher, M.; Kwon, G.; Seifert, S.; et al. Structure Sensitivity of Oxidative Dehydrogenation of Cyclohexane over FeO_x and Au/Fe_3O_4 Nanocrystals. *ACS Catal.* **2013**, *3*, 529–539.

Conclusions and perspectives

The thesis has focused on the development of new heterogeneous catalysts for green energy application, which is crucial for the transition to a sustainable future. In this context, the concept of heterogenization of metallic quantum clusters represents a promising approach. DFT allowed us to study a wide range of systems, from small gas phase models to larger and more complex ones, providing an insight into the reaction mechanism and the nature of the active site. In addition, the role of the surrounding has been investigated to explore its effect on metallic centers. Theoretical results have been complemented by experiments, initiating preparation of new catalytic materials.

The strategies for catalyst design are based on: i) integration of {CuH} metallic center within the MOF and ligand protection of a silver hydride cluster, ii) intrazeolite anchoring of the ligated Ru-cluster, and iii) deposition of monometallic and Pd-doped bimetallic Cu-clusters on metal oxide support. Each strategy has been chosen based on the properties of the surrounding and the specific application requirements.

The proposed MOF material for the production of hydrogen has shown the possibility of cooperatively promoting the decomposition of the formic acid reaction while simultaneously providing storage for hydrogen. Experimental results in the gas phase have confirmed that the charged system with {CuH} reactive center is an effective catalyst for the reaction. Furthermore, DFT calculations have shown that the reaction mechanism remains the same within the MOF environment. This opens a new direction for the design of MOF-based materials through the utilization of simpler gas phase systems that facilitate the modeling of more complex ones. One of the routes that is interesting for further exploration is using the MOF as a host for the confinement of the various guest molecules within a host/guest scheme. This is possible due to the porous nature of the material. Since new theoretical and experimental approaches continuously emerge, it is worthwhile to continue the investigation of MOFs and similar materials (COFs, POFs) not only for catalysis but also for drug delivery [145], bioimaging [146], and solar cell application [147].

Ligands in the silver ligated hydrides provide protection and stabilization of the Ag core, while also directly playing a role in the fragmentation chemistry. Moreover, ligands

in ligated Ru-cluster act as protection against interaction with the zeolite framework. The reaction mechanism and energetics of CO methanation remain the same inside the zeolite cage, with an unchanged catalytic site. This demonstrates a promising approach for the design of highly active and selective heterogeneous catalyst for CO methanation with potential application in fuel cells. In the future, the robust zeolitic environment could be used for the confinement of other (ligand protected) clusters to study various reaction types.

The small subnanometer tetramer clusters at zirconium oxide have been shown as efficient catalysts for CO_2 conversion to methane and methanol, both experimentally and theoretically. The results have shown that the size and the morphology of the support affect the catalyst performance, demonstrating a new way to tailor its properties. Furthermore, doping of Cu-cluster with Pd reduces the barriers for hydrogenation, illustrating the potential for improving catalytic performance. The presented findings also indicate the possibility of tuning the catalyst selectivity through temperature. The proven potential of zirconium oxide as a synergistic support could be used further by finding the optimal composition of the supported cluster catalyst for the hydrogenation reactions.

Altogether, the thesis highlights the advantages of systematically including metallic quantum clusters within various nanostructured materials for designing new heterogeneous catalysts. In addition, the study contributes to understanding of the role of different surroundings on catalytic properties. In this regard, the DFT method has elucidated the nature of the active site, surrounding, as well as the details of the reaction mechanism. Although there are still challenges and limitations associated with the DFT use, it will continue to advance in the future. Together with different experimental techniques, theoretical approaches will ensure better characterization of the physicochemical properties of the highly complicated systems. The presented research added to the rapidly expanding field of nanocatalysis that enables the development of new renewable solutions for accelerating the much-needed green transition.

References

[1] J. N. Armor. "A history of industrial catalysis". In: *Catalysis Today* 163.1 (2011), pp. 3–9.

[2] J. Berzelius. "Quelques idées sur une nouvelle force agissant dans les combinaisons des corps organiques". In: *Ann. Chim* 61 (1836), pp. 146–151.

[3] K. Kakaei, M. D. Esrafili, and A. Ehsani. "Chapter 1 - Introduction to Catalysis". In: *Graphene Surfaces*. Ed. by K. Kakaei, M. D. Esrafili, and A. Ehsani. Vol. 27. Interface Science and Technology. Elsevier, (2019), pp. 1–21.

[4] D. Cole-Hamilton and R. Tooze. "Homogeneous catalysis—advantages and problems". In: *Catalyst Separation, Recovery and Recycling: Chemistry and Process Design* (2006), pp. 1–8.

[5] R. Chatterjee, P. Bhanja, and A. Bhaumik. "The design and synthesis of heterogeneous catalysts for environmental applications". In: *Dalton Transactions* 50.14 (2021), pp. 4765–4771.

[6] E. Roduner. "Understanding catalysis". In: *Chemical Society Reviews* 43.24 (2014), pp. 8226–8239.

[7] U. Heiz and U. Landman. *Nanocatalysis*. Springer Science & Business Media, (2007).

[8] F. F. Tao, W. F. Schneider, and P. V. Kamat. *Heterogeneous catalysis at nanoscale for energy applications*. John Wiley & Sons, (2015).

[9] R. Pielke Jr, M. G. Burgess, and J. Ritchie. "Plausible 2005–2050 emissions scenarios project between 2 $^{\circ}C$ and 3 $^{\circ}C$ of warming by 2100". In: *Environmental Research Letters* 17.2 (2022), p. 024027.

[10] M. Amin, H. H. Shah, A. G. Fareed, W. U. Khan, E. Chung, A. Zia, Z. U. R. Farooqi, and C. Lee. "Hydrogen production through renewable and non-renewable energy processes and their impact on climate change". In: *International Journal of Hydrogen Energy* (2022).

[11] M.-R. de Valladares. "Global trends and outlook for hydrogen". In: *International Energy Agency* (2017).

References

[12] W. Lubitz and W. Tumas. "Hydrogen: an overview". In: *Chemical reviews* 107.10 (2007), pp. 3900–3903.

[13] U. Eberle, M. Felderhoff, and F. Schueth. "Chemical and physical solutions for hydrogen storage". In: *Angewandte Chemie International Edition* 48.36 (2009), pp. 6608–6630.

[14] J. Sculley, D. Yuan, and H.-C. Zhou. "The current status of hydrogen storage in metal–organic frameworks—updated". In: *Energy & Environmental Science* 4.8 (2011), pp. 2721–2735.

[15] X. Yu, Z. Tang, D. Sun, L. Ouyang, and M. Zhu. "Recent advances and remaining challenges of nanostructured materials for hydrogen storage applications". In: *Progress in Materials Science* 88 (2017), pp. 1–48.

[16] T. Len and R. Luque. "Addressing the CO_2 challenge through thermocatalytic hydrogenation to carbon monoxide, methanol and methane". In: *Green Chemistry* 25 (2 2023), pp. 490–521.

[17] J. Dufour, D. Serrano, J. Galvez, J. Moreno, and C. Garcia. "Life cycle assessment of processes for hydrogen production. Environmental feasibility and reduction of greenhouse gases emissions". In: *International journal of hydrogen energy* 34.3 (2009), pp. 1370–1376.

[18] Z. Abdin, A. Zafaranloo, A. Rafiee, W. Mérida, W. Lipiński, and K. R. Khalilpour. "Hydrogen as an energy vector". In: *Renewable and sustainable energy reviews* 120 (2020), p. 109620.

[19] M. Solakidou, A. Gemenetzi, G. Koutsikou, M. Theodorakopoulos, Y. Deligiannakis, and M. Louloudi. "Cost efficiency analysis of H_2 production from formic acid by molecular catalysts". In: *Energies* 16.4 (2023), p. 1723.

[20] J. Eppinger and K.-W. Huang. "Formic acid as a hydrogen energy carrier". In: *ACS Energy Letters* 2.1 (2017), pp. 188–195.

[21] H. Zhong, M. Iguchi, M. Chatterjee, Y. Himeda, Q. Xu, and H. Kawanami. "Formic acid-based liquid organic hydrogen carrier system with heterogeneous catalysts". In: *Advanced Sustainable Systems* 2.2 (2018), p. 1700161.

[22] P. Sabatier and A. Mailhe. "Catalytic decomposition of formic acid". In: *Compt. Rend* 152 (1912), pp. 1212–1215.

[23] P. Mars, J. Scholten, and P. Zwietering. "The catalytic decomposition of formic acid". In: *Advances in Catalysis*. Vol. 14. Elsevier, (1963), pp. 35–113.

References

[24] K. Saito, T. Shiose, O. Takahashi, Y. Hidaka, F. Aiba, and K. Tabayashi. "Unimolecular decomposition of formic acid in the gas phase on the ratio of the competing reaction channels". In: *The Journal of Physical Chemistry A* 109.24 (2005), pp. 5352–5357.

[25] S. Enthaler, J. von Langermann, and T. Schmidt. "Carbon dioxide and formic acid—the couple for environmental-friendly hydrogen storage?" In: *Energy & Environmental Science* 3.9 (2010), pp. 1207–1217.

[26] N. Onishi, M. Iguchi, X. Yang, R. Kanega, H. Kawanami, Q. Xu, and Y. Himeda. "Development of effective catalysts for hydrogen storage technology using formic acid". In: *Advanced Energy Materials* 9.23 (2019), p. 1801275.

[27] A. Al-Nayili, H. S. Majdi, T. M. Albayati, and N. M. C. Saady. "Formic acid dehydrogenation using noble-metal nanoheterogeneous catalysts: Towards sustainable hydrogen-based energy". In: *Catalysts* 12.3 (2022), p. 324.

[28] A. Parekh. "Recent developments of proton exchange membranes for PEMFC: A review". In: *Frontiers in Energy Research* 10 (2022). ISSN: 2296-598X.

[29] J. Baschuk and X. Li. "Carbon monoxide poisoning of proton exchange membrane fuel cells". In: *International Journal of Energy Research* 25.8 (2001), pp. 695–713.

[30] V. F. Valdés-López, T. Mason, P. R. Shearing, and D. J. Brett. "Carbon monoxide poisoning and mitigation strategies for polymer electrolyte membrane fuel cells–A review". In: *Progress in Energy and Combustion Science* 79 (2020), p. 100842.

[31] Q. Li, R. He, J.-A. Gao, J. O. Jensen, and N. J. Bjerrum. "The CO poisoning effect in PEMFCs operational at temperatures up to 200 $°C$". In: *Journal of the Electrochemical Society* 150.12 (2003), A1599.

[32] X. Gang, L. Qingfeng, H. A. Hjuler, and N. J. Bjerrum. "Hydrogen oxidation on gas diffusion electrodes for phosphoric acid fuel cells in the presence of carbon monoxide and oxygen". In: *Journal of The Electrochemical Society* 142.9 (1995), p. 2890.

[33] L. Huang, S. Zaman, X. Tian, Z. Wang, W. Fang, and B. Y. Xia. "Advanced platinum-based oxygen reduction electrocatalysts for fuel cells". In: *Accounts of Chemical Research* 54.2 (2021), pp. 311–322.

[34] W. Liang, Y. Wang, L. Zhao, W. Guo, D. Li, W. Qin, H. Wu, Y. Sun, and L. Jiang. "3D anisotropic Au@Pt–Pd hemispherical nanostructures as efficient electrocatalysts for methanol, ethanol, and formic acid oxidation reaction". In: *Advanced Materials* 33.30 (2021), p. 2100713.

[35] B. C. Steele and A. Heinzel. "Materials for fuel-cell technologies". In: *Nature* 414.6861 (2001), pp. 345–352.

[36] P. Wang, Y. Bu, J. Liu, Q. Li, H. Wang, and W. Yang. "Atomic deformation mechanism and interface toughening in metastable high entropy alloy". In: *Materials Today* 37 (2020), pp. 64–73.

[37] W. Luo, Y. Jiang, M. Wang, D. Lu, X. Sun, and H. Zhang. "Design strategies of Pt-based electrocatalysts and tolerance strategies in fuel cells: A review". In: *RSC Advances* 13.7 (2023), pp. 4803–4822.

[38] P. Jing, X. Gong, B. Liu, and J. Zhang. "Recent advances in synergistic effect promoted catalysts for preferential oxidation of carbon monoxide". In: *Catalysis Science & Technology* 10.4 (2020), pp. 919–934.

[39] X. Wang, Y. Li, Y. Wang, H. Zhang, Z. Jin, X. Yang, Z. Shi, L. Liang, Z. Wu, Z. Jiang, et al. "Proton exchange membrane fuel cells powered with both CO and H_2". In: *Proceedings of the National Academy of Sciences* 118.43 (2021), e2107332118.

[40] I. E. Agency. *World Energy Outlook 2022*. (2022), p. 524. URL: https://www.oecd-ilibrary.org/content/publication/3a469970-en.

[41] J. Klankermayer and W. Leitner. "Harnessing renewable energy with CO_2 for the chemical value chain: Challenges and opportunities for catalysis". In: *Philosophical Transactions of the Royal Society A: Mathematical, Physical and Engineering Sciences* 374.2061 (2016), p. 20150315.

[42] A. D. Kamkeng, M. Wang, J. Hu, W. Du, and F. Qian. "Transformation technologies for CO_2 utilisation: Current status, challenges and future prospects". In: *Chemical Engineering Journal* 409 (2021), p. 128138.

[43] A. Saravanan, D.-V. N. Vo, S. Jeevanantham, V. Bhuvaneswari, V. A. Narayanan, P. Yaashikaa, S. Swetha, B. Reshma, et al. "A comprehensive review on different approaches for CO_2 utilization and conversion pathways". In: *Chemical Engineering Science* 236 (2021), p. 116515.

[44] W. Zhang, Y. Hu, L. Ma, G. Zhu, Y. Wang, X. Xue, R. Chen, S. Yang, and Z. Jin. "Progress and perspective of electrocatalytic CO_2 reduction for renewable carbonaceous fuels and chemicals". In: *Advanced Science* 5.1 (2018), p. 1700275.

[45] S. Nahar, M. Zain, A. A. H. Kadhum, H. A. Hasan, and M. R. Hasan. "Advances in photocatalytic CO_2 reduction with water: A review". In: *Materials* 10.6 (2017), p. 629.

[46] T. J. Erb and J. Zarzycki. "Biochemical and synthetic biology approaches to improve photosynthetic CO_2-fixation". In: *Current opinion in chemical biology* 34 (2016), pp. 72–79.

[47] N. Podrojková, V. Sans, A. Oriňak, and R. Oriňaková. "Recent developments in the modelling of heterogeneous catalysts for CO_2 conversion to chemicals". In: *ChemCatChem* 12.7 (2020), pp. 1802–1825.

[48] C. Liu, B. Yang, E. Tyo, S. Seifert, J. DeBartolo, B. von Issendorff, P. Zapol, S. Vajda, and L. A. Curtiss. "Carbon dioxide conversion to methanol over size-selected Cu_4 clusters at low pressures". In: *Journal of the American Chemical Society* 137.27 (2015), pp. 8676–8679.

[49] B. Yang, C. Liu, A. Halder, E. C. Tyo, A. B. Martinson, S. Seifert, P. Zapol, L. A. Curtiss, and S. Vajda. "Copper cluster size effect in methanol synthesis from CO_2". In: *The Journal of Physical Chemistry C* 121.19 (2017), pp. 10406–10412.

[50] X. Zhang, J.-X. Liu, B. Zijlstra, I. A. Filot, Z. Zhou, S. Sun, and E. J. Hensen. "Optimum Cu nanoparticle catalysts for CO_2 hydrogenation towards methanol". In: *Nano Energy* 43 (2018), pp. 200–209.

[51] R. Guil-López, N. Mota, J. Llorente, E. Millán, B. Pawelec, J. L. G. Fierro, and R. Navarro. "Methanol synthesis from CO_2: A review of the latest developments in heterogeneous catalysis". In: *Materials* 12.23 (2019), p. 3902.

[52] U. J. Etim, Y. Song, and Z. Zhong. "Improving the Cu/ZnO-based catalysts for carbon dioxide hydrogenation to methanol, and the use of methanol as a renewable energy storage media". In: *Frontiers in Energy Research* 8 (2020), p. 545431.

[53] Z. Cui, S. Meng, Y. Yi, A. Jafarzadeh, S. Li, E. C. Neyts, Y. Hao, L. Li, X. Zhang, X. Wang, et al. "Plasma-catalytic methanol synthesis from CO_2 hydrogenation over a supported Cu cluster catalyst: Insights into the reaction mechanism". In: *ACS Catalysis* 12.2 (2022), pp. 1326–1337.

[54] H. Lei, R. Nie, G. Wu, and Z. Hou. "Hydrogenation of CO_2 to CH_3OH over Cu/ZnO catalysts with different ZnO morphology". In: *Fuel* 154 (2015), pp. 161–166.

[55] S. Kattel, P. J. Ramírez, J. G. Chen, J. A. Rodriguez, and P. Liu. "Active sites for CO_2 hydrogenation to methanol on Cu/ZnO catalysts". In: *Science* 355.6331 (2017), pp. 1296–1299.

[56] M. Tawalbeh, R. M. N. Javed, A. Al-Othman, and F. Almomani. "The novel contribution of non-noble metal catalysts for intensified carbon dioxide hydrogenation: Recent challenges and opportunities". In: *Energy Conversion and Management* 279 (2023), p. 116755.

[57] O. Martin and J. Pérez-Ramírez. "New and revisited insights into the promotion of methanol synthesis catalysts by CO_2". In: *Catalysis Science & Technology* 3.12 (2013), pp. 3343–3352.

References

[58] B. Rungtaweevoranit, J. Baek, J. R. Araujo, B. S. Archanjo, K. M. Choi, O. M. Yaghi, and G. A. Somorjai. "Copper nanocrystals encapsulated in Zr-based metal–organic frameworks for highly selective CO_2 hydrogenation to methanol". In: *Nano letters* 16.12 (2016), pp. 7645–7649.

[59] E. S. Gutterød, A. Lazzarini, T. Fjermestad, G. Kaur, M. Manzoli, S. Bordiga, S. Svelle, K. P. Lillerud, E. Skúlason, S. Øien-Ødegaard, et al. "Hydrogenation of CO_2 to methanol by Pt nanoparticles encapsulated in UiO-67: Deciphering the role of the metal–organic framework". In: *Journal of the American Chemical Society* 142.2 (2019), pp. 999–1009.

[60] T. Stolar, A. Prašnikar, V. Martinez, B. Karadeniz, A. Bjelić, G. Mali, T. Friščić, B. Likozar, and K. Užarević. "Scalable mechanochemical amorphization of bimetallic Cu-Zn MOF-74 catalyst for selective CO_2 reduction reaction to methanol". In: *ACS Applied Materials & Interfaces* 13.2 (2021), pp. 3070–3077.

[61] Y. Chen and T. Mu. "Conversion of CO_2 to value-added products mediated by ionic liquids". In: *Green Chemistry* 21.10 (2019), pp. 2544–2574.

[62] N. D. Mohd Ridzuan, M. S. Shaharun, M. A. Anawar, and I. Ud-Din. "Ni-based catalyst for carbon dioxide methanation: A review on performance and progress". In: *Catalysts* 12.5 (2022), p. 469.

[63] A. Bruix, J. T. Margraf, M. Andersen, and K. Reuter. "First-principles-based multiscale modelling of heterogeneous catalysis". In: *Nature Catalysis* 2.8 (2019), pp. 659–670.

[64] B. W. Chen, L. Xu, and M. Mavrikakis. "Computational methods in heterogeneous catalysis". In: *Chemical Reviews* 121.2 (2020), pp. 1007–1048.

[65] S. Mourdikoudis, R. M. Pallares, and N. T. Thanh. "Characterization techniques for nanoparticles: comparison and complementarity upon studying nanoparticle properties". In: *Nanoscale* 10.27 (2018), pp. 12871–12934.

[66] J. A. Keith, J. Anton, P. Kaghazchi, and T. Jacob. *Modeling catalytic reactions on surfaces with density functional theory*. John Wiley & Sons, Ltd. Chap. 1, pp. 1–38. ISBN: 9783527639878.

[67] F. Jensen. *Introduction to computational chemistry*. John Wiley & Sons, (2017).

[68] A. J. Cohen, P. Mori-Sánchez, and W. Yang. "Challenges for density functional theory". In: *Chemical reviews* 112.1 (2012), pp. 289–320.

[69] K. Burke and L. O. Wagner. "DFT in a nutshell". In: *International Journal of Quantum Chemistry* 113.2 (2013), pp. 96–101.

References

[70] K. Berland, V. R. Cooper, K. Lee, E. Schröder, T. Thonhauser, P. Hyldgaard, and B. I. Lundqvist. "Van der Waals forces in density functional theory: A review of the vdW-DF method". In: *Reports on Progress in Physics* 78.6 (2015), p. 066501.

[71] S. Grimme, J. Antony, S. Ehrlich, and H. Krieg. "A consistent and accurate ab initio parametrization of density functional dispersion correction (DFT-D) for the 94 elements H-Pu". In: *The Journal of chemical physics* 132.15 (2010), p. 154104.

[72] L. Goerigk. "A comprehensive overview of the DFT-D3 London-dispersion correction". In: *Non-Covalent Interactions in Quantum Chemistry and Physics* (2017), pp. 195–219.

[73] A. J. Price, K. R. Bryenton, and E. R. Johnson. "Requirements for an accurate dispersion-corrected density functional". In: *The Journal of Chemical Physics* 154.23 (2021), p. 230902.

[74] A. D. Becke. "Density-functional exchange-energy approximation with correct asymptotic behavior". In: *Physical review A* 38.6 (1988), p. 3098.

[75] C. Lee, W. Yang, and R. G. Parr. "Development of the Colle-Salvetti correlation-energy formula into a functional of the electron density". In: *Physical review B* 37.2 (1988), p. 785.

[76] A. D. Becke. "Density-functional thermochemistry. III. The role of exact exchange". In: *The Journal of Chemical Physics* 98.7 (1993), pp. 5648–5652.

[77] F. Weigend and R. Ahlrichs. "Balanced basis sets of split valence, triple zeta valence and quadruple zeta valence quality for H to Rn: Design and assessment of accuracy". In: *Physical Chemistry Chemical Physics* 7.18 (2005), pp. 3297–3305.

[78] F. Weigend. "Accurate Coulomb-fitting basis sets for H to Rn". In: *Physical chemistry chemical physics* 8.9 (2006), pp. 1057–1065.

[79] J. P. Perdew, K. Burke, and M. Ernzerhof. "Generalized gradient approximation made simple". In: *Physical review letters* 77.18 (1996), p. 3865.

[80] J. P. Perdew, K. Burke, and M. Ernzerhof. "Generalized gradient approximation made simple [Phys. Rev. Lett. 77, 3865 (1996)]". In: *Physical review letters* 78 (7 1997), pp. 1396–1396.

[81] S. Stocker, G. Csányi, K. Reuter, and J. T. Margraf. "Machine learning in chemical reaction space". In: *Nature communications* 11.1 (2020), p. 5505.

[82] H. B. Schlegel. "Exploring potential energy surfaces for chemical reactions: An overview of some practical methods". In: *Journal of computational chemistry* 24.12 (2003), pp. 1514–1527.

References

[83] H. P. Hratchian and H. B. Schlegel. "Finding minima, transition states, and following reaction pathways on ab initio potential energy surfaces". In: *Theory and applications of computational chemistry*. Elsevier, (2005), pp. 195–249.

[84] J. Simons and J. Nichols. "Strategies for walking on potential energy surfaces using local quadratic approximations". In: *International Journal of Quantum Chemistry* 38.S24 (1990), pp. 263–276.

[85] H. B. Schlegel. "Geometry optimization". In: *Wiley Interdisciplinary Reviews: Computational Molecular Science* 1.5 (2011), pp. 790–809.

[86] M. Frisch, G. Trucks, H. Schlegel, G. Scuseria, M. Robb, J. Cheeseman, G. Scalmani, V. Barone, G. Petersson, H. Nakatsuji, et al. "Gaussian 16, Revision A. 03, Gaussian". In: *Inc., Wallingford CT* 3 (2016).

[87] C. Peng and H. Bernhard Schlegel. "Combining synchronous transit and quasi-Newton methods to find transition states". In: *Israel Journal of Chemistry* 33.4 (1993), pp. 449–454.

[88] C. Peng, P. Y. Ayala, H. B. Schlegel, and M. J. Frisch. "Using redundant internal coordinates to optimize equilibrium geometries and transition states". In: *Journal of Computational Chemistry* 17.1 (1996), pp. 49–56.

[89] H. B. Schlegel. "Optimization of equilibrium geometries and transition structures". In: *Journal of Computational Chemistry* 3.2 (1982), pp. 214–218.

[90] K. Fukui. "Formulation of the reaction coordinate". In: *The Journal of Physical Chemistry* 74.23 (1970), pp. 4161–4163.

[91] K. Fukui. "The path of chemical reactions-the IRC approach". In: *Accounts of chemical research* 14.12 (1981), pp. 363–368.

[92] Y. Chai, W. Shang, W. Li, G. Wu, W. Dai, N. Guan, and L. Li. "Noble metal particles confined in zeolites: Synthesis, characterization, and applications". In: *Advanced Science* 6.16 (2019), p. 1900299.

[93] K. Li and J. G. Chen. "CO_2 hydrogenation to methanol over ZrO_2-containing catalysts: Insights into ZrO_2 induced synergy". In: *ACS catalysis* 9.9 (2019), pp. 7840–7861.

[94] M. F. Matus and H. Häkkinen. "Understanding ligand-protected noble metal nanoclusters at work". In: *Nature Reviews Materials* (2023), pp. 1–18.

[95] A. Zavras, G. N. Khairallah, M. Krstić, M. Girod, S. Daly, R. Antoine, P. Maitre, R. J. Mulder, S.-A. Alexander, V. Bonačić-Koutecký, et al. "Ligand-induced substrate steering and reshaping of $[Ag_2(H)]^+$ scaffold for selective CO_2 extrusion from formic acid". In: *Nature communications* 7.1 (2016), p. 11746.

References

[96]   A. J. Jordan, G. Lalic, and J. P. Sadighi. "Coinage metal hydrides: Synthesis, characterization, and reactivity". In: *Chemical Reviews* 116.15 (2016), pp. 8318–8372.

[97]   A. Zavras, M. Krstić, P. Dugourd, V. Bonačić-Koutecký, and R. A. O'Hair. "Selectivity effects in bimetallic catalysis: Role of the metal sites in the decomposition of formic acid into H_2 and CO_2 by the coinage metal binuclear complexes [dppmMM(H)]$^+$". In: *ChemCatChem* 9.7 (2017), pp. 1298–1302.

[98]   A. U. Czaja, N. Trukhan, and U. Müller. "Industrial applications of metal–organic frameworks". In: *Chemical Society Reviews* 38.5 (2009), pp. 1284–1293.

[99]   H. Furukawa, K. E. Cordova, M. O'Keeffe, and O. M. Yaghi. "The chemistry and applications of metal-organic frameworks". In: *Science* 341.6149 (2013), p. 1230444.

[100] Y.-B. Huang, J. Liang, X.-S. Wang, and R. Cao. "Multifunctional metal–organic framework catalysts: Synergistic catalysis and tandem reactions". In: *Chemical Society Reviews* 46.1 (2017), pp. 126–157.

[101] J.-S. Qin, S. Yuan, C. Lollar, J. Pang, A. Alsalme, and H.-C. Zhou. "Stable metal–organic frameworks as a host platform for catalysis and biomimetics". In: *Chemical Communications* 54.34 (2018), pp. 4231–4249.

[102] K. Sumida, D. L. Rogow, J. A. Mason, T. M. McDonald, E. D. Bloch, Z. R. Herm, T.-H. Bae, and J. R. Long. "Carbon dioxide capture in metal–organic frameworks". In: *Chemical reviews* 112.2 (2012), pp. 724–781.

[103] A. Ahmed, S. Seth, J. Purewal, A. G. Wong-Foy, M. Veenstra, A. J. Matzger, and D. J. Siegel. "Exceptional hydrogen storage achieved by screening nearly half a million metal-organic frameworks". In: *Nature communications* 10.1 (2019), p. 1568.

[104] K. Suresh, D. Aulakh, J. Purewal, D. J. Siegel, M. Veenstra, and A. J. Matzger. "Optimizing hydrogen storage in MOFs through engineering of crystal morphology and control of crystal size". In: *Journal of the American Chemical Society* 143.28 (2021), pp. 10727–10734.

[105] S. M. Rogge, A. Bavykina, J. Hajek, H. Garcia, A. I. Olivos-Suarez, A. Sepúlveda-Escribano, A. Vimont, G. Clet, P. Bazin, F. Kapteijn, et al. "Metal–organic and covalent organic frameworks as single-site catalysts". In: *Chemical Society Reviews* 46.11 (2017), pp. 3134–3184.

[106] Y. Bai, Y. Dou, L.-H. Xie, W. Rutledge, J.-R. Li, and H.-C. Zhou. "Zr-based metal–organic frameworks: design, synthesis, structure, and applications". In: *Chemical Society Reviews* 45.8 (2016), pp. 2327–2367.

[107] H. Fei and S. M. Cohen. "A robust, catalytic metal–organic framework with open 2, 2-bipyridine sites". In: *Chemical Communications* 50.37 (2014), pp. 4810–4812.

References

[108]   R. A. O'Hair, A. Mravak, M. Krstić, and V. Bonačić-Kouteckỳ. "Models facilitating the design of a new metal-organic framework catalyst for the selective decomposition of formic acid into hydrogen and carbon dioxide". In: *ChemCatChem* 11.10 (2019), pp. 2443–2448.

[109]   J. R. Khusnutdinova and D. Milstein. "Metal–ligand cooperation". In: *Angewandte Chemie International Edition* 54.42 (2015), pp. 12236–12273.

[110]   J. Fang, B. Zhang, Q. Yao, Y. Yang, J. Xie, and N. Yan. "Recent advances in the synthesis and catalytic applications of ligand-protected, atomically precise metal nanoclusters". In: *Coordination Chemistry Reviews* 322 (2016), pp. 1–29.

[111]   A. S. Weller and J. S. McIndoe. "Reversible binding of dihydrogen in multimetallic complexes". In: *European Journal of Inorganic Chemistry* 2007.28 (2007), pp. 4411–4423.

[112]   M. Girod, M. Krstić, R. Antoine, L. MacAleese, J. Lemoine, A. Zavras, G. N. Khairallah, V. Bonačić-Kouteckỳ, P. Dugourd, and R. A. O'Hair. "Formation and characterisation of the silver hydride nanocluster cation $[Ag_3H_2((Ph_2P)_2CH_2)]^+$ and its release of hydrogen". In: *Chemistry–A European Journal* 20.50 (2014), pp. 16626–16633.

[113]   M. Krstić, A. Zavras, G. N. Khairallah, P. Dugourd, V. Bonačić-Kouteckỳ, and R. A. O'Hair. "ESI/MS investigation of routes to the formation of silver hydride nanocluster dications $[Ag_xH_{x-2}L_y]^{2+}$ and gas-phase unimolecular chemistry of $[Ag_{10}H_8L_6]^{2+}$". In: *International Journal of Mass Spectrometry* 413 (2017), pp. 97–105.

[114]   H. Z. Ma, A. I. McKay, A. Mravak, M. S. Scholz, J. M. White, R. J. Mulder, E. J. Bieske, V. Bonačić-Kouteckỳ, and R. A. O'Hair. "Structural characterization and gas-phase studies of the $[Ag_{10}H_8L_6]^{2+}$ nanocluster dication". In: *Nanoscale* 11.47 (2019), pp. 22880–22889.

[115]   S. Takano, H. Hirai, S. Muramatsu, and T. Tsukuda. "Hydride-mediated controlled growth of a bimetallic $(Pd@Au_8)^{2+}$ superatom to a hydride-doped $(HPd@Au_{10})^{3+}$ superatom". In: *Journal of the American Chemical Society* 140.39 (2018), pp. 12314–12317.

[116]   S. Eckle, Y. Denkwitz, and R. J. Behm. "Activity, selectivity, and adsorbed reaction intermediates/reaction side products in the selective methanation of CO in reformate gases on supported Ru catalysts". In: *Journal of Catalysis* 269.2 (2010), pp. 255–268.

References

[117] S. Tada, R. Kikuchi, K. Urasaki, and S. Satokawa. "Effect of reduction pretreatment and support materials on selective CO methanation over supported Ru catalysts". In: *Applied Catalysis A: General* 404.1-2 (2011), pp. 149–154.

[118] "Influence of the catalyst loading on the activity and the CO selectivity of supported Ru catalysts in the selective methanation of CO in CO_2 containing feed gases". In: *Catalysis Today* 181.1 (2012), pp. 40–51.

[119] S. Li, D. Gong, H. Tang, Z. Ma, Z.-T. Liu, and Y. Liu. "Preparation of bimetallic Ni@Ru nanoparticles supported on SiO_2 and their catalytic performance for CO methanation". In: *Chemical Engineering Journal* 334 (2018), pp. 2167–2178.

[120] S. Chen, A. M. Abdel-Mageed, C. Gauckler, S. E. Olesen, I. Chorkendorff, and R. J. Behm. "Selective CO methanation on isostructural Ru nanocatalysts: the role of support effects". In: *Journal of catalysis* 373 (2019), pp. 103–115.

[121] A. M. Abdel-Mageed, K. Wiese, M. Parlinska-Wojtan, J. Rabeah, A. Brückner, and R. J. Behm. "Encapsulation of Ru nanoparticles: Modifying the reactivity toward CO and CO_2 methanation on highly active Ru/TiO_2 catalysts". In: *Applied Catalysis B: Environmental* 270 (2020), p. 118846.

[122] A. Muñoz, A. Pérez, O. Laguna, L. Bobadilla, M. Centeno, J. Odriozola, et al. "The effect of support surface hydroxyls on selective CO methanation with Ru based catalysts". In: *Applied Catalysis A: General* 641 (2022), p. 118678.

[123] S. M. Lang, T. M. Bernhardt, M. Krstić, and V. Bonačić-Kouteckỳ. "The origin of the selectivity and activity of ruthenium-cluster catalysts for fuel-cell feed-gas purification: A gas-phase approach". In: *Angewandte Chemie International Edition* 53.21 (2014), pp. 5467–5471.

[124] S. M. Lang, S. U. Förtig, T. M. Bernhardt, M. Krstić, and V. Bonačić-Koutecký. "Gas-phase synthesis and structure of Wade-type ruthenium carbonyl and hydrido carbonyl clusters". In: *The Journal of Physical Chemistry A* 118.37 (2014), pp. 8356–8359.

[125] Y. Li and J. Yu. "Emerging applications of zeolites in catalysis, separation and host–guest assembly". In: *Nature Reviews Materials* 6.12 (2021), pp. 1156–1174.

[126] D. Farrusseng and A. Tuel. "Zeolite-encapsulated catalysts: Challenges and prospects". In: *Encapsulated Catalysts* (2017), pp. 335–386.

[127] S.-M. Wu, X.-Y. Yang, and C. Janiak. "Confinement effects in zeolite-confined noble metals". In: *Angewandte Chemie* 131.36 (2019), pp. 12468–12482.

[128] H. Xu and P. Wu. "New progress in zeolite synthesis and catalysis". In: *National science review* 9.9 (2022), nwac045.

[129]   M. Krstić, Q. Jin, G. N. Khairallah, R. A. O'Hair, and V. Bonačić-Kouteckỳ. "How to translate the $[LCu_2(H)]^+$-catalysed selective decomposition of formic acid into H_2 and CO_2 from the gas phase into a zeolite". In: *ChemCatChem* 10.5 (2018), pp. 1173–1177.

[130]   R. I. Amos, F. Heinroth, B. Chan, S. Zheng, B. S. Haynes, C. J. Easton, A. F. Masters, L. Radom, and T. Maschmeyer. "Hydrogen from formic acid through its selective disproportionation over sodium germanate-A non-transition-metal catalysis system". In: *Angewandte Chemie* 126.42 (2014), pp. 11457–11461.

[131]   G.-C. Shen, A. Liu, T. Shido, and M. Ichikawa. "CO hydrogenation towards higher alcohols catalysed on SiO_2-grafted and zeolite-entrapped Ru, Co and RuCo bimetallic clusters: Their EXAFS and FTIR characterization and catalytic performances". In: *Topics in Catalysis* 2 (1995), pp. 141–154.

[132]   G.-C. Shen, A. M. Liu, and M. Ichikawa. "Comprehensive structural and spectroscopic study of intrazeolite anchoring of ruthenium carbonyl clusters". In: *Journal of the Chemical Society, Faraday Transactions* 94.9 (1998), pp. 1353–1362.

[133]   M. Ichikawa, W. Pan, Y. Imada, M. Yamaguchi, K. Isobe, and T. Shido. "Surface-grafted metal oxide clusters and metal carbonyl clusters in zeolite micropores; XAFS/FTIR/TPD characterization and catalytic behavior". In: *Journal of Molecular Catalysis A: Chemical* 107.1 (1996), pp. 23–38.

[134]   D. Olson, W. Haag, and R. Lago. "Chemical and physical properties of the ZSM-5 substitutional series". In: *Journal of Catalysis* 61.2 (1980), pp. 390–396.

[135]   A. Mravak, M. Krstić, S. M. Lang, T. M. Bernhardt, and V. Bonačić-Kouteckỳ. "Intrazeolite CO methanation by small ruthenium carbonyl complexes: Translation from free clusters into the cage". In: *ChemCatChem* 12.15 (2020), pp. 3857–3862.

[136]   G.-C. Shen, A. M. Liu, and M. Ichikawa. "Ruthenium carbonyl clusters in faujasite cages: synthesis and characterization". In: *Inorganic chemistry* 37.21 (1998), pp. 5497–5506.

[137]   E. C. Tyo and S. Vajda. "Catalysis by clusters with precise numbers of atoms". In: *Nature nanotechnology* 10.7 (2015), pp. 577–588.

[138]   J. Jašık, A. Fortunelli, and S. Vajda. "Exploring the materials space in the smallest particle size range: from heterogeneous catalysis to electrocatalysis and photocatalysis". In: *Physical Chemistry Chemical Physics* 24.20 (2022), pp. 12083–12115.

[139]   B. Zandkarimi, G. Sun, A. Halder, S. Seifert, S. Vajda, P. Sautet, and A. N. Alexandrova. "Interpreting the operando XANES of surface-supported subnanometer clusters: when fluxionality, oxidation state, and size effect fight". In: *The Journal of Physical Chemistry C* 124.18 (2020), pp. 10057–10066.

[140] S. Vajda and M. G. White. "Catalysis applications of size-selected cluster deposition". In: *ACS catalysis* 5.12 (2015), pp. 7152–7176.

[141] E. Kauppi, K. Honkala, A. Krause, J. Kanervo, and L. Lefferts. "ZrO$_2$ acting as a redox catalyst". In: *Topics in catalysis* 59 (2016), pp. 823–832.

[142] S. Kouva, K. Honkala, L. Lefferts, and J. Kanervo. "Monoclinic zirconia, its surface sites and their interaction with carbon monoxide". In: *Catalysis science & technology* 5.7 (2015), pp. 3473–3490.

[143] A. Halder, C. Lenardi, J. Timoshenko, A. Mravak, B. Yang, L. K. Kolipaka, C. Piazzoni, S. Seifert, V. Bonačić-Kouteckỳ, A. I. Frenkel, et al. "CO$_2$ methanation on Cu-cluster decorated zirconia supports with different morphology: A combined experimental in situ GIXANES/GISAXS, ex situ XPS and theoretical DFT study". In: *ACS Catalysis* 11.10 (2021), pp. 6210–6224.

[144] A. Mravak, S. Vajda, and V. Bonačić-Koutecký. "Mechanism of catalytic CO$_2$ hydrogenation to methane and methanol using a bimetallic Cu$_3$Pd cluster at a zirconia support". In: *The Journal of Physical Chemistry C* 126.43 (2022), pp. 18306–18312.

[145] W. Cai, J. Wang, C. Chu, W. Chen, C. Wu, and G. Liu. "Metal–organic framework-based stimuli-responsive systems for drug delivery". In: *Advanced Science* 6.1 (2019), p. 1801526.

[146] J. K. Zaręba, M. Nyk, and M. Samoć. "Nonlinear optical properties of emerging nano-and microcrystalline materials". In: *Advanced Optical Materials* 9.23 (2021), p. 2100216.

[147] M. E. Hilal, A. Aboulouard, A. R. Akbar, H. A. Younus, N. Horzum, and F. Verpoort. "Progress of MOF-derived functional materials toward industrialization in solar cells and metal-air batteries". In: *Catalysts* 10.8 (2020), p. 897.

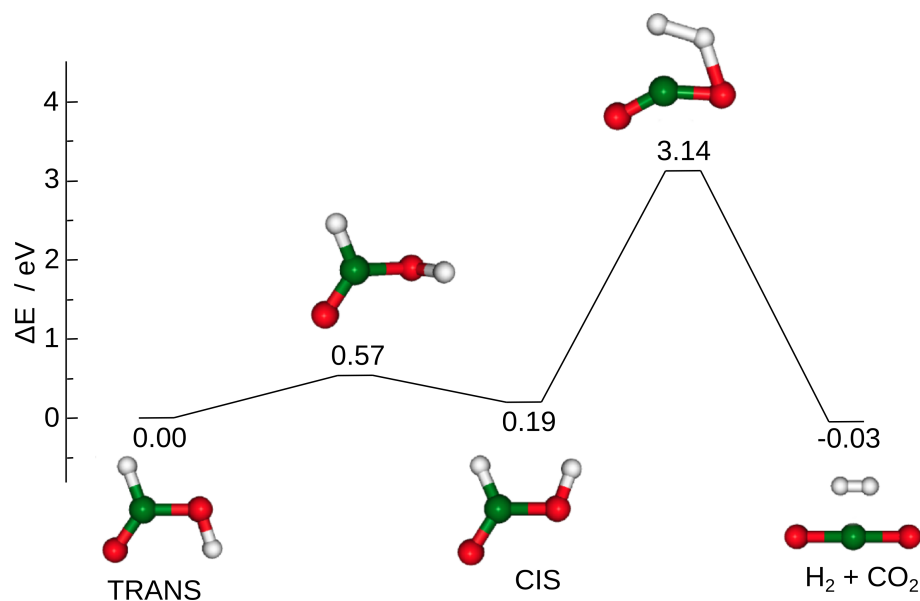# Appendix to Chapter 2

Supplementary to Section 2.1

Figure S1: DFT-calculated energy profile for decarboxylation of formic acid in the absence of a catalyst. All structures were fully optimized using DFT method with the hybrid B3LYP functional and def2-TZVP atomic basis set which has been used for all atoms. Color coding of atoms: green – carbon, red – oxygen, white – hydrogen.
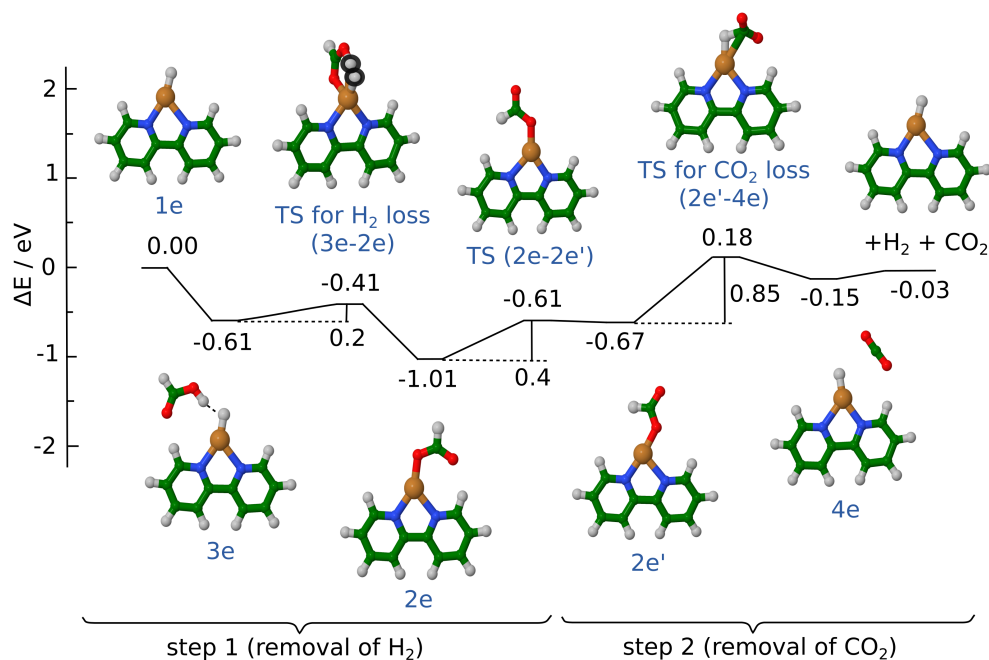
Figure S2: DFT-calculated energy profile for the two reaction steps in the catalytic cycle for [(bipy)Cu(H)], 1e in the gas-phase. All structures were fully optimized using DFT method with the hybrid B3LYP functional and def2-TZVP atomic basis set which has been used for all atoms. Color coding of atoms: green – carbon, red – oxygen, white – hydrogen, blue – nitrogen, brown – copper.
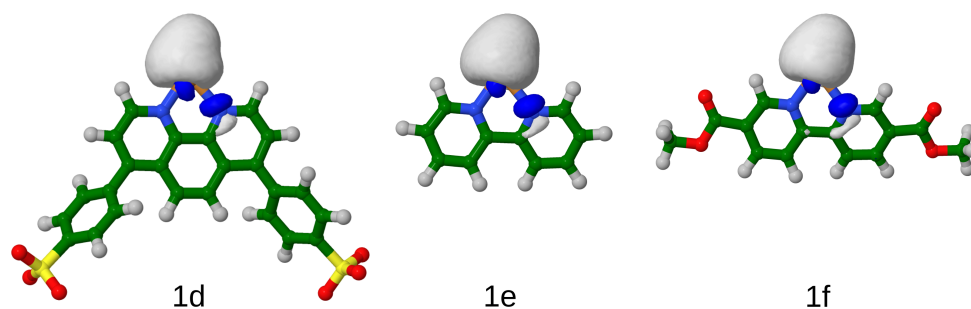

Figure S3: DFT-calculated HOMOs for the N,N-bidentate{CuH} complexes 1d, 1e and 1f. All structures were fully optimized using DFT method with the hybrid B3LYP functional and def2-TZVP atomic basis set which has been used for all atoms.
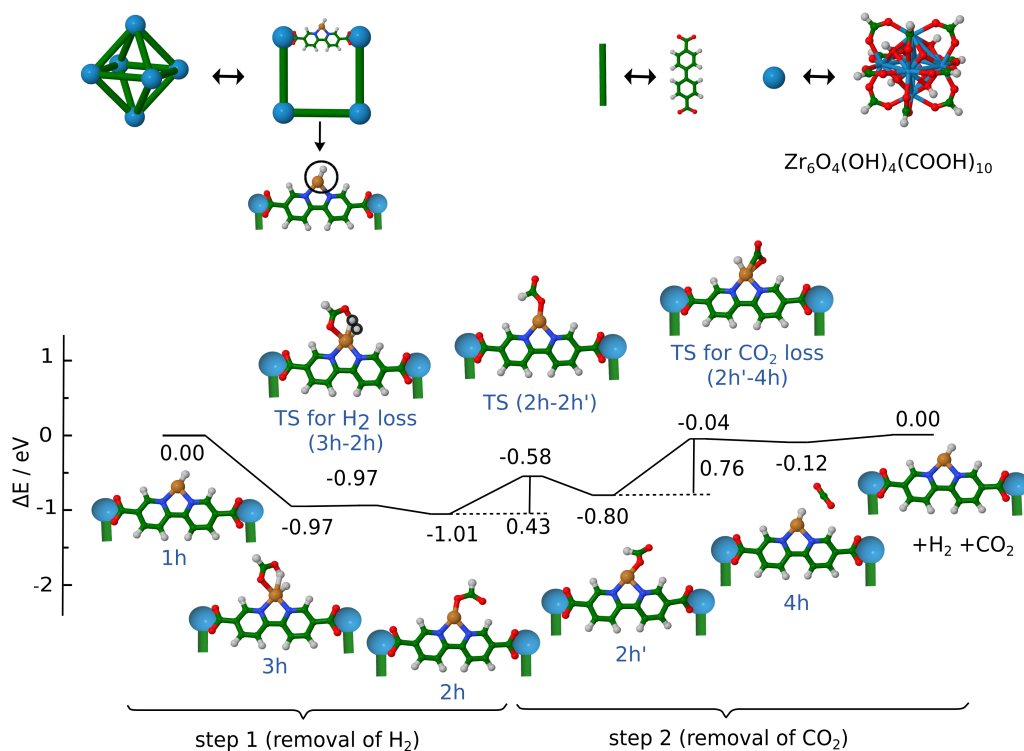
Figure S4: DFT-calculated energy profile for the two reaction steps in the catalytic cycle for the model MOF system 1h. All structures were fully optimized using DFT method with the PBE functional with resolution of identity (W06), def2-SVP atomic basis set and relativistic ECP for Zr atoms. Square of the octahedron consists of 3 biphenyl chains labeled by green sticks, 1 (bipy*)Cu(H) chain and 4 $Zr_6O_4(OH)_4(COOH)_{10}$ nodes in the corners labeled by blue spheres.

Table S1: Summary of key Gibbs energies ΔG associated with steps I and II.

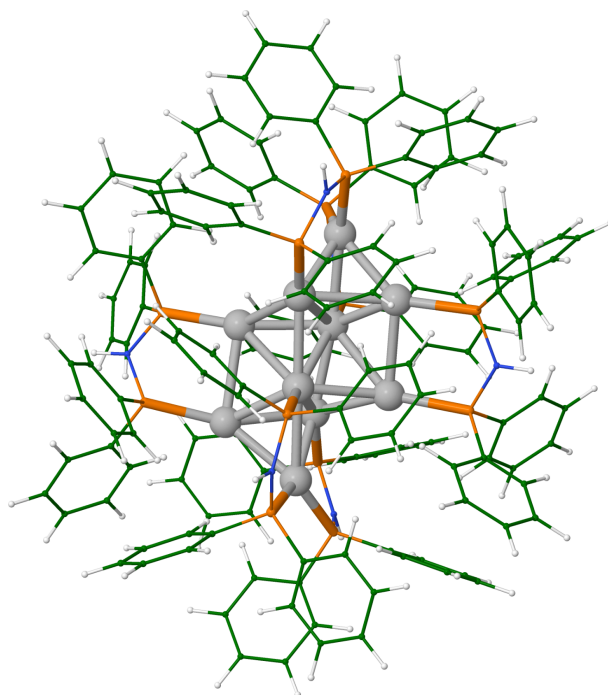| Model	3	TS3-2	2	TS2-2'	2'	TS2'-4	4
[(phen*)Cu(H)]$^{2-}$, 1d	-0.19	-0.04	-1.00	-0.84	-0.93	-0.12	-0.43
[(bipy*)Cu(H)], 1f	-0.08	-0.05	-0.91	-0.58	-0.64	0.13	-0.40
[UiO-67(bipy)Cu(H)in], 1g	-0.51	-0.56	-1.05	-0.64	-0.66	-0.22	-0.36

Supplementary to Section 2.2

Figure S17: Fully optimized structure of $[Ag_{10}(dppa)_6]^{2+}$. Color legend: Ag (silver); P (orange); N (blue); H (white) and C (green).
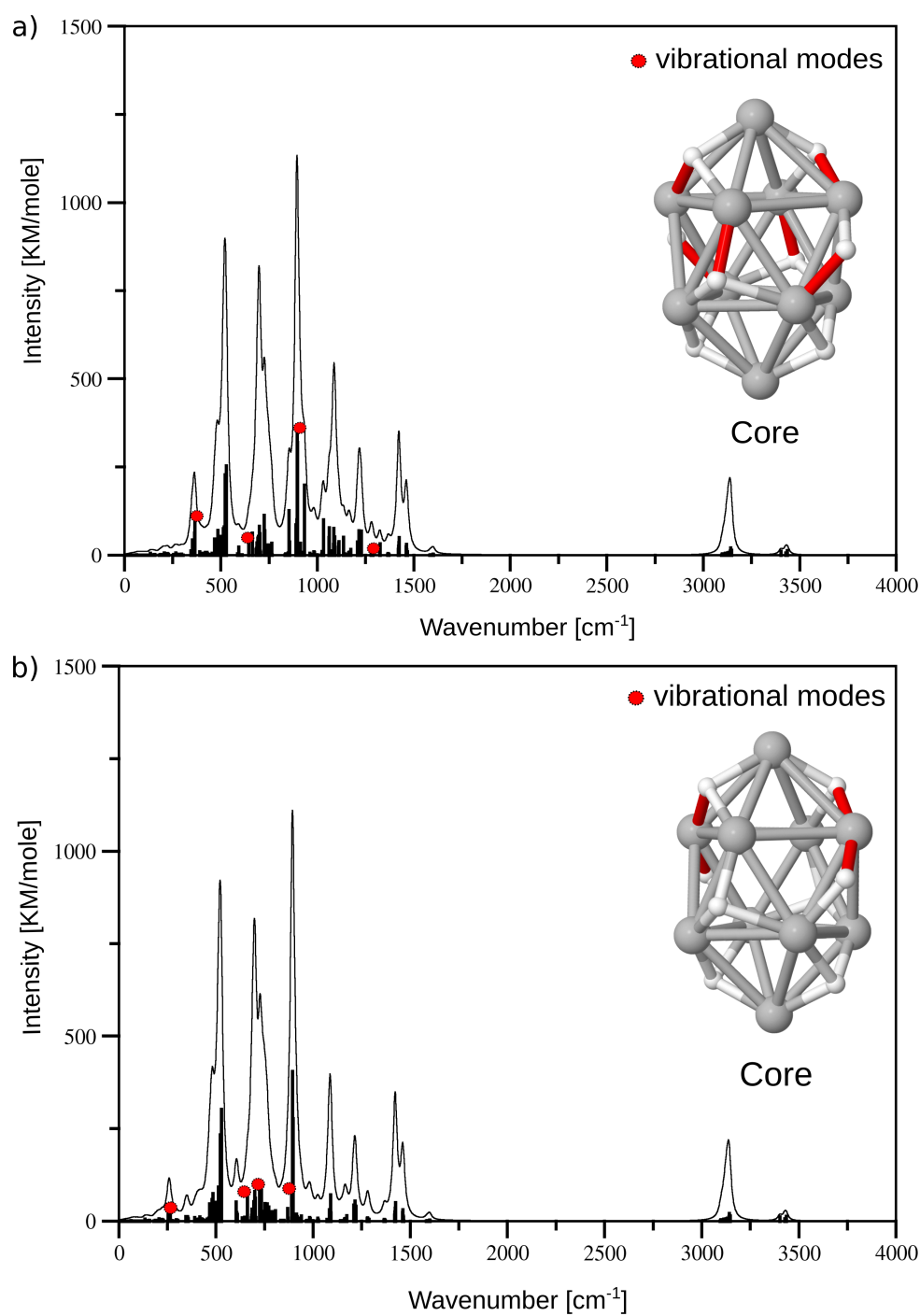
Figure S18: Predicted IR spectra of a) $[Ag_{10}H_8(dppa)_6]^{2+}$ and b) $[Ag_{10}D_8(dppa)_6]^{2+}$. Red dots are assigned to stretching and bending modes of Ag-H or Ag-D.

Appendix to Chapter 3
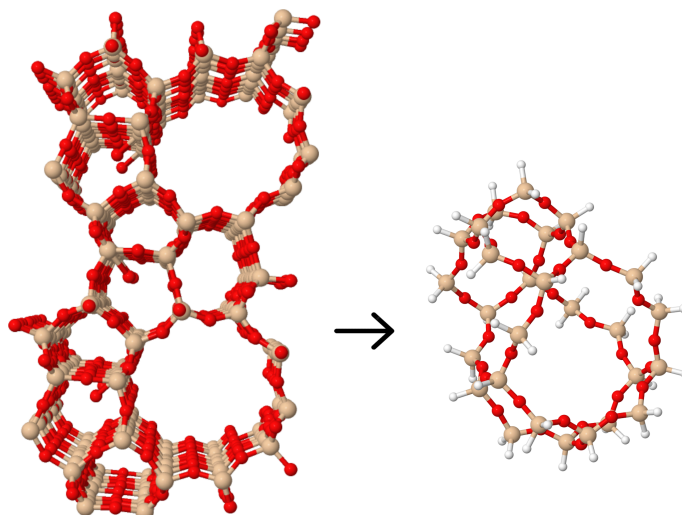
Supplementary to Section 3.1

Figure S1: Structure of the ZSM-5 zeolite framework (left) and optimized structure representing ZSM-5 unit (right). The model consists of 28 Si and 77 O atoms. The terminal O atoms are replaced by 42 H atoms. The cross sections for the small and large pore in our calculated model are 5.2 x 5.8 Å and 8.2 x 8.8 Å, respectively.

Table S1: Ru-Ru bond distances (in Å) of non-ligated and ligated Ru_4^+ cluster in the gas phase and inside the zeolite. The figure below the table provides the labeling for the Ru atoms.

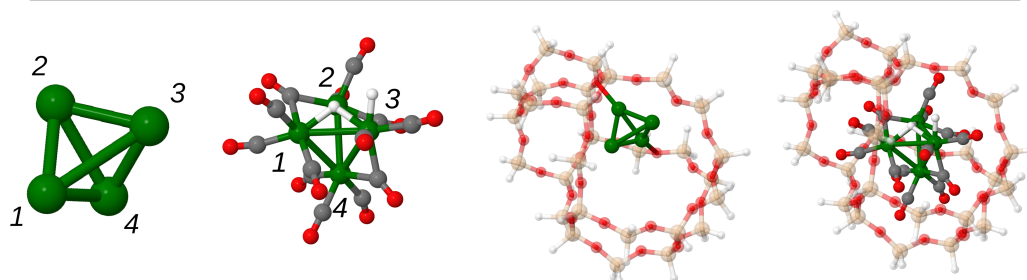|	Ru_4^+	$Ru_4CO_{13}H_2^+$	Ru_4^+/ZSM-5	$Ru_4CO_{13}H_2^+$/ZSM-5
Ru1-Ru2	2.45	2.76	2.29	2.74
Ru1-Ru3	2.63	3.07	2.92	2.96
Ru1-Ru4	2.26	2.88	2.28	2.91
Ru2-Ru3	2.75	2.80	2.30	2.83
Ru2-Ru4	2.64	2.96	2.68	3.00
Ru3-Ru4	2.26	2.84	2.29	2.92

Table S2: Distances between Ru and C atoms (in) of free and zeolite anchored $Ru_4(CO)_{13}H_2^+$. The labeling of atoms is shown in the figure below the table.

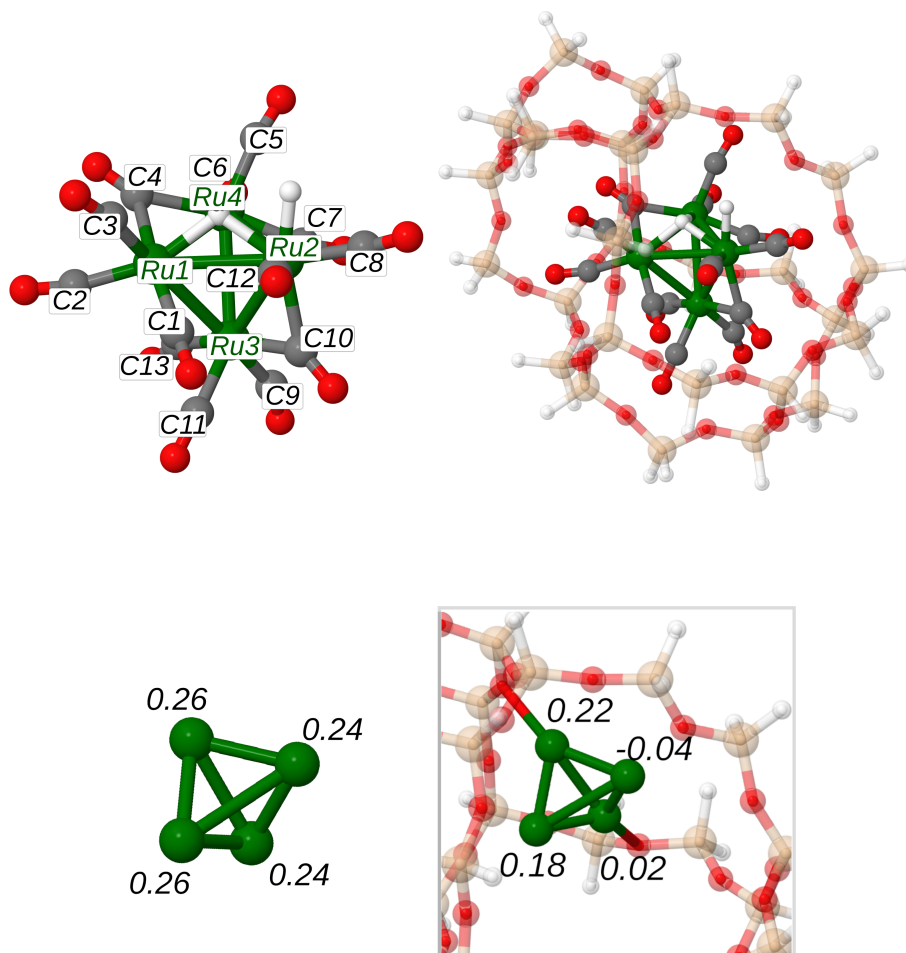|	$Ru_4CO_{13}H_2^+$	$Ru_4CO_{13}H_2^+$/ZSM-5
Ru1-C3	1.92	1.90
Ru2-C12	1.89	1.89
Ru2-C8	1.90	1.91
Ru1-C2	1.90	1.90
Ru1-C1	1.91	1.89
Ru3-C11	1.90	1.89
Ru3-C13	1.92	1.89
Ru3-C9	1.92	1.93
Ru2-C10	2.20	2.13
Ru3-C10	2.11	2.18
Ru2-C7	2.35	2.33
Ru4-C7	2.00	1.98
Ru4-C5	1.90	1.89
Ru1-C4	2.28	2.22
Ru4-C4	2.05	2.11
Ru4-C6	1.90	1.88

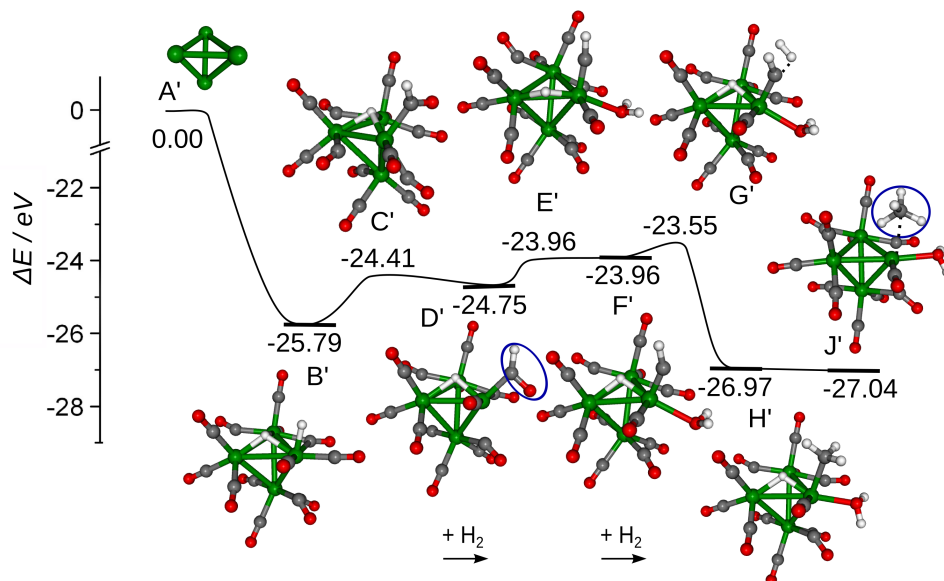Figure S2: Mulliken charges of free Ru_4^+ and of Ru_4^+ inside the zeolite pore.

Figure S3: DFT-calculated energy profile for CO methanation mediated by the hydrido carbonyl complex $Ru_4CO_{13}H_2^+$. The figure has been adapted from the reference [7] of the article in Section 3.1 with permission from the John Wiley & Sons. Ru, C, O, and H atoms are depicted as green, gray, red, and white spheres.

Table S3: Energies of the local minima and transition states (in eV) of the reaction pathways shown in Figure 2 for the $Ru_4CO_{13}H_2^+$/ZSM-5 model and shown in Figure S2 for gas phase $Ru_4CO_{13}H_2^+$. The structures of $Ru_4CO_{13}H_2^+$/ZSM-5 are denoted as A, B, etc. and the structures of $Ru_4CO_{13}H_2^+$ are denoted as A', B', etc. The energies are given relative to the energy of structures B and B', respectively.

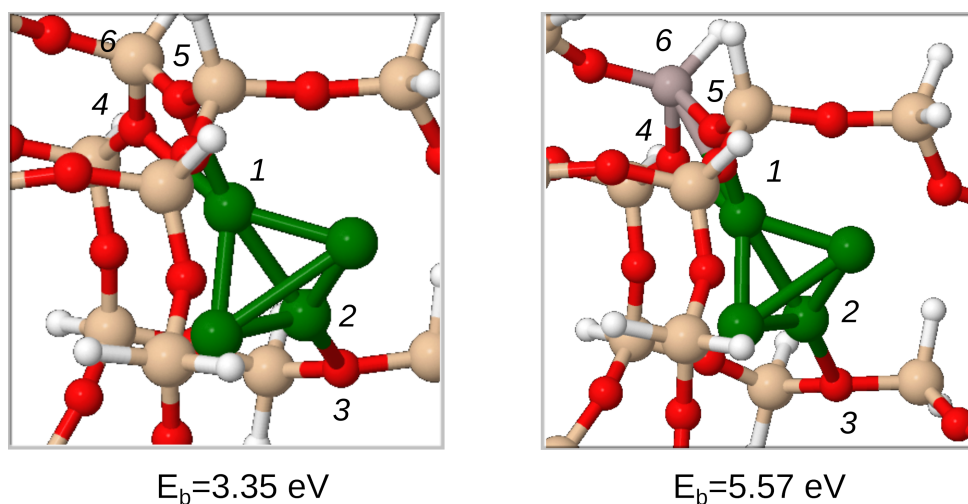|	$Ru_4CO_{13}H_2^+$/ZSM-5	$Ru_4CO_{13}H_2^+$
B/B'	0.00	0.00
C/C'	+1.43	+1.38
D/D'	+0.97	+1.04
E/E'	+2.09	+1.83
F/F'	+1.81	+1.83
G/G'	+2.90	+2.24
H/H'	-1.23	-1.18
I/I'	-0.84	—
J/J'	-1.56	-1.25

E_b=3.35 eV $\qquad\qquad\qquad\qquad$ E_b=5.57 eV

Figure S4: Optimized structures of a) Ru_4^+ (spin multiplicity 2) inside the pore of the ZSM-5 zeolite consisting of Si and O atoms only and b) Ru_4^+ (spin multiplicity 1) inside an Al-doped pore of the ZSM-5 zeolite. Ru, Al, Si, and O atom are depicted by green, violet, pink, and red spheres, respectively.

Table S4: Distances (in Å) between Ru and O, Si, and Al atoms of Ru_4^+ anchored in a Si-only and a Al-doped ZSM-5 zeolite pore. The labeling of the atoms is shown in Figure S4.

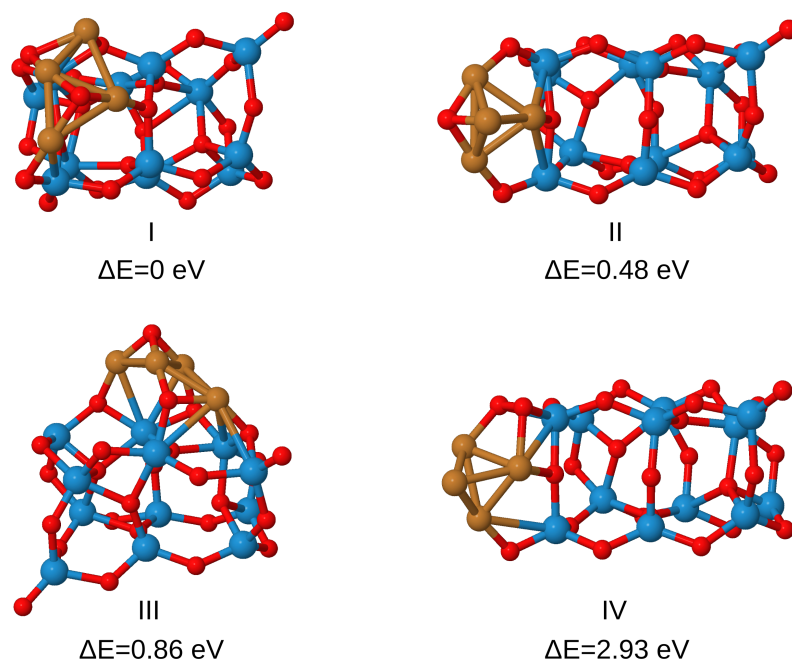|	Ru_4^+/ZSM-5	Ru_4^+/Al-doped ZSM-5
Ru1-O4	2.43	2.14
Ru1-O5	2.55	2.18
Ru2-O3	2.54	2.52
Ru1-Si6	3.14	—
Ru1-Al6	—	2.95

Appendix to Chapter 4

Supplementary to Section 4.1

I
ΔE=0 eV

II
ΔE=0.48 eV

III
ΔE=0.86 eV

IV
ΔE=2.93 eV

Figure S9: Isomers of $Cu_4O_2/Zr_{12}O_{24}$ illustrating energetically favorable isomer, with Cu_4 rhombic structure interacting with Zr and O atoms of $Zr_{12}O_{24}$ unit.

I
ΔE=0 eV

II
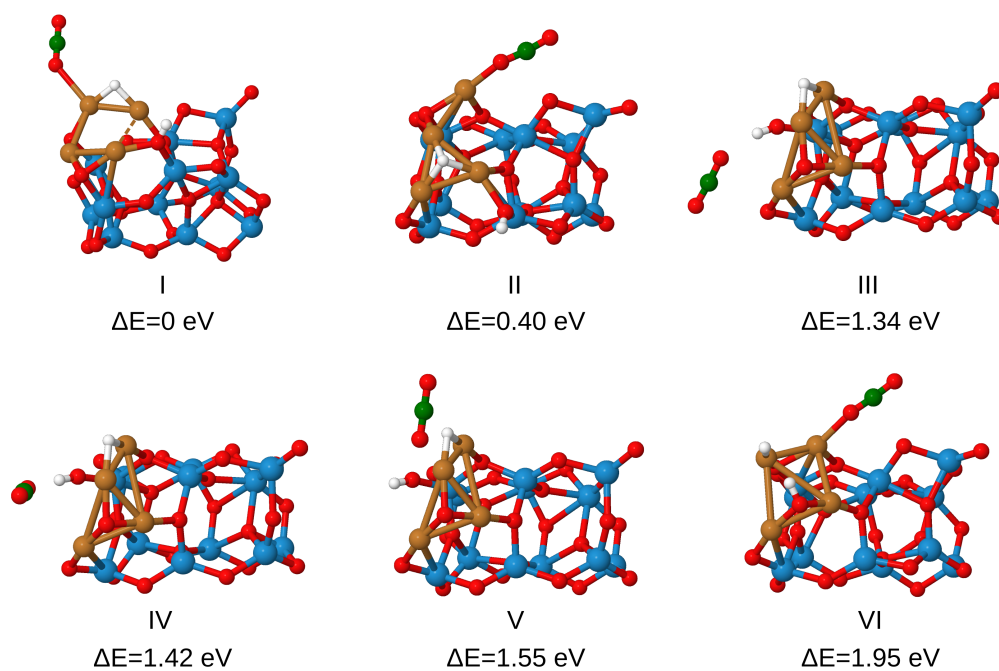ΔE=0.40 eV

III
ΔE=1.34 eV

IV
ΔE=1.42 eV

V
ΔE=1.55 eV

VI
ΔE=1.95 eV

Figure S10: Isomers of $Cu_4O_2/Zr_{12}O_{24}$ with bound H_2 and CO_2. The lowest energy isomer I serves as a starting point for methanation reaction and involves CO_2 bound to one Cu atom from Cu_4O_2 subunit.
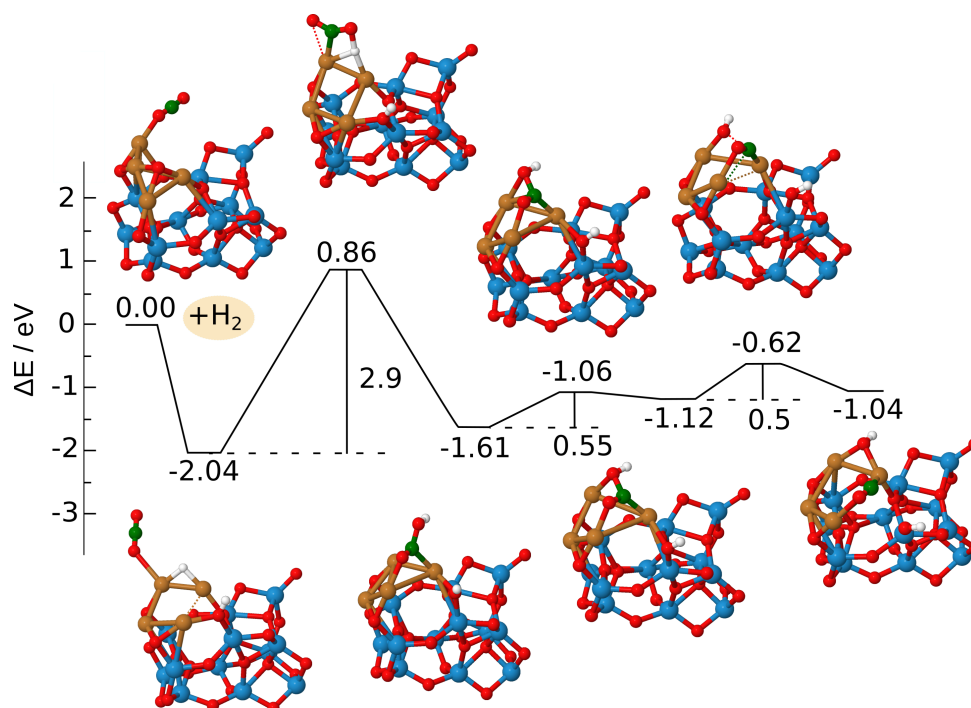
Figure S11: DFT-calculated energy profile for -COOH formation at $Cu_4O_2/Zr_{12}O_{24}$, using B3LYP functional and def2-TZVP basis with relativistic ECP for Zr atoms.

Supplementary to Section 4.2

Table S1: Values of the relative electronic (ΔE) and activation energies (E$_a$), of Gibbs relative (ΔG) and activation energies at 298.15 K (G$_a$) at the bimetallic cluster/support for the first and second hydrogenation step (A-K) of the methanation reaction.

	ΔE [eV]	E$_a$	$\Delta G_{298K}[eV]$	G$_a$
A	0.00		0.00	
B	-2.01		-1.45	
B'	-1.58	0.43	-0.95	0.49
C	-1.62		-0.97	
C'	-1.48	0.14	-0.85	0.12
D	-1.60		-0.92	
D'	-1.26	0.34	-0.58	0.33
E	-2.48		-1.70	
E'	-1.90	0.58	-1.12	0.57
F	-1.91		-1.19	
F'	-1.83	0.08	-1.08	0.11
G	-2.72		-1.92	
G'	-1.89	0.83	-0.77	1.15
H	-2.40		-1.15	
H'	-1.31	1.09	-0.06	1.08
I	-2.21		-0.79	
I'	-2.12	0.09	-0.68	0.11
J	-2.29		-0.84	
J'	-1.97	0.32	-0.50	0.33
K	-2.30		-0.86	

Table S2: Values of the relative electronic (ΔE) and activation energies (E_a), of Gibbs relative (ΔG) and activation energies at 298.15 K (G_a) at the bimetallic cluster/support for the third and fourth hydrogenation step (K'-V) of the methanation reaction, and for methanol branch (q'-s).

	ΔE [eV]	E_a	ΔG_{298K} [eV]	G_a
K'	-1.70	0.60	-0.41	0.45
L	-1.99		-0.74	
L'	-1.89	0.10	-0.26	0.49
M	-2.72		-0.93	
N	-2.04		-0.82	
N'	-1.98	0.06	-0.69	0.12
O	-2.03		-0.72	
O'	-1.85	0.18	-0.57	0.15
P	-2.17		-0.78	
P'	-2.09	0.08	-0.71	0.06
Q	-2.77		-1.32	
Q'	-0.52	2.25	0.88	2.20
R	-1.42		-0.06	
R'	0.41	1.83	1.67	1.73
S	-0.20		0.67	
S'	0.13	0.33	1.38	0.71
T	-1.13		0.28	
T'	-0.78	0.35	0.58	0.30
U	-3.00		-1.51	
V	-1.57		-0.65	
q'	-2.64	0.13	-0.74	0.58
q"	-2.43	0.34	-0.61	0.71
r	-3.50		-1.55	
s	-2.49		-1.11	
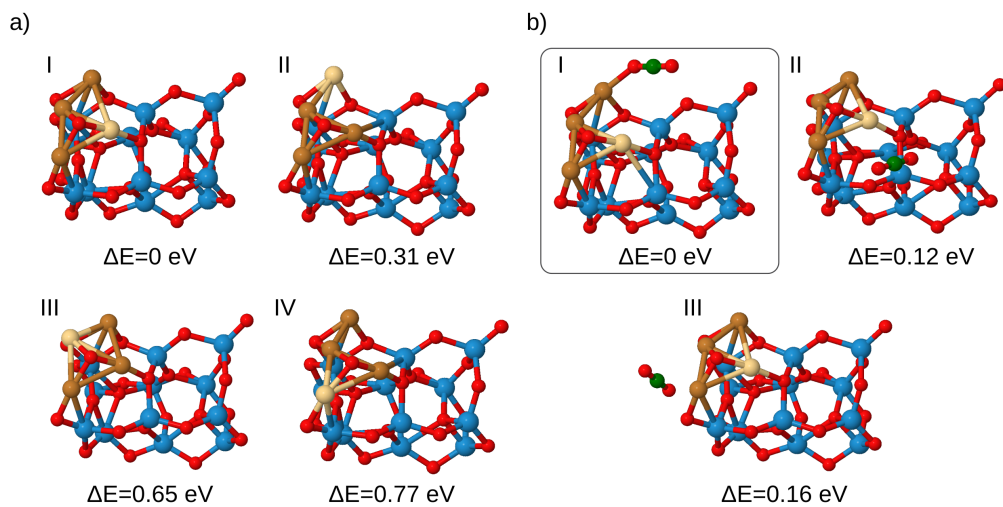
Figure S1: Isomers for a) $Cu_3PdO_2/Zr_{12}O_{24}$, and b) $CO_2-Cu_3PdO_2/Zr_{12}O_{24}$ with the window denoting the lowest energy isomer.

Table S3: Values of the relative electronic (ΔE) and activation energies (E_a) at the monometallic cluster/support for the first and second hydrogenation step (A-K) of the methanation reaction.

	ΔE [eV]	E_a
A	0.00	
B	-2.27	
B'	/	/
C	/	
C'	-1.23	1.04
D	-1.53	
D'	-1.44	0.09
E	-2.44	
E'	-2.25	0.19
F	-2.64	
F'	-2.20	0.44
G	-2.95	
G'	-2.10	0.85
H	-2.82	
H'	-1.56	1.26
I	-2.57	
I'	-2.43	0.14
J	-2.71	
J'	-2.35	0.37
K	-2.53	
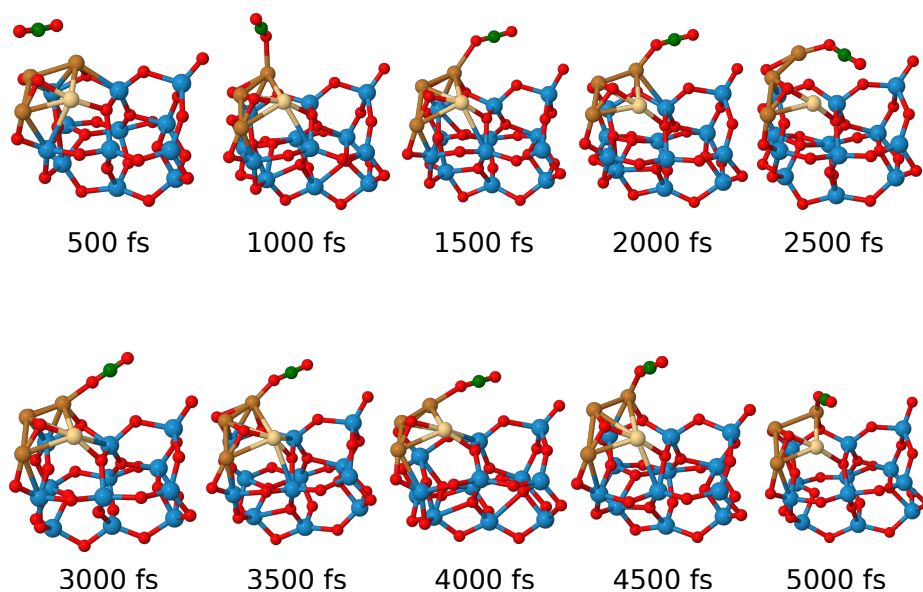
Figure S2: DFT-MD calculations have been employed in order to determine the preferential binding site of CO_2 on $Cu_3PdO_2/Zr_{12}O_{24}$.

Table S4: Values of the relative electronic (ΔE) and activation energies (E_a) at the monometallic cluster/support for the third and fourth hydrogenation step (K'-V) of the methanation reaction, and for methanol branch (q'-s).

	ΔE [eV]	E_a
K'	-2.01	0.52
L	-2.40	
L'	-1.86	0.54
M	-2.39	
N	-2.18	
N'	/	/
O	/	
O'	/	/
P	/	
P'	-1.64	0.54
Q	-3.13	
Q'	-0.94	2.19
R	-1.02	
R'	1.00	2.02
S	0.10	
S'	0.40	0.30
T	-1.43	
T'	-1.15	0.28
U	-3.31	
V	-1.61	
q'	-2.57	0.56
r	-3.18	
s	-2.78	
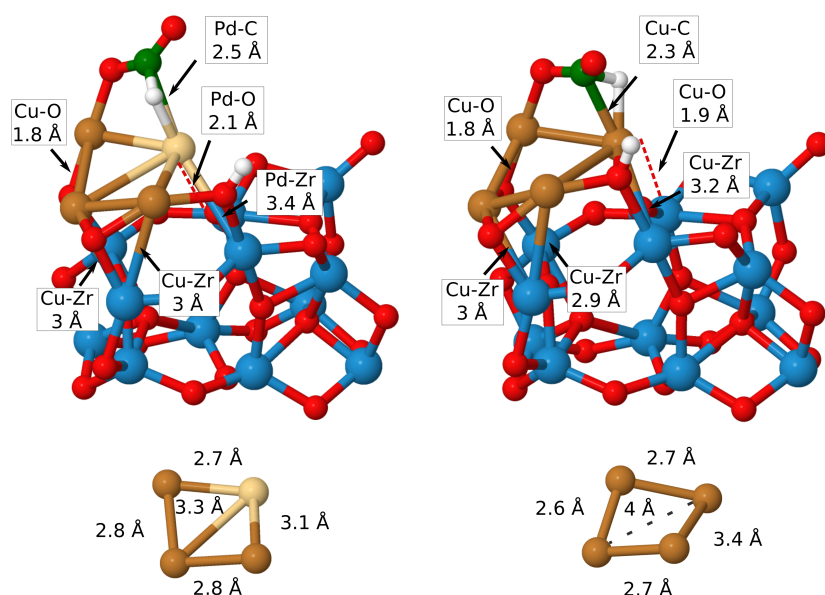
Figure S3: Comparison of chosen bond lengths between $Cu_3PdO_2/Zr_{12}O_{24}$, $Cu_4O_2/Zr_{12}O_{24}$, and their metallic tetramer subunits.
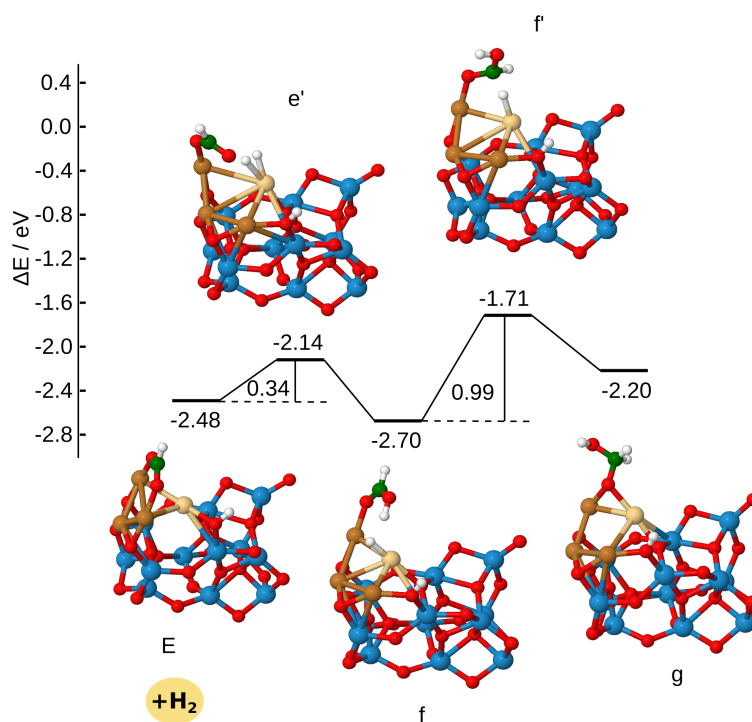

Figure S4: Branch of the energy profile for the second hydrogenation step of the methanation reaction taking place at Pd atom.
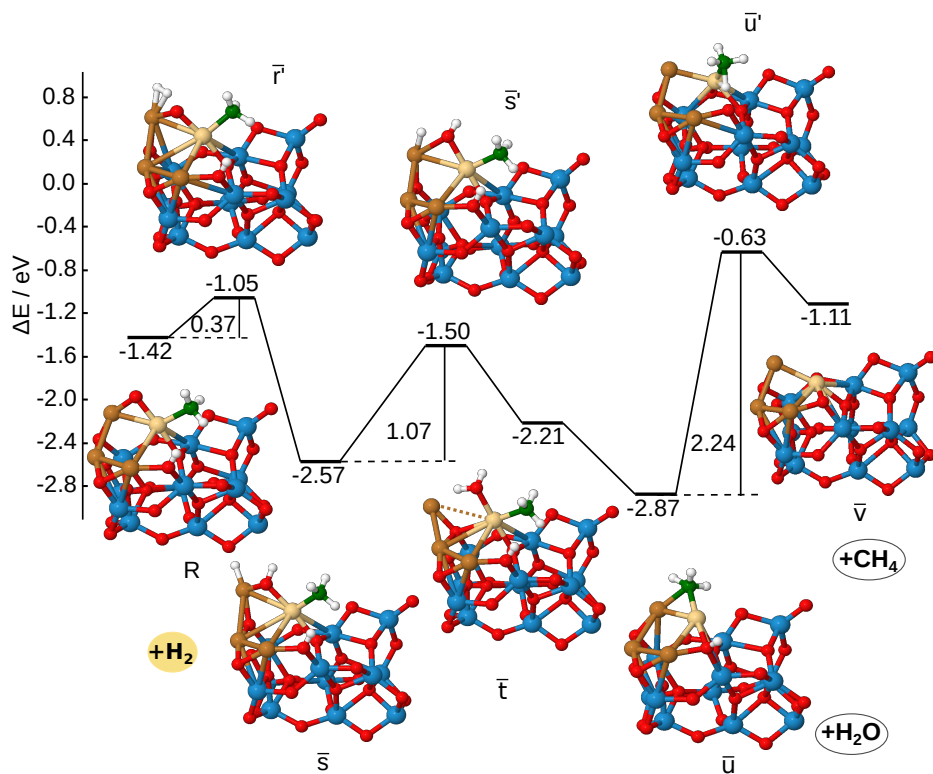
Figure S5: Branch I) of the energy profile for the methanation reaction within the 4th hydrogenation step for the formation of H_2O and CH_4.
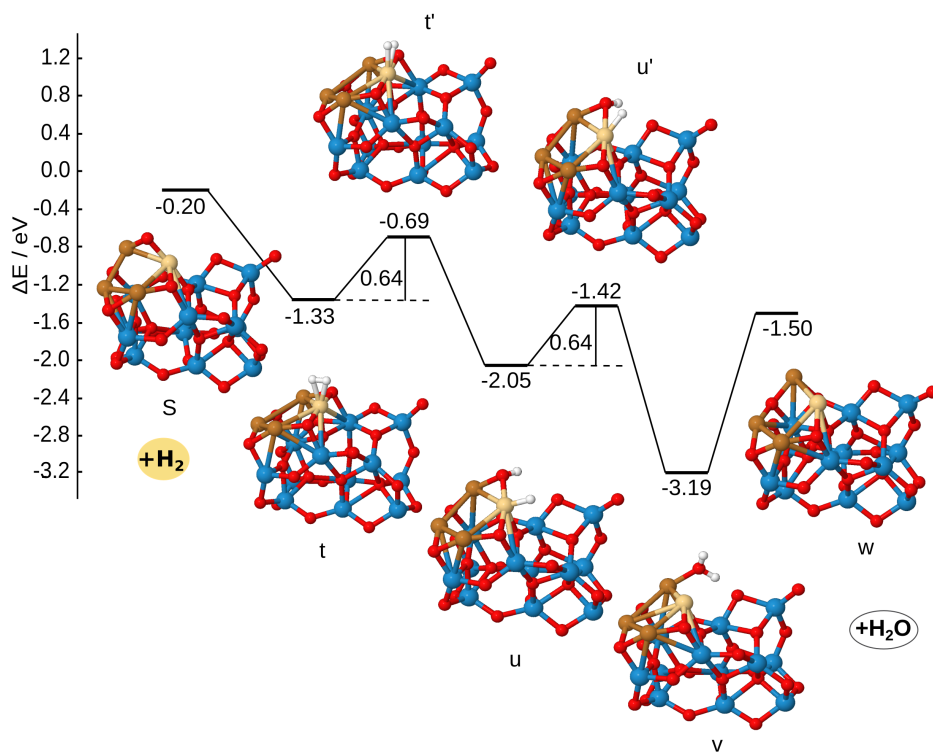

Figure S6: Branch II) of the energy profile for the methanation reaction within the 4th hydrogenation step for the formation of the second H_2O mediated by Pd atom.
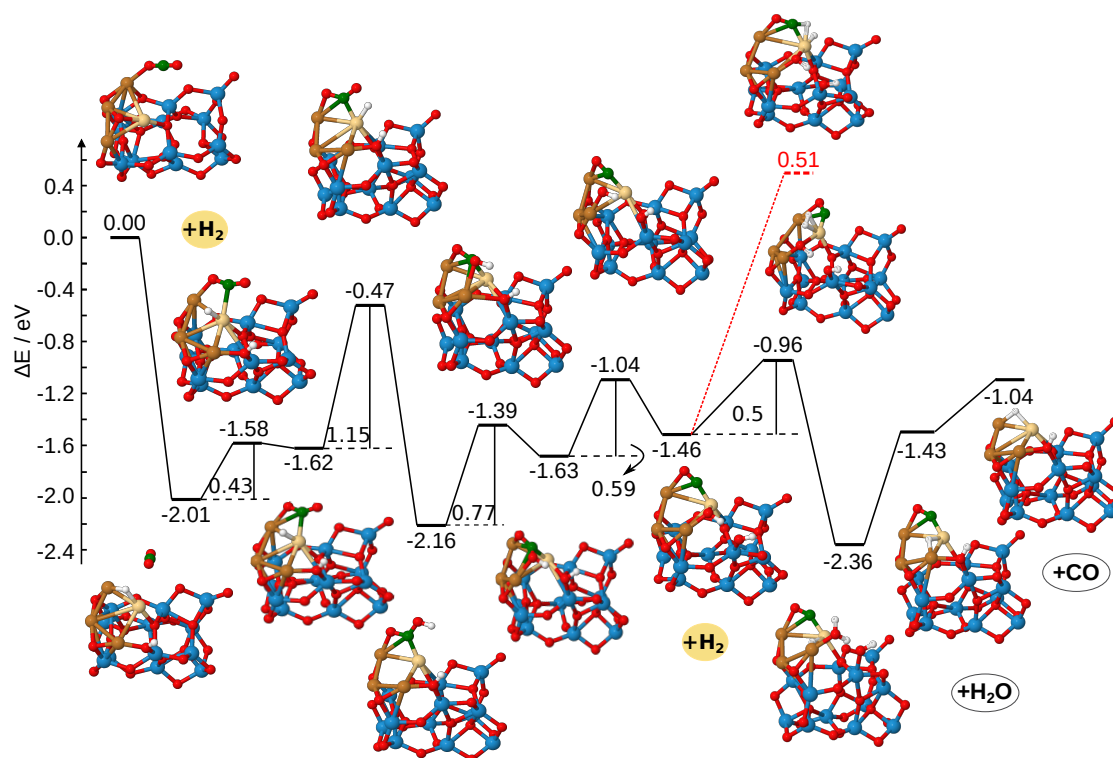
Figure S7: RWGS pathway at $Cu_3PdO_2/Zr_{12}O_{24}$ showing higher energy values compared to the formate route. Dotted red line represents transition state for the formation of -OCH.
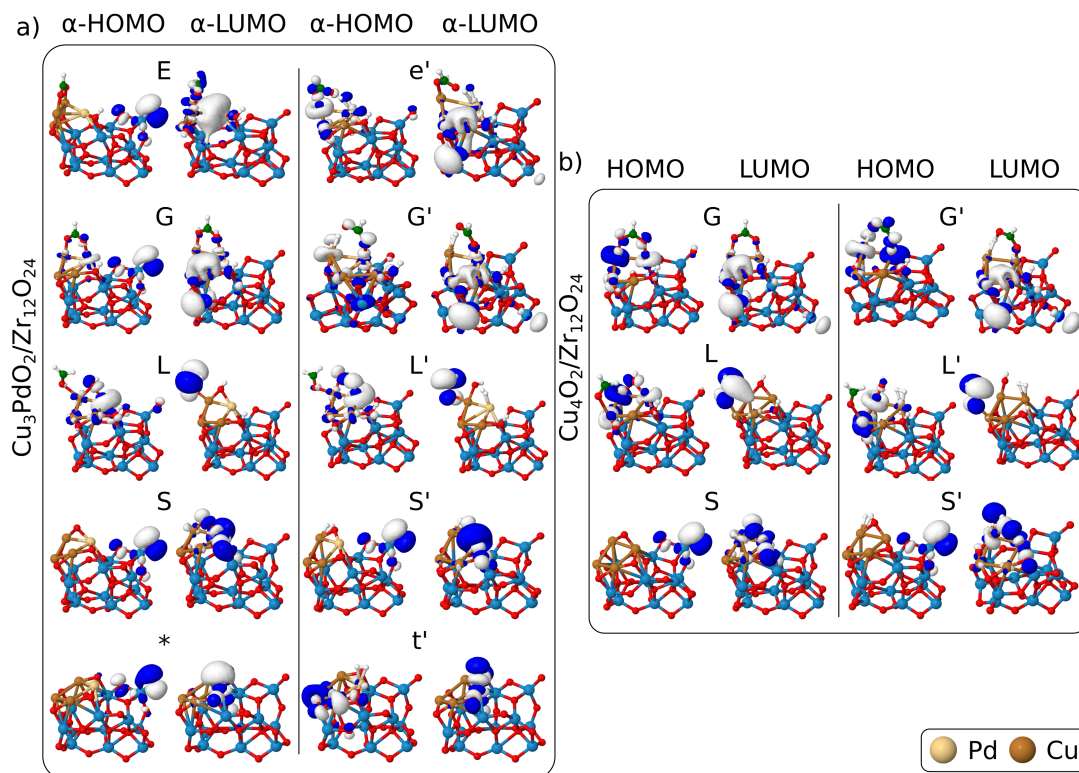
Figure S8: Molecular orbitals of selected minima and transition states within hydrogenation steps for a) $Cu_3PdO_2/Zr_{12}O_{24}$, and b) $Cu_4O_2/Zr_{12}O_{24}$.

Table S5: Charge transfer (based on natural charges) at the Cu or Pd atom between the minimum (Min) and transition state (TS) associated with the 2nd, 3rd and 4th hydrogenation step for bimetallic (Cu_3PdO_2) and monometallic cluster (Cu_4O_2) at support. Notice that the minimum * belongs to the 4th hydrogenation step and is not shown in Figure S6. Activation energies (E_a) for each TS are given in eV.

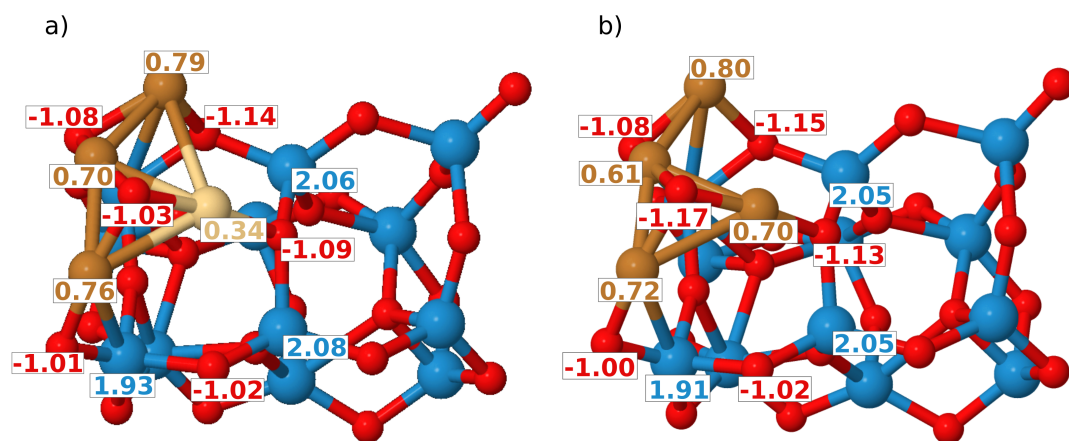|	$Cu_3PdO_2/Zr_{12}O_{24}$		
Min-TS	Cu	Pd	E_a [eV]
G-G'	0.11		0.83
E-e'		0.02	0.34
L-L'		0.27	0.10
S-S'	0.20		0.33
*-t'		0.31	0.64
	$Cu_4O_2/Zr_{12}O_{24}$		
G-G'	0.10		0.85
L-L'	0.08		0.54
S-S'	0.01		0.30

Figure S9: Analysis of natural charges for a) bimetallic (Cu_3PdO_2), and b) monometallic (Cu_4O_2) cluster at support, indicating larger charge transfer from the monometallic cluster to the support compared to the bimetallic cluster.

Curriculum Vitae

ANTONIJA MRAVAK

Date of birth: 06.08.1991
Place of birth: Split, Croatia
e-mail: antonija@stim.unist.hr

EDUCATION

- 2018.-today
  Postgraduate university study in Biophysics, Faculty of Science, University of Split

- 2013.-2016.
  Graduate university study in Physics, Faculty of Science, University of Split

- 2010.-2013.
  Undergraduate university study in Physics, Faculty of Science, University of Split

- 2006.-2010.
  IV. gymnasium "Marko Marulić", Split

EMPLOYMENT

- 2018.-today
  Research Asistent/PhD student at Center of Excellence for Science and Technology-Integration of Mediterranean region (STIM), University of Split, Croatia

- September-December 2017.
  Physics teacher, Elementary school "Prof. Filip Lukas", Kaštel Stari

- January-July 2017.
  Internship at Institut for Science and Technology (IST), Klosterneuburg, Austria

CONFERENCES, WORKSHOPS

- 2023. J. Heyrovský Institute, Prague, Czech Republic, "Cluster Meeting 2023"
  Poster: "CO_2 conversion on monometallic and bimetallic Pd-doped copper tetramer clusters at zirconia support"

- 2022. Virtual Symposium COSY (COST Action) WG3 S-1, "Confined Metal and Metal-Oxide Nanoparticles and Clusters Down to the Subnanometer Scale"
  Presentation: "Mechanism of catalytic CO_2 hydrogenation to methane and methanol using a bimetallic Cu_3Pd cluster at zirconia support"

- 2021. MedILS, Split, Croatia, "System approaches in cancer"

- 2021. MedILS, Split, Croatia, "Advances in biomedical research IV"

- 2019. University of Split, STIM, Croatia "Interdisciplinary endeavour in technology at nanoscale, water and environment"
  Poster: "Design of a new metal-organic framework catalyst for hydrogen storage: theoretical and experimental assessment"

- 2019. University of Split, Croatia, "4th Grandmaster Early-Career Workshop in Physics"
  Poster : "Design of a new metal-organic framework catalyst for hydrogen storage"

- 2018. Lyon, France, "Annual International associated laboratory NCBA workshop"
  Presentation: "Catalytic properties of ligated metal hydrides for decomposition of formic acid into H_2 and CO_2; transferring gas phase mechanism into metal-organic framework (MOF)"

AWARDS

- L'Oréal Adria and UNESCO scholarship "For Woman in Science", 2023.

- Poster award, 2nd place, at "Interdisciplinary endeavour in technology at nanoscale, water and environment", University of Split, 2019.

- Dean award, Faculty of Science, University of Split, 2016.

- Dean award, Faculty of Science, University of Split, 2013.

Publications

1. Margarita Bužančić Milosavljević, Antonija Mravak, Martina Perić Bakulić, Vlasta Bonačić-Koutecký, (2023). Model systems for dye-sensitized solar cells: cyanidin-silver nanocluster hybrids at TiO_2 support. *RSC Adv.*, 13, 6010-6016.

2. Antonija Mravak, Stefan Vajda, and Vlasta Bonačić-Koutecký, (2022). Mechanism of catalytic CO_2 hydrogenation to methane and methanol using a bimetallic Cu_3Pd cluster at a zirconia support. *J. Phys Chem. C*, 126(43), 18306-18312.

3. Avik Halder, Cristina Lenardi, Janis Timoshenko, Antonija Mravak†, Bing Yang, Lakshmi K Kolipaka, Claudio Piazzoni, Sönke Seifert, Vlasta Bonačić-Koutecký, Anatoly I. Frenkel, Paolo Milani, and Stefan Vajda, (2021). CO_2 methanation on Cu-cluster decorated zirconia supports with different morphology: A combined experimental in situ GIXANES/GISAXS, ex situ XPS and theoretical DFT study. *ACS Catal*, 11(10), 6210-6224.

4. Steven Daly, Sebastian Weske, Antonija Mravak†, Marjan Krstić, Alexander Kulesza, Rodolphe Antoine, Vlasta Bonačić-Koutecký, Philippe Dugourd, Konrad Koszinowski, Richard A. J. O'Hair, (2021). Phenyl argentate aggregates $[Ag_nPh_{n+1}]^-$ ($n = 2 - 8$): models for the self-assembly of atom-precise polynuclear organometallics. *J. Chem. Phys.*, 154, 224301.

5. Antonija Mravak, Marjan Krstić, Sandra M. Lang, Thorsten M. Bernhardt, and Vlasta Bonačić-Koutecký, (2020). Intrazeolite CO methanation by small ruthenium carbonyl complexes: Translation from free clusters into the cage. *ChemCatChem*, 12(15), 3857-3862.

6. Howard Z. Ma, Alasdair I. McKay, Antonija Mravak, Michael S. Scholz, Jonathan M. White, Roger J. Mulder, Evan J. Bieske, Vlasta Bonačić-Koutecký, and Richard A. J. O'Hair, (2019). Structural characterization and gas-phase studies of the $[Ag_{10}H_8(L)_6]^{2+}$ nanocluster dication. *Nanoscale*, 11(47), 22880-22889.

7. Richard A. J. O'Hair, Antonija Mravak, Marjan Krstić, and Vlasta Bonačić-Koutecký, (2019). Models facilitating the design of a new metal-organic framework catalyst for the selective decomposition of formic acid into hydrogen and carbon dioxide. *ChemCatChem*, 11(10), 2443-2448.

8. Athanasios Zavras, Antonija Mravak, Margarita Bužančić, Jonathan M. White, Vlasta Bonačić-Koutecký, Richard A. J. O'Hair, (2019). Structure of the ligated Ag_{60} nanoparticle $[Cl@Ag_{12}@Ag_{48}(dppm)_{12}]$ (where dppm = bis(diphenylphosphino)methane). *Chinese J. Chem. Phys.*, 32(2), 182-186.

† equal contribution